Université de Montréal

Genome-wide CRISPR screens for the interrogation of genome integrity maintenance networks

Par

Yahya Benslimane

Programme de Biologie Moléculaire, option Biologie des Systèmes

Faculté de Médecine

Thèse présentée en vue de l'obtention du grade de Philosophiae Doctor (Ph. D.)

en Biologie Moléculaire, option Biologie des Systèmes

Août 2020

Université de Montréal

Unité académique : Institut de Recherche en Immunologie et Cancer, Faculté de Médecine

---

Cette thèse intitulée

Genome-wide CRISPR screens for the interrogation of genome integrity maintenance networks

Présentée par

Yahya Benslimane

A été évalué(e) par un jury composé des personnes suivantes

Jean-Claude Labbé
Président-rapporteur

Lea Harrington
Directeur de recherche

Frédérick Antoine Mallette
Membre du jury

Alexandre Orthwein
Examinateur externe (pour une thèse)

Résumé

Le matériel génétique (l'ADN) d'un organisme contient l'information nécessaire à sa survie, sa croissance et sa reproduction. La perte de cette information affecte grandement la santé de l'organisme et cette altération est l'un des facteurs les plus courants dans le vieillissement ou le cancer. Quasiment toutes les cellules d'un organisme contiennent une copie de ce matériel génétique, communément appelé le génome, et font usage de plusieurs mécanismes pour en réparer les sections endommagées ainsi que pour le copier avec précision lors de la division cellulaire. Nous avons cherché à étudier les processus cellulaires qui maintiennent la stabilité génomique en inactivant systématiquement chacun des gènes avec la technique de criblage par CRISPR afin d'en étudier les rôles. Nous avons effectué ces criblages à l'échelle du génome dans des lignées cellulaires humaines en combinaison avec des perturbations chimiques dans le but d'identifier l'effet du traitement chimique ou le rôle de gènes qui exacerbent ou atténuent la perturbation.

Nous nous sommes d'abord concentrés sur le resvératrol, une molécule initialement extraite de plantes qui a démontré des propriétés antivieillissement dans certains organismes modèles ainsi que la capacité d'inhiber la prolifération cellulaire. Notre criblage génétique a révélé que le resvératrol inhibait la réplication de l'ADN. En comparant les effets cellulaires du resvératrol à l'hydroxyurée, un agent connu pour causer du stress réplicatif, nous avons montré que ces deux traitements menaient à une diminution similaire de la progression de la fourche de réplication ainsi qu'à une activation de la signalisation en réponse au stress réplicatif. Nous avons également démontré que l'inhibition de la réplication de l'ADN dans les cellules humaines par le resvératrol est l'un des effets principaux de la molécule sur la prolifération cellulaire et ne requiert pas la présence de la déacétylase d'histone Sirtuin-1, protéine qui a été suggérée comme étant la cible principale du resvératrol pour son effet antivieillissement.

Nous avons également étudié la perturbation d'un second processus cellulaire, soit le maintien des télomères. Ces séquences spéciales aux extrémités des chromosomes sont indispensables à la protection du génome et leur érosion graduelle est contrebalancée par

l'activité enzymatique de la télomérase. Nous avons effectué un crible génétique par CRISPR à l'échelle du génome dans une lignée cellulaire dont nous avons inhibé la télomérase en utilisant BIBR1532, un inhibiteur spécifique de la télomérase. Nous avons découvert une forte interaction génétique entre la télomérase et C16orf72, un gène non-annoté que nous avons nommé TAPR1. Nous avons montré que les cellules déficientes en TAPR1 possèdent des niveaux élevés de la protéine p53, un facteur de transcription central à la réponse cellulaire aux dommages télomériques et aux dommages à l'ADN. Nous suggérons que TAPR1 agit comme un inhibiteur de la stabilité protéique de p53.

En somme, ces travaux mettent en évidence la capacité des cribles génétiques CRISPR à approfondir nos connaissances sur le fonctionnement des processus de maintien de la stabilité génomique chez l'humain.

Mots-clés: CRISPR-Cas9, criblage génétique, réplication de l'ADN, telomères, inhibition de la télomérase, stress réplicatif, resvératrol, C16orf72, p53, prolifération cellulaire.

Abstract

The genetic material (DNA) of an organism contains the necessary information for survival, growth and reproduction. Loss of this information strongly impacts the health of the organism and is the leading factor in aging and cancer. Almost all cells in an organism contain a copy of said genetic material (genome) and employ several mechanisms to repair any damaged section of the genome and to accurately copy it during cell division. We sought to understand the cellular processes by which cells maintain genome stability by systematically inactivating individual genes to uncover their role using pooled CRISPR-Cas9 screening. We employed genome-wide CRISPR screening in human cell lines in combination with specific chemical perturbations to identify gene deletions that enhance or suppress the phenotype of the chemical treatment, thereby shedding light on the effect of the treatment or the role of said enhancer/suppressor genes.

We first focused on resveratrol; a small molecule first discovered in plants that has been suggested to extend lifespan in model organisms while also inhibiting cell proliferation *ex vivo*. Chemical-genetic screening pinpointed a role of resveratrol in inhibition of DNA replication. When we compared the cellular effects of resveratrol to hydroxyurea, a known inducer of replicative stress, we found that both treatments led to slower replication fork progression and activation of signaling in response to replicative stress. Importantly, we showed that the inhibition of DNA replication by resveratrol in human cells is a primary effect on cell proliferation and independent of the histone deacetylase Sirtuin-1, which has been implicated as the primary target in lifespan extension by resveratrol.

We then studied the perturbation of a second cellular process, namely telomere maintenance. These specialized sequences at the termini of chromosomes are critical for the protection of chromosome ends and their erosion is counteracted by the enzymatic activity of telomerase. We performed a genome-wide CRISPR screen in cells that were concomitantly treated with a specific telomerase inhibitor, BIBR1532. We uncovered a strong genetic interaction between telomerase and a previously unannotated gene, C16orf72, which we named TAPR1. We found that TAPR1-depleted cells led to elevated p53 levels, a transcription factor central for the

cellular response to telomeric and global DNA damage. We propose that TAPR1 is a negative regulator of p53 protein levels by promoting its turnover.

Altogether, these studies highlight the power of CRISPR-Cas9 in genetic screening to uncover novel insight into the human genome stability maintenance network.

Keywords: CRISPR-Cas9, genome-wide screen, DNA replication, telomeres, telomerase inhibition, replicative stress, resveratrol, C16orf72, p53, cell proliferation.

Table of contents

List of tables

List of figures

List of abbreviations

a-EJ	alternative end-joining
AAVS1	Adeno-Associated Virus integration Site 1
ADP	Adenosine diphosphate
ALT	Alternative lengthening of telomeres
ANOVA	Analysis of variance
APC/C	Anaphase-Promoting Complex / Cyclosome
ATP	Adenosine triphosphate
pre-B ALL	pre-B acute lymphoblastic leukemia
bp	base pair
c-NHEJ	canonical non-homologous end-joining
Cas9	CRISPR associated protein 9
CDK	CYCLIN-dependent kinase
cDNA	complementary DNA
CDP	Cytidine diphosphate
CMG	CDC45-MCM-GINS
CRANKS	Condition-specific Robust Analytics and Normalization for Knockout Screens
CRISPR	Clustered Regularly Interspaced Short Palindromic Repeats
dADP	Deoxyadenosine diphosphate
dATP	Deoxyadenosine triphosphate
dCDP	Deoxycytidine diphosphate
DDK	DBF4-dependent kinase
DDR	DNA damage response
dGDP	Deoxyguanosine diphosphate
DMSO	Dimethyl sulfoxide
dNTP	Deoxyribonucleoside triphosphate
DSB	Double-stranded break
dsDNA	Double-stranded DNA
dUDP	Deoxyuridine diphosphate
dUMP	Deoxyuridine monophosphate
dUTP	Deoxyuridine triphosphate
EdU	5-ethynyl-2'-deoxyuridine
FDR	False discovery rate
G_1	Gap 1 phase
G_2	Gap 2 phase

GDP	Guanosine diphosphate
GI	Genetic interaction
GI_{50}	Half-maximal Growth Inhibitory concentration
GO	Gene ontology
γH2AX	Phospho-Ser139 histone H2AX
HR	Homologous recombination
hTR	Human Telomerase RNA component
HU	Hydroxyurea
IC_{50}	Half-maximal Inhibitory Concentration
ICL	Interstrand Crosslink
Indel	Insertion/Deletion
kb	Kilobase
KO	Knockout
MCM	Minichromosome Maintenance helicase protein complex
MMR	Mismatch Repair
p53	Tumor protein p53
PAM	Protospacer adjacent motif
PRR	Post-replicative repair
PTS	Pterostilbene
qTRAP	Quantitative Telomerase Repeat Amplification Protocol
RANKS	Robust Analytics and Normalization for Knockout Screens
RNA-Seq	RNA Sequencing
RNR	Ribonucleotide reductase
rNDP	Ribonucleoside diphosphate
rNTP	Ribonucleoside triphosphate
RP	Ribosomal Proteins
rRNA	Ribosomal RNA
RSV	Resveratrol
S-phase	Synthesis phase
sgRNA	Synthetic guide RNA
ssDNA	Single-stranded DNA
SSL	Synthetic sick/lethal
T-loop	Telomeric-loop
TAPR1	Telomerase Attrition and P53 Regulator 1
TDP	Thymidine diphosphate

TERT	Telomerase Reverse Transcriptase
TIDE	Tracking of Indels by Decomposition
TTP	Thymidine triphosphate
UDP	Uridine diphosphate
WT	Wild-type

"The first principle is that you must not fool yourself and you are the easiest person to fool."

– Richard P. Feynman

Acknowledgments

First and foremost, I would like to thank my supervisor Dr. Lea Harrington for the opportunity to work in her laboratory and for giving me the freedom to tackle and think about different scientific questions. I will forever be grateful for the autonomy that was afforded to me in developing my critical thinking. It has been a long and winding road but I have always felt unwavering support. I would also like to thank Dr. Mike Tyers for the guidance throughout the years, for all the collaboration ideas and for always pushing me to “think big”. I am also grateful for the members of my thesis committee, Dr. Alain Verreault and Dr. Daniel Zenklusen for their support and advice throughout the years.

I want to thank all past and present members of the Harrington and Tyers labs. Even if I consider myself lucky to have been able to embark on this scientific journey, lab work can sometimes be unforgiving, but the harder days were made better by the interactions that I had with each and every one of you. Special thanks to Thierry and Jasmin for sharing their scientific knowledge and for their precious time in answering my outrageous amount of questions; to María for all the help, jokes and insightful conversations (sometimes related to science); to Josephine for her kindness, her know-how and her unwillingness to let me work without eating; to Roger for his helpfulness and for all the animated scientific discussions; to Danielle for accepting to join and help me in my scientific (and athletic) endeavours and to Luisa and Manon for all the logistical assistance throughout the years. I would also like to thank all the IRIC scientific platforms personnel for their time and assistance as well as IRIC academic affairs for their help navigating the bureaucracy of a PhD.

Every time I was asked how I dealt with difficult situations that arose, I would reply that I am surrounded by amazing people that help me put everything in perspective. I would like to thank the following groups of friends for their time, support, laughter, drinks and general pursuit of happiness: “The -ichaels”, “Gros chefs bandits”, “Fight Club”, “Los Boyos”, “Game de Risk”, “Codon Madness”, “Jean-Brillant crew”, et al.

Finally, I would like to thank my family for making me the person I am today; my aunts, uncles, cousins and grandparents for their kindness, their support and for the moments we spent together, may there be a million more. Special thanks to Mehdi for his helpfulness, sense of humour and outside-the-box thinking; to Hamza for the telepathic jokes, for pushing me out of my comfort zone throughout the years and for teaching me that when someone offers you what you are worth…ask for more; to Lina for the laughter, the late night philosophical discussions and for balancing out my emotional-informational scale. I would like to thank my brother Seddik for his wisdom, his kindness and for always pushing me to become a better person. Last but not least, I would like to thank my parents, without whom my doctoral studies wouldn't have been possible. I am forever grateful for the support throughout the years, for sharing with me your thirst for knowledge and for teaching me to never settle for averageness and always strive for greatness. I hope to one day repay the sacrifices you have made for me.

Chapter 1 – Introduction

1.1 Genetic heredity and genome stability maintenance

Charles Darwin's theory of evolution has revolutionized modern biology but lacked an explanation of the underlying mechanism of inheritance of selectable traits[1]. The identification of deoxyribonucleic acid (DNA) as the hereditary material and its double-helix structure alluded to a copying mechanism that would enable predictable inheritance[2-5]. This semi-conservative replication mechanism and all the associated processes necessary for the preservation and propagation of genetic information are an amazing prowess of evolution. This genome stability maintenance cellular network needs to repair the 10^4-10^5 potentially mutagenic DNA lesions per cell per day that affect the genome in order to copy the genetic material with great fidelity[6, 7]. Understanding the underlying genetic network responsible for genome stability entails not only the identification of the genes and their function but also the connectivity between these genes and the modules in which they operate that gives rise to the network architecture. Recent developments in genome editing tools have allowed an unprecedented access to functional genomics screens in human cells and a systems-level characterization of genome stability.

1.2 Cell cycle overview

The eukaryotic cell cycle is an intricate process designed to ensure that cell division leads to the proper copying and segregation of genetic material from a mother cell to two daughter cells along with any other components needed to restart the cell cycle for subsequent divisions. The cell cycle in humans can be separated in 4 different steps, each serving a precise role. The cells first grow in size and prepare for DNA replication in a phase called G_1, which is followed by

S-phase where the genome is duplicated. There is a second Gap phase called G_2 where cells assess the integrity of the genome and prepare for the segregation of the genetic material in a phase called mitosis (M)[8].

At its core, cell cycle progression is controlled by the protein abundance and activity of CYCLINs (A, B, D and E-type) and CYCLIN-dependant kinases (CDK1, 2, 4 and 6)[9]. Our current simplified model involves multiple feedback (positive and negative) loops, starting in G_1 where CDK1 and 2 activity are low due to anaphase promoting complex/cyclosome (APC/C) mediated degradation and transcriptional repression of their respective CYCLINs. CYCLIN D-CDK4/6 phosphorylate RB, p107 and p130 leading to the activation of the E2F transcriptional program which includes CYCLIN A, CYCLIN E and EMI1[10, 11]. CYCLIN A and E bind to CDK2, leading to the phosphorylation of several substrates such as RB and CDH1 causing it to dissociate and be replaced by EMI1, a direct inhibitor of APC/C^{CDH1}. This in turns will increase CDK2 activity and reinforce the G_1/S transition, which greenlights the replication of DNA[10, 11] (Figure 1.1, p. 29; see section 1.3.1 for details).

CYCLIN B levels increase throughout S and G_2 phases, form complexes with CDK1 but are maintained inactive through CDK1 phosphorylation by MYT1 and WEE1 kinases. As CYCLIN B levels accumulate past a certain threshold, CYCLIN B-CDK1 complexes can phosphorylate WEE1 and MYT1 to inhibit these kinases as well as phosphorylate and activate CDC25 phosphatases (CDC25B/C for the G_2/M transition), antagonizing the inhibition of CDK1 by WEE1 and MYT1[12]. The high CYCLIN B-CDK1 activity (along with Polo-like kinase 1, Aurora kinase A and Aurora kinase B activity) trigger the early events of mitosis. As a result of CYCLIN B-CDK1 activity, APC/C phosphorylation increases the binding of CDC20 which is fully activated upon kinetochore binding

with mitotic spindle microtubules and creation of tension (satisfaction of the Spindle Assembly Checkpoint)[11, 13]. The fully active APC/C^{CDC20} promotes the degradation of CYCLIN B and Securin, which allows Cohesin cleavage by Separase and subsequent sister chromatid separation[14]. The resulting low CYCLIN B-CDK1 activity in late mitosis results in high CDH1 levels and binding with APC/C and the resulting APC/C^{CDH1} complex degrades CDC20 and re-creating the initial conditions of low CDK1/2 activity in daughter cells after cytokinesis.

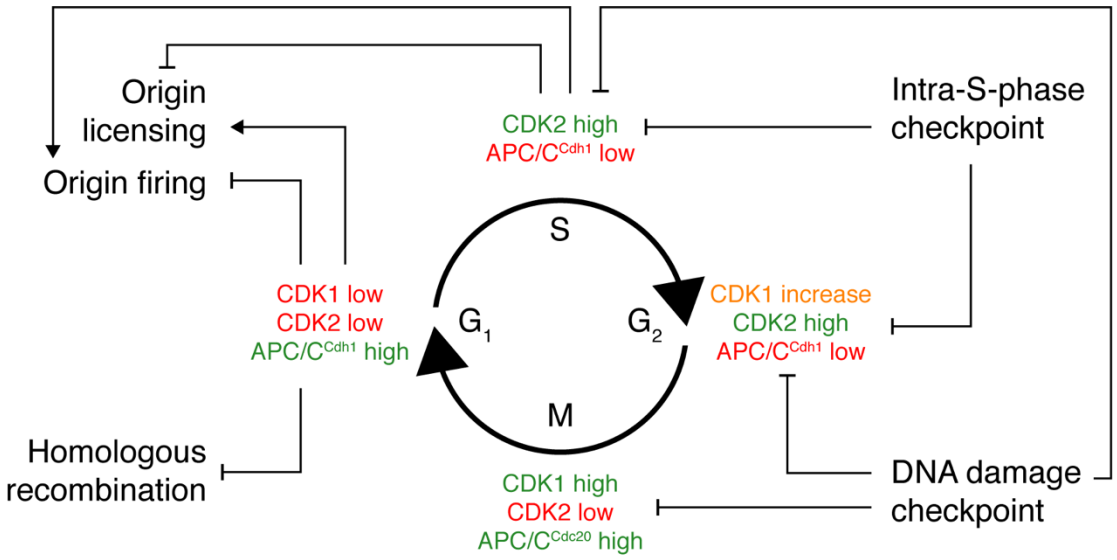

Figure 1.1 | Simplified schematic of CDK oscillations at different phases of the cell cycle.
Cell cycle phases are indicated along with the respective CDK and APC/C levels. Connectivity between the CDK levels and indicated processes are represented by pointed arrows for activation and blunt arrows for inhibition.

1.3 DNA replication

Genetic material duplication is an integral part of cell division and is thus tightly controlled. The machinery responsible for DNA replication carries a specific sequence of events needed to ensure the full replication of the genome, in a timely manner with low error rate[15]. Eukaryotic DNA replication can be viewed as three distinct steps: (1) replication initiation, (2) replication elongation and finally (3) replication termination.

1.3.1 Replication initiation

Given the size of eukaryotic genomes (6 billion base pairs for diploid human cells), DNA replication needs to occur simultaneously at different locations of the genome in order to increase the replication speed[16]. In *S. cerevisiae*, the origins of replications are bound by the Origin Recognition Complex (ORC) in a sequence-specific manner but the binding of ORC to origins in higher eukaryotes does not seem to be sequence-specific, with some evidence of enrichment of binding in nucleosome-free regions[17-21]. In late mitosis and G_1, as CDK activity is low, the ORC complex binds to the origins and recruits CDC6. This serves as a landing pad for the MCM helicase (MCM2-7) a hexameric ring in complex with CDT1 and the binding to ORC-CDC6 likely mediates the opening of the ring to allow dsDNA insertion[22-26]. A second MCM-CDT1 complex is then recruited to the origin, creating a head-to-head double-hexamer conformation of the helicase and origin licensing is completed upon subsequent dissociation of ORC, CDC6 and CDT1[27, 28]. As cells enter S-phase, CDK activity inhibits the activity of ORC1, CDC6 and MCM-CDT1 complexes, and Geminin sequesters CDT1 in S-phase and G_2 before the APC/C-dependent degradation of Geminin in the subsequent G_1[29-34]. These layers of regulation constrain origin licensing to G_1 to prevent genomic DNA re-replication.

Origin firing at the onset of S-phase begins with the CMG (CDC45-GINS-MCM) complex assembly at licensed origins, a process that is better understood in budding yeast where it has been recently reconstituted with purified proteins[35-37]. Upon MCM phosphorylation by Cdc7-Dbf4 (DDK, DBF4-Dependent Kinase), Sld3 (Treslin in humans), Sld7 (MTBP in humans) and Cdc45 are recruited to the helicase complex and CDK-dependent phosphorylation of Sld3 and Sld2 promotes their binding to Dpb11 (TopBP1 in humans) and recruitment to the origin along with GINS and DNA polymerase ϵ (Polϵ)[38-41]. In humans, an additional complex formed by MCM10, RECQ4, and AND-1 (Ctf4 in yeast) is recruited along with DNA polymerase α (Polα) to the CMG helicase[42, 43]. Recent biochemical reconstitutions have shown that MCM10 binding to the CMG helicase promotes the translocation of the two hexamers towards one another, unwinding the intervening dsDNA and melting it into ssDNA. This is thought to promote the switch of the MCM helicase from encircling dsDNA to encircling ssDNA, triggering helicase activity and fork unwinding[44]. Interestingly, eukaryotic cells license more origins that are not fired during S-phase and stay dormant unless needed to complete S-phase[45, 46]. Moreover, since several origin firing factors (such as CDC45 in mammalian cells) are suggested to be limiting, not all origins replicate simultaneously and are staggered during S-phase[47-49]. Transcriptionally active regions of the genomes typically act as early-firing origins while late-firing origins are enriched in heterochromatin regions, potentially due to restricted accessibility of the firing factors[19, 21].

1.3.2 Replication elongation

After origin firing, CMG helicases start unwinding the antiparallel duplex DNA and create a bi-directional replication fork with two ssDNA strands to be used as templates. DNA polymerization is carried out by DNA polymerases in a 5’-3’ fashion and this directionality means

that two different modes of replication occur at a fork[50]. The leading strand can be copied continuously as the fork progresses and the CMG helicase translocates in a 3'-5' direction on the leading strand template, while the lagging strand is copied in discontinued segments (called Okazaki fragments)[51, 52]. On both of these strands, Polα-primase first creates a short RNA primer that is then elongated as DNA by a primase-polymerase switch in Polα[53]. This free 3' DNA end is then extended by Polϵ on the leading strand or Polδ on the lagging strand[54-56]. In spite of the different mechanisms of leading and lagging strand synthesis, both polymerases remain coupled (via Ctf4 in yeast) to the CMG helicase and the lagging strand template DNA loops out and is coated by the ssDNA binding trimeric protein complex RPA[57-59]. This coupling is ensured by several processivity factors that associate with the CMG helicase and polymerases to form the replisome such as Timeless, TIPIN and Claspin (Tof1, Csm3 and Mrc1 in budding yeast) as well as PCNA along with its loader RFC[50, 60-63]. The replisome stability and processivity ensure a tight coupling between the unwinding by CMG helicases and DNA polymerization to avoid creating too much ssDNA, a signal of replicative stress (see section 1.4.1).

As the fork progresses, the Okazaki fragments on the lagging strand need to be joined in one continuous strand in a process called fragment maturation[64, 65]. Once Polδ reaches the 5' end of the following fragment, it iterates through multiple rounds of strand-displacement synthesis to create short 5' flaps that are recognized by the endonuclease FEN1 and degraded in a process called nick translation[66, 67]. If the strand displacement creates a 5' flap that is too long, the DNA2 endonucleases cleaves it until it becomes an adequate substrate for FEN1[68]. After degradation of the RNA primer, DNA ligase 1 acts on the nick between the Okazaki fragments to join them into one continuous strand.

1.3.3 Replication termination

As two replication forks are converging towards one another, the dsDNA unwinding performed by CMG helicases causes positive supercoiling in the intervening un-replicated DNA[69]. In order to complete DNA replication, this topological stress needs to be resolved by topoisomerases (Topo II) that remove the positive supercoiling. Rotation of the replication fork can also relieve the stress ahead of the fork and lead to the formation of pre-catenanes behind the fork (which are later de-catenated by Topo II)[69]. Once the CMG helicases converge towards one another, the remaining dsDNA is unwound, and the two helicases cross over and switch from encircling ssDNA to dsDNA[70, 71]. Replisome unloading is then initiated by the ubiquitination of MCM7 by SCF^{Dia2} in budding yeast ($Cullin2^{LLR1}$ in *C. elegans* and *X. laevis*) before the Cdc48/p97 segregase (VCP in humans) disassembles the replisome[72-75]. CMG disassembly in budding yeast is dependent on Dia2 as cells lacking that gene retain replisomes until the following G_1. In higher eukaryotes, cells lacking the activity of $Cullin2^{LLR1}$ retain replisomes until the end of S-phase, with rapid disassembly during mitosis that is driven by the ubiquitination of MCM7 by the TRAIP ubiquitin ligase[76].

1.3.4 Determinants of DNA replication fidelity

1.3.4.1 DNA polymerase

One of the main determinants of replication fidelity is nucleotide incorporation by DNA polymerase[77] (Figure 1.2, p. 38). In the main replicative DNA polymerases (α, δ and ϵ), an induced fit mechanism ensures that a conformational change that places the reactive residues of the catalytic site occurs when adequate interactions are established between the template base and the correct incoming nucleotide[78]. Misincorporation is thus energetically disfavored due to the

incorrect catalytic site geometry and occurs with a lower rate and causes 3' mispairing that decreases the rate of subsequent extension of the DNA[79-81]. A second activity present in most replicative polymerases (δ and ϵ in humans) is a slower 3'-5' exonuclease activity that proofreads a wrong nucleotide incorporated by the polymerase activity by removing it and allowing a subsequent correct incorporation[82].

Two additional cellular components pose a threat to the correct nucleotide incorporation and need specific pathways to minimize their mutagenic potential. Ribonucleotides (rNTPs) are present in a much higher concentration than deoxyribonucleotides and can be used as substrates by DNA polymerase as they form the correct base pairing[83]. DNA polymerases contain a tyrosine that acts as a steric gate by restricting incorporation of rNTPs that possess the hydroxyl group at the 2' position of the ribose[84]. Nonetheless, replicative polymerases still incorporate ribonucleotides with a significant rate which are subsequently removed by RNAseH2 and Topoisomerase I[85]. A second important metabolite is dUTP, a precursor of nucleotide synthesis, which is hydrolyzed into dUMP by dUTPase thereby increasing the ratio of TTP/dUTP and reducing the rate of dUTP incorporation into DNA[86].

1.3.4.2 Ribonucleotide reductase

DNA polymerase selectivity is strongly dependent on the relative concentrations of the different substrates it can use and the maintenance of deoxyribonucleotides (dNTPs) is of paramount importance (Figure 1.2, p. 38). Deoxyribonucleotides are synthesized from rNTPs by the catalytic activity of an enzyme called ribonucleotide reductase (RNR)[87]. Human RNR is a class I RNR (same class as the well-studied *E. coli* and *S. cerevisiae* RNRs) and is constituted of two subunits, the large RRM1 (α) that bears the catalytic site and the small RRM2 (β) subunits where

the diferric-tyrosyl radical used for catalysis is formed[88]. RNR is active as a tetramer (α2β2) and it reduces ADP, GDP, CDP and UDP to dADP, dGDP, dCDP and dUDP and is thus the rate limiting enzyme for generation of the necessary dNTPs for DNA replication and DNA repair (after dUDP/dCDP conversion to TDP by additional enzymes)[87]. It is critical to ensure that a balanced pool of dNTPs is maintained at all times since low dNTP levels cause the DNA polymerase to stall while high or unbalanced nucleotide pools will lead to an increased mutational load potentially through interference with DNA polymerase nucleotide specificity selection[89, 90].

Several mechanisms that ensure the adequate activity and substrate specificity of RNR are maintained throughout the cell cycle. First, an allosteric site on the RRM1 subunit called the activity site (A-site) controls the overall catalysis of the enzyme[91]. The A-site can be bound by both ATP and dATP, and the enzyme is inhibited when dATP is bound to the A-site. Although ATP is present at a higher concentration in cells, dATP has a higher affinity for the A-site, which allows this negative feedback of RNR activity in context of high dNTP levels[92, 93]. Recent structural studies have suggested that the missing 2'-OH allows dATP to bind deeper within the A-site, changing the landscape of hydrogen bonds with several amino acids within the binding pocket. This in turn will lead to a change in the quaternary structure of RNR towards an inhibitory hexamer structure (α6) complex that prevents the formation of the α2β2 active complex[92, 93]. Several residues within the A-site such as Asp57 or Asp16 abrogate the ability of dATP to reduce RNR activity when bound in the A-site[94, 95]. A second allosteric site on RRM1 influences specificity (S-site) by modulating which rNDP will be preferentially used as substrate as it is in contact with the catalytic site of the enzyme via a flexible loop (loop 2) and is critical for the maintenance of a balanced nucleotide pool[91]. When bound to the S-site, ATP or dATP promotes the reduction of CDP and UDP, TTP promotes

the reduction of GDP and finally GDP promotes the reduction of ADP. The dual roles played by ATP and dATP in allosteric regulation of RNR activity are governed by the differential affinity for the A-site and the S-site[96, 97]. ATP has a similar affinity for both sites while dATP has a 10-20 times higher affinity for the S-site, which means that at lower dATP concentrations, it will act as an activator of CDP/UDP reduction while acting as a general inhibitor of RNR activity at higher concentrations[91, 97]. Several mutations on loop 2 lead to an imbalance of dNTP pools and higher mutagenesis in *S. cerevisiae*[98].

In addition to the biochemical intricacies detailed above, mammalian RNR is also subject to regulation at the cellular level, both during a normal cell cycle as well when DNA replication is perturbed[99] (see section 1.4.1 for detail). The RRM1 protein has a long half-life and its levels are constant during the cell cycle[100]. In contrast, the RRM2 subunit is upregulated by the E2F1 transcriptional program as well as the relaxation of the repressive binding of E2F4 to the RRM2 promoter upon entry of cells into S-phase[101]. RRM2 is also under cell cycle-dependent proteolytic control in which it is degraded in G_2 by the $SCF^{CYCLIN\ F}$ complex (after Thr33 phosphorylation by CDK1 and CDK2) and by APC/C^{CDH1} in G_1[102, 103]. This results in high levels of RRM2 (the limiting subunit for activity) specifically during S-phase when dNTP synthesis requirements are highest. Finally, several proteins act as inhibitors of RNR activity such as Sml1 and Dif1 in *S. cerevisiae*, Spd1 in *S. pombe* and IRBIT in humans[99, 104]. Sml1 has been suggested to bind Rnr1 (one of the large subunits of RNR) and prevent the catalytic cysteines reduction necessary for reactivation while Dif1 imports the small subunit of RNR (Rnr2-Rnr4 in *S. cerevisiae*) into the nucleus and sequesters it away from the cytoplasmic large subunit of RNR[105-107]. Spd1 in *S. pombe* seems to exert similar functions than both Sml1 and Dif1 and all three proteins are degraded during S-

phase allowing for a high RNR activity[99, 108]. In humans IRBIT (AHCYL1) was recently shown to bind RRM1 and inhibit its activity. Interestingly, IRBIT binding to the large subunit of RNR seems to be dependent on the allosteric state of the enzyme and could have a role in stabilizing the dATP-bound conformation within the A-site, thereby ensuring proper inhibition of RNR even in presence of the high physiological ATP concentration[104].

1.3.4.3 Mismatch repair

The fidelity mechanisms discussed above are not perfect and still lead to base substitutions and insertions and deletions (indels) during the normal course of DNA replication which are corrected by the mismatch repair (MMR) proteins[77, 109] (Figure 1.2, p. 38). Biochemical studies suggest that the MutSα heterodimer (MSH2-MSH6) recognizes base substitutions and 1-bp indels while the MutSβ heterodimer (MSH2-MSH3) recognizes larger indels but overlap in their recognition has been reported in some cellular contexts[110, 111]. The main MutL endonuclease (MutLα: MLH1-PMS2) is recruited to the MutS-DNA complexes and creates a nick that initiates the repair process by exonuclease-mediated removal of the mismatch, DNA polymerase fill-in and strand ligation[109]. A key process in mismatch repair is strand discrimination to repair the newly replicated strand to avoid mutagenesis. In *E. coli*, where the MMR process has been extensively studied, the parental strand is methylated which directs the repair to the nascent strand, but this mechanism is not conserved in eukaryotes[109]. The current model for strand specificity in MMR is thought to be directed by nicks in the nascent strand and to be stimulated by PCNA[112, 113]. This model is supported in budding yeast by the observation that lagging strand errors are repaired more efficiently, potentially due to the Okazaki fragment creating a higher nick density[114]. This asymmetric MMR efficiency is thought to compensate for the lower fidelity of lagging strand

synthesis by Pol δ compared to leading strand synthesis by Pol ϵ, resulting in a comparable overall strand replication fidelity[115].

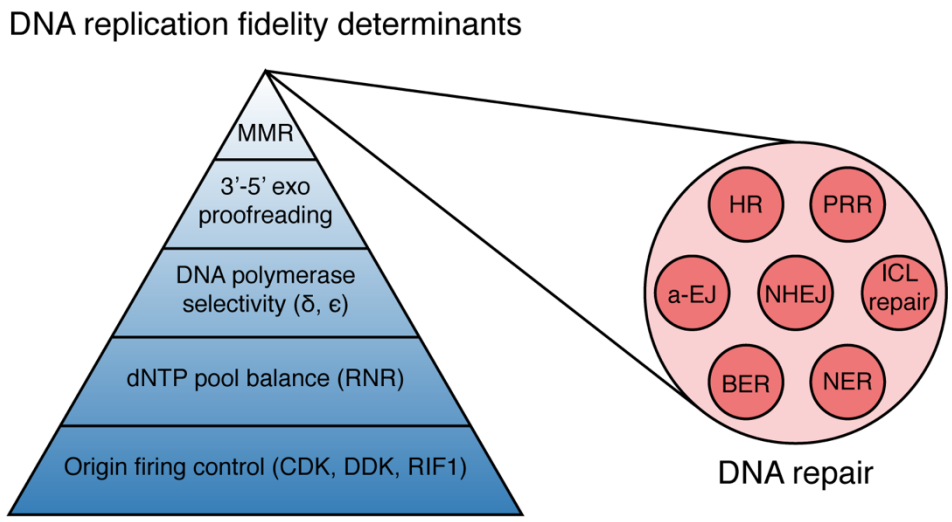

Figure 1.2 | Cellular processes involved in ensuring DNA replication fidelity.
Mechanisms inherent to DNA replication are shown in the left. A subset of DNA repair pathways ensuring genome stability when replication fork progression is impaired are shown in the right-side of the figure (exo: exonuclease).

1.4 Genome stability maintenance mechanisms

1.4.1 Cellular response to replicative stress

Fork progression during DNA replication can be hindered by multiple factors that typically lead to uncoupling of the replisome helicase and polymerase and an excess of ssDNA, a condition generally called replicative stress. Examples of such factors are limiting nucleotide pools, DNA polymerase inhibition, template base lesions, inter-strand crosslinks (ICLs), protein-DNA crosslinks or DNA secondary structures[116]. Most of these causes of replicative stress have dedicated responses such as the Fanconi anemia pathway for resolution of ICLs, post-replicative

repair (PRR) translesion synthesis polymerases and error-free template switching for the bypass of base lesions or the action of BLM and WRN helicases for the unwinding of DNA secondary structures[117-119]. A global response to replicative stress termed the intra-S-phase checkpoint responds to an excess of ssDNA and is critical for the completion of DNA replication, irrespective of the underlying cause of fork progression impairment[120].

The main goal of the intra-S-phase checkpoint is to halt cell cycle progression to mitosis until DNA replication can be completed and it does so by activating the Chk1 kinase to inhibit CDK activity[121, 122]. Intra-S-phase checkpoint activation begins by the trimeric protein RPA binding to the excessive ssDNA stretches created by uncoupling of replisome helicase and polymerase[120]. This will in turn recruit ATRIP and the ATR kinase to the stalled replication fork. Another protein complex that is recruited by the RPA-ssDNA platform is RAD17 in complex with RFC2-5, which serves as a clamp loader for the PCNA-related 9-1-1 complex (RAD9, RAD1, HUS1). The 9-1-1 complex will in turn recruit the TopBP1 protein to lead to the full activation of the ATR kinase and the phosphorylation of its effector kinase Chk1 on Ser317 and Ser 345[122-128]. This will in turn lead to phosphorylation of CDC25 phosphatases, decreasing their ability to remove the inhibitory Tyr15 phosphorylation on CDKs thereby halting cell cycle progression[129, 130].

Another important role of the intra-S-phase checkpoint is the inhibition of late origin firing to avoid the exacerbation of ssDNA and focus all limiting resources to rescue the stalled replication forks. When the intra-S-phase checkpoint is inhibited, RPA is increasingly bound to ssDNA and becomes limited, leading to RPA exhaustion and replication catastrophe[131, 132]. Inhibition of origin firing is performed by Chk1 both by inhibiting CDK-dependent target phosphorylation as well as counteracting DDK-dependent target phosphorylation. RIF1 controls

origin replication timing through its interaction with protein phosphatase 1 (PP1) by recruiting it to the licenced origins and counteract CDC7-dependent phosphorylation of MCM proteins. RIF1 phosphorylation by CDK in unperturbed S-phase disrupts the interaction between RIF1 and PP1, allowing origin firing to happen while the intra-S-phase checkpoint inhibition of CDK prevents origin firing[133, 134]. Paradoxically, dormant origins in the vicinity of stalled forks are allowed to fire and can converge onto and recue stalled forks. These dormant origins constitute the bulk of licensed origins in G_1 and prevention of this excess licensing by reduction of MCM protein levels sensitizes cells to replicative stress, highlighting their importance in rescuing stalled forks[45, 135, 136]. The mechanism by which global origin firing is inhibited while local origin firing near the stalled fork is permitted is still not fully understood.

Finally, activation of ATR and Chk1 by replicative stress leads to a remodelling of the proteome in order to cope with such stress[137, 138]. One of the multiple targets of Chk1 is the E2F transcriptional program repressor E2F6. Phosphorylation of E2F6 promotes its dissociation from E2F promoters and increases the expression of genes that are typically expressed at the G_1/S transition and the persistence of the E2F transcriptional program during replicative stress helps cells cope with replicative stress[137]. One such protein is the RNR small subunit RRM2, which leads to an increase dNTP levels, a functional scheme reminiscent of the increase of RNR activity in budding yeast by Mec1/Rad53 activation during replicative stress[139-141]. A remodelling of the proteome locally at the fork allows its stabilization through modulation of nuclease (e.g. EXO1, DNA2, MUS81) or helicase (e.g. BLM, WRN, SMARCAL1) access and prevent fork breakage and the creation of double-stranded breaks[142, 143].

1.4.2 DNA repair of double-stranded breaks

Genotoxic lesions have dedicated repair mechanisms that respond to specific lesions such as the Fanconi anemia pathway for ICLs or base excision repair and nucleotide excision repair for damaged DNA bases[144]. Failure to detect and repair such lesions can lead to the creation of double-stranded breaks (DSBs) that need additional mechanisms to maintain genome stability. These breaks, either caused by exogenous genotoxic agents or by endogenous events such as replication fork collapse, require an urgent response from the cell to avoid chromosome mis-segregation in mitosis[145] (Figure 1.2, p. 38). Two major pathways respond to double-stranded breaks in cells, the error-prone non-homologous end-joining (NHEJ) and the error-free homologous recombination (HR)[144, 146]. Homologous recombination requires a sister chromatid (or other homologous sequence) as well as extensive resection of the break to expose ssDNA for homology search. Most regulatory mechanisms that channel repair towards NHEJ or HR impact repair pathway choice by sensing and integrating the cell cycle phase or by regulating end-resection[147, 148].

1.4.2.1 End-resection control

Upon detection of a break, both the Ku70/Ku80 heterodimer (Ku) as well as the PARP1 protein are amongst the first proteins detected at the ends[149]. The MRN complex (MRE11-RAD50-NBS1) is recruited by PARP1 to the break where it will recruit the ATM kinase, critical for the signalling cascade of DSBs[150]. ATM will phosphorylate the histone variant H2AX around the break (resulting in γH2AX), which recruits MDC1, another target of ATM[151]. Phospho-MDC1 recruits the E3 ligases RNF8 and RNF168 to ubiquitinate histone H2A to finally recruit 53BP1, a major player in DSB end-protection. 53BP1, in complex with RIF1, REV7 and the newly discovered shieldin

complex, counteracts resection by recruiting the CST complex (CTC1-STN1-TEN1) and DNA Polα to fill-in exonuclease-dependent resection at the break[152-154].

1.4.2.2 Canonical non-homologous end-joining and alternative end-joining

Given the cellular abundance of the Ku complex and its affinity for ends with minimal ssDNA stretches, the major pathway of repair of DSBs in cells is non-homologous end-joining, in which the two ends of a break will be ligated with one another[148]. Canonical NHEJ (c-NHEJ) begins by Ku-dependent recruitment of the DNA-PK kinase which is activated by autophosphorylation, followed by recruitment of the Artemis and APLF nucleases to process non-ligatable ends if necessary. Ligase 4 (LIG4) in complex with XRCC4 (stimulates LIG4 catalytic activity) and XLF are then recruited to the break to ligate both ends[144, 146]. Alternative end-joining (a-EJ) can occur in PARP1-bound ends through the recruitment of the MRN complex (MRE11-RAD50-NBS1)[150]. MRE11 initiates the resection of the ends but the ssDNA stretches created are insufficient for HR. In the absence of such extensive resection, these partially processed ends can anneal with one another if there are any microhomologies between the ssDNA strands, via DNA polymerase θ. Ends can be subsequently ligated by DNA ligase 3 (LIG3), which typically results in insertions and deletions[155].

1.4.2.3 Homologous recombination

During S and G_2 phases of the cell cycle, cells become permissive to homologous recombination by relaxing DSB end-protection. Once the MRN complex is loaded onto the break, binding of CtIP stimulates the endonucleolytic activity of MRN[156]. DNA resection then proceeds 3'-5' by the exonuclease activity of MRN as well as by the 5'-3' exonuclease activities of EXO1 and DNA2/BLM[157]. This created ssDNA is first bound by RPA before switching to RAD51-coated ssDNA

promoted by the BRCA1-BRCA2-PALB2 complex (the interaction between BRCA1 and PALB2 is restricted in G_1)[152, 158]. The RAD51 nucleofilament is critical for strand invasion into the homologous sequence to form Holliday junctions[159]. After strand extension, these Holliday junctions can either undergo dissolution through branch migration by the BTR complex (BLM-TOP3a-RMI1-RMI2) or resolution through nuclease activity of the SLX4 complex (SLX4-SLX1/MUS81-EME1) and GEN1[160, 161]. The switch from NHEJ to HR that occurs at late S-phase is controlled by multiple mechanisms such as CDK-dependent phosphorylation of CtIP, as seen by unscheduled resection in cells expressing the T847E phospho-mimetic mutant during G_1[156]. Other CDK targets such as EXO1 and NBS1 as well as the HR negative regulator HELB phosphorylation channels DSB repair towards HR[162-164].

1.4.2.4 DNA damage checkpoint

In cells without any DNA damage, the ATM kinase is present as an inactive homodimer that undergoes autophosphorylation at Ser1981 and dissociates into active monomers upon DSB detection by the MRN complex[151, 165]. ATM phosphorylates many substrates to modulate DNA repair and cell cycle arrest, of which many are shared with the ATR kinase, highlighting the high connectivity between these two similar damage sensing kinases[166]. The effector kinase Chk2 is one of the main targets of ATM activation by DSBs and undergoes dimerization upon its phosphorylation on Thr68, followed by autophosphorylation of its kinase domain for full activation[167]. Chk2 will then phosphorylate the CDC25C phosphatase, creating a binding site for the 14-3-3σ protein and preventing the de-phosphorylation of CDK1, which leads to arrest in G_2/M[130, 168, 169].

A second critical target of ATM is the tumor suppressor p53, a tetrameric transcription factor that is activated upon phosphorylation of Ser15 (by ATM) and Ser20 (by Chk1/Chk2) which increases the expression of p53 target genes responsible for growth arrest, DNA repair and apoptosis[170-173]. In undamaged cells, p53 protein levels are maintained low mainly via the action of the MDM2 E3 ubiquitin ligase to trigger p53 proteasomal degradation. MDMX interacts both with MDM2 to stabilize it and with p53 to inhibit the transactivation of p53 transcriptional targets[174-176]. MDM2 and MDMX are both targets of ATM and their phosphorylation leads to the stabilization of p53 and activation of p21 (*CDKN1A*) a CDK inhibitor that is one of the main effectors of p53 for growth arrest[171, 177, 178]. Upon expression, p21 will bind mainly to CDK2-CYCLIN E to inhibit its kinase activity and lead to arrest at the G_1/S transition[179]. Interestingly, p53 also triggers the expression of *MDM2* as well as *PPM1D* (Wip1), a phosphatase that counteracts ATM-dependent phosphorylation creating a negative feedback to reduce p53 levels and activity[180]. Several other E3 ligases that downregulate p53 protein levels such as PIRH2, COP1, TRIM24 or TRIM32 are transcriptionally upregulated by p53 creating similar autoregulatory feedback loops that are highly redundant[181-184]. These negative feedback loops give rise to pulses of p53 activity upon damage and these pulse dynamics have been suggested to be a mechanism to first elicit growth arrest until the damage is repaired before triggering senescence or apoptosis if the damage persists[185-187].

1.5 Telomeric DNA is a special locus of genome stability maintenance

While there is no clear consensus on the evolutionary advantage that linear chromosomes confer to cells, maintenance of genome stability in cells with linear chromosomes requires a solution to two specific problems: (1) the end-protection problem and (2) the end- replication

problem. Most eukaryotes have evolved a similar solution to these problems, an array of repetitive DNA sequences (TTAGGG) of several kilobases at the end of chromosomes called telomeres[188].

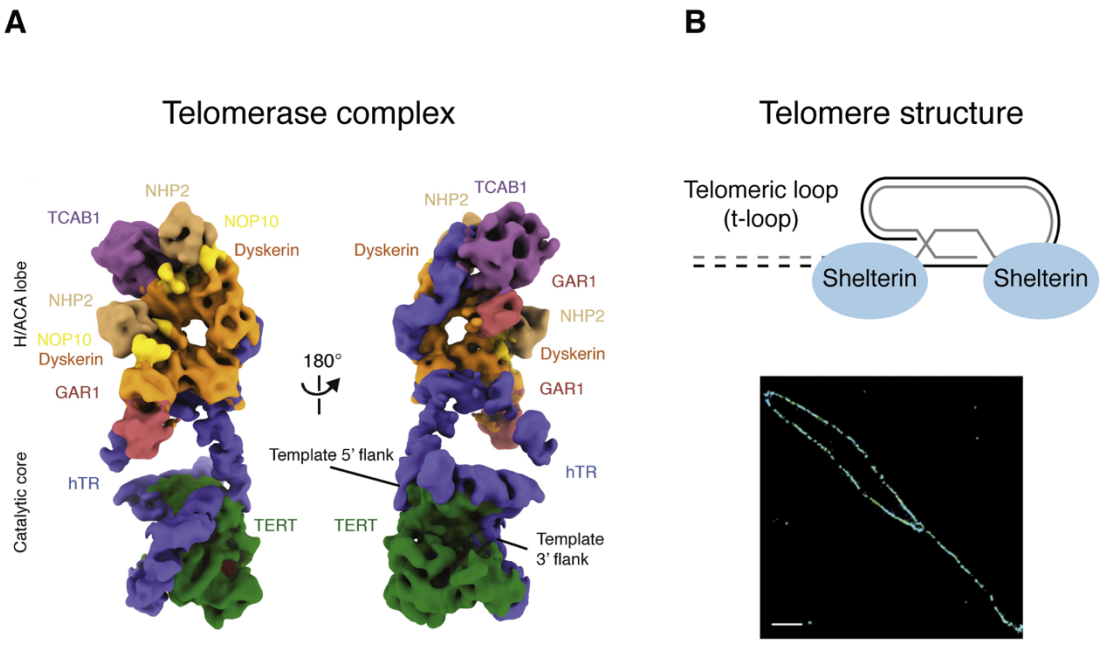

Figure 1.3 | Mammalian telomerase and telomeres structure.

A. Cryo-EM structure of human telomerase shows the two lobes (catalytic and H/ACA) of the enzyme. Adapted with permission from Elsevier: Current Opinion in Structural Biology (Nguyen et al.)[189]. **B.** Schematic of the shelterin-bound t-loop formed at the telomere (top) along with a super-resolution (STORM) fluorescence microscope image of a fixed mouse t-loop (bottom). Adapted with permission from Elsevier: Cell (Doksani et al.)[190].

1.5.1 The end-protection problem

Telomeres are constituted of a double-stranded region and a single-stranded overhang region (G-overhang) at the termini. Several layers bring about the protection of chromosome ends, the first one being the formation of a higher order structure called a telomeric loop (T-

loop)[190]. The single-stranded overhang loops back and invades the double-stranded region, displacing the G-rich strand of that invaded region into a D-loop (displacement loop). Telomeric DNA is bound by a complex of 6 different proteins called shelterin, which also stabilizes the T-loop[191] (Figure 1.3-B, p. 45). Double-stranded telomeric DNA is bound by Telomeric Repeat Factor 1 and 2 (TRF1 and TRF2) in a sequence-specific manner with RAP1 being associated with TRF2. Single-stranded DNA is bound by POT1 in complex with TPP1, and sequence-specific binding of POT1 to single-stranded telomeric DNA prevents binding of RPA. Finally, TIN2 binds to TRF1 and TRF2, stabilizing their interaction with double-stranded DNA and subsequently acting as a platform for the recruitment of TPP1. These interactions serve as a bridge between the double and single-stranded binding subunits of shelterin to promote high-order complex formation[191, 192]. The protective t-loop formation is TRF2-dependent and is unwinded by the RTEL1 helicase during telomere replication[193]. A recent study identified a CDK-controlled phospho-switch on TRF2 (Ser365) that restricts the recruitment of RTEL1 to S-phase[194]. Removal of mammalian shelterin from telomeres causes telomere deprotection which unleashes the DNA damage response due to the lack of antagonization of the six following pathways: (1) ATM signaling, (2) ATR signaling, (3) canonical NHEJ, (4) alternative end-joining, (5) homologous recombination and (6) end resection[195, 196].

1.5.2 The end-replication problem

Given the asymmetry of DNA replication between the leading and lagging strands, the ends of linear chromosomes cannot be fully copied due to the need of an RNA primer on the lagging strand. In order to avoid the loss of essential genetic material, telomeres act as a buffer and are eroded (by 50-200 bp) every cell division[197, 198]. This measured telomere loss is higher

than the expected loss from the dynamics of RNA primase alone and is likely caused by additional loss during overhang processing. Mammalian somatic cells undergo progressive shortening of telomeres until they reach a critically short state, which is proposed to reduce the number of potential binding sites for shelterin, which uncaps telomeres and triggers a persistent DNA damage response. Given the telomere length heterogeneity in cells and stochastic nature of telomere loss, not all telomeres will be uncapped at the same time[199]. The lack of telomere capping triggers a persistent DNA damage response that activates both ATM and ATR signalling in cells, which ultimately leads to p53 activation and p21 mediated cell cycle arrest[200-202]. This phenomenon limits the number of cell division a cell can undergo, termed the Hayflick limit, and leads to the accumulation of senescent cells ex vivo[203, 204]. Genetically engineered mice that exhibit a lower incidence of critically short telomeres or mice with a deletion of the Cdkn1a gene (locus from which p21 is expressed) show an increase of cellular proliferative capacity and reduced tissue dysfunction, suggesting a partial role of telomere shortening in aging-dependent senescent cell accumulation in vivo[205-207]. If the first growth barrier (termed M1) is bypassed through the inhibition of p53 or Rb, cells undergo additional telomere shortening until they reach a state of crisis (M2) that triggers cell death[202, 208-210].

1.5.2.1 Telomerase

Cells that need to maintain a high proliferative capacity such as stem cells need to counteract this telomere shortening and do so via the expression of telomerase, which is typically transcriptionally repressed in somatic cells[211]. The core telomerase enzyme is a reverse transcriptase (Telomerase Reverse Transcriptase, TERT) in association with a telomeric RNA (hTR) that binds the ends of telomeres and copies a template present on hTR (AAUCCCAAUC) to

elongate the G-rich strand[189, 212]. Telomerase exhibits an interesting catalytic cycle in which the 3' end of the DNA substrate binds the end of the template and TERT adds telomeric repeats by copying 6 nucleotides in quick succession (nucleotide addition processivity). A template boundary element on hTR prevents TERT from copying addition nucleotide and preserve telomere sequence fidelity. Once TERT reaches the end of the template, a translocation of the DNA substrate on the RNA template occurs which places the new DNA 3' end and the template back into TERT catalytic site (repeat addition processivity)[213]. Several factors have been shown to impact processivity of telomerase activity in vitro such as residues on the TERT subunit and the presence of shelterin subunits TPP1 and POT1[214]. In cells, telomerase undergoes multiple assembly steps in the nucleus and in the Cajal bodies and forms a complex with H/ACA proteins (Dyskerin, NOP10, NHP2 and GAR1) as well as TCAB1, each binding to specific regions on hTR[189, 212] (Figure 1.3-A, p. 45).

The dynamics of telomere length maintenance in cells is an intriguing question given the low number of enzymes that are present in cells and the low number of potential substrates (chromosome ends)[215]. The recruitment of telomerase to telomeres is ATM-dependent and mediated through contacts between residues on TPP1 and residues at the N-terminus of TERT (e.g. K78)[216, 217]. Mutations of those residues abrogate the recruitment of telomerase and proper telomere maintenance, which can be restored by introducing the reciprocal charge-reversal mutations[218]. Once recruited to telomeres, telomerase has been shown to exhibit two different types of behaviors, a transient scanning mode and a more long-lived binding suggested to be due to the binding of telomerase of the telomeric 3' end and elongation of said telomere[219]. Telomere elongation in cells is coupled to DNA replication and has been shown to preferentially act on the shortest telomeres when telomerase was re-expressed in a model that was undergoing telomere

shortening, whereas all telomeres seem to be used as substrates in cancer cells maintaining a stable telomere length[220]. The ability to discriminate between different telomere lengths in a cell is suggested to act through the differential stoichiometries and affinity of the different shelterin subunits using a protein counting model that restricts accessibility of telomerase[192].

1.5.2.2 Telomere maintenance in cancer

Cancer cells also require unlimited proliferative capacity and around 85-90% of cancer cells do so via the expression of telomerase to elongate telomeres[221]. Mutations in the TERT promoter have recently been recognized as the most common non-coding mutation in several types of cancer and increase the expression of TERT via the creation of ETS factor binding sites such as GABP[222, 223]. The telomere-negative cancers maintain telomere length via an alternative lengthening of telomere (ALT) mechanism that uses recombination between the telomeric arrays on different chromosomes to prevent the accumulation of critically short telomeres[224]. Replicative stress within a telomere during S-phase leads to unresolved stalled replication forks that are a substrate for ALT-mediated telomere lengthening in subsequent phases of the cell cycle[225, 226]. These stalled forks will be repaired by either a RAD51-dependent homologous recombination mechanism or a RAD52-dependent break-induced synthesis mechanism, thereby extending telomeres[224, 227]. Interestingly, recent reports identified tumors where telomerase expression or ALT hallmarks are not detected, and telomeres undergo shortening[228, 229]. This lack of telomere maintenance mechanisms has been attributed to the very high starting telomere length in these tumors that allows for several cell divisions before growth arrest, which has been previously suggested in a cell line model with transient expression of telomerase[228-230].

Given the high prevalence of telomerase activation in cancer, it quickly became an attractive target for the development of specific inhibitors that would inhibit cancer cell growth, but no small-molecule inhibitor has been successful in clinical trials[231, 232]. It is still unclear if more potent inhibitors and better patient stratification would be beneficial, or if telomerase inhibition is inherently refractory to targeting due to the lag before the appearance of critically short telomeres or resistance through alternative lengthening of telomeres mechanisms[233, 234]. Interestingly, critically short telomeres impose a barrier to tumorigenesis only when the p53 checkpoint is not perturbed. When p53 has been inactivated (as is the case for around 50% of tumours), critically short telomeres can promote tumorigenesis due to fusions between the different telomeres, which lead to breaks during chromosome segregation (termed Breakage-Fusion-Bridge cycles)[235]. These telomeric fusions can give rise to the complex chromosomal rearrangements that are often observed in tumors by also involving mutagenic processes such as chromotripsis and kataegis[236-238].

1.6 CRISPR as a tool for genetic screening and network mapping in human cells

Large-scale genetic screens have been performed in several model organisms given their tractable genetics, but it is in the budding yeast *S. cerevisiae* where the most extensive characterisation of the effect of genetic perturbation has been performed. The whole-genome map of digenic genetic interactions revealed the high connectivity between genes performing similar functions and trigenic genetic interactions have started to chip away at complex interactions that were masked by the presence of redundant gene paralogs[239, 240]. The ability to perform similar reverse genetic screens in human cells has been revolutionized by the use CRISPR-

based genome editing[241]. This revolution has been accompanied by technological improvements of unprecedented speed and new tools and applications are constantly developed.

1.6.1 Cas9 mediated knockouts in human cells

The CRISPR-Cas system was first described as a bacterial adaptive immunity mechanism that allow bacteria and archaea to defend against invading species such as phages[242, 243]. Foreign sequences are integrated into the genome and expressed as short RNAs in complex with a nuclease that cuts a nucleic acid template if it detects a match with the RNA sequence[242, 243]. Among the different types and classes of CRISPR-Cas systems, the one derived from *Streptococcus Pyogenes* is the best characterized to date and has been adapted to perform genome editing in human cells[244-246]. The *S. pyogenes* nuclease called Cas9 acts as an RNA-guided DNA nuclease and cuts both strands of DNA using two distinct domains (RuvC and HNH domains). The cuts are directed by a short 20 bp sequence called a crRNA (CRISPR RNA) that is complementary to the target DNA and is in complex with Cas9 along with a scaffold RNA called tracrRNA (Trans-activating CRISPR RNA)[241]. The last requirement for the system is need of a PAM (Protospacer Adjacent Motif, NGG for SpCas9) sequence downstream of the target sequence that is necessary for the stable binding of Cas9 to the target DNA and its subsequent cutting (3-4 bp upstream of the PAM sequence)[241]. A chimera of the two RNA components has been engineered which allows the essential features from both the crRNA and the tracrRNA to be present on a single RNA molecule called sgRNA (synthetic guide RNA) and simplifies precise genomic editing[246]. Several studies have uncovered sgRNA sequence determinants for optimal Cas9-mediated gene knockout in order to maximize on-target efficiency and minimize off-target cutting (with some mismatch tolerance)[247].

Once double-stranded breaks are induced in human cells, the regular DNA repair machinery takes over in order to handle this DNA lesion. While homologous recombination can be used to perform homology-directed repair, such genome editing has been notoriously hard to achieve with high enough efficiency in human cells and several strategies have been employed to modulate the DNA repair pathways in favor of homologous recombination for the desired outcomes[248]. In contrast, Non-homologous end joining is the favored pathway through which these DSBs are repaired, leading to insertions or deletions (indels) that will often cause a frameshift (unless indel is a multiple of 3) if the targeted sequence is within a protein-coding sequence[152]. This will result in a loss-of-function mutation through a premature stop codon and nonsense mediated decay of the mRNA. Interestingly, the profile of indels that occur upon DSB repair in human cells was shown to be unique for each target sequence and a recent study from Chakrabarti and colleagues points to the nucleotide at position -4 as a determinant of the indel profile, which places it in the vicinity of the cut[249-253]. Moreover, since Cas9 leads to blunt cuts, c-NHEJ seems to be the pathway of choice, while a-EJ acts with delayed kinetics on breaks and generates a different profile of indels[249-253].

Prior to CRISPR systems being adapted for use in mammalian cells, targeted gene disruption was performed using RNA interference (RNAi) technology where short interfering RNAs are introduced into cells and promote the degradation of complementary target mRNAs after loading into the RNA induced silencing complex[254, 255]. While both technologies are complementary for gene disruption, several differences lead to specific advantages that need to be considered during experimental design. RNAi uses the endogenous microRNA (miRNA) interference pathway which minimizes the genetic engineering required for gene disruption but

can potentially create artefacts if the exogenous RNAi used out-competes endogenous miRNAs[256]. Gene knockdowns by RNAi are easily reversible and can lead to a phenotype with faster kinetics than the relatively slower CRISPR technology and disruption kinetics are not affected by chromatin accessibility and gene dosage[251, 257, 258]. While the partial gene disruption usually obtained by RNAi can lead to a hypomorphic phenotype that is desirable for specific experimental conditions, a stable and irreversible disruption is best achieved using the CRISPR technology owing to the ability to modify the genome with high efficiency. Finally, another striking advantage of CRISPR for gene knockout is the reduced off-target disruption due to the requirement of a PAM sequence adjacent to the target site and chromatin accessibility constrains that are incorporated into the guide RNA design to favour the intended target relative to potential off-target sites[259, 260].

1.6.2 Large-scale knockout screening approach to network mapping

Genetic screening can be performed using two different formats: (1) an arrayed format using defined positions on multi-well plates or (2) a pooled format where barcoding is used to deconvolute and identify each genotype. Arrayed genetic screens have the advantage of allowing more complex phenotypic characterisation of the different genotypes but does not scale very well if genome-wide query is necessary and can suffer from batch effects[261]. The ever-diminishing cost of next-generation sequencing has unleashed the power of pooled screening for genome-wide loss-of-function (CRISPRko) screens in human cells.

Several sgRNA libraries have been designed each with a different number of target genes, number of sgRNAs targeting each genes and number of control (or non-targeting) sgRNAs, including the Extended-Knockout (EKO) library used in this thesis which has 278,754 sgRNAs that

target 19084 RefSeq genes (10 sgRNAs per gene), 3,872 hypothetical genes and 20,852 alternatively spliced exons[262-266]. These libraries, upon transduction into Cas9 expressing cell lines, were used in pooled screens to identify genes essential for optimal cell proliferation by using sgRNA frequency within the library after a set number of doublings as a readout. By analyzing the data from the different cell lines, several key insights were made: (1) core essential genes are shared among all cell lines and are involved in processes such as DNA replication and ribosome biogenesis[262-266], (2) some genes exert a context-dependent effect on cell proliferation only in a subset of cell lines which could shed light towards genetic vulnerabilities of mutation-harboring cancer cells and[264, 266] (3) Cas9-induced double-stranded breaks can cause a target-independent effect by activating the DDR checkpoints in cells and are more prevalent if the target copy number is high (such as in aneuploid cancer cells)[258, 267]. Several consortiums are currently increasing the number of cell lines in which genome-wide profiling of essential genes has been performed and where the context-dependency of the essential genes is investigated using transcriptomic, proteomic and genomic characterization of the cell lines[268, 269].

Several groups have also used a different strategy to the CRISPRko, namely transcriptional activation or repression (CRISPRa/CRISPRi respectively)[269-273]. In this approach, Cas9 harbors mutations in the RuvC and HNH nuclease domain that renders it catalytically dead (termed dCas9) but nevertheless able to complex with the sgRNA and bind its intended genomic target. This catalytically dead Cas9 is fused with protein domains such as KRAB (CRISPRi) or VP64 (CRISPRa) to repress or activate transcription of a target gene[269-273]. In both cases, the sgRNA needs to be complementary to the promoter of the intended target and preferably close to the transcriptional start site for maximal efficiency of transcriptional regulation. While CRISPRi and CRISPRko both

serve a similar purpose, transcriptional repression has the advantage of shutting down the expression of all isoforms of a given gene, probe the effect of non-coding RNAs as well as circumventing the confounding effect double-stranded breaks can have on the proliferation phenotype[274, 275]. CRISPRa provides complementary information to CRISPRi and CRISPRko, where the effect of increased gene dosage on the phenotype of interest is measured. Of note, while cell proliferation is one of the most common readouts of gene perturbation in the context of these large-scale screens, several groups have published elegant screen designs to address specific questions[276]. Fluorescent-based readouts (either by tagging a protein of interest or via antibody detection) and subsequent fluorescent-activated cell sorting (FACS) have allowed researchers to identify genes that modulate expression and protein stability of genes within a pathway of interest[276, 277].

A key area of development is the ability of multiplexing the genetic perturbations to target more than 1 gene and study genetic interactions (GI), as similar studies in yeast have allowed researchers to identify genes that belong to the same protein complex, work in the same pathway or in parallel pathways based on the degree of correlation in their GIs[278]. Another benefit of multiplexing sgRNAs to target more than 1 gene is the ability to inactivate gene paralogs simultaneously. These genes often escape functional characterization when knocked out on their own due to compensation by the paralogs and multiplexed targeting would shed light on the redundancy between these genes and the evolutionary divergence in specific contexts[279]. Combinatorial complexity (~ 200 million in human cells) currently limits the scale at which digenic interactions are probed and only small subsets of genes of interest have been queried. While delivery of multiple Cas9 sgRNAs is feasible, recombination between the sgRNA expression

cassettes and the competition between sgRNAs increases noise in the screen[280-282]. This issue has been circumvented by the use of two separate Cas9 proteins from different species (such as *S. pyogenes* and *S. aureus*) and their respective sgRNA scaffolds[283, 284]. A different nuclease called Cpf1 or Cas12a has an RNase activity that allows processing of a polycistronic sgRNA expression cassette and simple multiplexed editing[285, 286]. The RNase activity has recently been harnessed in a method called CHyMEra to process hybrid sgRNA cassettes (both Cas9 and Cas12a scaffolds to avoid competition between sgRNAs) and detected digenic interactions between 672 human paralog pairs as well as genetic interactions in the context of mTOR inhibition[279].

GI mapping can also reveal convergence of different pathways as seen in the CRISPRi-mediated perturbation of 222,784 pairs where a strong negative genetic interaction between FDPS, an enzyme in the mevalonate pathway and HUS1, part of the 9-1-1 complex involved in the response to replicative stress and DNA damage[287]. This interaction was mediated by the accumulation of isopentenyl pyrophosphate (the substrate of FDPS), which causes deoxynucleotide depletion and subsequent replicative stress that is detrimental in the absence of HUS1[124, 128, 287]. Finally, an orthogonal approach has been used where the asymmetric digenic perturbations were performed using a CRISPRko and CRISPRa simultaneously in the human K562 cell line[288]. Measuring the growth phenotype of cells where gene A has been inactivated while gene B has been overexpressed allowed the directionality in the genetic interaction to be inferred (If A is upstream or downstream of B).

1.6.2.1 CRISPR chemical-genetic screens

While multiplexed genetic screens inform on the role of proteins in different genetic contexts, a complementary way to interrogate genetic networks is through the use of chemical

perturbations. Pioneering studies in yeast characterized the effect of DNA damaging agents on several DNA repair genes to parse out the role of pathways in dealing with the different types of DNA lesions[289]. This led the way to more comprehensive studies where the genome deletion collection was treated with a large library of small molecules in order to identify gene deletions that led to novel growth phenotypes[290-292]. Since the scale required for systematic profiling gene-gene interactions in human cells is much larger than in simpler eukaryotes, chemical-gene interactions can act as a proxy to elucidate the roles the queried genes. One clear caveat is the fact that the chemical treatments used in these screens rarely behave as precise chemical probes that mimic perfectly a genetic perturbation and more likely act through pleiotropic effects that affect multiple nodes of the cellular network[293]. While this could be considered a disadvantage, small molecules can be used to inhibit a specific activity of a protein without affecting other roles that the protein plays in order to increase the resolution at which the interactions with a given gene can be measured. Chemical-genetic screens can still identify genes that respond to the different perturbations similarly and thus allow the identification of such co-functional genes, hinting at their roles in the same cellular pathways[290, 292] (Figure 1.4, p. 57).

Beyond the role of chemical-genetic screens in the identification of the functional connections between different genes, information about genetic interactions can be harnessed for therapeutic applications in oncology[290, 294]. Negative genetic interactions can be leveraged into potential synergy between inhibitors targeting the gene products involved in the genetic interaction and lead to increased killing of cancer cells[280, 282, 295]. Chemical-genetic interactions can also be used to identify genetic mutations in cancer cells that render cells sensitive or resistant to a specific inhibitor with an interesting pharmacological profile, thus allowing a precise targeting

of patients[294]. This concept is the main tenet of synthetic lethality in cancer treatment in order to increase of the therapeutic window of a given drug[296]. In a purely fundamental genetic framework, synthetic lethality can be defined as the phenomenon where a pair of genes do not lead to a viability phenotype when individually inactivated but a drastic lethality phenotype is observed upon simultaneous disruption. Harnessing this concept in cancer therapeutic discovery allows the identification chemical-gene combinations that make cancer cells with disruption of a gene highly sensitive to a chemical inhibitor relative to normal cells[289]. A mutation that confers an advantage to cancer cells is selected in the population but concomitantly creates a vulnerability that can be exploited for the specific killing of the mutation-bearing cancer cells. The best example of synthetic lethality in cancer therapy is the successful clinical use of PARP inhibitors in BRCA-mutant ovarian tumours where PARP inhibition has been suggested to overload tumor cells with DSBs that are usually efficiently repaired when BRCA1/2 genes are intact[297, 298]. CRISPR-based genetic screening in a large panel of characterized cancer cell lines was used to predict gene or gene/biomarker pairs that would lead to a synthetic lethal interaction that is amenable to pre-clinical/clinical development[299]. Chemical-genetic interactions can also be used to identify the cellular targets or the mechanism-of-action of compounds of therapeutic interest, allowing researchers to stratify patients most likely to respond to the therapy[300, 301].

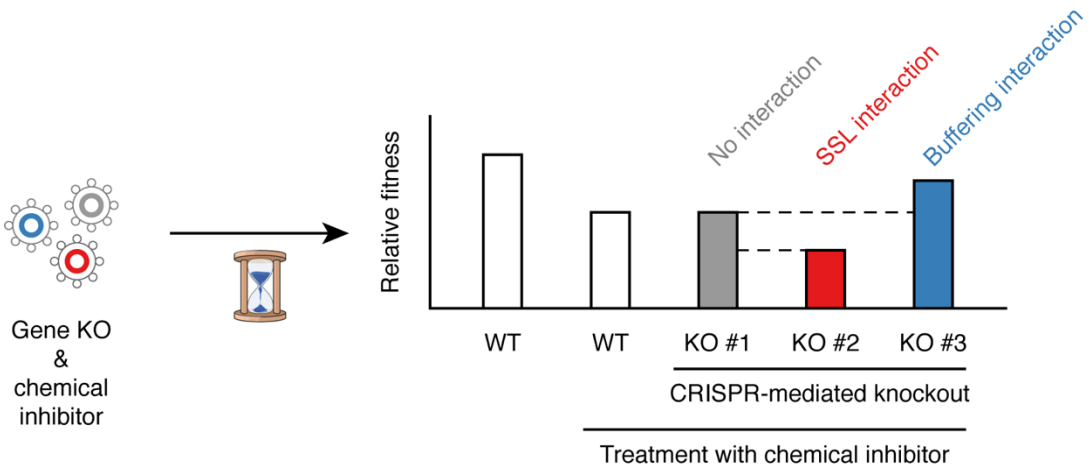

Figure 1.4 | Measurement of chemical-genetic interactions by CRISPR-based screening. Screen example with a proliferation readout is depicted where the chemical inhibitor is typically used at a partially inhibitory dose. Knockouts (KO) that exhibit a lower fitness relative to wild-type (WT) cells are said to exhibit a negative genetic interaction with the compound (synthetic sick/lethal – SSL) while compounds that exhibit an increased fitness relative to wild-type cells are considered to positively interact with the compound (buffering).

DNA damaging agents are amongst the most commonly used chemotherapeutic agents. Profiling their chemical-genetic interaction profile would inform on cellular pathway convergence for the repair of specific types of genotoxic lesions and could be leveraged into combination therapies that reduce the risk of resistance emergence within a tumor[302]. Genes with previously unknown function in DNA repair could also increase the panel of druggable cellular targets or biomarkers for precision therapy. Recent chemical-genetic screens with PARP or ATR inhibitors identified strong negative interactions with genes encoding subunits of ribonuclease H2, with the sensitivity to PARP inhibition being associated with deficient ribonucleotide excision repair[303, 304]. Several chemical-genetic screens for suppressors of sensitivity of BRCA1 deficient cells to PARP inhibition were also instrumental in identifying the shieldin complex, the long sought-after

effector of 53BP1 end-protection[154]. Genome-wide screens also pointed to deficient mismatch repair as resistance mechanism to 6-thioguanine and temozolomide due to the inability to recognize the lesions caused by these genotoxic agents[263, 305]. Finally, more comprehensive studies have used multiple ATR inhibitors or a panel of 27 different genotoxicity agents to identify new genes involved in BER (APEX2), HR (HROB), NHEJ (ERCC6L2) and transcription coupled-NER (ELOF1, STK19) by clustering with known genes involved in the respective pathways[306-309]. All these recent studies establish CRISPR-mediated chemical-genetic screening as a powerful tool for the mapping of genome stability network.

1.6.2.2 Putative mechanism-of-action of resveratrol

Resveratrol is a small molecule that has garnered a lot of attention since it was described as having cancer chemo-preventive effects has upwards of 15000 references on PubMed since the publication of the study in 1997[310]. A second activity of resveratrol that led to an increase of interest in this molecule was the observation that it could stimulate the activity of the SIRT1 histone deacetylase homolog in budding yeast (Sir2) leading to lifespan extension[311]. In mice, resveratrol demonstrated a lifespan-extending activity only in mice fed a high-fat diet but not in mice fed with a regular diet[312]. While mice fed a regular diet don't show any lifespan extension benefit from resveratrol, they do nevertheless show a delay of aging-related deterioration[313]. Human clinical trials have shown limited and sometimes contradictory effects when looking at the therapeutic application of resveratrol in the amelioration of clinical manifestations of type II diabetes, cardiovascular diseases, non-alcoholic fatty liver disease, neurological diseases as well as inflammatory diseases, possibly due to the poor bioavailability of resveratrol[314].

Several proteins have been suggested as the targets of resveratrol in vivo, but a more detailed investigation was conducted for the modulation of two putative targets involved in cellular metabolism, the aforementioned deacetylase SIRT1 as well as AMPK kinase[315]. AMPK is a known metabolic sensor that is activated in response to high AMP:ATP ratios while SIRT1 could act as a metabolic sensor through the use of NAD+ as a cofactor for the deacetylase enzymatic activity[316, 317]. The benefits of resveratrol on metabolism and mitochondrial function have been shown to require both the kinase activity of AMPK and deacetylase activity of SIRT1 to promote mitochondrial biogenesis via PGC1α[318-323]. Finally, while the activation of the AMPK-SIRT1-PGC1α pathway by resveratrol in mitochondrial biogenesis is clear, the role of such modulation on cellular proliferation and lifespan extension is still debated.

1.7 Objectives

In this thesis, we used CRISPR-based chemical-genetic screening to explore the cellular network, with a focus on processes pertaining to genome stability. An example of such work is presented in chapter 2, where we characterized the mechanism-of-action of resveratrol, a molecule that has been shown to extend lifespan in several model organisms. Through an unbiased survey of chemical-genetic interactions with resveratrol, we pinpointed the main cellular effect on human cell proliferation of resveratrol to be replicative stress.

In chapter 3, we identified several genetic backgrounds that act as enhancers or suppressors of telomerase inhibition in a human pre-B ALL cell line. We focused specifically on a gene called *TAPR1* (*C16orf72*) that exhibited a negative genetic interaction when telomerase activity was perturbed. We uncovered a role, for this gene of previously unknown function, as a negative regulator of p53 protein levels, a known effector of the telomeric shortening response.

Chapter 2 – Genome-wide screens reveal that resveratrol induces replicative stress in human cells

Yahya Benslimane[1], Thierry Bertomeu[1#], Jasmin Coulombe-Huntington[1#], Mary McQuaid[2#], María Sánchez-Osuna[1], David Papadopoli[3], Daina Avizonis[4], Mariana De Sa Tavares Russo[4], Caroline Huard[1], Ivan Topisirovic[3], Hugo Wurtele[2], Mike Tyers[1], Lea Harrington[1*]

1 Institute for Research in Immunology and Cancer, Université de Montréal, P.O. Box 6128, Downtown Station, Montréal, Québec H3C 3J7, Canada

2 Centre de recherche de l'Hôpital Maisonneuve-Rosemont, 5415 boulevard de l'Assomption, Montréal, H1T 2M4, Canada.

3 Gerald Bronfman Department of Oncology, Departments of Biochemistry and Experimental Medicine and Lady Davis Institute for Medical Research, Jewish General Hospital, McGill University, Montréal, Québec H3T 1E2, Canada

4 Goodman Cancer Research Center, Metabolomics Core Facility, 1160 Pine Avenue West rm 418, Montréal, Québec H3A 1A3, Canada

*Correspondence: lea.harrington@umontreal.ca

[#] These authors contributed equally to the study.

Molecular cell. 2020;79(5):846-856.E8. doi:10.1016/j.molcel.2020.07.010

2.1 Author contributions

Yahya Benslimane: Study conception, performed all experiments unless stated otherwise below, analyzed all data, wrote the manuscript with input from all co-authors.

Thierry Bertomeu: Study conception, performed CRISPR screens (Figure 2.1D, Supplementary figure 2.1B), general discussion.

Jasmin Coulombe-Huntington: Analyzed NextSeq sequencing of sgRNA frequency in CRISPR screens (Figure 2.1D, Supplementary figure 2.1B, E), general discussion.

Mary McQuaid: Performed and analyzed DNA fiber assay and RPA/γH2AX binding on chromatin (Figure 2.3C, D, F-H).

María Sánchez-Osuna: Performed resveratrol chemical-genetic screen in Jurkat cells (Supplementary figure 2.1E).

David Papadopoli: Performed dNTP level measurement by LC/MS (Figure 2.3A).

Daina Avizonis: Performed dNTP level measurement by LC/MS (Figure 2.3A).

Mariana De Sa Tavares Russo: Performed dNTP level measurement by LC/MS (Figure 2.3A).

Caroline Huard: Performed CRISPR screens (Figure 2.1D, Supplementary figure 2.1B).

Ivan Topisirovic: Analyzed dNTP level measurement, general discussion.

Hugo Wurtele: Analyzed DNA fiber assay and RPA/γH2AX binding on chromatin, general discussion

Mike Tyers: Study conception, analyzed data and general discussion

Lea Harrington: Study conception, analyzed data and wrote manuscript with input from all co-authors.

2.2 Abstract

Resveratrol is a natural product associated with wide-ranging effects in animal and cellular models including lifespan extension. To identify the genetic target of resveratrol in human cells, we conducted genome-wide CRISPR-Cas9 screens to pinpoint genes that confer sensitivity or resistance to resveratrol. An extensive network of DNA damage response and replicative stress genes exhibited genetic interactions with resveratrol and its analog pterostilbene. These genetic profiles showed similarity to the response to hydroxyurea, an inhibitor of ribonucleotide reductase that causes replicative stress. Resveratrol, pterostilbene and hydroxyurea caused similar depletion of nucleotide pools, inhibition of replication fork progression and induction of replicative stress. The ability of resveratrol to inhibit cell proliferation and S phase transit was independent of the histone deacetylase Sirtuin 1, which has been implicated in lifespan extension by resveratrol. These results establish that a primary impact of resveratrol on human cell proliferation is the induction of low-level replicative stress.

2.3 Introduction

Resveratrol (RSV), a phenylpropanoid first isolated in 1939 from the flowering plant *Veratrum grandiflorum* O. Loes, has sparked considerable scientific interest for its ability to extend lifespan in *S. cerevisiae, C. elegans*, and *D. melanogaster*, as well as *M. musculus* fed on a high-fat diet[324-326]. Several mechanisms have been proposed for lifespan extension by RSV, including metabolic effects mediated via sirtuin activation[311, 312, 318, 327]. The mechanisms by which lifespan extension occurs upon exposure to resveratrol, and its dependency upon Sirtuin 1 (SIRT1), are still being actively debated[315, 326, 328-331]. The age-related modulation of metabolism by resveratrol has also been linked to the activation of AMPK or the inhibition of cAMP phosphodiesterases[319, 332, 333]. In other instances, resveratrol inhibits cell proliferation, either via inhibition of cyclooxygenases or the activation of SIRT1[310, 334, 335]. These broad effects suggest that the target(s) of resveratrol and its analogs, such as pterostilbene[336, 337], have not yet been fully elucidated.

CRISPR-Cas9 gene editing technology enables genome-wide interrogation of genes required for cell proliferation in different contexts and is a powerful tool to investigate the mechanism-of-action of chemical entities. Chemogenomic screens, in which pooled genome-wide CRISPR knockout cell populations are treated with a compound of interest, can provide important information regarding the mechanism-of-action of the compound. Specifically, gene deletions that are enriched or depleted in the presence of a compound reflect cellular networks that either mediate or buffer against compound action, respectively. Comparison of these genome-wide profiles can then be used to infer relationships with other chemicals or gene knockouts that exhibit similar profiles[301, 338]. Here, we use a genome-wide CRISPR-Cas9 approach to undertake

an unbiased characterization of the genetic pathways through which resveratrol and pterostilbene affect cell proliferation.

2.4 Results

2.4.1 Genome-wide CRISPR knockout screens identify common chemical-genetic interactions between resveratrol, pterostilbene and hydroxyurea

We conducted a CRISPR-Cas9 genome-wide screen in NALM-6 cells, a pre-B ALL cell line well suited to genome-wide screens owing to its near diploid karyotype, ability to grow in suspension and high level of knockout efficiency[264]. Cells were treated with resveratrol (RSV) or pterostilbene (PTS) at a concentration at which NALM-6 cell proliferation was partially inhibited (16 μM) to facilitate identification of gene knockouts conferring either sensitivity or resistance (Figure 2.1A, p. 64). To place this dosage in the context of the extensive literature pertaining to RSV, yeast lifespan can be extended with 10 μM RSV[311], and in studies of human cells, RSV concentrations ranging from 5 to 100 μM are routinely used[315]. Knockouts were induced with Cas9 and the EKO synthetic guide RNAs (sgRNA) library targeting 19,084 RefSeq genes, 3,872 predicted genes and 20,852 alternatively spliced exons (Figure 2.1B, p. 64; Methods)[264, 339]. We scored genes whose targeting sgRNAs were differentially depleted or enriched in each screen, relative to DMSO-treated and untreated control cells, using a published algorithm called RANKS[264]. Within the synthetic sick/lethal (SSL) interactions identified, we found a significantly enriched set of genes involved in DNA replication and genomic integrity in common between resveratrol and pterostilbene (Figure 2.1D, p. 64; Supplementary figure 2.1A, p. 91). Unexpectedly, we found the genetic profiles of RSV and PTS significantly overlapped with that of hydroxyurea (HU), a well-established inhibitor of ribonucleotide reductase that causes replicative

stress due to dNTP pool depletion[340-342] (Figure 2.1A, 2.1C-D, p. 64; Supplementary figure 2.1A-B, p. 91).

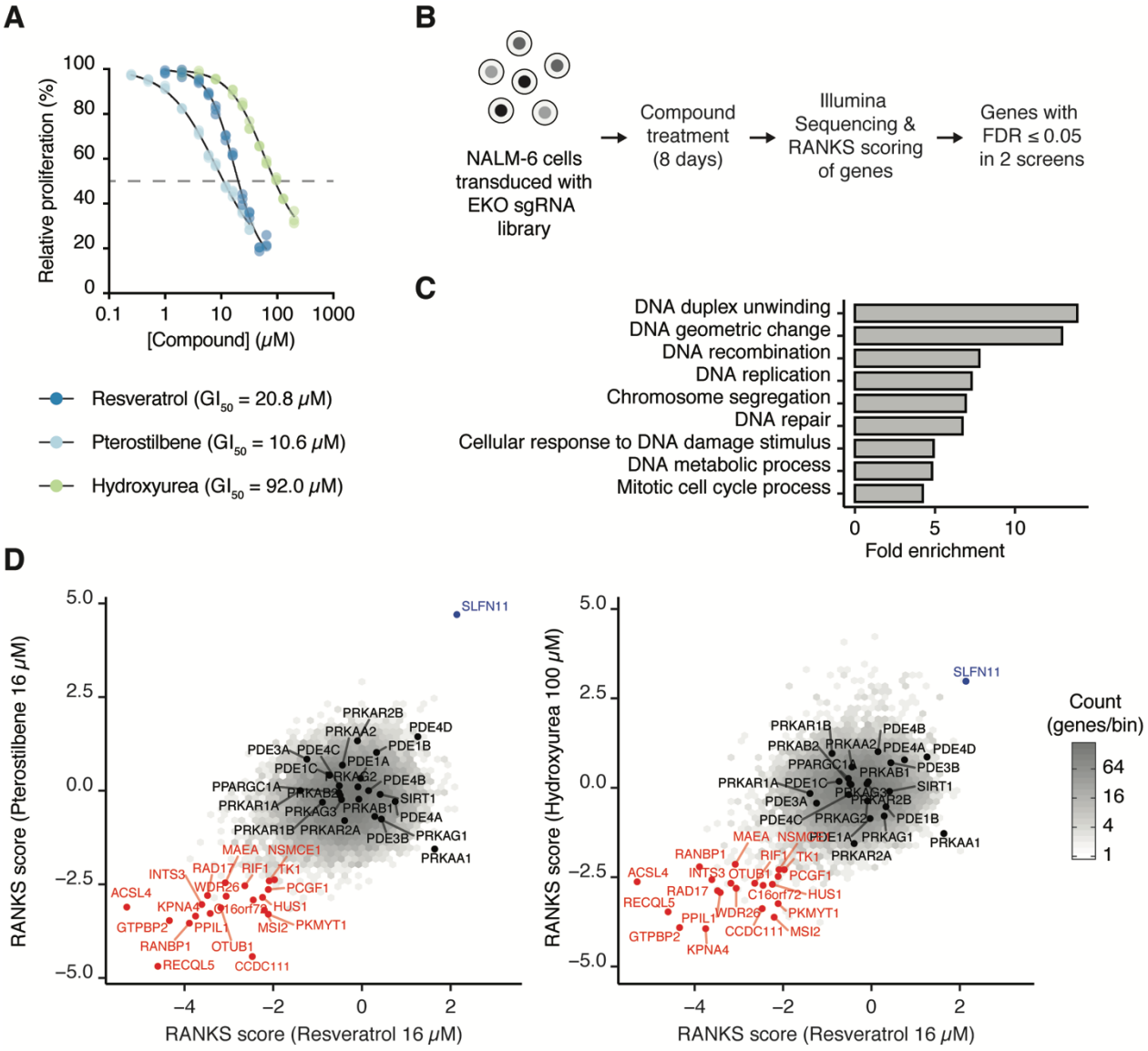

Figure 2.1 | Genome-wide CRISPR knockout screens identify common chemical-genetic interactions between resveratrol, pterostilbene and hydroxyurea.

A. Growth inhibition dose-response curves of NALM-6 cells treated for 72h with resveratrol (RSV), pterostilbene (PTS) and hydroxyurea (HU) relative to DMSO (0.1% v/v) controls. Dashed line represents a 50% inhibition of proliferation (GI_{50}) (n=3). **B.** Schematic of the CRISPR genome-wide

knockout screens and analysis using the RANKS algorithm. **C.** Gene ontology (GO) terms (biological processes with less than 1000 terms) enriched in the list of common synthetic lethal hits (in at least two of the 3 screens). **D.** Scatter plots show genes in the RSV screen compared to either PTS or HU. Shades of grey in each hexagonal bin represent gene count, and genes highlighted in red represent hits common to the three genome-wide screens (*SLFN11* shown in blue as an example of a buffering genetic interaction). Genes highlighted in black represent subunits of other published cellular targets of RSV such as *SIRT1*, *AMPK*, *PGC-1*α and *PDE-1, 3, 4*.

We performed an additional genome-wide CRISPR-Cas9 screen in the T-ALL Jurkat cell line, using the non-inducible TKOv3 sgRNA library (Supplementary figure 2.1C, p. 91)[343]. Using a RSV dosage that resulted in partial growth inhibition of Jurkat cells (25 μM), we scored SSL genetic interactions using the same RANKS algorithm as used in the NALM-6 analysis, and found that the top 300 SSL genes showed a statistically significant overlap with the top 300 SSL genes in NALM-6 cells (Supplementary figure 2.1D-E, p. 91). These common hits were enriched for genes involved in the progression of DNA replication (Supplementary figure 2.1F, p. 91). Thus, our unbiased genome-wide screening approach uncovered regulation of DNA replication as a major genetic signature upon RSV treatment across different cell lines and different sgRNA libraries.

2.4.2 Network analysis of chemical-genetic interactions with resveratrol, pterostilbene and hydroxyurea reveals critical modules implicated in the intra-S phase checkpoint

Examination of the chemical-genetic interactions in NALM-6 cells for each of the three compounds revealed that many of the common hits between the screens converge upon processes implicated in DNA replication and DNA repair (Supplementary figure 2.2, p. 93). Gene products whose disruption sensitized cells to RSV, PTS or HU included: CCDC111, a unique

primase-polymerase suggested to rescue stalled replication forks on the leading strand of DNA[344, 345]; the RFC complex (RFC2, 3 and 5), which is necessary for loading of PCNA onto DNA during DNA replication[123]; and RAD17, which complexes with RFC proteins (RFC2-5) to load the PCNA-related 9-1-1 complex (RAD9A, HUS1, RAD1) onto DNA, which in turn leads to activation of ATR kinase and the intra-S phase checkpoint in response to replicative stress (Figure 2.2A, p. 67)[124-128].

Given the importance of the CHK1 effector kinase in response to replicative stress, we treated NALM-6 cells with RSV or HU and monitored ATR-mediated activation of CHK1 by phosphorylation of the S345 residue[122]. Immunoblotting revealed that phosphorylation of CHK1 S345 occurred after 12 or 24 h exposure to 12 or 24 μM RSV, with kinetics that paralleled HU-treated cells (Figure 2.2B, p. 67). We further explored this checkpoint response in NALM-6 cells, as well as Jurkat cells and non-transformed RPE1-TERT cells at different concentrations of RSV, PTS or HU in combination with chemical inhibitors of ATR, CHK1 or WEE1, a kinase that regulates the G_2/M transition and protects genome stability through effects on DNA replication initiation and nucleotide pool homeostasis[121, 346, 347]. These combinatorial treatments led to synergistic proliferation inhibition that was statistically significant as judged by Bliss additivity (Figure 2.2C, p. 67). These results demonstrate that the cellular response to RSV results in the activation of the DNA replication checkpoint.

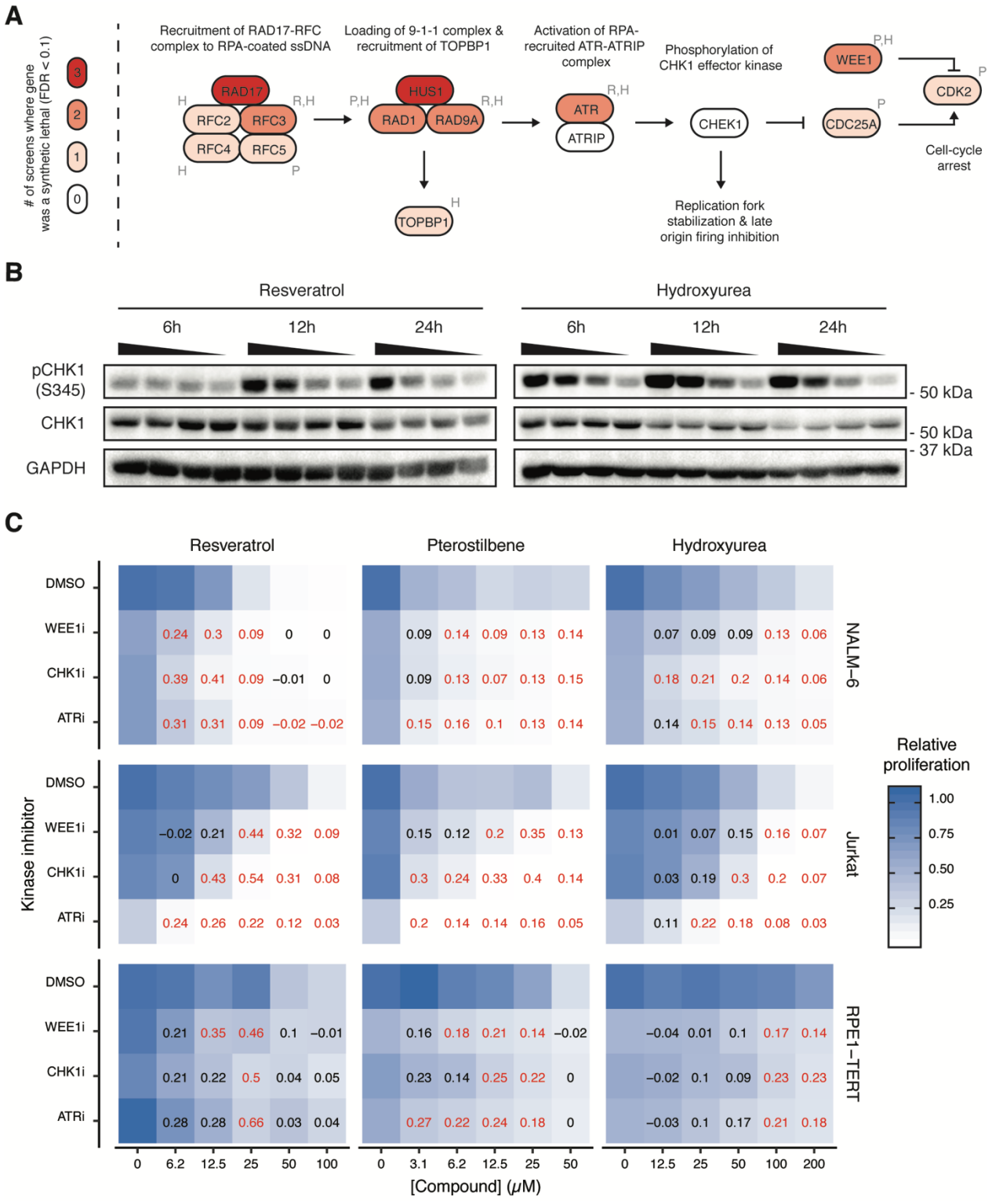

Figure 2.2 | Network analysis of chemical-genetic interactions with resveratrol, pterostilbene and hydroxyurea reveal critical modules implicated in the replication checkpoint.

A. Simplified schematic of the replication checkpoint with genes color-coded based on the number of screens where the knockout showed a synthetic sick/lethal (SSL) phenotype (FDR < 0.1). Genes are further annotated with the identity of the screen where the SSL phenotype was observed; R: resveratrol (RSV), P: pterostilbene (PTS), H: hydroxyurea (HU). **B.** Asynchronous NALM-6 cells were treated for the indicated times with RSV (24, 12, 6 µM or DMSO) or HU (100, 50, 25 µM or DMSO), and protein lysates were blotted using antibodies against the indicated antigens. (1 representative blot of 2 independent replicates). **C.** Proliferation of NALM-6 cells, Jurkat and RPE1-TERT cells upon treatment with RSV, PTS or HU at the indicated concentrations alone or in combination with ATRi (VE-821, 5 µM), CHK1i (MK-8776, 625 nM) or WEE1i (MK-1775, 125 nM). Bliss scores are indicated, and those that are statistically significant are highlighted in red (n=3). Statistical analysis was performed with two-way ANOVA, corrected for multiple comparisons (Sidak's test).

2.4.3 Resveratrol reduces deoxynucleotide triphosphate (dNTP) levels and inhibits DNA replication

Based on the overlapping genetic essentiality signatures of RSV, PTS and HU, we hypothesized that RSV and PTS might elicit replicative stress. To directly assess the impact of each compound on replicative stress, we measured dNTP levels in asynchronous NALM-6 cells by LC-MS quantification after a 4 h treatment. We observed a statistically significant decrease in dNTPs upon RSV or PTS treatment, which was comparable to the decrease observed in cells treated with HU (Figure 2.3A, p. 70). Previously published studies also noted a similarly modest reduction in dNTP pools upon HU treatment of mammalian and yeast cells, which was nonetheless sufficient to induce replicative stress[340, 341]. These results indicate that one of the initial consequences of treatment with RSV is interference with dNTP pool maintenance. We also observed a modest but statistically significant rescue of cell viability upon deoxyribonucleoside supplementation of cells

treated with RSV or PTS that was comparable to the effects observed in HU treated cells (Figure 2.3B, p. 70). This finding is consistent with previously published reports of limited rescue of HU-treated cells with deoxyribonucleosides[348-350]. To investigate whether the observed depletion of dNTP pools was sufficient to impede DNA replication fork progression and elicit an S-phase progression delay as reported previously[341], we used DNA fiber analysis to measure replication fork kinetics in NALM-6 cells. We observed a statistically significant decrease in replication fork progression upon treatment with RSV or PTS, again comparable to the effects of HU (Figure 2.3C-D, p. 70).

To test the downstream consequences of dNTP depletion and replication fork impairment on cell cycle progression, asynchronous NALM-6 cells were pulsed with 5-ethynyl-2'-deoxyuridine (EdU) after a 4 h treatment with RSV, PTS or HU to monitor nucleotide incorporation. Treatment with RSV, and to a lesser extent PTS, reduced EdU incorporation to a level comparable to that of HU (Supplementary figure 2.3A-B, p. 94). Progression through S-phase was also monitored in asynchronous NALM-6 and U2OS cells treated with RSV, PTS, or HU. All three compounds caused a delay in cell cycle progression with an accumulation of cells in S-phase, consistent with replicative stress induction (Figure 2.3E-F, p. 70; Supplementary figure 2.3C, p. 94).

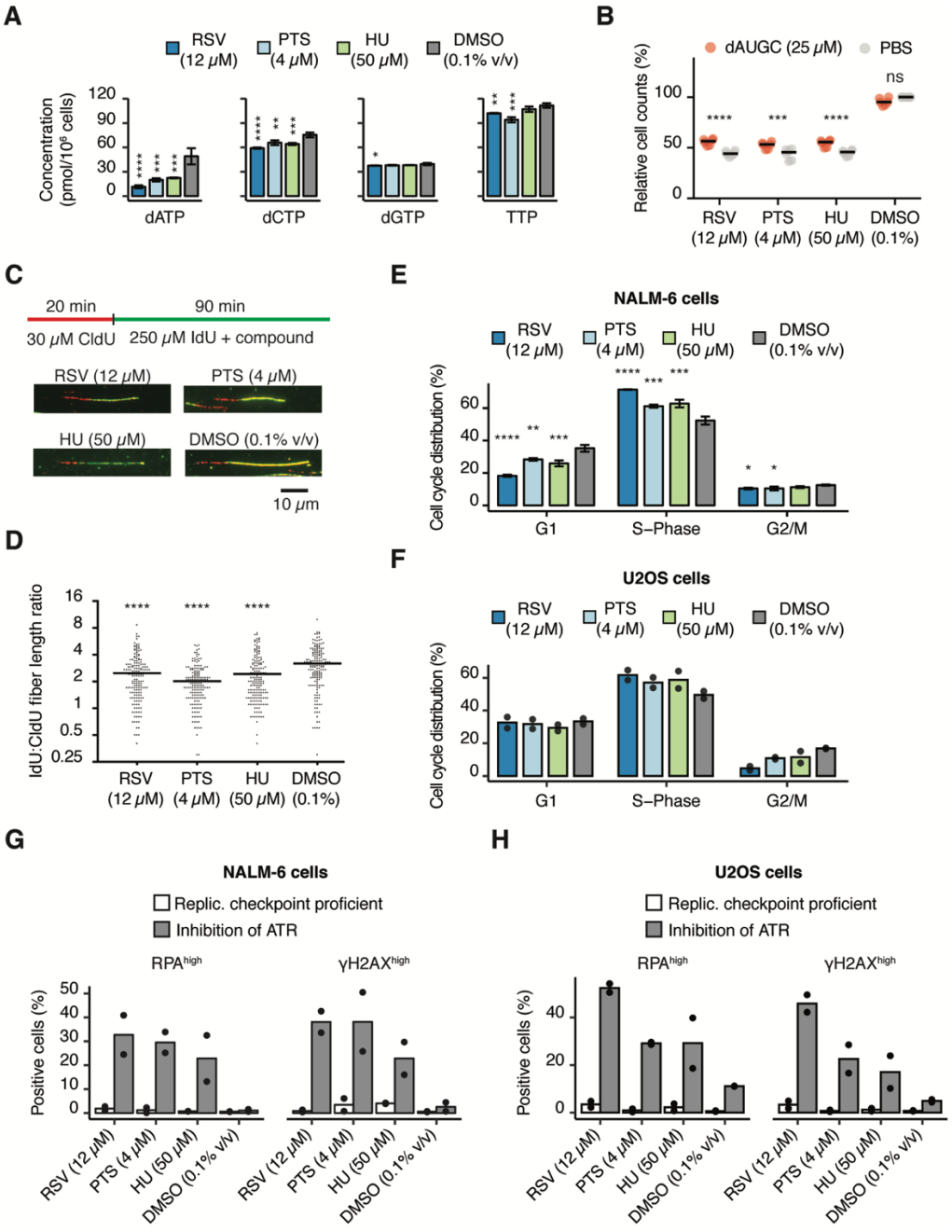

Figure 2.3 | Resveratrol or pterostilbene treatment reduces deoxynucleotide triphosphate (dNTP) levels and prevents completion of DNA replication.

A. Asynchronous NALM-6 cells were treated with the indicated compounds for 4h and dNTPs were extracted and quantified by LC-MS. Bar plots indicate the relative quantity of each dNTP (in pmol) normalized to number of cells used for the extraction (mean ± SD, n=3). **B.** NALM-6 cells were treated with the indicated compounds alone or in combination with deoxyribonucleosides

(25 μM each) and counted after 72h. Results are plotted relative to the DMSO-treated cells (mean ± SD, n = 6). **C.** DNA fiber analysis of NALM-6 cells pulsed with 30 μM CldU for 20 minutes, followed by 250 μM IdU with 12 μM RSV, 4 μM PTS, 50 μM HU or 0.025% DMSO (v/v) for 90 minutes. Representative fibers from each condition are shown. **D.** Ratio of IdU to CldU track length was measured using FIJI software; statistical significance was assessed using two-tailed Mann-Whitney test. **E, F.** Asynchronous NALM-6 **(E)** or U2OS **(F)** were pre-treated with indicated compounds and stained with EdU and propidium iodide followed by cell cycle gating using flow cytometry (NALM-6, n = 3; U2OS, n = 2). See Methods for details. **G, H.** Assessment of chromatin-bound proteins in NALM-6 **(G)** or U2OS **(H)** cells treated for 30 minutes with VE-821 (10 μM) or 0.1% DMSO (v/v) (n=2). See Methods for details. Statistical analyses were performed with one-way ANOVA, corrected for multiple comparisons unless otherwise indicated (*: p-value < 0.05, **: p-value < 0.01, ***: p-value < 0.001, ****: p-value < 0.0001).

After induction of replicative stress, the heterotrimeric RPA complex binds to ssDNA generated at stalled replication forks, which in turn promotes activation of ATR, the apical kinase of the S phase checkpoint response[351]. Lack of ATR activity causes exhaustion of RPA cellular pools upon HU, leading to widespread induction of DNA double-strand breaks at stalled replication forks in a phenomenon termed “replication catastrophe”[131]. We investigated whether ATR inhibition in NALM-6 or U2OS cells treated with RSV, PTS, or HU sensitized cells to replication fork catastrophe, which is typified by increased levels of γH2AX and DNA-bound RPA. For all three compounds, we observed a significant increase in the number of cells exhibiting elevated chromatin-bound RPA and γH2AX (Figure 2.3G-H, p. 70; Supplementary figure 2.3D-E, p. 94). These results support our genetic findings that, akin to HU, RSV and PTS suppress cell proliferation via inhibition of DNA replication.

2.4.4 Proliferation inhibition by resveratrol is modulated by DNA replication-related genes

To test individual genetic hits from the screens for their chemical-genetic interaction with RSV and PTS, we queried engineered deletions for a top sensitizer hit and a top resistance hit, *RECQL5* and *SLFN11,* respectively, for their sensitivity to RSV or PTS. *RECQL5* is a member of the RECQL helicase family that has multiple protective roles in replication fork progression and stability as well as in DNA damage repair[352-355]. *SLFN11* has been described as a restriction factor or 'executioner' for replication stress, due to its ability to induce irreversible DNA replication arrest under conditions of replicative stress[356, 357]. We engineered NALM-6 knockout populations in which *RECQL5* or *SLFN11* were disrupted via two different sgRNAs per gene (Supplementary figure 2.4A-C, p. 96; Supplementary table 2.1 & 2.2, p. 197-198). Upon competitive growth analysis of these populations, we found that *RECQL5* knockout cells had reduced relative fitness when treated with RSV, PTS or HU, while *SLFN11* knockout cells displayed an increased relative fitness (Figure 2.4B, p. 73; Supplementary figure 2.4D, p. 96). We also confirmed that *RECQL5* disruption in Jurkat cells resulted in a similar reduction in relative fitness when treated with RSV or PTS (Supplementary figure 2.4E p. 96). Furthermore, overexpression of the β-isoform of RECQL5 specifically rescued the fitness defect of *RECQL5* knockout cells in the presence of RSV or PTS (Supplementary figure 2.4F-G, p. 96; Supplementary table 2.2, p. 198). These results establish that *SLFN11* and *RECQL5* were *bona fide* hits in the CRISPR-Cas9 screens, and that the opposing effects of their disruption on cell viability are consistent with an influence of RSV and PTS on DNA replication.

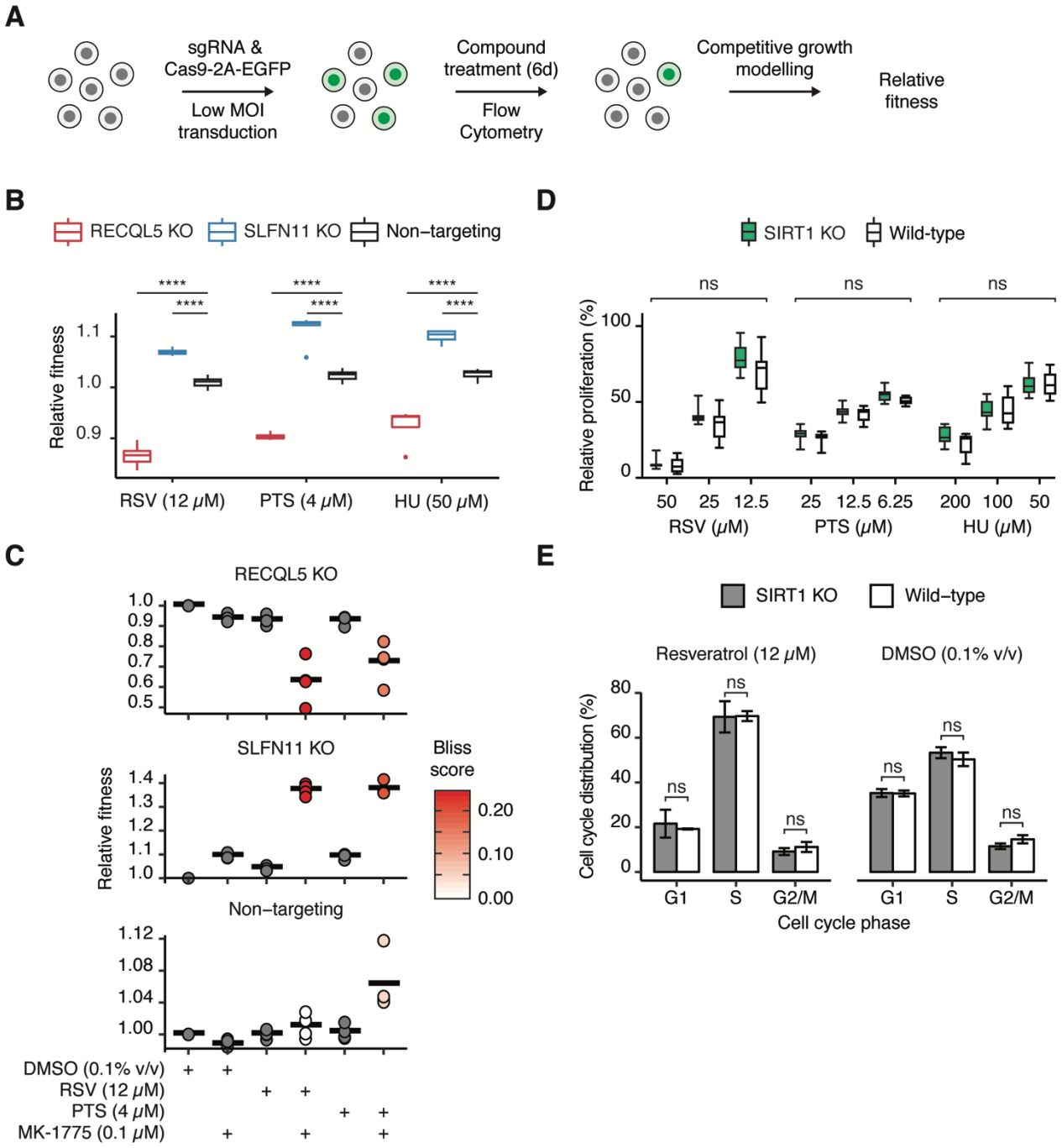

Figure 2.4 | Proliferation inhibition by resveratrol is modulated by deletion of DNA replication-related genes and is independent of SIRT1.

A. Competitive growth assay in NALM-6 cells. Flow cytometry was used to monitor EGFP-positive cells to measure their fitness relative to wild-type uninfected cells upon different treatments. **B.** The relative fitness of *RECQL5*-disrupted or *SLFN11*-disrupted NALM-6 cells in the presence of the

indicated compounds was measured by competitive growth assay (n ≥ 3). **C.** Relative fitness of *RECQL5*-, *SLFN11*-disrupted or non-targeting controls treated with 12 µM RSV or 4 µM PTS in combination with 0.1 µM MK-1775 was measured by competitive growth. Point color represents the average synergy, relative to single-agent treatments in grey (n=4). **D.** Proliferation of *SIRT1* KO (3 independent clones) or wild-type NALM-6 cells after 72h of treatment with the indicated compounds relative to 0.1% DMSO (v/v) (n ≥ 8). **E.** Asynchronous NALM-6 cells (4 independent SIRT1 KO clones used), pre-treated with the indicated compounds for 24h were pulsed with EdU (followed by click chemistry with Cy5.5-azide) and stained with propidium iodide followed by cell cycle gating using flow cytometry (mean ± SD, n = 3). Statistical analysis was performed with one-way ANOVA, corrected for multiple comparisons (ns: p-value > 0.05, ****: p-value < 0.0001).

Given the proliferation inhibition synergy observed between RSV, PTS or HU and WEE1 kinase inhibition (Figure 2.2C, p. 67), we tested if these combinatorial treatments could further exacerbate the phenotype of *RECQL5*- or *SLFN11*-disrupted cells. We found that chemical inhibition of WEE1 with the small molecule MK-1775 led to a synergistic reduction of fitness in *RECQL5*-disrupted cells treated with RSV or PTS relative to wild-type NALM-6 cells (Figure 2.4C, p. 73). Conversely, *SLFN11* knockout cells were resistant to the same combinatorial treatment and exhibited an increased relative fitness (Figure 2.4C, p. 73). These results indicate that the growth inhibition induced by RSV or PTS is exacerbated by replicative stress-inducing treatments.

2.4.5 Proliferation inhibition by resveratrol is independent of SIRT1

SIRT1 was not identified as a hit in our screens as its disruption conferred neither a protective nor a sensitizing effect on NALM-6 or Jurkat cell proliferation in the presence of RSV or PTS (Figure 2.1D, p. 64; Supplementary figure 2.1E, p. 91). To validate this result, we generated *SIRT1* knockout clonal NALM-6 cells by targeting the first exon of the gene with two different

sgRNAs (Supplementary figure 2.4H, p. 96; Supplementary table 2.2, p. 198). After treatment of 3 independent *SIRT1* knockout clones with RSV or PTS, no difference in proliferation was observed relative to non-targeting controls (Figure 2.4D, p. 73). *SIRT1* knockout NALM-6 cells treated with RSV also showed a similar cell cycle distribution and EdU incorporation level as control non-targeted cells (Figure 2.4E, p. 73; Supplementary figure 2.4I, p. 96). Other known targets of RSV with functions in metabolism, for example AMP kinase (AMPK) signaling and mitochondrial biogenesis (PGC1-α)[315, 318, 358, 359], were also not recovered as hits in the CRISPR-Cas9 screens (Figure 2.1D, p. 64; Supplementary figure 2.1B, 2.1E, p. 91). These findings show that, in NALM-6 cells, the absence of *SIRT1* does not impact the ability of RSV to inhibit cell proliferation and S-phase transit.

2.5 Discussion

We uncovered a concordance of chemical-genetic interactions between RSV, its chemical analog PTS and HU that suggests replicative stress is a primary mechanism-of-action by which these compounds inhibit human cell proliferation. To our knowledge, this is the first instance in which the cellular effect of RSV has been probed by a genome-wide screen. Some previous studies support our findings, including the observation that RSV inhibits purified mammalian RNR and impedes DNA synthesis[360] and studies showing that RSV or the analog 4,4'-dihydroxy-trans-stilbene (DHS) inhibit RNR and induce replicative stress in mammalian cells[361-366]. We did not observe an influence of SIRT1 on cell cycle progression or proliferation in response to RSV, even at concentrations that in other studies elicited phenotypes influenced by SIRT1[334, 367-371].

Our study does not address the role of RSV, or its *SIRT1*-dependence, in other contexts such as lifespan prolongation. However, it is of note that previous studies have linked replicative stress and lifespan[372, 373]. In *S. cerevisiae* the DNA damage-activated kinase Rad53 is a master regulator of replicative stress[374]. Deletion of *RAD53* shortens chronological lifespan[375], whereas overproduced Rad53[376] or DNA-damaging agents such as HU extend yeast lifespan in some contexts[377]. Overexpression of the yeast sirtuin ortholog Sir2 or the DNA replication/recombination RAP1-interacting factor, Rif1, extend replicative lifespan[378-382] and also regulate DNA replication origins at the rDNA locus and elsewhere[47, 381, 383-387]. Recently, low doses of RSV (2.5 μM) were found to protect genome stability via a reduction in replication stress-associated DSBs in murine 3T3 cells[388]. We speculate that resveratrol might elicit a type of hormesis[389, 390], whereby low-level replicative stress may be beneficial in some contexts. Despite the existing wealth of literature on the impact of RSV in cell and animal models, our unbiased genome-wide screens yield new insight that a conserved feature of the response to RSV in human cells is the induction of replicative stress. Further studies will be needed to understand the intriguing interplay between RSV-induced replicative stress and cell physiology.

2.6 Methods

2.6.1 Cell culture

NALM-6 and Jurkat cells were grown in 10% FBS (v/v) (Wisent) RPMI 1640 medium (Wisent), RPE1-TERT and HEK293T cells were grown in 10% FBS (v/v) DMEM medium (Wisent), and U2OS cells were grown in 10% FBS (v/v) DMEM medium (Gibco) supplemented with L-Glutamine and Penicillin/Streptomycin at 5% (v/v) CO_2 and 37°C. A NALM-6 clone with inducible expression of

Cas9 used for the CRISPR knockout screen has been previously described[264]. All cell lines used for this study were confirmed to be mycoplasma-negative by standard multiplex PCR. Cells were sub-cultured every 2-3 days and the asynchronous NALM-6 cell population propagated at 4 x 10^5 cells/mL every day for 3 days.

2.6.2 Single sgRNA cloning

The LentiCRISPRv2GFP plasmid (a gift from David Feldser, Addgene #82416)[391] and single sgRNA cloning was performed according to Sanjana et al.[392]. Briefly, the plasmid was digested with FastDigest Esp3I and dephosphorylation with FastAP, and the resulting product was purified by gel extraction. sgRNA sequences were designed with the "sgRNA Designer" tool[247] and ordered along with the reverse-complement sequence as oligonucleotides from IDT. For each sgRNA used in this study (see Supplementary table 2.1 for sgRNA sequence, p. 197), the sgRNA oligonucleotide and its respective reverse-complement oligonucleotide were phosphorylated with PNK and annealed in a thermocycler. The resulting double-stranded oligonucleotide was ligated with the digested LentiCRISPRv2GFP plasmid with T4 DNA ligase and transformed into Stbl3 cells (ThermoFisher). The final plasmids were purified and sequence-verified to confirm the proper sgRNA sequence was inserted downstream of the U6 promoter.

2.6.3 Genome-wide CRISPR knockout screens

A NALM-6 clone with inducible Cas9 expression previously transduced with the EKO library was used to perform the genome-wide knockout screens[264]. The frozen uninduced library was thawed in RPMI 1640 media containing 10% FBS (v/v) and Cas9 expression was induced with doxycycline at 2 µg/mL. After 7-8 days of doxycycline treatment (7 days for RSV; 8 days for PTS), the pooled library was split in different T-75 flasks (28 x 10^6 cells per flask, corresponding to ~100 cells/sgRNA

for the 278,754 different sgRNAs in the EKO library) at 4 x 10^5 cells/mL. Compounds (16 µM Resveratrol, 16 µM Pterostilbene, 100 µM Hydroxyurea or DMSO only) were added (at 1000X) to a final DMSO concentration of 0.1% (v/v). Cells were counted every 2 days, and upon reaching 8 x 10^5 cells/mL the library primary titer of 28 x 10^6 cells were reseeded at 4 x 10^5 cells/mL in the presence of fresh compound for a total of 8 days. The genome-wide screen in Jurkat cells was performed by transduction of cells with the lentiviral TKOv3 library as described[343] with some modifications. Briefly, 120 x 10^6 cells were infected at an MOI of 0.5 corresponding to a coverage of 800 cells/sgRNA for the 71,090 sgRNA in the TKOv3 library. Two days after infection, cells were selected with 0.5 µg/mL puromycin for 2 days. 36 x 10^6 Jurkat cells were then treated with 25 µM resveratrol or DMSO 0.1% (v/v) for 12 days and sub-cultured every 3 days with fresh compound added. Compound concentrations were based on the approximate IC30 for each line (NALM-6, 16 µM; Jurkat, 25 µM) (data not shown). After the compound treatments, cells were collected, genomic DNA was extracted using a Gentra Puregene Cell kit according to manufacturer's instructions (Qiagen #158388) and the sgRNA sequences were PCR-amplified. sgRNA frequencies were obtained by next-generation sequencing (Illumina HiSeq2000 or NextSeq 500, as indicated in NCBI GEO record GSE150232). Reads were aligned using Bowtie2.2.5[393] in the forward direction only (--norc option) with otherwise default parameters and total read counts per sgRNA tabulated. Read counts from the different sequencing lanes for the same sample were summed. Read counts from all control samples and time-points from each experiment were summed (for further details see NCBI GEO record GSE150232). Control samples were pooled irrespective of whether they were treated with DMSO 0.1% (v/v) or untreated (i.e. no DMSO), as no DMSO-specific signature was observed and pooling together read counts from all controls provided

additional statistical power. Context-dependent gene essentiality was calculated using the RANKS algorithm as previously described[264]. Gene ontology terms enrichment was calculated with the "gprofiler2" package in R where the 'hit genes' list was considered an unordered query and only 'GO biological processes' was used as a data source with subsequent filtering for GO terms that contain less than 1000 terms[394]. Statistical significance of the overlap between the top 100 or 300 genetic (synthetic sick/lethal or buffering) interactions was calculated using the hypergeometric test in R.

2.6.4 Clonal knockouts in NALM-6 cells

Clonal knockouts were generated via nucleofection of NALM-6 cells with the respective sgRNA-expressing LentiCRISPRv2GFP plasmids with the SF Cell Line 4D-Nucleofector X Kit L. NALM-6 cells (1 x 10^6 cells per nucleofection) were centrifuged at 90 x *g* for 10 minutes and resuspended in 100 µL of nucleofection solution. The respective plasmids (2 µg) were added to the cell suspension and subjected to the CV-104 pulse on the 4D nucleofector (Lonza). Cells were immediately transferred to a 12-well plate with pre-warmed media (37°C) and incubated overnight. Clones were selected the next day by EGFP-positive single cell sorting on a BD FACSAria II and genotyped with Sanger sequencing of the target locus after expansion of the clones.

2.6.5 Lentiviral transduction of NALM-6 and Jurkat cells

LentiCRISPRv2-EGFP plasmids were packaged into lentiviral particles via co-transfection within HEK293T cells (in a 10-cm plate) with 9 µg of the plasmid along with 6 µg of psPAX2 (A gift from Didier Trono; Addgene #12260) and 3 µg of pCMV-VSV-G (A gift from Bob Weinberg; Addgene #8454)[395] with 5 µg/mL of polyethylenimine (PEI 25000) in DMEM 10% FBS (v/v). After a 16 h incubation, media was removed and replaced with DMEM 2% FBS (v/v) and incubated for 32

hours. Lentiviruses were recovered and filtered with a 0.45 µm filter and stored at -80 °C after addition of concentrated storage buffer (final concentration: 5% sucrose (w/v), 2 mM MgCl2, 10 mM HEPES). Lentiviral particles were mixed with protamine sulfate at a concentration of 20 µg/mL in a final volume of 1 mL and incubated for 15 minutes. This solution was subsequently added to 1 x 10^6 NALM-6 cells (1 mL) and incubated for 48 hours at 37 °C. EGFP-positive cells percentage was measured on a BD FACSCanto II after proper FSC/SSC gating to calculate transduction efficiency.

2.6.6 Indel decomposition and genotyping

Cells that were subjected to indel sequencing were collected (2 x 10^5 to 4 x 10^5 cells) and genomic DNA was extracted with the PrepGEM Tissue kit. Each respective targeted genomic region was amplified by PCR with the KAPA HiFi HotStart enzyme and primers specific to each locus. PCR products were purified with silica-based columns and standard Sanger sequencing was performed (see Supplementary table 2.1 for primer sequence, p. 195). The TIDE analysis method was used for indel decomposition of the sequencing traces with the ICE online tool (https://ice.synthego.com/)[396]. Indel efficiency for each knockout population was calculated as the indel quantification by TIDE normalized by the EGFP+ percentage as a proxy for transduction efficiency. Clonal knockout genotype was inferred directly from the sequencing chromatogram indel decomposition.

2.6.7 Relative proliferation assays

NALM-6 or Jurkat cells were seeded at 1 x 10^5 cells/mL in 24-well plates and compounds were added at a 1:1000 dilution of a working stock solution (in 100% DMSO (v/v)), to yield a final DMSO concentration of 0.1% (v/v). The deoxyribonucleoside complementation was performed with an

equimolar (25 µM) mix of deoxyadenosine, deoxyguanosine, deoxycytidine and deoxyuridine (dU was used as a precursor of TTP in place of thymidine to avoid a potential thymidine block). After 72 hours of incubation at 37°C, cell concentration was measured on a Beckman-Coulter Z2 Counter after application of standard thresholds to exclude debris. Relative proliferation was calculated as a ratio of the population doubling of the treatment to the population doubling of the respective DMSO control (e.g. Figure 2.1A, p. 64). Relative cell counts (e.g. Figure 2.3B, p. 70) were calculated as the ratio of cell counts for the indicated treatment relative to the cell count of the DMSO-treated control. For the luminescence-based measurements of relative proliferation, the CellTiter-Glo reagent was used. Briefly, 8000 NALM-6, 8000 Jurkat or 1600 RPE1-TERT cells were seeded in 96-well plates with the indicated compound concentrations (RPE1-TERT cells were left overnight to regain adherence before addition of compounds) and incubated for 72h. After the incubation period, CellTiter-Glo reagent was diluted 1:3 (in fresh DMEM with 10% FBS (v/v) for RPE1-TERT cells or directly in the suspension culture for NALM-6 and Jurkat cells) and luminescence was measured on a Tecan M1000pro plate reader with an integration time of 1000 ms. Relative proliferation was calculated as a ratio of average luminescence of the treatment to the average luminescence of the plate-matched DMSO control. Where indicated, the relative proliferation data were fitted as a 4-parameter nonlinear regression with GraphPad Prism 8 to obtain the dose-response curves.

2.6.8 Competitive growth assays

NALM-6 or Jurkat cells were transduced with LentiCRISPRv2GFP lentiviral particles at a low multiplicity of infection (MOI) in order to obtain a transduction efficiency between 30-70%. These cells were propagated in culture for 14 days and indel efficiency was measured as detailed above.

The cells were seeded at 1 x 10^5 cells/mL and treated with the respective compounds for 6 days (sub-cultured 3 days after compound addition with fresh compound) and EGFP-positive cells percentage was measured (at day 0, 3 and 6 of compound treatment) on a BD FACSCanto II after FSC/SSC gating. Relative fitness (F) for each genotype was calculated as the rate at which knockout cells in the population (EGFP-positive, N_{KO}) were superceded by wild-type cells (EGFP-negative, N_{WT}) or vice versa with the following formula to calculate the ratio between the cells within the population (R_d, where d represents the number of days after compound addition):

$$R_d = \frac{N_{KO} \times 2^{d \times G_{KO}}}{N_{WT} \times 2^{d \times G_{WT}}}$$

For each compound treatment, the resulting relative proliferation of the cell population (I) was used to normalize the maximal rate that a cell subpopulation can dominate the culture:

$$R_d = R_0 \times 2^{d(G_{KO} - G_{WT})I}$$

The ratio R_d was log-transformed (base 2), plotted relative to the day of treatment and linear regression was performed to extract the slope. This slope was used to calculate the growth rate of knockout cells for each genotype G_{KO} and normalized to the wild-type cells growth rate (G_{WT} = 1.25 doublings/day on average for NALM-6 cells) to achieve the relative fitness value (F):

$$F = \frac{G_{KO}}{G_{WT}}$$

2.6.9 dNTP extraction and quantification by LC-MS

All LC/MS grade solvents and salts were purchased from Fisher (Ottawa, Ontario, Canada): water, acetonitrile (ACN), methanol (MeOH), formic acid, ammonium acetate and ammonium formate. The authentic metabolite standards were purchased from Sigma-Aldrich Co. (Oakville, Ontario,

Canada). Asynchronous NALM-6 cells were treated with the indicated compounds for 4 hours. After the treatment period, cells were centrifuged and rinsed three times in cold 150 mM ammonium formate (pH 7.4). Cells were centrifuged and quenched on dry ice following the addition of 380ul of 50% methanol/water (v/v) and 220 µl acetonitrile (ACN) (both reagents pre-chilled to -20 °C). Cells were then subjected to bead beating for 2 min at 30 Hz (Eppendorf Tissue-lyser). Lipids were partitioned through the addition 600 µL of cold dichloromethane and 300 µL of cold H_2O. The upper aqueous layer was then removed and dried using a vacuum centrifuge with sample temperature maintained at -4^oC (LabConco). Samples were resuspended in 30 µL H_2O and subjected to LC-MS analysis.

The relative concentrations of the triphospho-deoxy nucleotides were measured using a triple quadrupole mass spectrometer (QQQ 6470) equipped with a 1290 ultra high-pressure liquid chromatography system (Agilent Technologies, Santa Clara, California, USA). Chromatographic separation was achieved using a Scherzo SM-C18 column 3 µm, 3.0×150 mm (Imtakt Corp, JAPAN). The chromatographic gradient was initiated at 100% mobile phase A (5 mM ammonium acetate in water) with a 5 min gradient to 100% B (200 mM ammonium acetate in 20% ACN / 80% water) at a flow rate of 0.4 mL/min, followed by a 5 min hold time at 100% mobile phase B and a subsequent re-equilibration time (6 min) before the next injection. Multiple reaction monitoring (MRM) transitions were optimized on standards for each metabolite quantitated. Transitions for quantifier and qualifier ions were respectively 492 → 136 and 492 → 119, 81, 53 for dATP (retention time 6.89 min); 508 → 152 and 508 → 135, 110, 81 for dGTP (retention time 6.65 min); 468→ 112 and 468 → 95, 81, 53 for dCTP (retention time 5.79 min); 500 → 81 and 500 → 483, 53 for TTP (ammonium adduct; retention time 6.2 min). An Agilent JetStream^{TM} electro-spray

ionization source was used in positive ionization mode with a gas temperature and flow were set at 300°C and 5 L/min respectively, nebulizer pressure was set at 45 psi and capillary voltage was set at 3500V. Relative concentrations were determined from external calibration curves prepared in water. Ion suppression artifacts were not corrected; thus, the presented metabolite levels are relative to the external calibration curves and should not be considered as absolute concentrations. Data were analyzed using MassHunter Quant (Agilent Technologies).

2.6.10 EdU incorporation in NALM-6 cells

Asynchronous NALM-6 cells were treated with the indicated compounds and incubated at 37 °C for 4 hours. The cells were then treated with 5-ethynyl-2'-deoxyuridine (EdU) at 3 μM for 60 minutes. After the EdU pulse, cells were collected, washed in PBS and fixed in 2% paraformaldehyde (w/v). Fluorescent labeling of incorporated EdU was performed with click chemistry solution (25 mM $CuSO_4$, 5 mM ascorbic acid and 5 μM AlexaFluor488-Azide) for 30 minutes followed by flow cytometry on a BD FACSCanto II to measure AF488 fluorescence intensity.

2.6.11 Measurement of cell cycle progression

Asynchronous NALM-6 cells were treated with the indicated compounds and incubated at 37°C for 24 hours. Cells were then pulsed with 10 μM EdU before being collected, and fixed in 4% paraformaldehyde (w/v). Fluorescent labeling of incorporated EdU was performed with click chemistry solution (25 mM $CuSO_4$, 5 mM ascorbic acid and 5 μM Cy5.5-Azide) for 30 minutes at 37 °C. Cells were then washed and incubated with propidium iodide (PI) staining solution (0.1% Triton X-100 (v/v), 200 μg/mL RNAse A, 20 μg/mL PI) for 30 minutes at 37°C with mild agitation followed by flow cytometry on a BD LSRFortessa to measure Cy5.5 and PI fluorescence intensity.

2.6.12 DNA fiber assay

The DNA fiber analysis procedure was adapted from that of Chaudhuri et al[397]. Briefly, 6 x 10^6 asynchronously growing cells were pelleted and resuspended in 10 mL 30 µM CldU in RPMI 1640 medium. After 20 minutes at 37˚C, cells were pelleted, washed once with 10 mL PBS, and resuspended in 20 mL 250 µM IdU in RPMI 1640 medium. Cells were split between 4 dishes and treated with 12 µM resveratrol, 4 µM pterostilbene, 50 µM hydroxyurea or an equivalent volume of DMSO (0.025% v/v). After 90 minutes at 37˚C, cells were pelleted, washed once with 5 mL PBS, then resuspended in 500 µL PBS. A 2 µL drop of cells was placed on a microscope slide and allowed to dry until its volume was visibly reduced. Seven µL of lysis buffer (50 mM EDTA, 0.5% SDS (w/v) in 200 mM Tris pH 7.5) was then added to the drop and incubated for 3 minutes before tilting the slide at a 25˚ angle to allow the drop to run down the slide. Slides were dried horizontally, then fixed 10 minutes in a Coplin jar using ice cold 3:1 methanol:acetic (v/v) acid. Slides were washed once in water, denatured 80 minutes in 2.5 M HCl and washed three times in PBS before proceeding with immunostaining. Slides were blocked in 5% BSA (w/v) in PBS in a humid chamber 20 minutes at room temperature (RT), then incubated with anti-BrdU (rat monoclonal [BU1/75 (ICR1)], 1:400; cross-reacts with CldU) and anti-BrdU (mouse monoclonal (Clone B44), 1:25; cross-reacts with IdU) 90 minutes at RT, followed by Alexa Fluor 594 goat anti-rat IgG (H+L) (1:100) and Alexa Fluor 488 goat anti-mouse IgG (H+L) (1:100) for 60 minutes at RT in the dark. Cover slips were mounted using Immuno-Fluore Mounting Medium (MP Biomedicals). Images were captured at 60 X magnification using a DeltaVision Imaging System (GE Lifesciences), and analysis was performed using FIJI software (NIH).

2.6.13 Measurement of RPA and γH2AX loading on chromatin

The association of RPA and γH2AX with chromatin was quantified by flow cytometry as previously described[398]. Briefly, cells were treated with 10 μM ATR inhibitor VE-821 or an equivalent volume of DMSO (0.1% v/v) for 30 minutes prior to the addition of 12 μM resveratrol, 4 μM pterostilbene, 50 μM hydroxyurea or an equivalent volume of DMSO (0.025% v/v) for 24 hours (NALM-6 cells) or 6 hours (U2OS cells; timepoints were optimized to minimize toxicity of ATR inhibition alone). After treatment, cells were permeabilized for 10 minutes in 0.2% Triton X-100 (v/v) in PBS, then fixed for 30 minutes in 2% formaldehyde (v/v) in PBS and stored at 4˚C in 3% heat-inactivated FBS (w/v), 0.09% sodium azide (w/v) in PBS. After 16 hours, cells were immunostained with anti-phospho-histone H2A.X (Ser139) (mouse monoclonal [clone JBW301], 1:200) and anti-RPA70 (rabbit monoclonal [EPR3472], 1:200) in 1:10 Perm/Wash Buffer 1 hour at RT, followed by Alexa Fluor 488 goat anti-mouse IgG (H+L) (1:200) and Alexa Fluor 594 goat anti-rabbit IgG (H+L) (1:200) in 1:10 BP Perm Wash for 30 minutes at room temperature in the dark. Cells were resuspended in Analysis Buffer (0.5 μg/mL DAPI, 250 μg/mL RNase, 0.02% sodium azide (w/v), 1 mg/mL BSA in PBS) for 30 minutes at 37˚C. Flow cytometry was performed using a BD LSRFortessa cell analyzer with BD FACSDiva software (BD Biosciences), and analysis performed with FlowJo software.

2.6.14 Protein-protein interaction network analysis

Protein interactions between the gene hits common to at least two screens were retrieved from the BioGRID database using the GeneMania and EsyN tools[399-401]. Genes that show protein-protein interactions with the aforementioned gene hits but only scored as a hit in 1 screen were added to expand the network. An additional 12 genes were chosen for visualization purposes,

shown in white in Figure S2, that were not hits in the RSV screen but exhibited multiple interactions with other hits.

2.6.15 Western blots

Cells were washed once in PBS and lysed on ice for 30 minutes in NP-40 lysis buffer (50 mM Tris-HCl pH 6.8, 150 mM NaCl, 1% (v/v) NP-40, 1X protease inhibitor cocktail (cOmplete EDTA-free, Roche), 1X phosphatase inhibitor cocktail (PhosSTOP, Roche). Protein lysates were cleared by centrifugation at 13000 *x g* for 15 minutes at 4 °C and supernatant protein concentration was measured using a modified Lowry method (DC protein assay, Bio-Rad). 30 µg of protein lysates were resolved on an 8% or 10% (v/v) SDS-PAGE gel and transferred to a 0.22 µm nitrocellulose membrane. Membranes were blocked with 5% BSA (for phospho-Chk1 immunoblotting) or 3% (w/v) milk in TBS-Tween 0.05% (v/v) (TBST) before blotting using the following antibody dilutions in TBST: S345 phospho-CHK1 (1:2000), CHK1 (1:2000), RECQL5 (1:1000), SLFN11 (1:1000), SIRT1 (1:1000), GAPDH (1:5000), α-Tubulin (1:5000) followed by incubation with the respective HRP-conjugated secondary antibodies (1:10000 dilution in 3% (w/v) milk in TBST or, for phospho-CHK1 immunoblots in TBST containing 5% BSA (w/v)). Blots were developed by incubation with ECL substrate and chemiluminescence was measured using a ChemiDoc MP (Bio-Rad). See Supplementary table 2.3 (p. 199) for antibody RRIDs.

2.6.16 RECQL5 complementation assay

The *RECQL5* beta-isoform cDNA sequence was retrieved from the NCBI CCDS database (CCDS42380.1) and ordered from Twist Biosciences as a sequence-verified plasmid (kanamycin resistant) with a C-terminal P2A tag (5'-GCCACGAACTTCTCTCTGTTAAAGCAAGCAGGAGACGT GGAAGAAAACCCCGGTCCC-3') with the full insert flanked by SapI restriction enzyme sites. The

desired insert was retrieved by restriction digest with SapI. The pHAGE-EGFP backbone (kindly provided by E. Gagnon and modified from pHAGE-EF1aL-eGFP; a gift from Darrell Kotton [Addgene, plasmid 126686]) was amplified by PCR to add the overlap sequences to the insert followed by DpnI digestion to remove the parental backbone. Gibson assembly[402] was used to ligate the two fragments to clone the *RECQL5* cDNA in the pHAGE lentiviral backbone under the control of the EF1a promoter for constitutive expression and upstream of the P2A-EGFP sequence, and the resulting reaction was transformed in Stbl3 cells (ThermoFisher) and selected with ampicillin. The construct was sequence verified, packaged into lentiviral particles and transduced into clonal *RECQL5* KO or non-targeting control cells (n=3 clones per genotype). Flow cytometry was used to track RECQL5-overexpressing cells during the 6-day treatment with resveratrol (12 µM), pterostilbene (4 µM) or DMSO 0.1% (v/v). The RECQL5-overexpressing cells enrichment was calculated as the ratio of EGFP-positive cells at each day relative to day 0 in resveratrol or pterostilbene-treated cells divided by the ratio of EGFP-positive cells at each day relative to day 0 in DMSO-treated cells. Data is shown as the log-transformed (base 2) ratio relative to the day of treatment.

2.6.17 Quantification and statistical analysis

All statistical analyses were performed on PRISM 8 (www.graphpad.com). Statistical significance between the respective treatments was carried out with a Student t-test, or, when more than two treatments were compared, with ANOVA using the Sidak or Tukey correction for multiple comparisons. Synergy between MK-1775 and resveratrol/pterostilbene on the relative fitness of *RECQL5*- or *SLFN11*-disrupted NALM-6 cells was calculated using the Bliss model of synergy. Since relative fitness as calculated above from competition growth assays is a divergent score around

1, the relative fitness of wild-type cells (F = 1) was subtracted from the relative fitness of each treatment and the absolute value of the difference is used as the fractional response in the Bliss model[403]. Assessment of the statistical significance of the Bliss score was performed using two-way ANOVA to compare the log-transformed measured relative proliferation to the expected additivity (based on the single-agent treatments) using error propagation to estimate the uncertainty of each measurement[404]. The relevant statistical details for each experiment, including the number of biological replicates, are also listed in the figure legends.

2.7 Acknowledgements

The authors thank the IRIC cytometry, high-throughput screening and genomics facilities, as well as Corinne St-Denis for technical assistance. We thank Steve Elledge for providing NALM-6 cells, Jason Moffat for providing the TKOv3 library, and Étienne Gagnon for providing the modified pHAGE-EGFP plasmid. The Goodman Cancer Research Centre Metabolomics facility at McGill University is supported by the Terry Fox Foundation, Quebec Breast Cancer Foundation, The Dr. R. John Fraser and Mrs. Clara M. Fraser Memorial Trust, and McGill University. This research was supported by the Canadian Institutes for Health Research (367427 to L.H.; FDN-167277 to M.T.), and a Genomics Technology Platform award from Genome Canada and Genome Quebec (M.T. and co-PI: Pierre Thibault, IRIC). Salaries were supported by the Fonds de Recherche du Quebec – Nature et Technologie (FRQ-NT) and the Cole Foundation (Y.B), an Institute for Data Valorisation (IVADO) postdoctoral fellowship (J. C.-H.), Canadian Institutes for Health Research (CIHR) postdoctoral fellowship (D.P.), a Junior 2 Research Scholar of the Fonds de Recherche du Québec-Santé salary award (FRQ-S) (H.W.), Senior Scholar of the Fonds de Recherche du Québec-

Santé salary award (FRQ-S) (I.T.) and a Canada Research Chair in Systems and Synthetic Biology (M.T.).

2.8 Additional information

The authors declare no competing interests.

CRISPR screen full dataset and Key Resource Table available at: doi:10.1016/j.molcel.2020.07.010

The accession number for the CRISPR-Cas9 high-throughput screen sequences reported in this paper is: https://www.ncbi.nlm.nih.gov/geo/query/acc.cgi?acc=GSE150232

Raw data have been deposited to Mendeley data: https://doi.org/10.17632/9w4g54bv43.1

2.9 Supplementary information

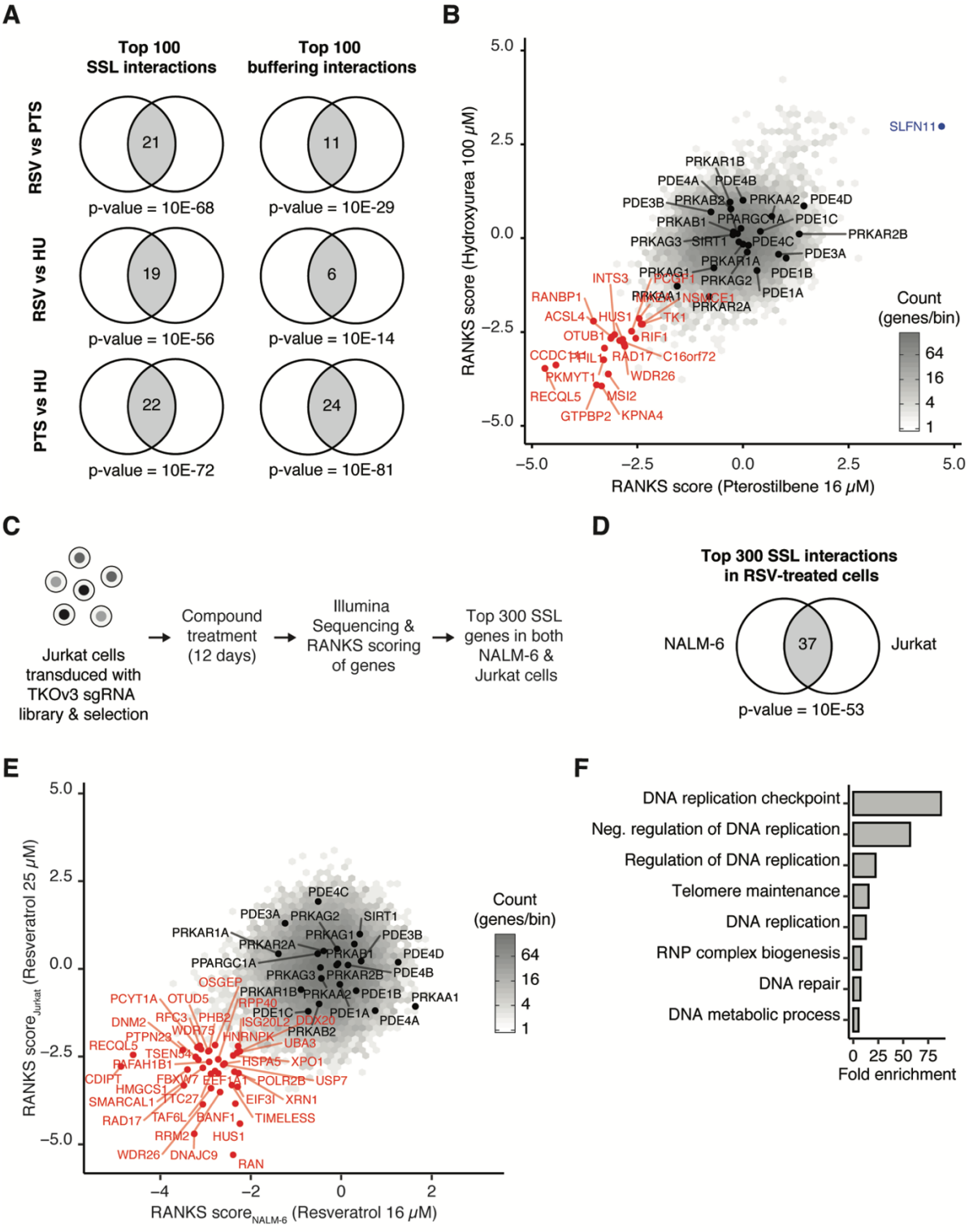

Supplementary figure 2.1 | Additional results of genome-wide CRISPR knockout screens with resveratrol, pterostilbene and hydroxyurea.

A. Top 100 synthetic sick/lethal (SSL) and buffering genetic interactions in the screens with 16 μM resveratrol, 16 μM pterostilbene or 100 μM hydroxyurea were used to calculate the statistical significance of the overlap (shown as number of genes in common in the grey-shaded area) between the indicated lists of genes using the hypergeometric test. **B.** Scatter plots show the RANKS scores for all genes (not italicized to aid visualization) in the pterostilbene screen compared to hydroxyurea. Shades of grey of each hexagonal bin represent the gene count in the bin and genes highlighted in red represent hits common to the three genome-wide screens (with *SLFN11* shown in blue as an example of a buffering genetic interaction) while genes highlighted in black represent subunits of presumed cellular targets of resveratrol such as *SIRT1*, *AMPK*, *PGC-1*α and *PDE-1, 3, 4*. **C.** Schematic of the CRISPR genome-wide knockout screens in Jurkat cells and analysis using the RANKS algorithm. **D.** Top 300 synthetic sick/lethal (SSL) in the genome-wide screens of NALM-6 cells treated with 16 μM resveratrol, and Jurkat cells treated with 25 μM resveratrol were used to calculate that statistical significance of the overlap (shown as number of genes in common in the grey-shaded area) between the indicated lists of genes using the hypergeometric test. **E.** Scatter plots show the RANKS scores for all genes (not italicized to aid visualization) in the resveratrol screen in NALM-6 cells compared to Jurkat cells. Shades of grey of each hexagonal bin represent the gene count in the bin and genes highlighted in red represent SSL hits common to the two cell lines while genes highlighted in black represent subunits of presumed cellular targets of resveratrol such as *SIRT1*, *AMPK*, *PGC-1*α and *PDE-1, 3, 4*. **F.** Gene ontology (GO) terms (biological processes with less than 1000 terms) enriched in the list of common SSL hits between the two cell lines (highlighted in red in panel E).

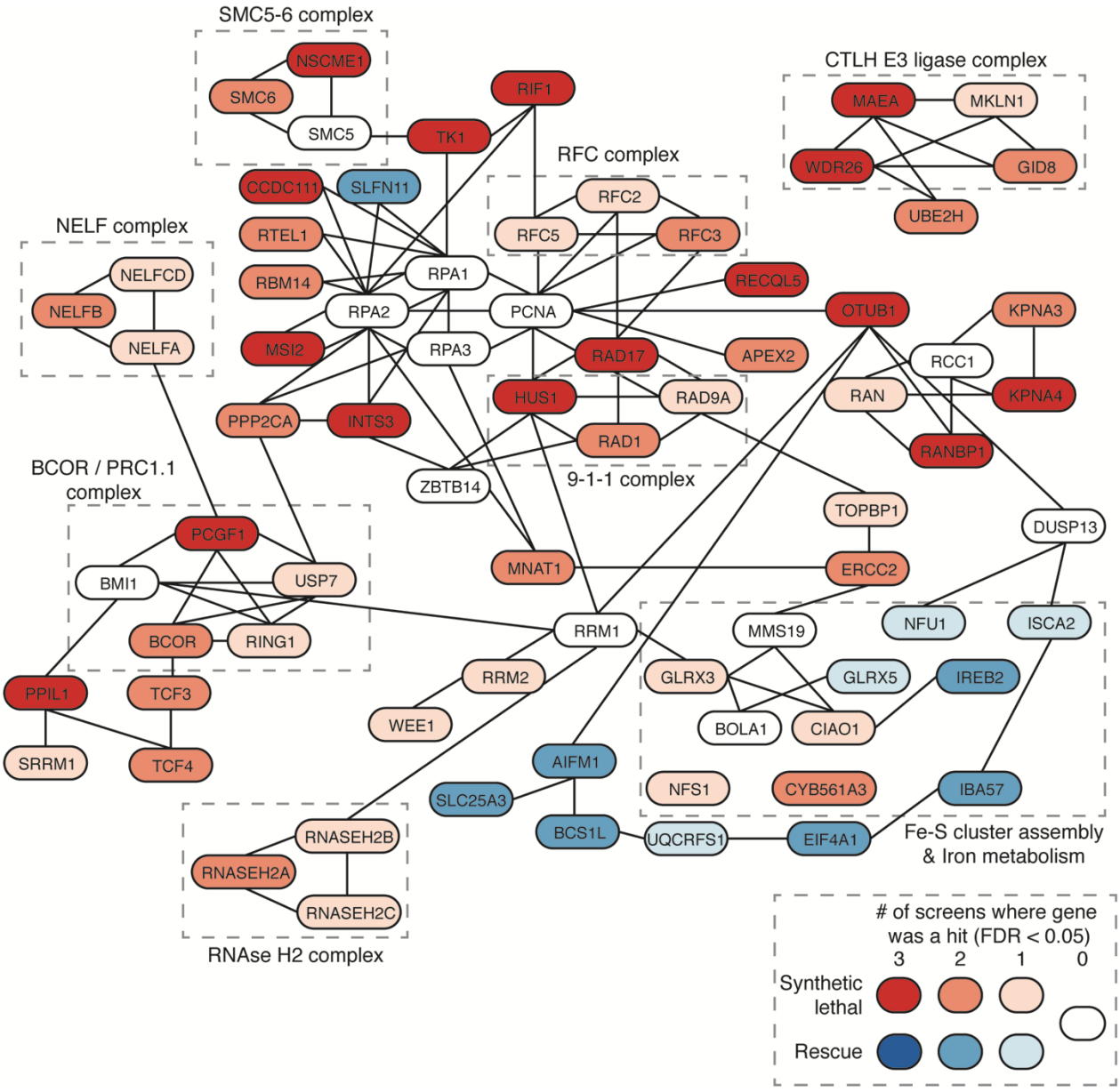

Supplementary figure 2.2 | Network analysis of chemo-genetic interactions with resveratrol, pterostilbene and hydroxyurea reveal critical modules implicated in genome integrity.

Network of gene hits recovered in the CRISPR screens with edges representing reported protein-protein interactions on BioGRID. The node color represents the number of screens in which the gene showed a chemo-genetic interaction (FDR < 0.05). An additional 12 genes that were not hits were added to the protein-protein interaction network for improved connectivity.

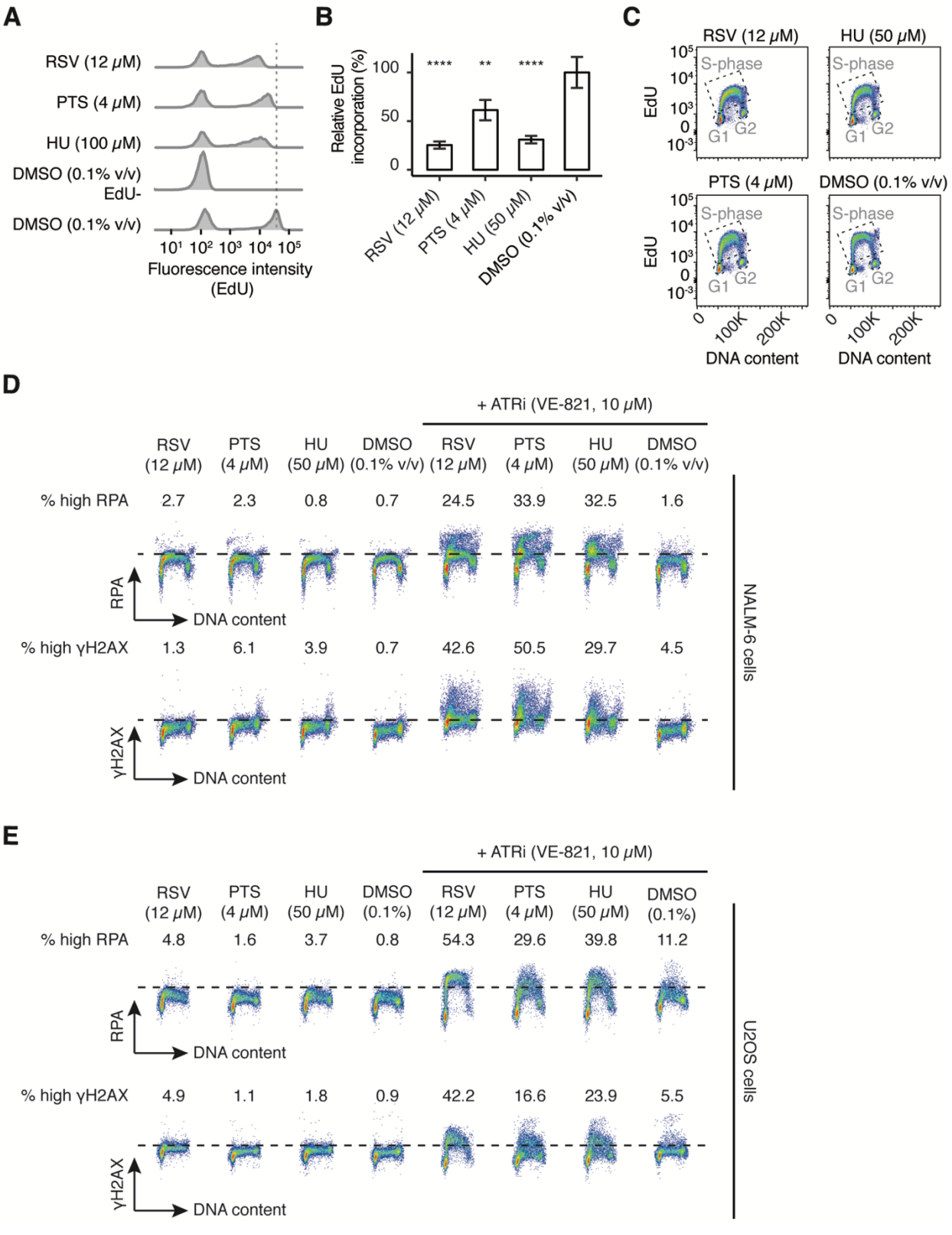

Supplementary figure 2.3 | Representative flow cytometry panels of NALM-6 cells treated with resveratrol.

A. Asynchronous NALM-6 cells were treated with the indicated compounds for 4h, pulsed with EdU and labeled by click-chemistry with AlexaFluor488 followed by flow cytometry measurement of EdU incorporation. **B.** EdU incorporation by FACS in asynchronous NALM-6 cells, treated as in (A), and calculated as the relative median fluorescence intensity (MFI) of EdU+/EdU- cells for each treatment relative to the relative MFI of DMSO-treated cells (Mean ± SD, n=3) **C.** Asynchronous NALM-6 cells were treated with the indicated compounds for 24h, pulsed with EdU before being fixed and stained with propidium iodide for DNA content measurement with flow cytometry. **D.** Representative flow cytometry panels of NALM-6 cells treated with the indicated compounds for 24h, after pre-treatment for 30 min with VE-821 (10 μM) where indicated. Cells underwent extraction and fixation followed by staining with antibodies against RPA and γH2AX, and DAPI; fluorescence intensities were measured by flow cytometry. **E.** Representative flow cytometry panels of U2OS cells treated with the indicated compounds for 6h, after pre-treatment for 30 min with VE-821 (10 μM) where indicated. Cells underwent extraction and fixation followed by staining with antibodies against RPA and γH2AX, and DAPI; fluorescence intensities were measured by flow cytometry. Statistical analyses were performed using one-way ANOVA, corrected for multiple comparisons unless otherwise indicated (*$p < 0.05$, **$p < 0.01$, ***$p < 0.001$, and ****$p < 0.0001$).

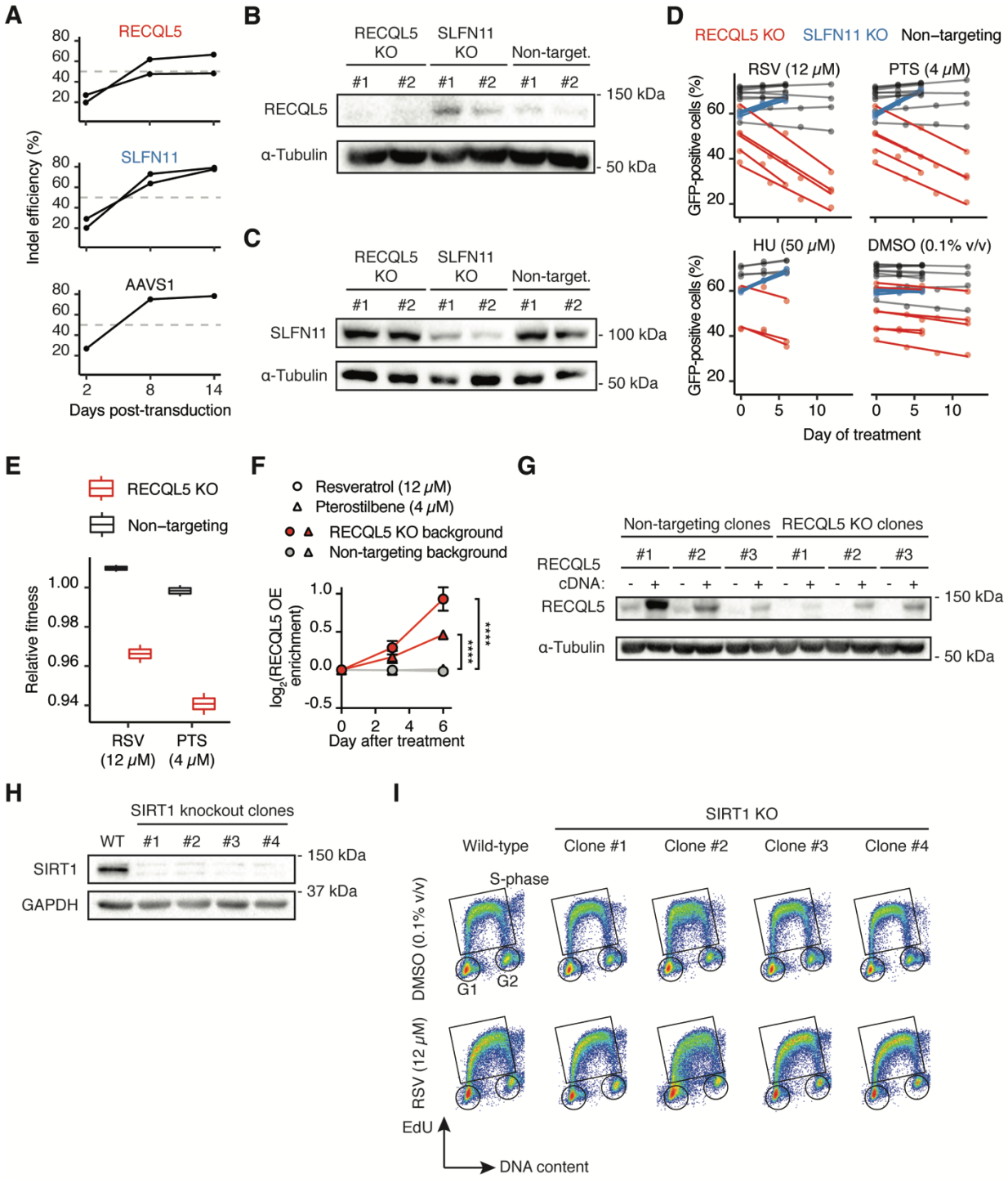

Supplementary figure 2.4 | Additional results of proliferation inhibition by resveratrol modulation by deletion of DNA replication-related genes.

A. Indel efficiency of NALM-6 population knockouts was quantified from the sequencing traces of the targeted locus for the indicated gene through indel decomposition with the TIDE method[396],

normalized to transduction efficiency and plotted relative to the days after lentiviral transduction for each sgRNA used. Grey dashed line represents an indel efficiency of 50%. **B.** EGFP-positive cells were sorted from the indicated NALM-6 knockout populations (17 days after transduction) by FACS and protein lysates were blotted using antibodies against RECQL5 and α-Tubulin. **C.** EGFP-positive cells were sorted from the indicated NALM-6 knockout populations (17 days after transduction) by FACS and protein lysates were blotted using antibodies against SLFN11 and α-Tubulin (1 representative blot of 2 independent replicates). **D.** Scatter plots of EGFP-positive cells relative to the days of treatment with the indicated compounds used to calculate relative fitness for each NALM-6 knockout population. Lines are used to connect separate time course treatments. **E.** The relative fitness of *RECQL5*-disrupted Jurkat cells in the presence of 12 µM resveratrol or 4 µM pterostilbene was measured by competitive growth assay during a 12-days treatment (n = 2). **F.** Clonal *RECQL5* KO or non-targeting control NALM-6 cells (3 independent clones of each genotype, shown as mean $\pm$ SD) were transduced with a plasmid overexpressing RECQL5-P2A-EGFP cDNA and treated with the indicated compounds or DMSO (0.1% v/v) for 6 days. Percentage of EGFP-positive cells was measured by flow cytometry and the enrichment of RECQL5 overexpressing cells is shown relative to DMSO and to day 0 for each cell line. **G.** Clonal RECQL5 KO or non-targeting control NALM-6 cells overexpressing RECQL5-P2A-EGFP were sorted by FACS and protein lysates were blotted (alongside the parental clone) using antibodies against RECQL5 and α-Tubulin (1 representative blot of 2 independent replicates). **H.** Clonal *SIRT1* KO or wild-type NALM-6 cells protein lysates were blotted using antibodies against SIRT1 and GAPDH (1 representative blot of 2 independent replicates). **I.** Representative flow cytometry panels of asynchronous *SIRT1* knockout or wild-type NALM-6 cells were treated with 12 µM resveratrol or 0.1% DMSO (v/v) for 24h, and pulsed with EdU before being fixed and stained with propidium iodide for DNA content measurement with flow cytometry. Statistical analyses were performed using one-way ANOVA, corrected for multiple comparisons unless otherwise indicated (*$p < 0.05$, **$p < 0.01$, ***$p < 0.001$, and ****$p < 0.0001$).

Chapter 3 – A genome-wide screen for essentiality upon telomerase inhibition identifies a novel p53 regulator, C16orf72/TAPR1

Yahya Benslimane, María Sánchez-Osuna, Jasmin Coulombe-Huntington, Thierry Bertomeu, Danielle Henry, Caroline Huard, Mike Tyers, Lea Harrington*

1. Institute for Research in Immunology and Cancer, Université de Montréal, P.O. Box 6128, Downtown Station, Montréal, Québec H3C 3J7, Canada

* Corresponding author: lea.harrington@umontreal.ca

3.1 Author contributions

Yahya Benslimane: Study conception, performed all experiments unless stated otherwise below, analyzed all data, wrote the manuscript with input from co-authors.

María Sánchez-Osuna: Performed BioID experiment (Figure 3.2E), technical assistance and general discussion.

Jasmin Coulombe-Huntington: Analyzed NextSeq sequencing of sgRNA frequency in CRISPR screens (Figure 3.1D), performed RNA-Seq mapping onto RefSeq transcripts (Figure 3.3A, Supplementary figure 3.4B), general discussion.

Thierry Bertomeu: Transduced NALM-6 cells with EKO sgRNA library used for CRISPR screens (Figure 3.1D), technical assistance and general discussion.

Danielle Henry: Generated a subset of cell lines used in Supplementary figure 3.1A and performed the experiments shown in Supplementary figure 3.5B-C.

Caroline Huard: Prepared sequencing libraries for CRISPR screens.

Mike Tyers: Study conception, analyzed data and general discussion

Lea Harrington: Study conception, analyzed data and wrote the manuscript with input from co-authors.

3.2 Abstract

Telomere erosion contributes to age-associated tissue dysfunction and senescence, and p53 plays a crucial role in this response. We undertook a genome-wide screen to identify gene deletions that sensitized p53-positive human cells to loss of telomere integrity, and uncovered a previously unannotated gene, *C16orf72*, which we term Telomere Attrition and p53 Response 1: *TAPR1*. CRISPR-Cas9 mediated deletion of *TAPR1* led to elevated p53 and induction of p53 transcriptional targets, and we observed a synthetic sick lethal relationship between *TAPR1*-disrupted cells and the loss of telomerase, or treatment with the topoisomerase II inhibitor doxorubicin. Stabilization of p53 with nutlin-3a further decreased cell fitness in cells lacking *TAPR1* or telomerase, whereas deletion of p53 rescued this decreased fitness of *TAPR1*-deleted cells. We propose that TAPR1 regulates p53 turnover, thereby tapering the p53-dependent response to telomere erosion. We discuss the possible implications of such a mechanism in the preservation of genome integrity and during the aging process.

3.3 Introduction

Telomeres, the repetitive DNA sequences found at the ends of eukaryotic chromosomes, are a lynchpin of genome integrity, and their maintenance is crucial to the proliferative capacity of normal and cancerous cells. The loss of telomere integrity, through telomere erosion or loss of protective complexes, elicits a DNA-damage response that shares characteristics with the response to a double-stranded DNA break[191]. Three defining principles of telomere integrity in humans are that (i) telomeres are comprised of G-rich repetitive sequences whose maintenance requires a cellular reverse transcriptase (telomerase) or alternative telomerase-independent mechanisms; (ii) telomere attrition eventually leads to genome instability, which in turn triggers cell cycle exit or apoptosis, and; (iii) in humans, p53 status plays a pivotal role in deciding the fate of cells in response to loss of telomere integrity or other types of DNA damage.

In many organisms, the telomerase reverse transcriptase (*TERT*) and its associated telomerase RNA component (hTR) add new telomeric DNA repeats to chromosome ends[405]. TERT is detected in stem cells, progenitor cells, and in several tissues during early development, but *TERT* is transcriptionally repressed in most adult human tissues[211]. It has been suggested that this downregulation serves a tumor suppressive function during aging, as ectopic *TERT* expression extends telomeres and confers cellular immortality to primary cells[203]. Moreover, promoter mutations that lead to *TERT* upregulation are frequently observed in cancer[222]. However, this putative tumor suppressive function leads to a paradoxical phenomenon in the context of a tissue with an increased senescent cell burden where the senescence-associated secretory phenotype (SASP) observed during telomere erosion or other types of senescence can serve to drive tumorigenesis[406-409].

One of the key properties that distinguishes primary human cells from cancer cells or other immortal populations is their limited replicative capacity in culture, called cellular senescence or the Hayflick limit[204]. The mechanisms by which critically eroded telomeres and other stressors induce cellular senescence share many similarities to the factors that drive tissue senescence during human aging[408, 409]. The time required to reach the Hayflick limit in culture is correlated with initial telomere length[197]. When telomeres become sufficiently eroded, cells with functional p53 undergo induction of p21 and cell cycle arrest[170, 200]. Cells without functional p53 may temporarily delay this first restriction point (called M1), but the eventual onset of telomere loss, fusions, or other genomic rearrangements leads to an M2 checkpoint at which apoptosis ensues[198, 208, 410-412]. The role of p53 in telomere-induced or other types of senescence is context-dependent, and is also influenced by mitochondrial activity, mTOR signaling and reactive oxygen species production[413, 414].

In humans and other organisms, cells can adapt to the loss of telomerase activity by maintaining telomeres via telomere-based recombination, or sometimes they appear to survive without any detectable telomere length maintenance mechanism[230, 415]. This multifaceted response is underscored by genome-wide screens in yeast, in which hundreds of genes affect the senescence of yeast strains lacking telomere maintenance mechanisms[416-418]. Yeast genome-wide screens have also uncovered a multitude of networks involved in replicative senescence, i.e. the limited number of times a mother cell is able to generate a daughter through budding[376]. In human cells, numerous gene networks that affect cellular senescence have been identified in genome-wide shRNA knockdown screens[419, 420]. For example, the ubiquitin ligase USP28 was

identified as an important mediator that links p53 induction and the SASP response during senescence[419], and it also plays a role in the response to DNA damage[421].

The advent of CRISPR-Cas9 technologies has greatly facilitated unbiased genetic approaches in human cells. We embarked on a genome-wide CRISPR-Cas9 screen to identify genes that modulate cell fitness in presence of critically eroded telomeres. Using a p53-positive pre-B acute lymphoblastic leukemia cell line, NALM-6, we carried out a chemical-genetic screen for genes whose deletion either sensitized or buffered against telomere erosion upon treatment with a characterized small-molecule telomerase-specific inhibitor, BIBR1532[422231, 232, 423-426]. BIBR1532 has been shown to be a mixed-type non-competitive inhibitor of telomerase enzymatic activity. The inhibition of telomerase has been suggested to be due to the binding of BIBR1532 to the FVYL pocket, a region on the TERT subunit that is close to hTR-binding residues. Mutations in the FVYL pocket have been shown to impact binding of TERT to hTR and lead to telomere attrition, which suggests that a potential mechanism-of-action of BIBR1532 is to interfere with the adequate binding of TERT and hTR[424]. Among the different chemical-genetic interactions identified, we showed that a gene of previously unknown function, *C16orf72*, which we tentatively name *TAPR1 (Telomere Attrition and P53 Response 1)*, influenced the response to telomere attrition via effects on p53 abundance and activity.

3.4 Results

3.4.1. Identification of chemical-genetic interactions with telomerase inhibition by BIBR1532 using CRISPR knockout screening

Given the known importance of p53 in the response to critically eroded telomeres, we chose to conduct our genome-wide CRISPR screen in the NALM-6 pre-B ALL cell line because it possesses wild-type p53[422], and is well suited to large-scale genetic screening owing to its ability to grown in suspension and a near-diploid karyotype[264, 427]. To ensure NALM-6 cells would respond to telomerase inhibition, we first confirmed their reliance on telomerase, and established that deletion of the telomerase reverse transcriptase (*TERT*) led to an eventual loss of proliferative capacity and onset of caspase activation concomitant with critical telomere erosion (Supplementary figure 3.1A-C, p. 133).

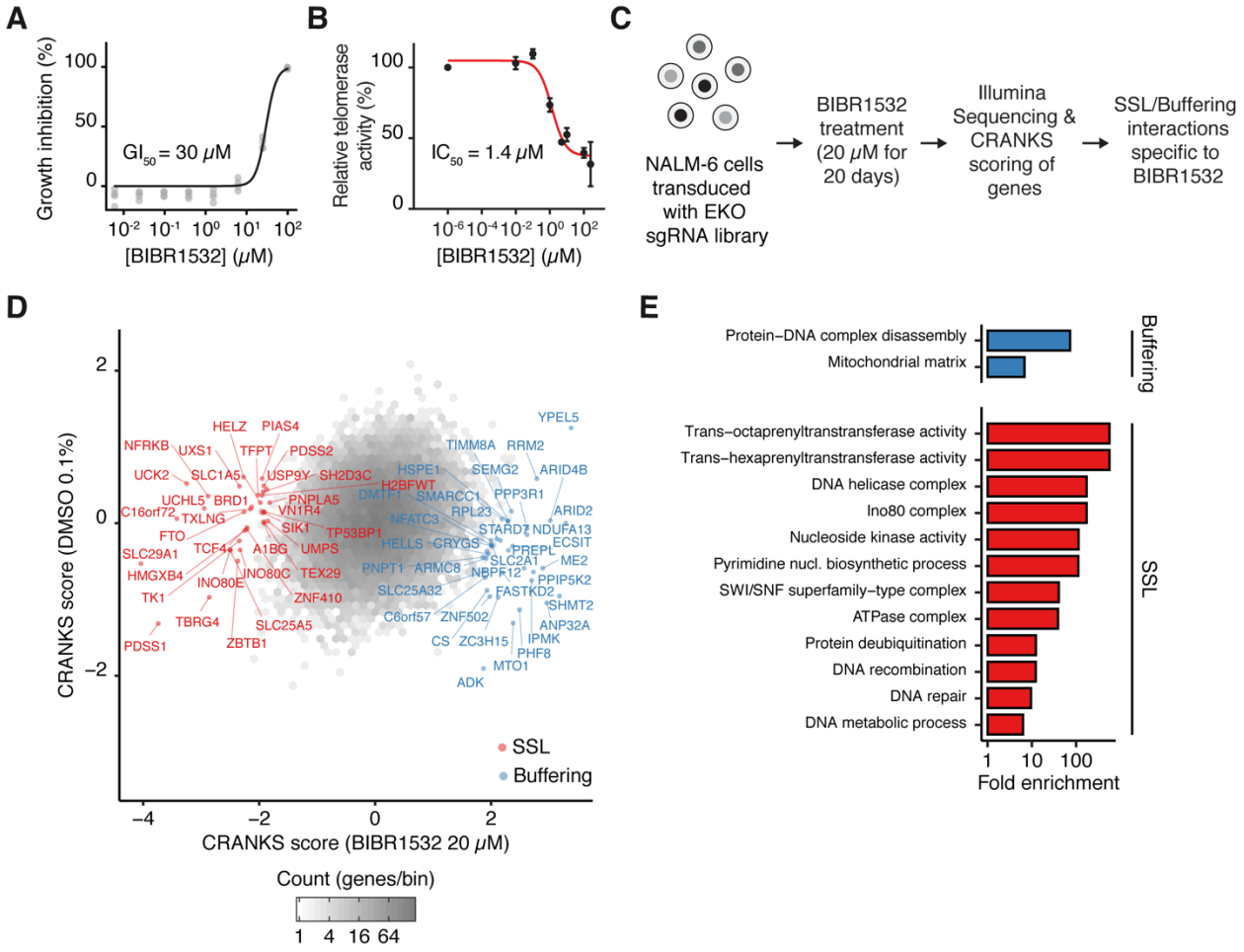

Figure 3.1 | Genome-wide CRISPR knockout screen identifies chemical-genetic interactions with telomerase inhibition by BIBR1532.

A. Growth inhibition of NALM-6 cells by treatment with the indicated concentrations of BIBR1532 for 72h (n=4). **B.** Inhibition of telomerase activity in NALM-6 cell lysates by BIBR1532 measured by qTRAP (n=3). **C.** Genome-wide CRISPR knockout screen schematic and genetic interaction identification using the CRANKS algorithm. **D.** Scatter plot showing the CRANKS scores from each gene knockout treated with BIBR1532 (20 µM) relative to DMSO (0.1% v/v). Shades of grey in each hexagonal bin represent gene count and synthetic sick/lethal (SSL) chemical-genetic interactions are labeled in red while buffering interactions are labeled in blue. **E.** Gene ontology (GO) term enrichment in the list of buffering or SSL hits.

To optimize the concentration of the telomerase inhibitor, BIBR1532, to employ in the genome-wide screen, we established that the IC_{50} for telomerase inhibition *in vitro* was 1.4 μM, with an IC_{50} of 30 μM for growth inhibition of NALM-6 cells, which are concentrations comparable to those employed in other studies[231, 232, 423, 425, 426]. (Figure 3.1A-B, p. 105). To facilitate the identification of gene deletions that either exacerbated or buffered against telomerase inhibition, we chose a concentration of 20 μM (~IC_{30}) to conduct the genome-wide screen. We confirmed this concentration was sufficient to elicit telomere erosion after 20 days of treatment relative to the vehicle control, 0.1% DMSO (v/v) (Supplementary figure 3.1C, p. 133). The genome-wide screen was carried out in NALM-6 cells via induction of Cas9 with doxycycline followed by transduction of the genome-wide sgRNA library, which contains 19,084 RefSeq genes, 3,872 predicted genes and 20,852 alternatively spliced exons[264, 339, 427], either in the presence of 0.1% DMSO (v/v) or 20 μM BIBR1532 for 20 days (Figure 3.1C, p. 105). Genomic DNA was isolated and Illumina sequencing was carried out, followed by analysis of the sgRNA frequencies (i.e. enriched or depleted) under each condition using an extension to a previously published algorithm, the Condition-specific RANKS (CRANKS, see methods for details)[264].

Amongst the gene deletions that exhibited a synthetic sick/lethal (SSL) interaction in cells treated with BIBR1532, we identified several genes involved in pyrimidine salvage (e.g. UCK2) or de novo pyrimidine synthesis (e.g. UMPS)[428]. Also amongst the top SSL interactions were PDSS1 and PDSS2, two enzymes involved in ubiquinone biosynthesis, a co-factor for the rate-limiting enzyme of de novo pyrimidine synthesis dihydroorotate dehydrogenase (DHODH)[428-430]. These hits are consistent with the known role of nucleotide pool homeostasis in preventing replicative stress and genomic instability, as cells that lack telomerase activity are known to be particularly

sensitive to replicative stress[431-434]. We also found that deletions of genes encoding subunits of the INO80 chromatin remodelling complex (INO80C, INO80E, TFPT, NFRKB, UCHL5) were SSL with BIBR1532 (Figure 3.1D-E, p. 105). This latter result is consistent with other studies that have described important roles for the INO80 complex in telomere replication, recombination and length homeostasis in yeast, plants and mice[435-439].

3.4.2 Chemical-genetic validation of genes that sensitize NALM-6 cells to telomere erosion

We chose the small molecule BIBR1532 because of the wealth of information available about its specificity for telomerase, including a co-crystal structure with *Tribolium castaneum* TERT[424]. Nonetheless, to address whether BIBR1532 may have off-target effects in NALM-6 cells at 20 μM, we assessed the relative fitness of telomerase-negative NALM-6 cells (*TERT* KO) treated with chemical inhibitors against a selected subset of the screen hits (Supplementary figure 3.2A-E, p. 134; see Methods). We measured the relative fitness of *TERT* KO NALM-6 cells in the presence of semi-inhibitory concentrations of inhibitors of the INO80 complex subunit UCHL5 (NSC-687852 and WP-1130), the nucleotide transporter SLC29A1 (NBMPR), and DHODH (atovaquone and brequinar)[440-445]. We observed a statistically significant reduction in the relative fitness of *TERT* KO cells when treated with each of these 5 compounds (Supplementary figure 3.2F-G, p. 134). The strong phenotype of DHODH deletion in cancer cells (including NALM-6) precluded an analysis of *DHODH* knockout cells (DepMap, Broad, 2020, public release 20Q2), however, consistent with its role in pyrimidine biosynthesis we found that supplementation of nucleosides rescued the sensitivity of *TERT* KO cells to DHODH inhibitors (Supplementary figure

3.2H, p. 134). These results suggest that the telomerase inhibitor BIBR1532 identified several genes whose loss-of-function or inhibition sensitized cells to loss of telomerase function.

3.4.3 Genetic validation of a synthetic sick-lethal interaction with *TAPR1* (*C16orf72*) in cells lacking the telomerase reverse transcriptase

One of the SSL interactions with BIBR1532 identified in the genome-wide CRISPR screen was an unnamed gene, *C16orf72* (Figure 3.1D, p. 105) hereafter referred to as *TAPR1* (Telomere Attrition and P53 Response 1). This gene encodes a predicted protein of 275 amino acids of unknown function, although it had been previously isolated in a high-throughput genetic screen as a gene whose deletion sensitized cells to ATR inhibition[309]. To understand the role of this gene deletion in inhibiting the proliferation of BIBR1532-treated cells, we disrupted *TAPR1* in NALM-6 cells with two different sgRNAs (targeting exon 1 and 2) and isolated clones disrupted for *TAPR1* (*TAPR1* KO) (Figure 3.2A, p. 109). Competitive growth modeling of the relative fitness of *TAPR1* deleted cells in wild-type NALM-6 cells versus NALM-6 cells also deleted for *TERT* revealed a statistically significant decrease in relative fitness in cells lacking *TAPR1* and *TERT* (Figure 3.2B-C, p. 109; Supplementary figure 3.3A, p. 136). These data show that *TAPR1* exhibits a SSL interaction that is specific to cells lacking telomerase, and is consistent with the mechanism-of-action of BIBR1532.

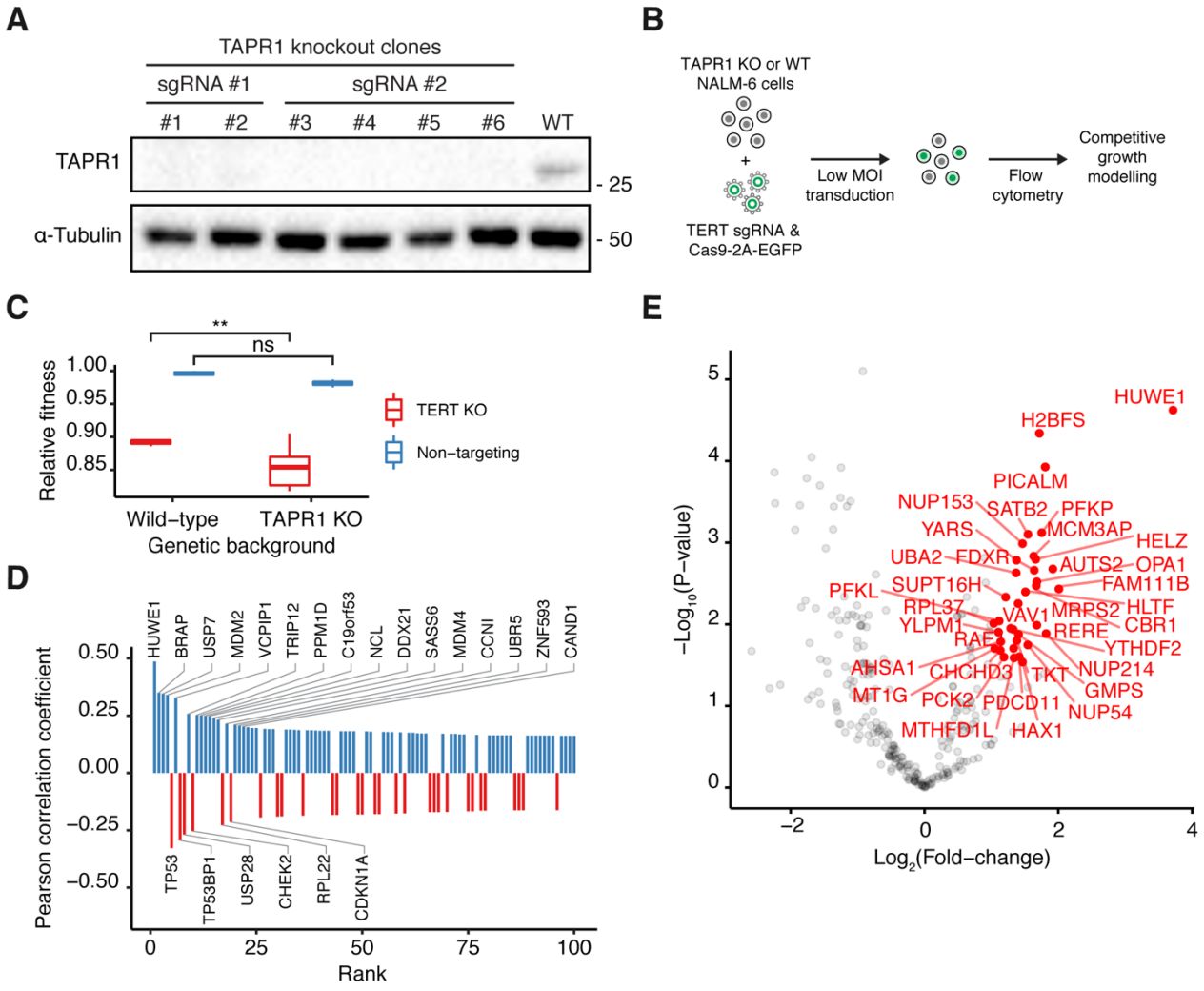

Figure 3.2 | *TAPR1* and *TERT* exhibit a synthetic sick/lethal interaction.

A. NALM-6 lysates from clonal *TAPR1*-disrupted (*TAPR1* KO) or wild-type NALM-6 cells were blotted against TAPR1 and α-tubulin (1 representative blot of 2 independent replicates). **B.** Schematic of competitive growth assays used to query the genetic interaction between *TAPR1* and *TERT*. **C.** Relative fitness of *TERT*-disrupted (*TERT* KO) or non-targeting control in wild-type or *TAPR1* KO NALM-6 cell background (n ≥ 3). **D.** Top 100 correlates with *TAPR1* for genetic dependency in the AVANA dataset (DepMap). Gene labels indicate correlates with an absolute value of the Pearson correlation higher than 0.2. **E.** Volcano plot showing TAPR1 protein-protein interactions measured by BioID. Proteins with a peptide count fold-change higher than 2 and a FDR lower than 0.1 are labeled in red (n ≥ 3).

3.4.4 Identification of interaction partners of TAPR1

A search of TAPR1 co-dependencies in 769 different cell lines[268] (www.depmap.com) revealed that the highest absolute Pearson correlation coefficients with TAPR1 were genes involved in replicative senescence and p53 signal transduction in response to DNA damage (Figure 3.2D, p. 109; Supplementary figure 3.3B, p. 136). For example, genes with the highest co-dependency included negative regulators of p53 activity such as *HUWE1, MDM2, MDM4, USP7, PPM1D*[174-176, 180, 446-449], whereas those genes with a negative co-dependency included positive p53 effectors such as *TP53* itself, *TP53BP1, USP28, ATM, CHEK2* and *CDKN1A* (p21)[172, 178, 179, 419, 421, 450-452]. To further examine physical interactors of TAPR1, we performed BioID in NALM-6 cells using TAPR1 as a bait (Figure 3.2E, p. 109; see Methods)[453]. The top interactor was the E3 ligase HUWE1, which is known to play a role in the degradation of p53, MYC, as well as many other substrates[454-456]. Other TAPR1 interactors identified in the BioID analysis included proteins involved in proteostasis[457, 458], the mRNA export machinery and the nuclear pore, such as MCM3AP, NUP214, NUP153, NUP54 and RAE1 (Supplementary figure 3.3C, p. 136)[459-462]. These data reveal that TAPR1 exhibits a wide array of genetic associations and physical interactions that suggest not only a role in the p53 response but also potential involvement in other biological processes.

3.4.5 The transcriptome of cells lacking *TAPR1* reveals signatures consistent with p53 signaling

To further probe the potential relationship between TAPR1 and p53 regulation, we used RNA-seq to assess the transcriptional response to deletion of either *TAPR1* or *TERT*. Transcriptomic analysis was carried out in confirmed NALM-6 clonal lines containing a *TAPR1*

deletion or non-targeting controls. Of the gene signatures upregulated in *TAPR1*-deficient cells, we found processes involved in the response to proteotoxic stress, including ribosome biogenesis (rRNA cleavage, SSU and LSU assembly) and chaperone-mediated protein folding (*HSP90AA1, HSP90B1, HSPA1A, HSPA5, HSPA8, HSPE1, HSPH1, DNAJA1*) (Figure 3.3A, p. 112; Supplementary figure 3.4A, p. 137)[463-467]. To compare these results to genes induced in cells that undergo telomere attrition, we analyzed the transcriptome of *TERT* KO NALM-6 cells in a similar fashion (Supplementary figure 3.4B-C, p. 137). We similarly detected an upregulation of p53-regulated genes, which exhibited a statistically significant overlap between the *TERT* KO and *TAPR*1 KO RNA-seq datasets (Figure 3.3B-C, p. 112; see Methods for further details). This upregulation of p53 transcriptional targets in *TERT* KO cells was accompanied by an increase in p53 levels (Supplementary figure 3.5A, p. 138). These results suggest that *TAPR1* deficiency modifies the transcriptome in a complex manner, and is associated with an upregulation of p53-regulated genes, a subset of which are also observed in *TERT*-deficient cells with eroded telomeres.

3.4.6 TAPR1 is a modulator of p53-mediated growth arrest

The associated upregulation of p53 and p53-responsive genes in cells lacking *TERT* suggested the possibility that TAPR1 may be required to attenuate the p53 response as telomeres become eroded. If this were true, then the stabilization of p53 should have an adverse effect on NALM-6 *TERT* KO cell fitness. We first confirmed that nutlin-3a, which inhibits the interaction of p53 with MDM2 and thereby stabilizes p53[468-470], upregulated p53-dependent genes such as *BAX*, *CDKN1*, and *MDM2* (Supplementary figure 3.5B, p. 138). We next tested the impact of nutlin-3a treatment on the cell fitness of *TERT* KO cells, and observed that nutlin-3a elicited a marked reduction in cell fitness compared with wild-type cells (Supplementary figure 3.5C, p. 138). This

negative impact of nutlin-3 on cell fitness was rescued in *TERT* KO cells in which *TP53* was also disrupted (Supplementary figure 3.5C, p. 138; compare black lines). These data show that NALM-6 cells exhibit a p53-dependent reduction in cell fitness upon the loss of telomere integrity.

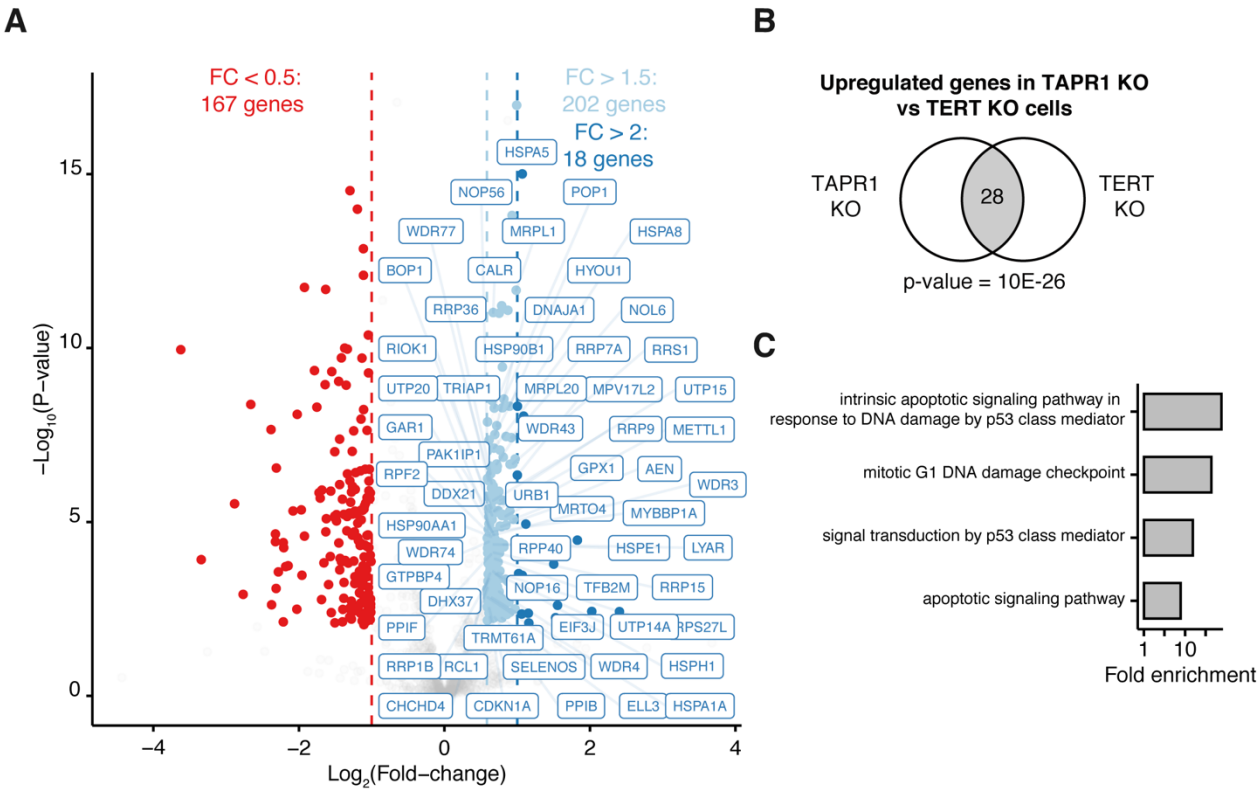

Figure 3.3 | The transcriptome of cells lacking *TAPR1* exhibits upregulation of p53 signaling.

A. Volcano plot showing transcriptome changes in *TAPR1* KO NALM-6 cells relative to non-targeting controls, differentially expressed genes (FDR < 0.05) are shown for the fold-change thresholds indicated. Upregulated genes within the enriched GO-terms are indicated (n ≥ 3). **B.** Upregulated genes in *TERT* KO and *TAPR1* KO were used to calculate that statistical significance of the overlap (shown as number of genes in common in the grey-shaded area) between the indicated lists of genes using the hypergeometric test. **C.** GO-term enrichment in the list of overlapping upregulated genes in *TERT* KO and *TAPR1* KO NALM-6 cells.

We observed a modest increase in p53 protein levels in *TAPR1*-deficient cells relative to wild-type cells, which was further evident after treatment with nutlin-3a (Figure 3.4A, p. 114). The relative fitness of *TAPR1*-deleted cells was also reduced in cells treated with nutlin-3a or doxorubicin (a topoisomerase II poison that activates p53 in response to DNA damage)[471] (Figure 3.4B, p. 114), concomitant with a statistically significant upregulation of the p53 transcriptional target *CDKN1A* (Figure 3.4C-D, p. 114). This data suggested that the increased sensitivity of *TAPR1*-deficient cells to nutlin-3a and doxorubicin could be due to increased p53 protein levels, which result in elevated *CDKN1A* expression and cell cycle arrest[177, 178]. We therefore tested the prediction that disruption of *TP53* would rescue the sensitivity of *TAPR1*-deficient cells to nutlin-3a. Competitive growth assays in cells disrupted for *TAPR1* or *TP53* alone, or both genes deleted together, were employed to assess the epistatic relationship with *TP53* (Figure 3.4E, p. 114; see Methods). We found that the reduced cell fitness of *TAPR1*-deficient cells treated with nutlin-3a treated was completely rescued in a *TP53*-deficient background, to an extent comparable to nutlin-3a treated *TP53*-deficient cells (Figure 3.4F, p. 114). These data suggest a role of TAPR1 in tapering the response to p53 upon MDM2 inhibition by nutlin-3a or doxorubicin-induced DNA damage.

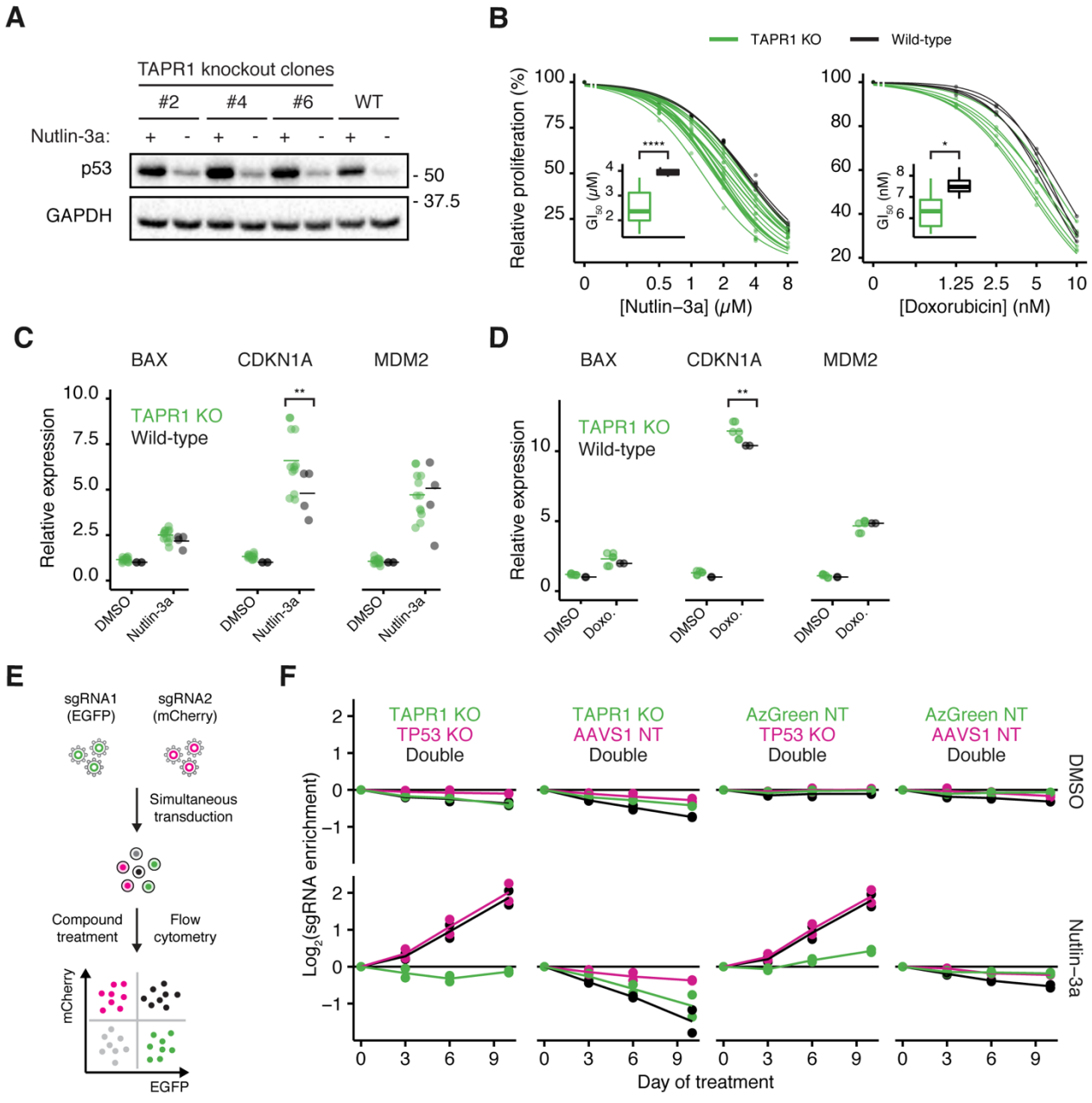

Figure 3.4 | TAPR1 is a modulator of p53 growth arrest activity.

A. NALM-6 lysates from clonal *TAPR1* KO or wild-type cells treated with nutlin-3a (2 µM, 4h) were blotted against p53 and GAPDH (1 representative blot of 3 independent replicates). **B.** Relative proliferation of *TAPR1* KO or wild-type cells treated with the indicated concentrations of nutlin-3a or doxorubicin for 72h. Dose-response curves were fitted and the GI_{50} concentration is shown as inset plots (n ≥ 3). **C.** Relative expression of the indicated transcripts in *TAPR1* KO or wild-type cells treated with 2 µM nutlin-3a or 0.1% (v/v) DMSO for 4 hours (n ≥ 4). **D.** Relative expression

of the indicated transcripts in *TAPR1* KO or wild-type cells treated with 0.5 µM doxorubicin or 0.1% (v/v) DMSO for 4 hours (n ≥ 2). **E.** Competitive growth assay schematic for NALM-6 cells transduced with non-targeting sgRNAs and sgRNAs targeting *TAPR1* and *TP53*. **F.** sgRNA enrichment in NALM-6 cells treated with 2 µM nutlin-3a or 0.1% (v/v) DMSO shown for the different *TAPR1*/*TP53* sgRNA combinations (lines represent the mean for two independent replicates).

3.5 Discussion

We conducted a genome-wide screen using CRISPR-Cas9 in the p53-positive cancer cell line, NALM-6, for gene deletions that sensitized cells to telomere erosion. We uncovered a previously unannotated gene, *C16orf72*, which we have tentatively named *TAPR1* (Telomere Attrition and P53 Response 1) as it exhibits a synthetic-sick-lethal interaction with telomerase inhibition or deletion of *TERT*, and appears to tapers the response to p53 upon MDM2 inhibition or DNA damage (Figure 3.5, p. 115). While the effect of TAPR1 on p53 levels could explain the genetic interaction detected between *TERT* and *TAPR1*, future experiments will address the impact of the modulation of p53 by TAPR1 when cells are undergoing DNA damage specific to short telomeres.

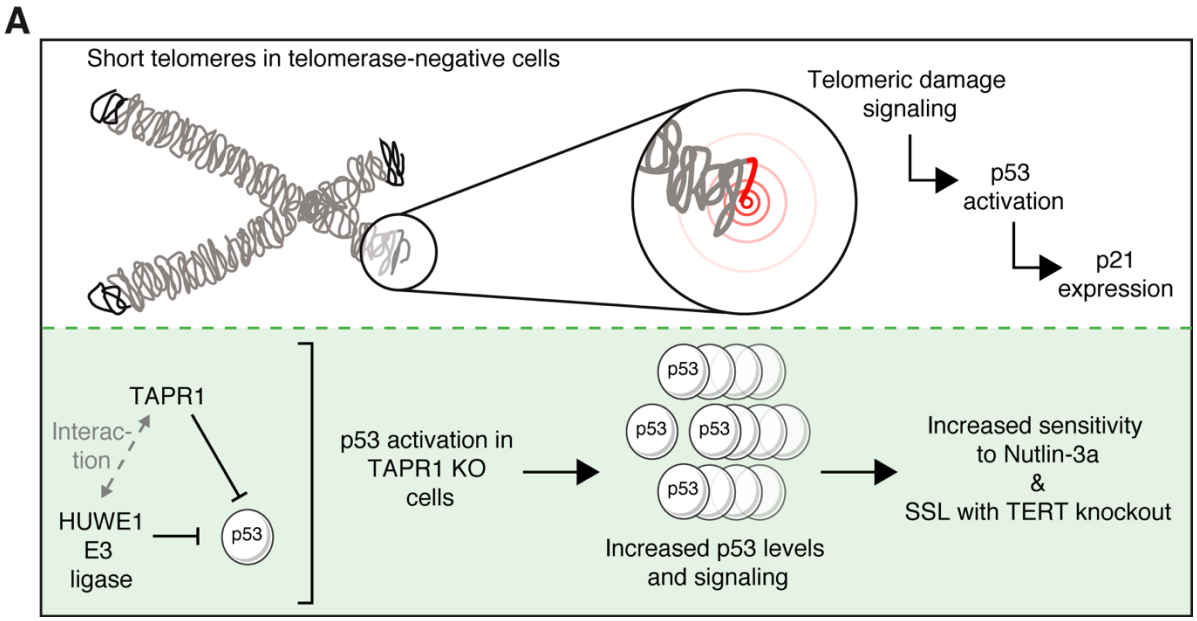

Figure 3.5 | Model of TAPR1 modulation of p53 signaling in the response to telomere shortening and p53 activation.

A. TAPR1 acts as a negative regulator of p53 protein levels similarly to HUWE1, an E3 ligase that interacts with TAPR1. Cells that are deficient for TAPR1 have higher p53 levels and are sensitive to conditions that activate p53-dependent growth arrest such as critically short telomeres.

Prior to this study, *TAPR1* was identified as a hit in separate genome-wide CRISPR-Cas9 chemo-genetic screens for sensitizers to ATR kinase inhibition or ribonucleotide reductase inhibition by hydroxyurea, respectively[309, 427]. TAPR1 was also identified as a hit in a high-throughput affinity mass spectrometry screens for protein interactors of the E3 ligase HUWE1[472, 473]. HUWE1 was identified as one of the top protein interactors with TAPR1 using BioID experiments. The reciprocity of these findings suggests that the HUWE1/TAPR1 interaction may be biologically relevant, especially as p53 is ubiquitinated by HUWE1 and measurements of p53 stability in cells where TAPR1 or HUWE1 are disrupted are currently ongoing[446, 474-477]. Tom1, the

Saccharomyces cerevisiae homologue of HUWE1, interacts with a protein of unknown function called YJR056C which possesses the same DUF4588 domain as TAPR1 (pfam database)[478, 479]. Further experimentation will determine if the interaction of HUWE1/TAPR1 and Tom1/Yjr056c occur via this evolutionarily conserved interaction domain, DUF4588. Tom1 and HUWE1 are also involved in the degradation of ribosomal (ERISQ pathway) and non-ribosomal proteins[478, 480], as well as the regulation of genes involved in ribosomal biogenesis (RiBi)[481, 482]. In humans, HUWE1 is involved in the response of p53 to proteostasis, including the imbalance between ribosomal protein (RP) and ribosomal RNA (rRNA) production[483, 484]. We also found other genes involved in proteostasis that were upregulated in *TAPR1*-deficient cells, including components of the CURI complex that coordinate the HSF1-dependent response to the imbalance between ribosomal proteins and rRNA[485-488], subunits of the ribosomal SSU and LSU processosome, and other transcriptional targets of HSF1[464, 489, 490] (Figure 3.3A, p. 112; Supplementary figure 3.6, p. 139). Future studies will determine if TAPR1 functions with HUWE1 in ribosomal protein quality control or in the HSF1-dependent response to proteotoxic stress, and what relationship these processes may have to the p53-dependent response to telomere erosion.

The role of p53 in modulating the Hayflick limit was first suggested by Shay, Peireira-Smith and Wright, who found a reversible ability of SV40 to temporarily bypass cellular senescence, only when the SV40 large T antigen retained its p53 or Rb binding domain[208]. Since then, numerous studies have established that p53, a key effector downstream of the ATM or ATR checkpoint, are crucial in determining how human cells respond to DNA damage or telomere-induced stress. Our choice of a p53-positive but immortal cancer cell line NALM-6 for the CRISPR-Cas9 screen enabled the identification of *TAPR1* as gene whose function enables cancer cells to belay the order to die

via the attenuation of p53 activation. We found that *TAPR1*-deficient cells were sensitive nutlin-3a and doxorubicin, and in a high throughput screen *TAPR1* deletion sensitized p53-negative cells to ATR inhibition[309], which suggests that the role of TAPR1 in the response to DNA damage is not limited to telomeres. It is intriguing to consider how telomere-induced stress could functionally overlap with proteotoxic stress, especially as aneuploidy is known to induce proteotoxic stress due to gene copy number imbalance[491-494].

A longstanding question has been the evolutionary trade-off of p53 in protecting the germline or somatic tissue integrity, versus the vulnerability to tumorigenesis upon p53 inactivation[495-499]. Because p53 is at the nexus of cancer and aging, it was proposed that its regulation may necessitate checks and balances that operate either upstream or downstream, but not at the levels of p53 itself[413]. Our work sheds new insight into this question. We show that TAPR1 does influence the response of cells to telomere-induced damage by directly influencing p53 levels. Future work will no doubt illuminate the precise genetic and cellular contexts in which TAPR1 is important for p53 function and other biological responses to stress, and how these functions intersect cancer and aging.

3.6 Methods

3.6.1 Cell culture

NALM-6 cells were grown in 10% FBS (v/v) RPMI 1640 medium and HEK293T cells were grown in 10% FBS (v/v) DMEM medium at 5% (v/v) CO_2 and 37°C and sub-cultured every 2-3 days. Parental and knockout cell lines used for this study were tested for mycoplasma contamination by standard multiplex PCR. Cells were sub-cultured every 2-3 days.

3.6.2 Proliferation assays

Chemicals used to probe relative proliferation were resuspended in DMSO and were obtained from the following suppliers: BIBR1532 (SelleckChem, #S1186), NSC-687852 (Cayman Chemical, #11324), WP-1130 (Cayman Chemical, #15227), Atovaquone (Tocris Bioscience, #6358), Brequinar (AdooQ Biosciences, #A12442-5), NBMPR (Cayman Chemical, #16403), Nucleosides (Millipore-Sigma, #ES-008-D), Nutlin-3a (Sigma, #SML0580), Doxorubicin (MedChem Express, #HY-15142). The CellTiter-Glo reagent (Promega, #G7573) was used to perform luminescence-based measurements of relative proliferation. Briefly compounds were diluted in DMSO and serially diluted 3-fold (or 4-fold for BIBR1532) and added to their respective wells in 384-well plates along with 9000 NALM-6 cells in a final volume of 50 µL (0.1% [v/v] DMSO). Plates were incubated for 72h at 37 °C before addition of the CellTiter-Glo reagent and luminescence measurement. Relative proliferation was calculated as a ratio of average luminescence of the treatment to the average luminescence of the DMSO controls and subtracted from 100% to obtain growth inhibition. Low-throughput proliferation assays were performed by seeding NALM-6 cells at 1 x 10^5 cells/mL in 24-well plates and compounds were added at a 1:1000 dilution of a after 2-fold serial dilutions to yield a final DMSO concentration of 0.1% (v/v). After 72 hours of incubation at 37°C, cell concentration was measured on a Beckman-Coulter Z2 Counter after debris exclusion by particle size gating. Relative proliferation was calculated as a ratio of the population doubling of the treatment to the population doubling of the respective DMSO control. Dose-response curves were fitted as 4-parameter nonlinear regression using R (with lower bound constrained at 0 and upper bound constrained at 100) and the half-maximal growth inhibition (GI_{50}) extracted from the fitted curves.

3.6.3 Targeted gene disruption using CRISPR-Cas9

Gene disruptions in NALM-6 cells was carried out using CRISPR-Cas9 editing as described previously[427]. Briefly, sgRNAs targeting a given gene were designed using "sgRNA designer" tool (https://portals.broadinstitute.org/gpp/public/analysis-tools/sgrna-design) before cloning into LentiCRISPRv2-Puro (Addgene #52961), LentiCRISPRv2-EGFP (Addgene #82416) or LentiCRISPRv2-mCherry (Addgene # 99154) using the procedure detailed in Sanjana et al[247, 392]. The resulting plasmids were purified and sequence-verified to confirm the proper sgRNA sequence was inserted downstream of the U6 promoter before lentiviral packaging in HEK293T using the psPAX2 (Addgene #12260) and VSVg (Addgene #8454) plasmids. Lentiviral transduction was performed by incubating viral particles with protamine sulfate (10 µg/mL) and 10^6 NALM-6 cells in a final volume of 2 mL for 48 hours at 37 °C. EGFP-positive and mCherry-positive cells percentage was measured on a BD FACSCanto II or BD LSRFortessa after proper FSC/SSC gating to calculate transduction efficiency. Clonal isolates of *TERT*-disrupted (*TERT* KO) cells or non-targeting controls were isolated by single cell sorting on a BD FACSAria II from NALM-6 cells transduced with LentiCRISPRv2-Puro expressing TERT or AAVS1 targeting sgRNAs after puromycin selection. Clonal *TAPR1*-disrupted cell isolates (*TAPR1* KO) were isolated by single cell sorting after nucleofection and overnight incubation of NALM-6 cells with the respective sgRNA-expressing LentiCRISPRv2GFP plasmids with the SF Cell Line 4D-Nucleofector X Kit L. Indel efficiency and clonal genotyping was performed on genomic DNA using target locus PCR amplification and sanger sequencing. The ICE online tool (https://ice.synthego.com/) was used for indel decomposition of the sequencing traces using the TIDE method[396]. Indel efficiency for each knockout population was calculated as the indel quantification by TIDE normalized by the EGFP+

percentage as a proxy for transduction efficiency. The genotype of each clonal population was inferred directly from the sequencing chromatogram indel decomposition. See Supplementary tables 3.1-3.2 (p. 200-201) for sgRNA sequences, PCR and sequencing primers and indel efficiency values.

3.6.4 Quantitative telomerase repeat amplification protocol (qTRAP)

Telomerase activity measurement was performed as previously described with minor modifications[500]. Briefly, 1 million NALM-6 cells were lysed in 100 µL of CHAPS buffer (10 mM Tris-HCl pH 7.5, 1 mM $MgCl_2$, 1 mM EGTA, 0.1 mM Benzamidine, 5 mM β-mercaptoethanol, 0.5% (w/v) CHAPS, 10% (v/v) glycerol) and protein quantification was performed using the Bradford assay. On the day of the assay, all cell lysates were diluted 1:10 in CHAPS buffer and NALM-6 cell standard curves were subsequently prepared by 2-fold serial dilutions. qPCR reactions were prepared in triplicate using the FastStart SYBR Green 2X mastermix (Roche, #4673484001), 1 mM EGTA, 0.8 µM ACX primer (5'-GCGCGGCTTACCCTTACCCTTACCCTAACC-3'), 0.8 µM TS primer (5'-AATCCGTCGAGCAGAGTT-3') and 2 µL of cell lysate (1000 cells/µL) in a final volume of 25 µL and incubated in the StepOnePlus thermocycler (Applied Biosystems) with the following program (30 min at 30 °C, 10 min at 95 °C, 40 cycles of 15 sec at 90 °C and 60 sec at 60 °C). Analysis of Relative Telomerase Activity (RTA) was performed by averaging the C_T in technical replicates and using the average C_T as x-values in the NALM-6 standard curve to retrieve the telomerase activity as cell number equivalent followed by normalization by the protein. For the measurement of telomerase activity inhibition in NALM-6 WT cells, BIBR1532 dilutions were prepared as 2.5% (v/v) DMSO working solutions and added for a final DMSO concentration of 0.2% (v/v) to reach the indicated BIBR1532 concentrations in the qPCR reactions. Analysis of Relative Telomerase Activity (RTA)

was performed by averaging the C_T in technical replicates and using the average C_T as x-values in the NALM-6 standard curve to retrieve the telomerase activity as cell number equivalent for each BIBR1532 concentration divided by the DMSO control. The RTA data was fitted with a 4-parameter nonlinear regression with GraphPad Prism 8 to obtain the dose-response curve and half-maximal inhibitory concentration (IC_{50}).

3.6.5 Caspase-3/7 activity measurement

Caspase-3/7 activity measurement was performed as previously described[501]. Briefly, *TERT*-disrupted (*TERT* KO) or non-targeting NALM-6 cells were collected at different days in culture and lysed in NP-40 buffer (50 mM Tris-HCl pH 6.8, 150 mM NaCl, 1% (v/v) NP-40, 1X cOmplete EDTA-free protease inhibitor cocktail) and protein quantification was performed using the Lowry method before storage at -20 °C. On the day of the assay, lysates were thawed on ice and 25 µg of protein lysate was mixed on ice with 2X Caspase assay buffer (40 mM HEPES-NaOH pH 7.2, 300 mM NaCl, 10 mM EDTA, 0.2% (w/v) CHAPS, 2% (v/v) NP-40, 20% (w/v) sucrose, 20 mM DTT, 50 µM Ac-DEVD-AFC [Cayman Chemical, #14459]). Assay plates were incubated at 35 °C for 20h and fluorescence intensity (excitation: 400 nm, emission: 505 nm) was measured every hour using a Tecan M1000pro plate reader. Relative caspase-3/7 activity was calculated as the slope of fluorescence intensity increase over time in the different samples relative to wild-type NALM-6 cells.

3.6.6 Telomeric Restriction Fragment length (TRF) analysis

Telomere length was assessed as previously described[502]. Briefly, genomic DNA was extracted from NALM-6 cells and treated with Proteinase K (0.1 mg/mL) before digestion with HinfI and RsaI. The electrophoresis of the digested DNA was performed in a 0.7% (w/v) agarose

in 0.5X TBE (Tris/Borate/EDTA) gel for 16h at 70V before gel denaturation, neutralization and drying. The hybridization was performed with [γ-^{32}P] ATP-labeled $(C_3TA_2)_3$ probe followed by washing and autoradiography on a phosphor storage screen and scanned using a Typhoon FLA-9500 phosphorimager (GE healthcare). The signal intensity in each line was measured using FIJI and the mean TRF length for each sample was calculated using the formula $(\Sigma(OD_i) / \Sigma(OD_i/L_i))$, where OD is the lane intensity at position *i* and L is the DNA size at position *i* as extrapolated from the HindIII-digested Lambda DNA ladder.

3.6.7 Genome-wide CRISPR screens

CRISPR knockout screen to identify chemical-genetic interactions with BIBR1532 was performed as previously described with the following changes[427]. A NALM-6 clone with inducible Cas9 expression previously transduced with the EKO library was treated with Doxycycline (2 µg/mL) for 8 days to induce Cas9 expression and knockout generation followed by treatment with 20 µM BIBR1532 or 0.1% (v/v) DMSO for 20 days (2 independent DMSO treatments were performed). After compound treatments, cells were collected, genomic DNA extracted and sgRNA sequences were PCR-amplified followed by Illumina sequencing. Reads were aligned using Bowtie2.2.5 in the forward direction only (--norc option) with otherwise default parameters and total read counts per sgRNA tabulated to obtain sgRNA frequencies[393]. Chemical-genetic interactions were scored using the CRANKS algorithm, an extension of the previously described RANKS algorithm[264]. Briefly, while the RANKS algorithm estimates p-values for individual sgRNAs with a fold-change more extreme than the one observed for control sgRNAs (non-targeting sgRNAs in the EKO library), the CRANKS algorithm estimates similar p-values by defining control sgRNAs as those targeting the 500 immediately more essential genes than the gene for which the

p-value is being calculated in order to control for growth-dependent dropout (or up to 500 for genes that are within the top 500 essential genes in NALM-6 cells). Gene essentiality ranking in NALM-6 cells was previously published and determined with the RANKS algorithm using only the core set of genes in the EKO library present in RefSeq[264]. The scores for each gene in the two DMSO controls are averaged and subtracted from the score in the BIBR1532-treated screen to calculate a differential score in order increase hit calling stringency. Synthetic sick/lethal (SSL) interaction hits are genes that are ranked in the 100 lowest scores in the BIBR1532 screen as well as in the 100 lowest differential scores. Buffering interaction hits are genes that are ranked in the 100 highest score in the BIBR1532 screen as well as in the 100 highest differential scores.

3.6.8 Competitive growth assays

Competitive growth assays of *TERT*-disrupted (*TERT* KO) cells were performed as described previously by transducing cells with LentiCRISPRv2-EGFP lentiviral particles targeting *TERT* at a low multiplicity of infection (MOI) to obtain a transduction efficiency between 30-70%[427]. Cells were propagated by sub-culturing every 3 days and were monitored for the percentage of *TERT* KO cells by flow cytometry on a BD FACSCanto II after FSC/SSC gating and indel sequencing. The ratio (R_d) of *TERT* KO cells (N_{KO}) to wild-type cells (N_{WT}) at a given day (d) is described by the following formula:

$$R_d = \frac{N_{KO} \times 2^{d \times G_{KO}}}{N_{WT} \times 2^{d \times G_{WT}}}$$

This formula is equivalent to:

$$R_d = R_0 \times 2^{d(G_{KO} - G_{WT})}$$

The ratio R_t was log-transformed (base 2) and linear regression relative to days in culture is used to extract the slope. This slope was used to calculate the growth rate of *TERT* KO cells for each genotype G_{KO} and normalized to the growth rate of wild-type cells (G_{WT} = 1.25 doublings/day on average for NALM-6 cells) to obtain the relative fitness value (F):

$$F = \frac{G_{KO}}{G_{WT}}$$

Two-population competitive growth assays were used to measure the relative cell fitness of *TERT* KO NALM-6 cells, either as a single knockout in an otherwise wild-type background, or in the presence of a second, separately disrupted gene (see below). For relative fitness measurement of cells lacking *TERT* alone, or cells lacking *TERT* and another gene (B), the relative fitness can be described by the following equation:

$$R_{d;B} = R_{0;B} \times 2^{d(G_{KO;B} - G_B)}$$

Where $G_{KO;B}$ describes the growth rate of cells in which *TERT* disruption is induced via CRISPR transduction as described above in NALM-6 cells already containing a disruption of another gene (*B*), and G_B is the number of doublings per day of NALM-6 cells lacking only gene *B*. In this context, relative fitness is given by the ratio of the growth rate of the *TERT* KO cell population in background B ($G_{KO;B}$) to the growth rate of the same *TERT* KO population a wild-type NALM-6 background ($G_{KO;WT}$):

$$F_B = \frac{G_{KO;B}}{G_{KO;WT}}$$

To investigate how chemical perturbations affect the relative fitness of *TERT* KO NALM-6, cells were seeded at 1 x 10^5 cells/mL and treated with the respective compounds for 6 days (sub-cultured 3 days after compound addition with fresh compound) and EGFP-positive cells percentage was measured (at day 0, 3 and 6 of compound treatment) on a BD FACSCanto II after FSC/SSC gating. Similar to the modelling described above, the effect of chemical perturbations on relative fitness can be modeled using the two following equations:

$$R_{d;cmpd} = R_0 \times 2^{d(G_{KO;cmpd} - G_{WT;cmpd})}$$

$$R_{d;DMSO} = R_0 \times 2^{d(G_{KO;DMSO} - G_{WT;DMSO})}$$

Where $G_{WT;DMSO}$ equals 1.25 doublings/day for NALM-6 cells and $G_{WT;cmpd}$ is the number of doublings that WT cells undergo in the compound treatment (derived from the average relative proliferation of WT cells transduced with non-targeting sgRNAs). $G_{KO;DMSO}$ is the growth rate of *TERT* KO cells without any chemical perturbation and $G_{KO;cmpd}$ is the value of interest and corresponds to the growth rate of *TERT* KO cells when treated with a given compound. Relative fitness is given by the following formula:

$$F_{cmpd} = \frac{G_{KO;cmpd} / G_{KO;DMSO}}{G_{WT;cmpd} / G_{WT;DMSO}}$$

3.6.9 Four-population competitive growth assay

Four-population competitive growth assays was performed as previously described with the following modifications[287]. NALM-6 cells were transduced simultaneously with LentiCRISPRv2-EGFP and LentiCRISPRv2-mCherry lentiviral particles at a low multiplicity of

infection (MOI) in order to obtain all 4 possible populations. Cells were propagated for 14 days in order to ensure indel formation approached a plateau and were subsequently seeded at 1 x 10^5 cells/mL and treated with the respective compounds for the indicated period of time (sub-cultured every 2-3 days with fresh compound) with measurement of EGFP- and mCherry-positive cells percentage by flow cytometry on a BD LSRFortessa analyzer after proper FSC/SSC gating. At each timepoint, $\log_2$ sgRNA enrichment is calculated by first taking the ratio of percentage of cells in each population (EGFP-positive, mCherry-positive, double-positive) to the percentage of WT cells (double-negative) and then normalizing by the ratio at day 0 before log-transforming the normalized ratio (base 2).

3.6.10 Western blots

Immunoblotting was performed as previously described[427]. Briefly, 30 µg of protein lysates were resolved on a 10% (v/v) SDS-PAGE gel and transferred to a 0.22 µm nitrocellulose membrane. Membranes were blocked with 3% (w/v) milk in TBS-Tween 0.05% (v/v) (TBST) before blotting using the following antibodies diluted in TBST: p53 (Santa Cruz #FL-393-G; 1:1000), C16orf72 (TAPR1) (ThermoFisher #TA501515; 1:2000), GAPDH (CST #2118; 1:5000), α-Tubulin (Abcam #ab176560; 1:5000) followed by incubation with the respective HRP-conjugated secondary antibodies (1:10000 dilution in 3% (w/v) milk in TBST). Blots were developed by incubation with ECL substrate and chemiluminescence was measured using a ChemiDoc MP (Bio-Rad).

3.6.11 qPCR measurement of mRNA relative expression

Cells were collected after the indicated treatments and resuspended in QIAzol (Qiagen, #79306) and RNA extraction using the miRNeasy mini kit (Qiagen, #217004) following the

manufacturer's instructions. Reverse transcription was performed on 0.5 µg of RNA after a treatment with DNAse I to remove any remaining genomic DNA followed by reverse transcription with random hexamers (ThermoFisher, #SO142) using the SuperScript IV enzyme (ThermoFisher, #18090050) following the manufacturer's instructions and cDNA is diluted 1:15 in ddH_2O before storage at -20 °C. qPCR reactions are carried by adding 3 µL of the diluted cDNA to 5 µL of PowerUP SYBR 2X mastermix (ThermoFisher, #A25776) and 2 µL of primer mixes for each target transcript (2 µM of each primer) before incubation in the Viia7 (Applied Biosystems) using the following program: 2 min at 95 °C followed by 40 cycles of 3 sec at 95 °C and 30 sec at 60 °C. Primer pair sequences used are as follows: CDKN1A (forward: 5'-CCTCATCCCGTGTTCTCCTTT-3', reverse: 5'-GTACCACCCAGCGGACAAGT-3'), MDM2 (forward: 5'-GGCCTGCTTTACATGTGCAA-3', reverse: 5'-GCACAATCATTTGAATTGGTTGTC-3'), BAX (forward: 5'-CCTTTTCTACTTTGCCAGCAAAC-3', reverse: 5'-GAGGCCGTCCCAACCAC-3'), GAPDH (forward: 5'-CAGCAACAGGGTGGTGGAC-3', reverse: 5'-CATTGCTGGGGCTGGTG-3'), HPRT1 (forward: 5'-TGACACTGGCAAAACAATGCA-3', reverse: 5'-GGTCCTTTTCACCAGCAAGCT-3'). Relative expression is measured using the $\Delta\Delta C_T$ method by using both housekeeping genes as internal controls as previously described[503].

3.6.12 Protein-protein interaction identification by BioID

The cDNA sequence of *C16orf72* (*TAPR1*) was retrieved from the CCDS database (#10538.1), ordered as a gBlock dsDNA fragment from IDT and cloned downstream of miniTurbo-FLAG under the control of a MNDU3 promoter using Gibson assembly[402, 453]. Proximity labeling of TAPR1 interactors was carried out as described previously, with the following modifications[504]. Briefly, NALM-6 expressing miniTurbo-TAPR1, miniTurbo-EGFP or miniTurbo-NLS-EGFP (3 replicates, 30 million cells per replicate) were grown in the presence of 50 µM biotin for 1h. Cells

are washed to remove excess biotin and cells are lysed in RIPA buffer supplemented with Benzonase (250U), sonicated on ice and cleared by centrifugation before protein quantification using the Lowry method. Pre-equilibrated Streptavidin-sepharose beads (GE Healthcare, #17511301) with RIPA buffer were incubated with 2 mg of protein lysate overnight at 4 °C with agitation followed with washes to remove non-specific binding. Samples were reconstituted in 50 mM ammonium bicarbonate with 10 mM TCEP [Tris(2-carboxyethyl)phosphine hydrochloride; Thermo Fisher Scientific], and vortexed for 1 h at 37°C. Chloroacetamide (Sigma-Aldrich) was added for alkylation to a final concentration of 55 mM. Samples were vortexed for another hour at 37°C. One microgram of trypsin was added, and digestion was performed for 8 h at 37°C. Samples were dried down and solubilized in 5% ACN-0.2% formic acid (FA). Peptides were loaded and separated on an home-made reversed-phase column (150-µm i.d. by 200 mm) with a 56-min gradient from 10 to 30% ACN-0.2% FA and a 600-nl/min flow rate on an Easy nLC-1000 instrument connected to an Orbitrap Fusion (Thermo Fisher Scientific, San Jose, CA). Each full MS spectrum acquired at a resolution of 60,000 was followed by tandem-MS (MS-MS) spectra acquisition on the most abundant multiply charged precursor ions for a maximum of 3s. Tandem-MS experiments were performed using collision-induced dissociation (CID) at a collision energy of 30%. The data were processed using PEAKS X (Bioinformatics Solutions, Waterloo, ON) and a Uniprot human database (20349 entries). Mass tolerances on precursor and fragment ions were 10 ppm and 0.3 Da, respectively. Fixed modification was carbamidomethyl (C). Variable selected posttranslational modifications were oxidation (M), deamidation (NQ), phosphorylation (STY). The data were visualized with Scaffold 4.3.0 (protein threshold, 99%, with at least 2 peptides identified and a false-discovery rate [FDR] of 1% for peptides). Tabulated total peptide count for

proteins identified in each sample were used for subsequent analysis after filtering to remove low-count proteins and only keep proteins that are detected in 2 out of 3 replicates of a given bait and that have a minimum of 5 peptides in a given bait. Median-ratio normalization is used to account for inter-sample total peptide count variability followed by log-transformation of the peptide counts (base 2, pseudo-count of 1 added to remove zeros)[505]. Potential contaminants were filtered by removing proteins that are present in at least 20% of experiments reported in the CRAPome database V1.1 (as at May 30th 2020)[506]. The average log2-transformed peptide counts for control baits (n=6) was subtracted from that of TAPR1 bait (n=3) to calculate the fold-change and the Welch t-test was used to calculate a p-value for each fold-change followed by p-value adjustment for multiple comparisons using the Benjamini-Hochberg method to obtain an FDR. Proteins with an FDR below 0.1 and a fold-change higher than 2 were considered as potential TAPR1 interactors.

3.6.13 Transcriptome analysis by RNA-Seq

RNA from 1 million clonal population of NALM-6 cells of the indicated genotypes was extracted using the QIAGEN Mini RNeasy kit according to the manufacturer's protocol. Presence of contamination with chemicals was assessed by nanodrop using 260/280 nm and 260/230 nm ratios. Total RNA was quantified by QuBit (ABI) and 1 µg of total RNA was used for library preparation. RNA quality control was assessed with the Bioanalyzer RNA 6000 Nano assay on the 2100 Bioanalyzer system (Agilent technologies) and all samples had a RIN of 10. Library preparation was done with the KAPA mRNAseq Hyperprep kit (KAPA, #KK8581). Libraries were quantified by QuBit and BioAnalyzer and diluted to 10 nM before normalization by qPCR using the KAPA library quantification kit (KAPA; #KK4973). Libraries were then pooled to equimolar

concentration. Sequencing was performed with the Illumina Nextseq500 on half a flowcell of Nextseq 75 cycles High Output v2 using 2.8 pM of the pooled libraries. Around 20 million single-end PF reads were generated per sample. RNA extraction, quality controls, library preparation and sequencing were performed at the Institute for Research in Immunology and Cancer's Genomics Platform. Reads were aligned with Bowtie2.2.5 (with default parameters) to all RefSeq transcripts (as at April 2018)[393]. Alignments with fewer than 2 inserted or deleted bases and a maximum edit distance of 5 (i.e. the sum of inserted, deleted, or mismatched bases) were counted to generate read counts per transcript and reads mapping to transcripts produced from the same gene locus were summed together to generate read counts per gene. The tabulated read counts per gene in knockout cells were analyzed for differential expression relative to non-targeting controls using the DESeq2 pipeline with the SARtools package on R[507, 508]. A random sample of 1000 non-differentially expressed genes is shown in volcano plots to aid with visualization, see Supplementary table 3.3 (p. 202) for differentially expressed genes in the indicated genotypes.

3.6.14 Gene list enrichment analysis

Statistical significance of the overlap between gene lists was calculated using the hypergeometric test in R. Gene ontology terms enrichment was calculated with the "gprofiler2" package in R where the gene lists were considered an unordered query and with subsequent filtering for GO terms (GO:BP, GO:CC, GO:MF as data sources) that contain less than 1000 terms with an adjusted p-value below 0.05[394]. Further filtering of the GO-terms was performed on the terms enriched to remove redundant GO-terms that share a high semantic similarity using the REVIGO tool (http://revigo.irb.hr/) to aid with visualization[509].

3.6.15 Global heatmap analysis

The different gene lists used for the heatmap were generated from experiments detailed above ("Upreg. in TERT KO", "Upreg. in TAPR1 KO", "SSL with BIBR1532", "Buffering with BIBR1532", "TAPR1 interac. (BioID)") or obtained from publicly available datasets. Genetic co-dependencies (top 100) were retrieved from the DepMap portal (AVANA dataset, 20Q2 public release) for each query gene (*TAPR1*, *HUWE1* and *TP53*)[268]. The consensus list of TP53 transcriptional targets was obtained from Fischer, 2017[510]. Finally, the list of HUWE1 interactors with at least 2 evidences was retrieved from the BioGRID database (as at July 7th 2020)[401]. All ten datasets were merged and filtered to keep only genes that are present in at least 2 datasets before one-hot encoding of the data as dummy variables. Heatmaps were generated using ClustVis (https://biit.cs.ut.ee/clustvis/)[511] without any scaling or row centering.

3.6.16 Statistical analysis

Unless otherwise indicated, statistical analyses were performed on PRISM 8 (www.graphpad.com). Statistical significance was carried out with a Student t-test (2 groups), or with ANOVA (more than 2 groups) using the Sidak or Tukey correction for multiple comparisons.

3.7 Acknowledgements

The authors thank Tsz-Wai Chu for assistance with the TRF protocol as well as past and present members of the laboratory for advice and discussion. We thank the IRIC cytometry, high-throughput screening, proteomics and genomics facilities for technical assistance. We thank Steve Elledge for providing NALM-6 cells. This research was supported by the Canadian Institutes for Health Research (367427 to L.H.; FDN-167277 to M.T.), and a Genomics Technology Platform award from Genome Canada and Genome Quebec (M.T. and co-PI: Pierre Thibault, IRIC). Salaries

were supported by the Fonds de Recherche du Quebec – Nature et Technologie (FRQ-NT) and the Cole Foundation (Y.B.), an Institute for Data Valorisation (IVADO) postdoctoral fellowship (J. C.-H.) a Canada Research Chair in Systems and Synthetic Biology (M.T.).

3.8 Supplementary information

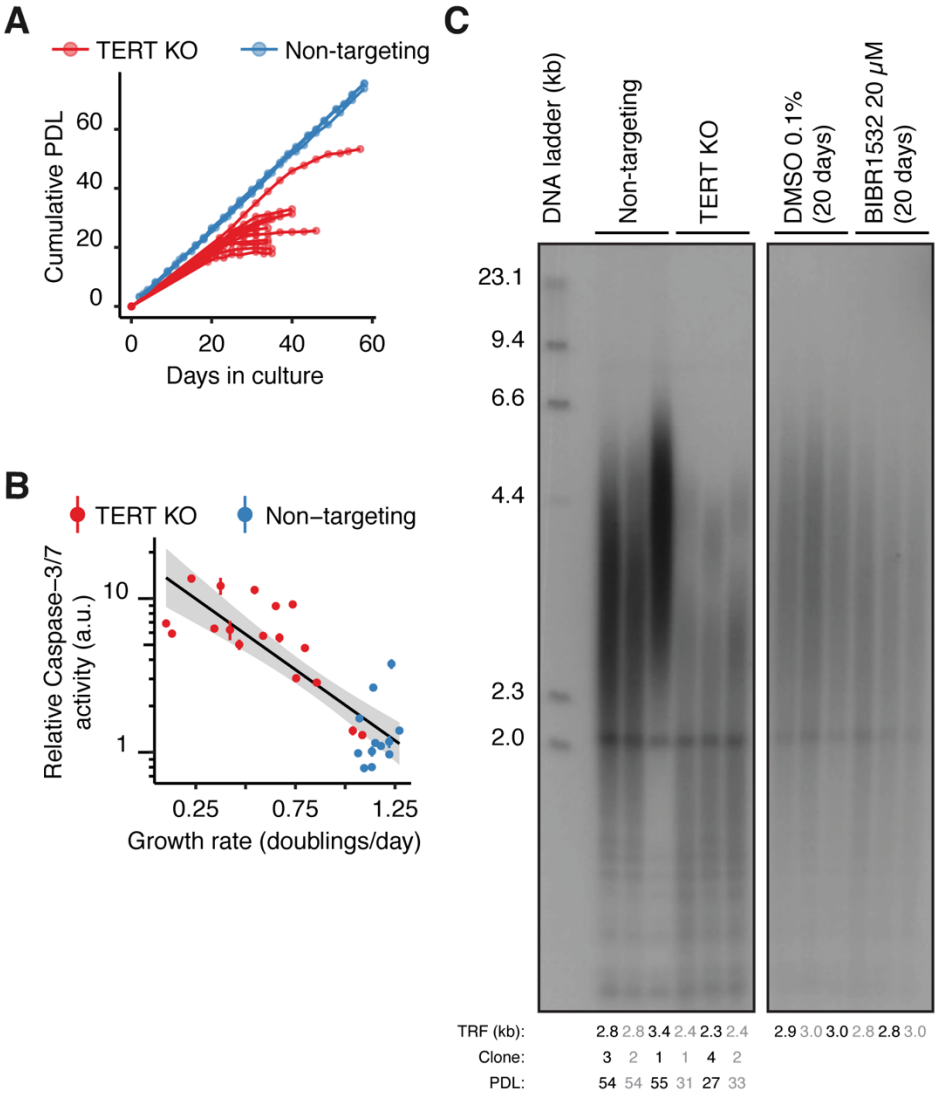

Supplementary figure 3.1 | Telomerase activity is necessary for long-term proliferation of NALM-6 cells.

A. Cumulative population doublings relative to days in culture in clonal *TERT* KO (n=12) or non-targeting control NALM-6 cells (n = 3). **B.** Relative Caspase-3/7 activity in *TERT* KO (4 independent clones) or non-targeting (3 independent clones) NALM-6 cell lysates relative to the growth rate at the time of lysate collection (n=3 technical replicates per sample). **C.** TRF measurement of telomere length of clonal *TERT* KO or non-targeting NALM-6 cells (left, population doublings at the time of collection is indicated below respective lanes) as well as cells treated with BIBR1532 or DMSO (right) for 20 days (n=3). Mean TRF length is quantified and indicated below each lane.

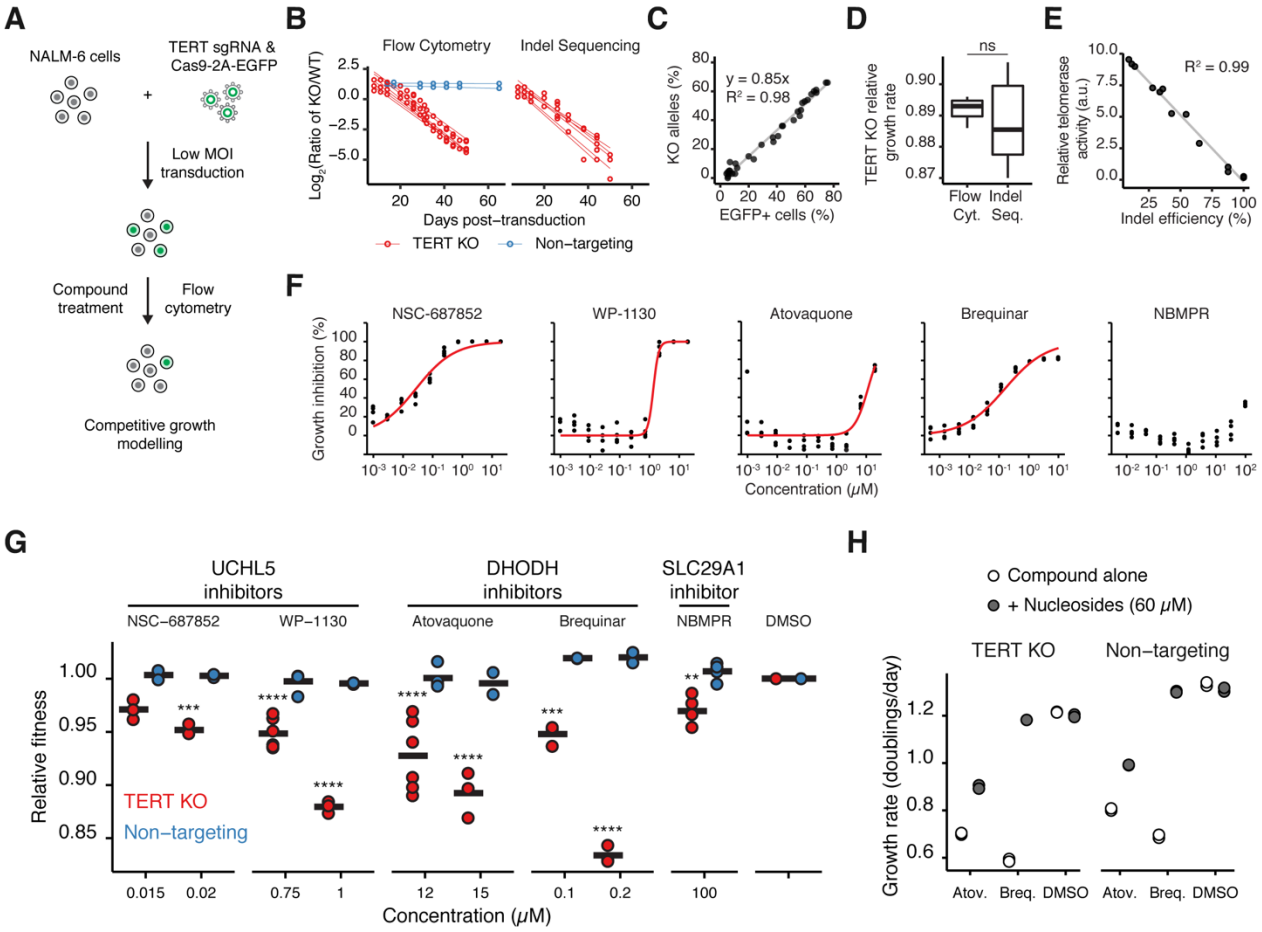

Supplementary figure 3.2 | On-target validation of chemical-genetic identified in CRISPR screen.

A. Competitive growth assay schematic in NALM-6 cells used to measure the relative fitness of *TERT* KO cells under different conditions. **B.** Log-transformed ratio of KO to WT cells as measured by flow cytometry or indel sequencing for mixed populations of TERT KO (n=6) or non-targeting (n=2) cells. **C.** A mixed population of cells targeted for *TERT* (measured by Sanger sequencing) relative to the transduction efficiency (GFP+ cells, measured by flow cytometry. **D.** The relative growth rate of *TERT* KO NALM-6 cells as measured by flow cytometry or indel sequencing (n = 6). **E.** Relative telomerase activity of NALM-6 cell lysates measured by qTRAP relative to the indel efficiency in the mixed cell populations. **F.** Growth inhibition of NALM-6 cells treated with the indicated compounds for 72h (n=4). **G.** Relative fitness of *TERT* KO (n ≥ 3) or non-targeting (n ≥ 2) mixed populations treated with the indicated compounds. **H.** Growth rate of TERT KO or non-targeting mixed populations treated with atovaquone (12 μM), brequinar (0.1 μM) or DMSO (0.1% v/v) with addition of nucleosides in the media (n=2).

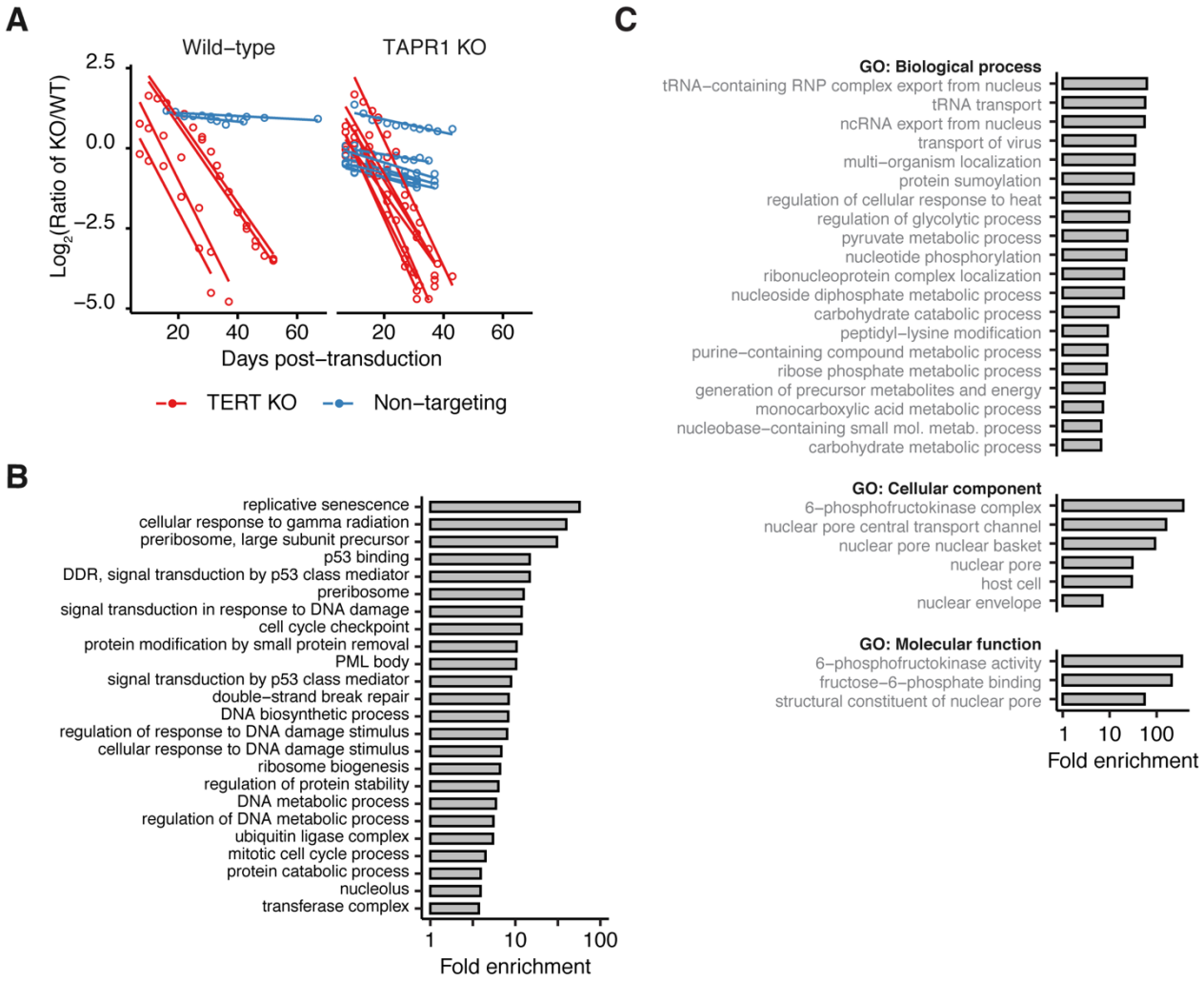

Supplementary figure 3.3 | Gene ontology term enrichment in lists of TAPR1 interaction partners.

A. Flow cytometry measurement of EGFP-positive *TERT* KO or non-targeting cells relative to the days post-transduction of *TAPR1* KO or wild-type NALM-6 cells (n ≥ 2). **B.** GO-term enrichment in the top 100 correlates with *TAPR1* for genetic dependency in the AVANA dataset (DepMap). **C.** GO-term enrichment in the list of TAPR1 protein interactors identified by BioID.

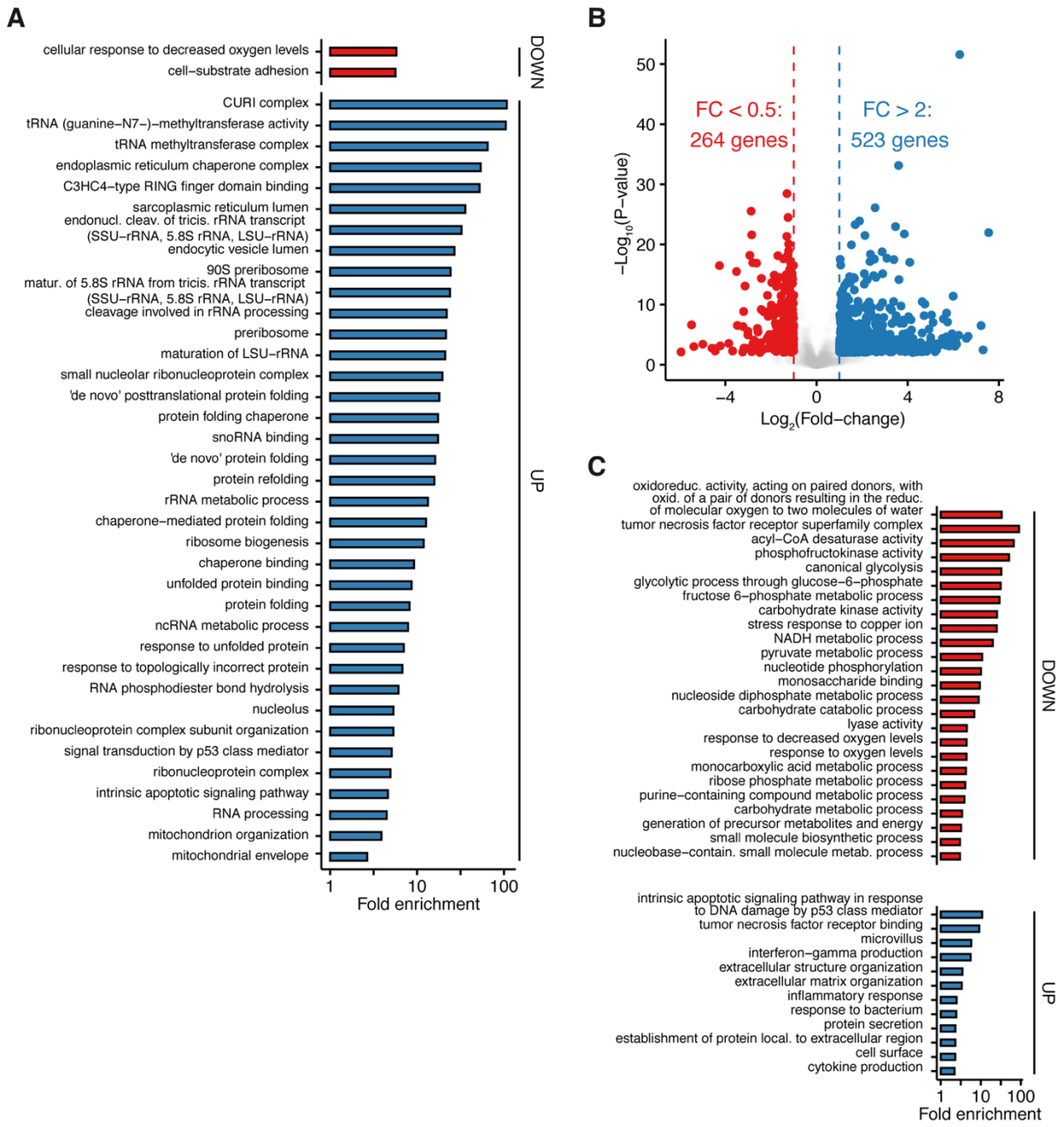

Supplementary figure 3.4 | Differentially expressed genes in *TAPR1*- and *TERT*-deficient NALM-6 cells.

A. GO-term enrichment in down-regulated genes (FC < -2) or up-regulated genes (FC > 1.5) in *TAPR1* KO NALM-6 cells. **B.** Volcano plot showing transcriptome changes in TERT KO NALM-6 cells approaching crisis relative to non-targeting controls, differentially expressed genes (FDR < 0.05) are shown for the different fold-change cutoffs (n = 3). **C.** GO-term enrichment in down-regulated genes (FC < -2) or up-regulated genes (FC > 2) in TERT KO NALM-6 cells.

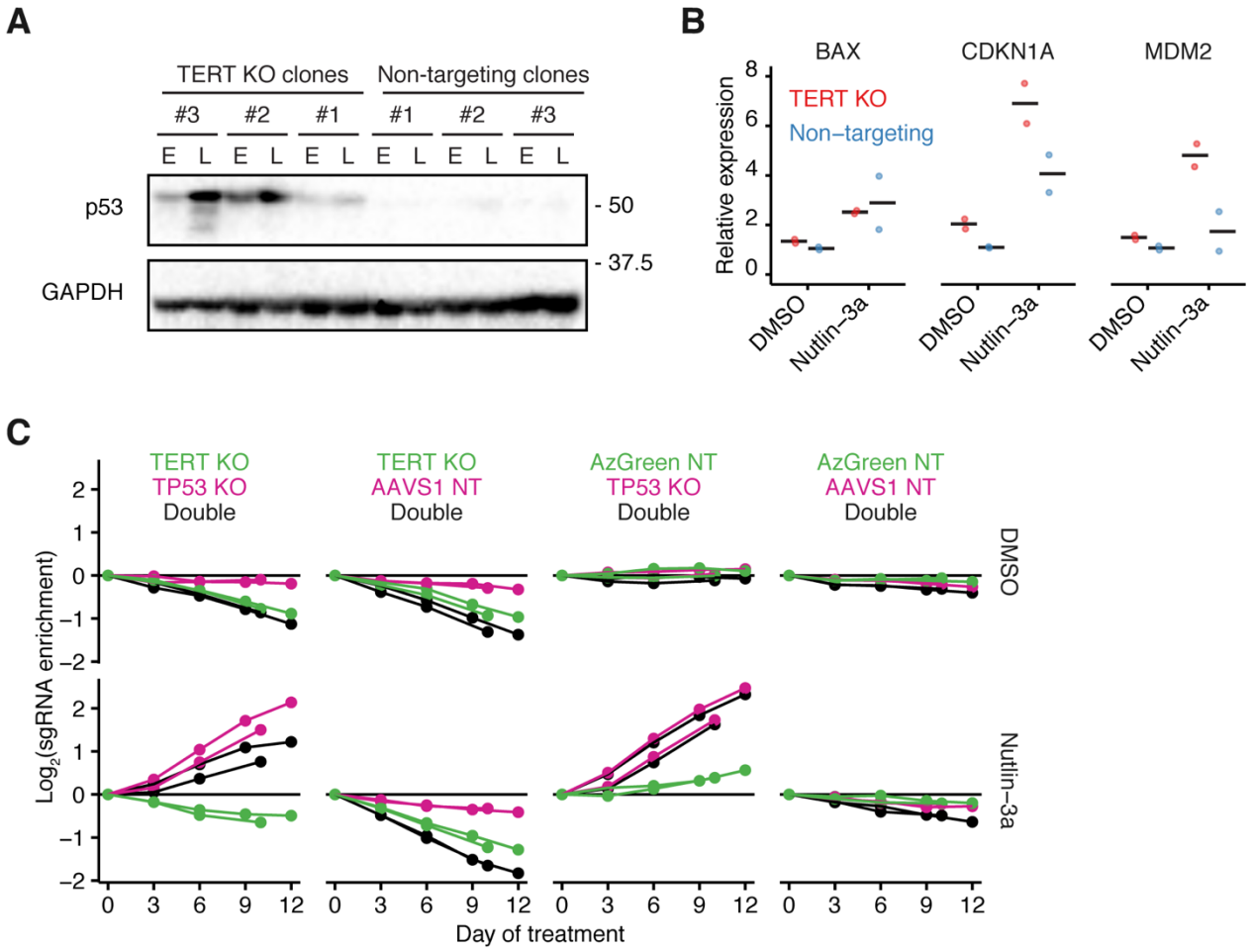

Supplementary figure 3.5 | p53 pathway activation in *TERT*-deficient NALM-6 cells.

A. Lysates from NALM-6 cells disrupted for *TERT* (*TERT* KO) or non-targeting controls collected at different timepoints after clonal selection (E: early, L: late) were blotted against p53 and GAPDH (1 representative blot of 2 independent replicates). **B.** Relative expression of the indicated transcripts in *TERT* KO cells or non-targeting controls (after EGFP-positive cell sorting from population knockouts) treated with 2 µM nutlin-3a or 0.1% (v/v) DMSO for 6 days (n = 2). **C.** sgRNA enrichment in NALM-6 cells treated with 2 µM nutlin-3a or 0.1% (v/v) DMSO shown for the different *TERT*/*TP53* sgRNA combinations (n=2).

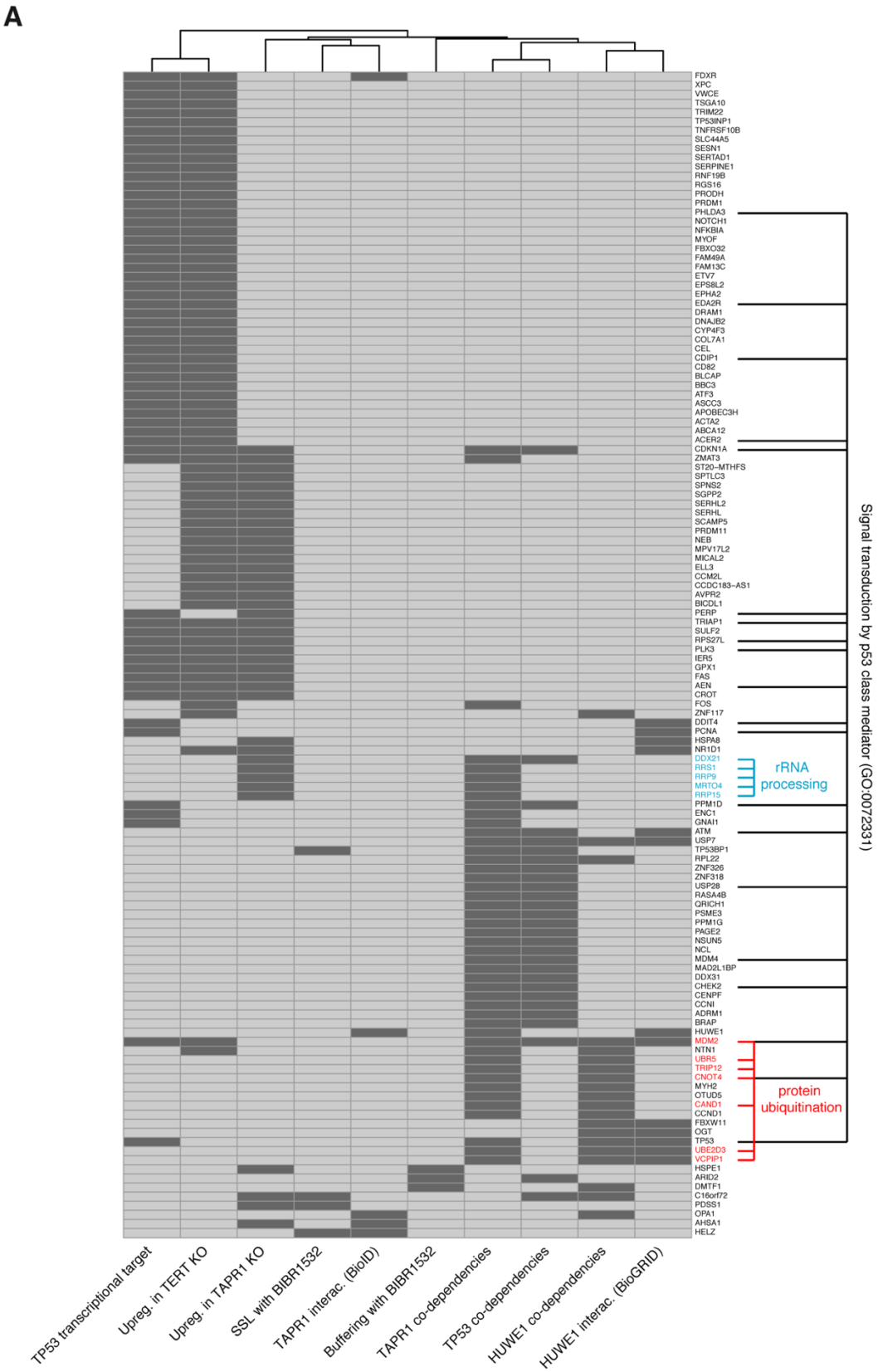

Supplementary figure 3.6 | *TAPR1-TERT* interaction data exploration.

A. Heatmap showing genes that are present as hits (indicated in dark grey) in at least two datasets (128 genes total for 10 datasets). Black lines indicate genes involved in p53 signal transduction (GO: 0072331). Common hits between *TAPR1* and *HUWE1* co-dependencies (Avana dataset) are enriched for genes involved in protein ubiquitination and are indicated in red. Common hits between *TAPR1* co-dependencies and genes upregulated in *TAPR1* KO cells are enriched for genes involved in rRNA processing and are indicated in light blue.

Chapter 4 – Discussion

4.1. Potential mechanisms by which resveratrol acts in human cells

The work presented in this thesis highlights the power of CRISPR-mediated genome editing to probe the genetic network of human cells. In chapter 2, we performed a genome-wide screen for enhancers and suppressors of resveratrol-mediated proliferation inhibition in human cells. This unbiased approach suggests that replicative stress induction exerts a major effect on proliferation in human cells. While this effect had been observed previously, the majority of literature on resveratrol points to the NAD-dependent deacetylase Sirtuin 1 (SIRT1) as the target of resveratrol and we show that the presence of SIRT1 in cells is not required for the replication stress observed. A potential target of resveratrol could be ribonucleotide reductase (RNR), similar to hydroxyurea[360, 365]. The direct inhibition of human RNR activity in cells by resveratrol remains to be shown, which could be performed using a combined CRISPRi/CRISPRa screening approach to identify knockouts that show sensitivity when the gene dosage is reduced and show resistance when the gene dosage is increased[512]. Applying this approach to RNR is not trivial, given the strong effect on cellular proliferation when the large subunit of RNR (RRM1) is deleted[264]. Alternatively, a definitive demonstration could be obtained with a tridimensional structure of RNR with resveratrol if mutations of residues that make contact with resveratrol could be established to be resistant to replicative stress. Interestingly, contrary to RNR inhibitors like gemcitabine that bind to the large subunit, hydroxyurea has been proposed to scavenge the radical on the small subunit of RNR (RRM2) by proximity rather than by direct binding[513, 514]. Resveratrol was first investigated

as an antioxidant, which fits with a working model of RNR inhibition, similar to hydroxyurea, by modulation of the redox state of the enzyme[310, 360].

The enzymology of RNR and its dependence on the cellular redox state as well as on cellular iron is of particular interest given that several chemical-genetic interactions observed with resveratrol, pterostilbene or hydroxyurea lie within genes involved in mitochondrial activity and integrity, as well as cellular iron homeostasis and iron-sulfur cluster biogenesis. In *E. coli*, hydroxyurea causes replicative stress, but the cytotoxicity is mediated by the creation of hydroxyl radicals through the iron-dependent Fenton reaction[515]. This process can be rescued by using thiourea, a hydroxyl radical scavenger, or by deleting *tonB* to reduce iron uptake by cells[515]. In yeast, several mutants that alter Iron-Sulfur (Fe-S) cluster biosynthesis are sensitive to hydroxyurea which could be explained by the prevalence of Fe-S clusters in proteins involved in DNA replication and DNA repair[516, 517]. These proteins are upregulated by the intra-S-phase checkpoint response (in yeast and in humans) which suggests that there is a concomitant increase of cellular iron for Fe-S cluster biogenesis to respond to replicative stress[137, 138, 517-519]. If a stress is acute, this regulated response could serve as a way to complete replication but a chronic exposure to hydroxyurea or resveratrol could maintain this response, leading to increased cellular iron and hydroxyl radical cytotoxicity through Fenton reactions[520, 521] (Figure 4.1, p. 143).

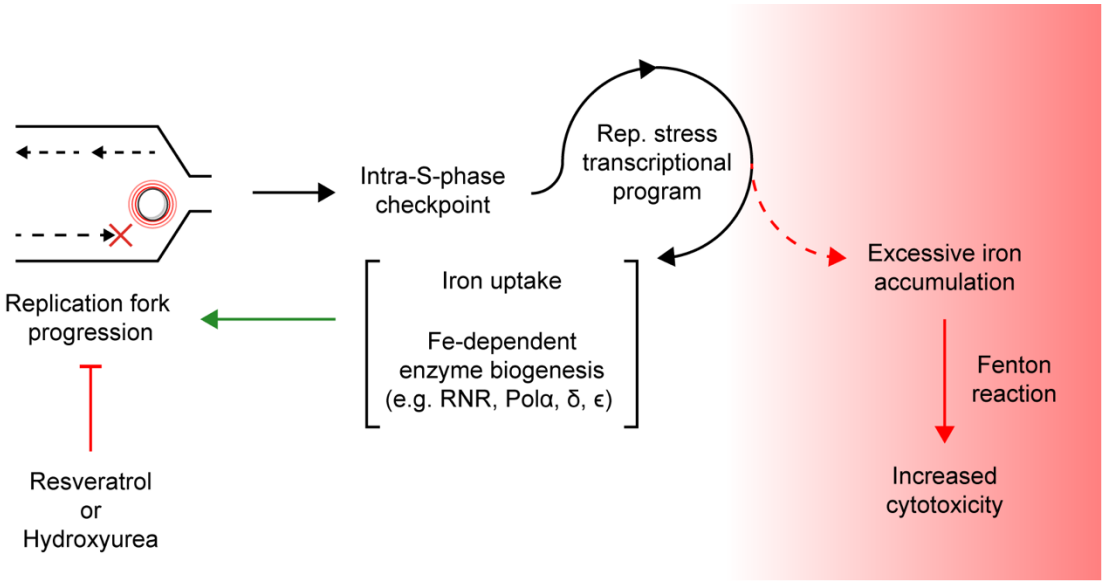

Figure 4.1 | Model of the interplay between DNA replication and iron metabolism

While the work presented in chapter 2 does not directly address the role of resveratrol in aging, it raises the question of the role of replicative stress in modulating the observed lifespan extension in model organisms. The induction of replicative stress could have a hormetic effect on lifespan where a full replication block is detrimental, but a low level of stress exerts a beneficial effect. A first possibility is that the intra-S-phase checkpoint activation remodels the proteome and could repair other types of cellular damage that would otherwise accumulate, a model that is supported by the increased replicative lifespan of budding yeast overexpressing the Rad53 checkpoint kinase[376]. A second alternative is that post-replicative processes such as DNA repair or epigenetic modifications (such as DNA methylation or histone post-translational modifications) show a better coupling with DNA replication in presence of low levels of replicative stress as loss of epigenetic marks on DNA is hallmark of aging[522]. It is tempting to speculate that the imposition of a checkpoint between DNA replication and the remainder of the cell cycle by replicative stress might allow enough time for any trailing post-replicative processes.

4.2 Telomeric damage sheds light on p53 signaling

In chapter 3, we used a human pre-B ALL NALM-6 cell line to uncover chemical-genetic interactions with telomerase inhibition by the well-characterized small-molecule BIBR1532. Several knockouts of genes involved in pyrimidine biosynthesis as well as in chromatin remodelling (INO80 complex) exhibited a synthetic-sick lethal (SSL) interaction with telomerase inhibition. While we identified several deletions that suppressed the effect of BIBR1532 on NALM-6 cells, no specific biological process was enriched within the list of hits, which could indicate that a higher level of telomeric damage is necessary to reveal suppressors or that a different experimental design (e.g. longer timepoints) may be required. We focused on a specific SSL interaction between the telomerase catalytic subunit *TERT* and the *TAPR1* (*C16orf72*) gene and we showed that this protein of previously unknown function acts as a negative regulator of p53 protein levels. We measured a higher increase of *CDKN1A* transcript levels in TAPR1-distrupted cells upon p53 activation which explains the reduced proliferation observed. While we did not detect such an increase for the other p53 targets *MDM2* and *BAX*, this can be explained by the known oscillatory activation of p53 upon transient damage[523]. P53 targets respond differently to this pulsatile activation and this response has been shown to be dependent on the mRNA stability of each target[187, 524]. Thus, the specific increase seen for *CDKN1A* transcripts could be explained by the conditions used for p53 activation. A detailed single-cell analysis of both p53 and downstream target activation over the course of multiple timepoints would uncover how TAPR1 depletion affects p53 pulsing parameters (such as amplitude and frequency of oscillations) and the effect on p53 transcriptional targets[185]. Since cell fate upon p53 activation has been shown to

be dependent on p53 dynamics, a modulation of the aforementioned oscillatory parameters by TAPR1 could change cell fate upon damage[523].

While the role of p53 in responding to telomeric damage has been described extensively, we do not yet know if the interaction between *TERT* and *TAPR1* is dependent on telomerase catalytic activity[200, 208]. TERT has recently been described to form a complex with the Hsp70 chaperone and have a role in telomeric end-protection that is independent of its catalytic activity[434]. To test this notion, one could assess if complementation of the *TAPR1-TERT* double knockout cells with cDNA of catalytically dead TERT (D868A, D869A) or telomeric recruitment-deficient TERT (K78E) could rescue the SSL interaction[219]. Such an experiment may also help tease out the role of de novo telomere addition by telomerase as one means to alleviate telomere loss due to fork collapse in the presence of replicative stress. Interestingly, *TP53*-targeting guide RNAs did not lead to a buffering phenotype in the BIBR1532 chemical-genetic screen with NALM-6 cells. One simple explanation could be that the shorter timepoint of 20 days examined was more successful at detecting SSL interactions rather than buffering interactions and a longer timepoint would allow the identification of genes involved in the p53 response to telomere erosion. Alternatively, a potential explanation of the lack of buffering phenotype of *TP53*-targeting guide RNAs could be specific to the NALM-6 cancer cell genetic background. It is possible that there is an inherent directionality in the genetic interaction between *TERT* and *TP53*, such as low p53 levels not being able to fully rescue the fitness defect of *TERT* KO cells, but high p53 levels leading to a sensitivity to short telomeres. A measurement of the cellular fitness upon orthogonal modulation by CRISPRa/CRISPRi of *TP53* expression combined with a knockout of *TERT* would begin to address this question[288].

Future studies are also required to determine if the protein interaction detected between TAPR1 and the E3 ligase HUWE1 is necessary and sufficient to decrease p53 levels, as HUWE1 has been reported to ubiquitinate p53 which leads to its degradation[446]. HUWE1 and the budding yeast homolog Tom1 also target unassembled ribosomal proteins for degradation in order to maintain proper ribosome biogenesis homeostasis[478]. Interestingly, treatments that interfere with ribosome biogenesis such as ribosomal RNA (rRNA) transcription inhibition by actinomycin D (RNA polymerase I inhibitor) activate p53 signaling through the release of unassembled ribosomal proteins that sequester the p53 negative regulator MDM2[484]. Ribosomal stress has also been proposed to be the mechanism by which p53 senses nucleotide (rNTPs) depletion (causes a reduction of rRNA transcription), which raises the intriguing possibility that the SSL interactions detected with genes involved in pyrimidine biosynthesis increase p53 levels by causing both replicative stress and ribosomal stress[525]. Notably, *TAPR1* deletion was also shown to induce sensitivity to replicative stress caused by resveratrol or hydroxyurea[427]. This phenotype can be explained by the recruitment of the HUWE1 E3 ligase to sites of stalled replication forks by PCNA to promote fork restart and TAPR1 could act as a co-factor of HUWE1 at stalled replication forks[526]. Alternatively, replicative stress in budding yeast and in MCM2-deficient mouse cells has been shown to lead to a decrease of ribosomal DNA repeat number, which could reduce the transcription of ribosomal RNA and thus increase the levels of unassembled ribosomal proteins triggering a p53-dependent growth arrest[527]. Future experiments on ribosomal protein levels and ribosomal RNA processing will inform on the extent of ribosomal stress in TAPR1 knockout cells and the functional role the interaction with the HUWE1 E3 ligase has to play[478, 485, 486] (Figure 4.2, p. 146).

While our use of the p53-positive NALM-6 cell line allowed us to identify genes that modulate the biologically relevant p53 pathway in response to telomere shortening, the full exploration of the telomere maintenance network would require a larger panel of cell lines to be screened using a isogenic *TERT* deletions multiplexed with genome-wide knockouts[284]. These cell lines should be selected to represent the different stages of (1) cellular transformation, (2) p53 mutation status and (3) TERT promoter status. Different stages of cellular transformation would allow to cluster genetic interactions based on the terminal mechanism growth arrest (cellular senescence *vs* apoptosis *vs* autophagic cell death)[200, 209, 210]. Selecting cell lines based on the p53 and *TERT* promoter mutational status would identify which genetic interactions converge on p53 signalling of telomeric damage or which genetic interactions arise due to proteome remodelling in response to TERT promoter mutations[222]. It would be interesting to profile the genetic interactions identified in terms of their ability to enhance or suppress the telomere insufficiency that is observed with clinically relevant mutations that are detected in telomeropathies, a group of diseases that stem from defective telomere maintenance due to mutations in telomeric proteins such as components of shelterin or the telomerase holoenzyme[528]. These experiments might reveal functional relationships that modulate the penetrance of the telomeropathies mutations, the severity of the symptoms or potential therapeutic interventions.

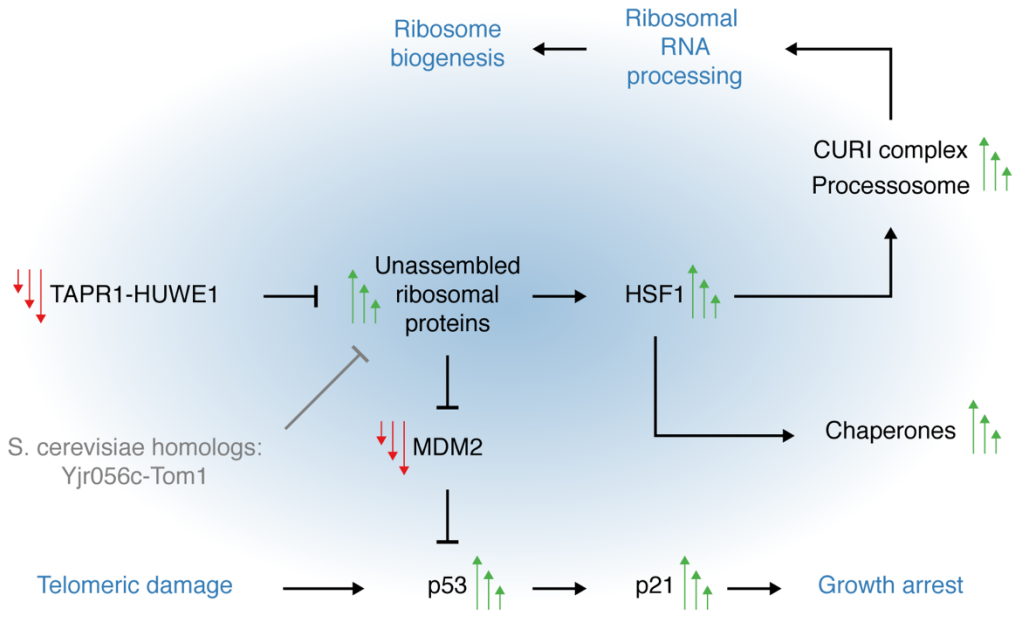

Figure 4.2 | Potential cellular wiring between TAPR1 function, ribosomal biogenesis and p53 signaling

Vertical red arrows depict a decrease, while green arrows indicate an increase of the associated factor based on the data presented in chapter 3 and the relevant literature.

4.3 Current and future genetic interaction mapping in mammalian cells

While CRISPR-based genetic screening holds great promise in delivering the breath of interaction mapping in mammalian cells that was previously achievable only in model organisms such as budding yeast, one should keep in mind that there are limitations that are specific to CRISPR or to the use of mammalian cells. Currently, Cas9 off-target cutting is inferred using computational predictions which are improving as methods to systematically measure genome-wide Cas9 cutting are being developed[247]. Commonly used sgRNA libraries mitigate the potential effect of off-target knockouts through the use of multiple sgRNAs per gene but more

improvements to sgRNA designs, combined with the use of Cas9 variants with improved specificity, could greatly reduce the number of required sgRNAs per gene thus allowing systematic genetic interaction mapping at a lower scale[529, 530]. A second feature at the level of sgRNA design relates to the fate of the double-stranded break to ensure that frameshift-introducing indels are favoured at the targeted locus. Even when indels that would lead to a non-sense mutation are introduced, proteomic analysis of the resulting truncated proteins that have been targeted by Cas9 shows a pervasive mechanism of exon skipping that serves to bypass the frameshift that is introduced[531]. A more rational design of sgRNAs that takes into account the sequence around the break and how the DNA repair machinery will process said break as well as targeting of essential exons that would result in a loss-of-function if skipped are needed to ensure that most sgRNAs included in the library result in productive knockouts[252, 531].

At the gene targets level, the number of paralog pairs of genes that are predicted to be redundant for a subset of their function is not negligible in mammalian genomes and said genes are typically lost in current single-targeting screening strategies due to the ability of the paralogs to compensate for loss of one another[279]. Multiplexing of knockouts by using the Cas12a enzyme or the CHyMEra system (achieves higher indel efficiency by combining Cas12a array processing activity with high Cas9 targeting activity) to target both paralogs simultaneously and prevent any compensation would help include the paralog pairs into the systematic interaction mapping[279, 286]. A second category of genes for which systematic interaction mapping is difficult is essential genes. A gene knockout that results in a mild defect in proliferation can be informative if the screen scoring algorithm used, such as the algorithm used in this thesis (Chapter 3) which accounts for such essentiality and corrects for it[264, 532]. Genes that result in a significant loss of

proliferation are lost when looking at chemical-gene or gene-gene interactions since the dynamic range with which one can detect suppressors or enhancers of the phenotype is very narrow. Given that such genes typically function within critical cellular functions, a strategy to characterize their interactions is necessary. One such strategy could be the use of CRISPRi with sgRNAs that result in an incomplete inhibition of transcription[533]. The resulting mild phenotype could then be queried for enhancing or suppressing interactions. Finally, a blind spot of the current implementation of CRISPRko screening is the genetic interaction landscape of long non-coding RNAs (lncRNAs). Since indels are unlikely to cause loss-of-function of a lncRNA, different strategies have been employed to study the role these molecules play. A CRISPRi-based targeting seems to be the best approach to investigate genetic interactions of long-non-coding RNAs[275]. Another previously unrecognized group of molecules are noncanonical open reading frames that have recently been shown to be translated and several of these micro-peptides play a role in cell proliferation as shown by CRISPR targeting[534].

The limitations discussed above are related to the precision and accuracy of CRISPR-based targeting in identifying candidate hits, but several developments are also underway whose goal is to increase the amount of information that is gained from systematic screening. The first development is the use of orthogonal approaches in multiplexed gene perturbations, such as a CRISPRi with a CRISPRa system[288]. This screening system not only queries the role of a gene by both knockdown and overexpression on a phenotype of interest, but also facilitates follow-up analysis of candidate hits by allowing researchers to infer the directionality of the identified interactions. Another exciting direction in terms of technological developments is the combination of CRISPR based screening with high-content measurements in order to obtain

measurements that are complementary to cell proliferation. Methods that combine CRISPR screening with fluorescence microscopy[535, 536], proteomic analysis by flow cytometry[537-539], transcriptome analysis[540-545] (scRNASeq) and chromatin analysis[539] (scATACSeq) have been described. While the current pace of technological development will most likely result in systematic genetic interaction maps in human cells in the next five years, the interpretability of these maps will require multimodal single-cell assays combined with genetic perturbations in order to map the genetic interactions within networks-of-interest onto the key regulatory nodes. The study of the genome stability maintenance sub-network presented in this thesis sheds light on the different layers of regulation that impinge on replication fidelity and telomere maintenance. Not only will this information aid our ability to dissect the complexities of telomere and DNA replication, it is also a step forward in our understanding of the molecular mechanisms that give rise to robust network architecture, both of which are critical for the development of adequate therapeutic interventions or the design and engineering of synthetic organisms.

References

1. Charlesworth B, Charlesworth D. Darwin and genetics. Genetics. 2009;183(3):757-66.
2. Hershey AD, Chase M. Independent functions of viral protein and nucleic acid in growth of bacteriophage. J Gen Physiol. 1952;36(1):39-56.
3. Avery OT, Macleod CM, McCarty M. Studies on the chemical nature of the substance inducing transformation of pneumococcal types : Induction of transformation by a desoxyribonucleic acid fraction isolated from pneumococcus type III. J Exp Med. 1944;79(2):137-58.
4. Watson JD, Crick FH. The structure of DNA. Cold Spring Harb Symp Quant Biol. 1953;18:123-31.
5. Meselson M, Stahl FW. The replication of DNA in Escherichia coli. Proc Natl Acad Sci U S A. 1958;44(7):671-82.
6. Hoeijmakers JH. DNA damage, aging, and cancer. N Engl J Med. 2009;361(15):1475-85.
7. Preston BD, Albertson TM, Herr AJ. DNA replication fidelity and cancer. Semin Cancer Biol. 2010;20(5):281-93.
8. Vermeulen K, Van Bockstaele DR, Berneman ZN. The cell cycle: a review of regulation, deregulation and therapeutic targets in cancer. Cell Prolif. 2003;36(3):131-49.
9. Malumbres M, Barbacid M. Mammalian cyclin-dependent kinases. Trends Biochem Sci. 2005;30(11):630-41.
10. Bertoli C, Skotheim JM, de Bruin RA. Control of cell cycle transcription during G1 and S phases. Nat Rev Mol Cell Biol. 2013;14(8):518-28.
11. Peters JM. The anaphase promoting complex/cyclosome: a machine designed to destroy. Nat Rev Mol Cell Biol. 2006;7(9):644-56.
12. Elbæk CR, Petrosius V, Sørensen CS. WEE1 kinase limits CDK activities to safeguard DNA replication and mitotic entry. Mutat Res. 2020;819-820:111694.
13. Lara-Gonzalez P, Westhorpe FG, Taylor SS. The spindle assembly checkpoint. Curr Biol. 2012;22(22):R966-80.

14. Hagting A, Den Elzen N, Vodermaier HC, Waizenegger IC, Peters JM, Pines J. Human securin proteolysis is controlled by the spindle checkpoint and reveals when the APC/C switches from activation by Cdc20 to Cdh1. J Cell Biol. 2002;157(7):1125-37.
15. Siddiqui K, On KF, Diffley JF. Regulating DNA replication in eukarya. Cold Spring Harb Perspect Biol. 2013;5(9).
16. Costa A, Hood IV, Berger JM. Mechanisms for initiating cellular DNA replication. Annu Rev Biochem. 2013;82:25-54.
17. Bell SP, Stillman B. ATP-dependent recognition of eukaryotic origins of DNA replication by a multiprotein complex. Nature. 1992;357(6374):128-34.
18. Takeda DY, Shibata Y, Parvin JD, Dutta A. Recruitment of ORC or CDC6 to DNA is sufficient to create an artificial origin of replication in mammalian cells. Genes Dev. 2005;19(23):2827-36.
19. Sequeira-Mendes J, Díaz-Uriarte R, Apedaile A, Huntley D, Brockdorff N, Gómez M. Transcription initiation activity sets replication origin efficiency in mammalian cells. PLoS Genet. 2009;5(4):e1000446.
20. Miotto B, Ji Z, Struhl K. Selectivity of ORC binding sites and the relation to replication timing, fragile sites, and deletions in cancers. Proc Natl Acad Sci U S A. 2016;113(33):E4810-9.
21. Petryk N, Kahli M, d'Aubenton-Carafa Y, Jaszczyszyn Y, Shen Y, Silvain M, et al. Replication landscape of the human genome. Nat Commun. 2016;7:10208.
22. Diffley JF, Cocker JH, Dowell SJ, Rowley A. Two steps in the assembly of complexes at yeast replication origins in vivo. Cell. 1994;78(2):303-16.
23. Donovan S, Harwood J, Drury LS, Diffley JF. Cdc6p-dependent loading of Mcm proteins onto pre-replicative chromatin in budding yeast. Proc Natl Acad Sci U S A. 1997;94(11):5611-6.
24. Seki T, Diffley JF. Stepwise assembly of initiation proteins at budding yeast replication origins in vitro. Proc Natl Acad Sci U S A. 2000;97(26):14115-20.

25. Cook JG, Park CH, Burke TW, Leone G, DeGregori J, Engel A, et al. Analysis of Cdc6 function in the assembly of mammalian prereplication complexes. Proc Natl Acad Sci U S A. 2002;99(3):1347-52.
26. Rialland M, Sola F, Santocanale C. Essential role of human CDT1 in DNA replication and chromatin licensing. J Cell Sci. 2002;115(Pt 7):1435-40.
27. Remus D, Beuron F, Tolun G, Griffith JD, Morris EP, Diffley JF. Concerted loading of Mcm2-7 double hexamers around DNA during DNA replication origin licensing. Cell. 2009;139(4):719-30.
28. Coster G, Diffley JFX. Bidirectional eukaryotic DNA replication is established by quasi-symmetrical helicase loading. Science. 2017;357(6348):314-8.
29. Dahmann C, Diffley JF, Nasmyth KA. S-phase-promoting cyclin-dependent kinases prevent re-replication by inhibiting the transition of replication origins to a pre-replicative state. Curr Biol. 1995;5(11):1257-69.
30. Jiang W, Wells NJ, Hunter T. Multistep regulation of DNA replication by Cdk phosphorylation of HsCdc6. Proc Natl Acad Sci U S A. 1999;96(11):6193-8.
31. Wohlschlegel JA, Dwyer BT, Dhar SK, Cvetic C, Walter JC, Dutta A. Inhibition of eukaryotic DNA replication by geminin binding to Cdt1. Science. 2000;290(5500):2309-12.
32. Nguyen VQ, Co C, Li JJ. Cyclin-dependent kinases prevent DNA re-replication through multiple mechanisms. Nature. 2001;411(6841):1068-73.
33. Li CJ, Vassilev A, DePamphilis ML. Role for Cdk1 (Cdc2)/cyclin A in preventing the mammalian origin recognition complex's largest subunit (Orc1) from binding to chromatin during mitosis. Mol Cell Biol. 2004;24(13):5875-86.
34. Nishitani H, Lygerou Z, Nishimoto T. Proteolysis of DNA replication licensing factor Cdt1 in S-phase is performed independently of geminin through its N-terminal region. J Biol Chem. 2004;279(29):30807-16.
35. Ilves I, Petojevic T, Pesavento JJ, Botchan MR. Activation of the MCM2-7 helicase by association with Cdc45 and GINS proteins. Mol Cell. 2010;37(2):247-58.
36. Yeeles JT, Deegan TD, Janska A, Early A, Diffley JF. Regulated eukaryotic DNA replication origin firing with purified proteins. Nature. 2015;519(7544):431-5.

37. Aparicio T, Guillou E, Coloma J, Montoya G, Méndez J. The human GINS complex associates with Cdc45 and MCM and is essential for DNA replication. Nucleic Acids Res. 2009;37(7):2087-95.
38. Zegerman P, Diffley JF. Phosphorylation of Sld2 and Sld3 by cyclin-dependent kinases promotes DNA replication in budding yeast. Nature. 2007;445(7125):281-5.
39. Kumagai A, Shevchenko A, Shevchenko A, Dunphy WG. Treslin collaborates with TopBP1 in triggering the initiation of DNA replication. Cell. 2010;140(3):349-59.
40. Muramatsu S, Hirai K, Tak YS, Kamimura Y, Araki H. CDK-dependent complex formation between replication proteins Dpb11, Sld2, Pol (epsilon}, and GINS in budding yeast. Genes Dev. 2010;24(6):602-12.
41. Bruck I, Kaplan DL. Conserved mechanism for coordinating replication fork helicase assembly with phosphorylation of the helicase. Proc Natl Acad Sci U S A. 2015;112(36):11223-8.
42. Zhu W, Ukomadu C, Jha S, Senga T, Dhar SK, Wohlschlegel JA, et al. Mcm10 and And-1/CTF4 recruit DNA polymerase alpha to chromatin for initiation of DNA replication. Genes Dev. 2007;21(18):2288-99.
43. Im JS, Ki SH, Farina A, Jung DS, Hurwitz J, Lee JK. Assembly of the Cdc45-Mcm2-7-GINS complex in human cells requires the Ctf4/And-1, RecQL4, and Mcm10 proteins. Proc Natl Acad Sci U S A. 2009;106(37):15628-32.
44. Douglas ME, Ali FA, Costa A, Diffley JFX. The mechanism of eukaryotic CMG helicase activation. Nature. 2018;555(7695):265-8.
45. Ge XQ, Jackson DA, Blow JJ. Dormant origins licensed by excess Mcm2-7 are required for human cells to survive replicative stress. Genes Dev. 2007;21(24):3331-41.
46. Ibarra A, Schwob E, Méndez J. Excess MCM proteins protect human cells from replicative stress by licensing backup origins of replication. Proc Natl Acad Sci U S A. 2008;105(26):8956-61.
47. Yamazaki S, Ishii A, Kanoh Y, Oda M, Nishito Y, Masai H. Rif1 regulates the replication timing domains on the human genome. EMBO J. 2012;31(18):3667-77.

48. Köhler C, Koalick D, Fabricius A, Parplys AC, Borgmann K, Pospiech H, et al. Cdc45 is limiting for replication initiation in humans. Cell Cycle. 2016;15(7):974-85.
49. Davé A, Cooley C, Garg M, Bianchi A. Protein phosphatase 1 recruitment by Rif1 regulates DNA replication origin firing by counteracting DDK activity. Cell Rep. 2014;7(1):53-61.
50. Burgers PMJ, Kunkel TA. Eukaryotic DNA Replication Fork. Annu Rev Biochem. 2017;86:417-38.
51. Fu YV, Yardimci H, Long DT, Ho TV, Guainazzi A, Bermudez VP, et al. Selective bypass of a lagging strand roadblock by the eukaryotic replicative DNA helicase. Cell. 2011;146(6):931-41.
52. Okazaki R, Okazaki T, Sakabe K, Sugimoto K, Sugino A. Mechanism of DNA chain growth. I. Possible discontinuity and unusual secondary structure of newly synthesized chains. Proc Natl Acad Sci U S A. 1968;59(2):598-605.
53. Baranovskiy AG, Babayeva ND, Zhang Y, Gu J, Suwa Y, Pavlov YI, et al. Mechanism of Concerted RNA-DNA Primer Synthesis by the Human Primosome. J Biol Chem. 2016;291(19):10006-20.
54. Clausen AR, Lujan SA, Burkholder AB, Orebaugh CD, Williams JS, Clausen MF, et al. Tracking replication enzymology in vivo by genome-wide mapping of ribonucleotide incorporation. Nat Struct Mol Biol. 2015;22(3):185-91.
55. Nick McElhinny SA, Gordenin DA, Stith CM, Burgers PM, Kunkel TA. Division of labor at the eukaryotic replication fork. Mol Cell. 2008;30(2):137-44.
56. Yeeles JTP, Janska A, Early A, Diffley JFX. How the Eukaryotic Replisome Achieves Rapid and Efficient DNA Replication. Mol Cell. 2017;65(1):105-16.
57. Bermudez VP, Farina A, Tappin I, Hurwitz J. Influence of the human cohesion establishment factor Ctf4/AND-1 on DNA replication. J Biol Chem. 2010;285(13):9493-505.
58. Gambus A, van Deursen F, Polychronopoulos D, Foltman M, Jones RC, Edmondson RD, et al. A key role for Ctf4 in coupling the MCM2-7 helicase to DNA polymerase alpha within the eukaryotic replisome. Embo j. 2009;28(19):2992-3004.

59. Hamdan SM, Loparo JJ, Takahashi M, Richardson CC, van Oijen AM. Dynamics of DNA replication loops reveal temporal control of lagging-strand synthesis. Nature. 2009;457(7227):336-9.
60. Leman AR, Noguchi C, Lee CY, Noguchi E. Human Timeless and Tipin stabilize replication forks and facilitate sister-chromatid cohesion. J Cell Sci. 2010;123(Pt 5):660-70.
61. Lewis JS, Spenkelink LM, Schauer GD, Hill FR, Georgescu RE, O'Donnell ME, et al. Single-molecule visualization of Saccharomyces cerevisiae leading-strand synthesis reveals dynamic interaction between MTC and the replisome. Proc Natl Acad Sci U S A. 2017;114(40):10630-5.
62. Petermann E, Helleday T, Caldecott KW. Claspin promotes normal replication fork rates in human cells. Mol Biol Cell. 2008;19(6):2373-8.
63. Xu X, Wang JT, Li M, Liu Y. TIMELESS Suppresses the Accumulation of Aberrant CDC45·MCM2-7·GINS Replicative Helicase Complexes on Human Chromatin. J Biol Chem. 2016;291(43):22544-58.
64. Balakrishnan L, Bambara RA. Okazaki fragment metabolism. Cold Spring Harb Perspect Biol. 2013;5(2).
65. Stodola JL, Burgers PM. Resolving individual steps of Okazaki-fragment maturation at a millisecond timescale. Nat Struct Mol Biol. 2016;23(5):402-8.
66. Garg P, Stith CM, Sabouri N, Johansson E, Burgers PM. Idling by DNA polymerase delta maintains a ligatable nick during lagging-strand DNA replication. Genes Dev. 2004;18(22):2764-73.
67. Dovrat D, Stodola JL, Burgers PM, Aharoni A. Sequential switching of binding partners on PCNA during in vitro Okazaki fragment maturation. Proc Natl Acad Sci U S A. 2014;111(39):14118-23.
68. Kang YH, Lee CH, Seo YS. Dna2 on the road to Okazaki fragment processing and genome stability in eukaryotes. Crit Rev Biochem Mol Biol. 2010;45(2):71-96.
69. Postow L, Crisona NJ, Peter BJ, Hardy CD, Cozzarelli NR. Topological challenges to DNA replication: conformations at the fork. Proc Natl Acad Sci U S A. 2001;98(15):8219-26.

70. Dewar JM, Walter JC. Mechanisms of DNA replication termination. Nat Rev Mol Cell Biol. 2017;18(8):507-16.
71. Dewar JM, Budzowska M, Walter JC. The mechanism of DNA replication termination in vertebrates. Nature. 2015;525(7569):345-50.
72. Moreno SP, Bailey R, Campion N, Herron S, Gambus A. Polyubiquitylation drives replisome disassembly at the termination of DNA replication. Science. 2014;346(6208):477-81.
73. Maric M, Maculins T, De Piccoli G, Labib K. Cdc48 and a ubiquitin ligase drive disassembly of the CMG helicase at the end of DNA replication. Science. 2014;346(6208):1253596.
74. Sonneville R, Moreno SP, Knebel A, Johnson C, Hastie CJ, Gartner A, et al. CUL-2(LRR-1) and UBXN-3 drive replisome disassembly during DNA replication termination and mitosis. Nat Cell Biol. 2017;19(5):468-79.
75. Dewar JM, Low E, Mann M, Räschle M, Walter JC. CRL2(Lrr1) promotes unloading of the vertebrate replisome from chromatin during replication termination. Genes Dev. 2017;31(3):275-90.
76. Sonneville R, Bhowmick R, Hoffmann S, Mailand N, Hickson ID, Labib K. TRAIP drives replisome disassembly and mitotic DNA repair synthesis at sites of incomplete DNA replication. Elife. 2019;8.
77. St Charles JA, Liberti SE, Williams JS, Lujan SA, Kunkel TA. Quantifying the contributions of base selectivity, proofreading and mismatch repair to nuclear DNA replication in Saccharomyces cerevisiae. DNA Repair (Amst). 2015;31:41-51.
78. Ganai RA, Johansson E. DNA Replication-A Matter of Fidelity. Mol Cell. 2016;62(5):745-55.
79. Batra VK, Beard WA, Pedersen LC, Wilson SH. Structures of DNA Polymerase Mispaired DNA Termini Transitioning to Pre-catalytic Complexes Support an Induced-Fit Fidelity Mechanism. Structure. 2016;24(11):1863-75.
80. Beard WA, Shock DD, Wilson SH. Influence of DNA structure on DNA polymerase beta active site function: extension of mutagenic DNA intermediates. J Biol Chem. 2004;279(30):31921-9.

81. Fortune JM, Pavlov YI, Welch CM, Johansson E, Burgers PM, Kunkel TA. Saccharomyces cerevisiae DNA polymerase delta: high fidelity for base substitutions but lower fidelity for single- and multi-base deletions. J Biol Chem. 2005;280(33):29980-7.
82. Reha-Krantz LJ. DNA polymerase proofreading: Multiple roles maintain genome stability. Biochim Biophys Acta. 2010;1804(5):1049-63.
83. Nick McElhinny SA, Watts BE, Kumar D, Watt DL, Lundström EB, Burgers PM, et al. Abundant ribonucleotide incorporation into DNA by yeast replicative polymerases. Proc Natl Acad Sci U S A. 2010;107(11):4949-54.
84. Joyce CM. Choosing the right sugar: how polymerases select a nucleotide substrate. Proc Natl Acad Sci U S A. 1997;94(5):1619-22.
85. Lazzaro F, Novarina D, Amara F, Watt DL, Stone JE, Costanzo V, et al. RNase H and postreplication repair protect cells from ribonucleotides incorporated in DNA. Mol Cell. 2012;45(1):99-110.
86. Vértessy BG, Tóth J. Keeping uracil out of DNA: physiological role, structure and catalytic mechanism of dUTPases. Acc Chem Res. 2009;42(1):97-106.
87. Greene BL, Kang G, Cui C, Bennati M, Nocera DG, Drennan CL, et al. Ribonucleotide Reductases: Structure, Chemistry, and Metabolism Suggest New Therapeutic Targets. Annu Rev Biochem. 2020;89:45-75.
88. Cotruvo JA, Stubbe J. Class I ribonucleotide reductases: metallocofactor assembly and repair in vitro and in vivo. Annu Rev Biochem. 2011;80:733-67.
89. Buckland RJ, Watt DL, Chittoor B, Nilsson AK, Kunkel TA, Chabes A. Increased and imbalanced dNTP pools symmetrically promote both leading and lagging strand replication infidelity. PLoS Genet. 2014;10(12):e1004846.
90. Kumar D, Abdulovic AL, Viberg J, Nilsson AK, Kunkel TA, Chabes A. Mechanisms of mutagenesis in vivo due to imbalanced dNTP pools. Nucleic Acids Res. 2011;39(4):1360-71.
91. Hofer A, Crona M, Logan DT, Sjöberg BM. DNA building blocks: keeping control of manufacture. Crit Rev Biochem Mol Biol. 2012;47(1):50-63.

92. Ando N, Li H, Brignole EJ, Thompson S, McLaughlin MI, Page JE, et al. Allosteric Inhibition of Human Ribonucleotide Reductase by dATP Entails the Stabilization of a Hexamer. Biochemistry. 2016;55(2):373-81.
93. Fairman JW, Wijerathna SR, Ahmad MF, Xu H, Nakano R, Jha S, et al. Structural basis for allosteric regulation of human ribonucleotide reductase by nucleotide-induced oligomerization. Nat Struct Mol Biol. 2011;18(3):316-22.
94. Chabes A, Georgieva B, Domkin V, Zhao X, Rothstein R, Thelander L. Survival of DNA damage in yeast directly depends on increased dNTP levels allowed by relaxed feedback inhibition of ribonucleotide reductase. Cell. 2003;112(3):391-401.
95. Reichard P, Eliasson R, Ingemarson R, Thelander L. Cross-talk between the allosteric effector-binding sites in mouse ribonucleotide reductase. J Biol Chem. 2000;275(42):33021-6.
96. Brignole EJ, Tsai KL, Chittuluru J, Li H, Aye Y, Penczek PA, et al. 3.3-Å resolution cryo-EM structure of human ribonucleotide reductase with substrate and allosteric regulators bound. Elife. 2018;7.
97. Zimanyi CM, Chen PY, Kang G, Funk MA, Drennan CL. Molecular basis for allosteric specificity regulation in class Ia ribonucleotide reductase from Escherichia coli. Elife. 2016;5:e07141.
98. Ahmad MF, Kaushal PS, Wan Q, Wijerathna SR, An X, Huang M, et al. Role of arginine 293 and glutamine 288 in communication between catalytic and allosteric sites in yeast ribonucleotide reductase. J Mol Biol. 2012;419(5):315-29.
99. Guarino E, Salguero I, Kearsey SE. Cellular regulation of ribonucleotide reductase in eukaryotes. Semin Cell Dev Biol. 2014;30:97-103.
100. Engström Y, Eriksson S, Jildevik I, Skog S, Thelander L, Tribukait B. Cell cycle-dependent expression of mammalian ribonucleotide reductase. Differential regulation of the two subunits. J Biol Chem. 1985;260(16):9114-6.
101. Chabes AL, Björklund S, Thelander L. S Phase-specific transcription of the mouse ribonucleotide reductase R2 gene requires both a proximal repressive E2F-binding site and an upstream promoter activating region. J Biol Chem. 2004;279(11):10796-807.

102. Chabes AL, Pfleger CM, Kirschner MW, Thelander L. Mouse ribonucleotide reductase R2 protein: a new target for anaphase-promoting complex-Cdh1-mediated proteolysis. Proc Natl Acad Sci U S A. 2003;100(7):3925-9.

103. D'Angiolella V, Donato V, Forrester FM, Jeong YT, Pellacani C, Kudo Y, et al. Cyclin F-mediated degradation of ribonucleotide reductase M2 controls genome integrity and DNA repair. Cell. 2012;149(5):1023-34.

104. Arnaoutov A, Dasso M. IRBIT is a novel regulator of ribonucleotide reductase in higher eukaryotes. Science. 2014;345(6203):1512-5.

105. Lee YD, Wang J, Stubbe J, Elledge SJ. Dif1 is a DNA-damage-regulated facilitator of nuclear import for ribonucleotide reductase. Mol Cell. 2008;32(1):70-80.

106. Perlstein DL, Ge J, Ortigosa AD, Robblee JH, Zhang Z, Huang M, et al. The active form of the Saccharomyces cerevisiae ribonucleotide reductase small subunit is a heterodimer in vitro and in vivo. Biochemistry. 2005;44(46):15366-77.

107. Zhang Z, Yang K, Chen CC, Feser J, Huang M. Role of the C terminus of the ribonucleotide reductase large subunit in enzyme regeneration and its inhibition by Sml1. Proc Natl Acad Sci U S A. 2007;104(7):2217-22.

108. Nestoras K, Mohammed AH, Schreurs AS, Fleck O, Watson AT, Poitelea M, et al. Regulation of ribonucleotide reductase by Spd1 involves multiple mechanisms. Genes Dev. 2010;24(11):1145-59.

109. Kunkel TA, Erie DA. Eukaryotic Mismatch Repair in Relation to DNA Replication. Annu Rev Genet. 2015;49:291-313.

110. Marsischky GT, Kolodner RD. Biochemical characterization of the interaction between the Saccharomyces cerevisiae MSH2-MSH6 complex and mispaired bases in DNA. J Biol Chem. 1999;274(38):26668-82.

111. Umar A, Risinger JI, Glaab WE, Tindall KR, Barrett JC, Kunkel TA. Functional overlap in mismatch repair by human MSH3 and MSH6. Genetics. 1998;148(4):1637-46.

112. Kadyrov FA, Dzantiev L, Constantin N, Modrich P. Endonucleolytic function of MutLalpha in human mismatch repair. Cell. 2006;126(2):297-308.

113. Pluciennik A, Dzantiev L, Iyer RR, Constantin N, Kadyrov FA, Modrich P. PCNA function in the activation and strand direction of MutLα endonuclease in mismatch repair. Proc Natl Acad Sci U S A. 2010;107(37):16066-71.
114. Pavlov YI, Mian IM, Kunkel TA. Evidence for preferential mismatch repair of lagging strand DNA replication errors in yeast. Curr Biol. 2003;13(9):744-8.
115. Andrianova MA, Bazykin GA, Nikolaev SI, Seplyarskiy VB. Human mismatch repair system balances mutation rates between strands by removing more mismatches from the lagging strand. Genome Res. 2017;27(8):1336-43.
116. Zeman MK, Cimprich KA. Causes and consequences of replication stress. Nat Cell Biol. 2014;16(1):2-9.
117. Kim H, D'Andrea AD. Regulation of DNA cross-link repair by the Fanconi anemia/BRCA pathway. Genes Dev. 2012;26(13):1393-408.
118. Marians KJ. Lesion Bypass and the Reactivation of Stalled Replication Forks. Annu Rev Biochem. 2018;87:217-38.
119. Mendoza O, Bourdoncle A, Boulé JB, Brosh RM, Jr., Mergny JL. G-quadruplexes and helicases. Nucleic Acids Res. 2016;44(5):1989-2006.
120. Iyer DR, Rhind N. The Intra-S Checkpoint Responses to DNA Damage. Genes (Basel). 2017;8(2).
121. Buisson R, Boisvert JL, Benes CH, Zou L. Distinct but Concerted Roles of ATR, DNA-PK, and Chk1 in Countering Replication Stress during S Phase. Mol Cell. 2015;59(6):1011-24.
122. Zhao H, Piwnica-Worms H. ATR-mediated checkpoint pathways regulate phosphorylation and activation of human Chk1. Mol Cell Biol. 2001;21(13):4129-39.
123. Bowman GD, O'Donnell M, Kuriyan J. Structural analysis of a eukaryotic sliding DNA clamp-clamp loader complex. Nature. 2004;429(6993):724-30.
124. Delacroix S, Wagner JM, Kobayashi M, Yamamoto K, Karnitz LM. The Rad9-Hus1-Rad1 (9-1-1) clamp activates checkpoint signaling via TopBP1. Genes Dev. 2007;21(12):1472-7.
125. Ellison V, Stillman B. Biochemical characterization of DNA damage checkpoint complexes: clamp loader and clamp complexes with specificity for 5' recessed DNA. PLoS Biol. 2003;1(2):E33.

126. Bermudez VP, Lindsey-Boltz LA, Cesare AJ, Maniwa Y, Griffith JD, Hurwitz J, et al. Loading of the human 9-1-1 checkpoint complex onto DNA by the checkpoint clamp loader hRad17-replication factor C complex in vitro. Proc Natl Acad Sci U S A. 2003;100(4):1633-8.

127. Zou L, Cortez D, Elledge SJ. Regulation of ATR substrate selection by Rad17-dependent loading of Rad9 complexes onto chromatin. Genes Dev. 2002;16(2):198-208.

128. Weiss RS, Matsuoka S, Elledge SJ, Leder P. Hus1 acts upstream of chk1 in a mammalian DNA damage response pathway. Curr Biol. 2002;12(1):73-7.

129. Sanchez Y, Wong C, Thoma RS, Richman R, Wu Z, Piwnica-Worms H, et al. Conservation of the Chk1 checkpoint pathway in mammals: linkage of DNA damage to Cdk regulation through Cdc25. Science. 1997;277(5331):1497-501.

130. Peng CY, Graves PR, Thoma RS, Wu Z, Shaw AS, Piwnica-Worms H. Mitotic and G2 checkpoint control: regulation of 14-3-3 protein binding by phosphorylation of Cdc25C on serine-216. Science. 1997;277(5331):1501-5.

131. Toledo LI, Altmeyer M, Rask MB, Lukas C, Larsen DH, Povlsen LK, et al. ATR prohibits replication catastrophe by preventing global exhaustion of RPA. Cell. 2013;155(5):1088-103.

132. Toledo L, Neelsen KJ, Lukas J. Replication Catastrophe: When a Checkpoint Fails because of Exhaustion. Mol Cell. 2017;66(6):735-49.

133. Hiraga SI, Ly T, Garzón J, Hořejší Z, Ohkubo YN, Endo A, et al. Human RIF1 and protein phosphatase 1 stimulate DNA replication origin licensing but suppress origin activation. EMBO Rep. 2017;18(3):403-19.

134. Moiseeva TN, Yin Y, Calderon MJ, Qian C, Schamus-Haynes S, Sugitani N, et al. An ATR and CHK1 kinase signaling mechanism that limits origin firing during unperturbed DNA replication. Proc Natl Acad Sci U S A. 2019;116(27):13374-83.

135. Courtot L, Hoffmann JS, Bergoglio V. The Protective Role of Dormant Origins in Response to Replicative Stress. Int J Mol Sci. 2018;19(11).

136. Kawabata T, Luebben SW, Yamaguchi S, Ilves I, Matise I, Buske T, et al. Stalled fork rescue via dormant replication origins in unchallenged S phase promotes proper chromosome segregation and tumor suppression. Mol Cell. 2011;41(5):543-53.

137. Bertoli C, Klier S, McGowan C, Wittenberg C, de Bruin RA. Chk1 inhibits E2F6 repressor function in response to replication stress to maintain cell-cycle transcription. Curr Biol. 2013;23(17):1629-37.

138. Herlihy AE, de Bruin RA. The Role of the Transcriptional Response to DNA Replication Stress. Genes (Basel). 2017;8(3).

139. Zhang YW, Jones TL, Martin SE, Caplen NJ, Pommier Y. Implication of checkpoint kinase-dependent up-regulation of ribonucleotide reductase R2 in DNA damage response. J Biol Chem. 2009;284(27):18085-95.

140. Andreson BL, Gupta A, Georgieva BP, Rothstein R. The ribonucleotide reductase inhibitor, Sml1, is sequentially phosphorylated, ubiquitylated and degraded in response to DNA damage. Nucleic Acids Res. 2010;38(19):6490-501.

141. Zhao X, Chabes A, Domkin V, Thelander L, Rothstein R. The ribonucleotide reductase inhibitor Sml1 is a new target of the Mec1/Rad53 kinase cascade during growth and in response to DNA damage. Embo j. 2001;20(13):3544-53.

142. De Piccoli G, Katou Y, Itoh T, Nakato R, Shirahige K, Labib K. Replisome stability at defective DNA replication forks is independent of S phase checkpoint kinases. Mol Cell. 2012;45(5):696-704.

143. Rickman K, Smogorzewska A. Advances in understanding DNA processing and protection at stalled replication forks. J Cell Biol. 2019;218(4):1096-107.

144. Ciccia A, Elledge SJ. The DNA damage response: making it safe to play with knives. Mol Cell. 2010;40(2):179-204.

145. Shen Z. Genomic instability and cancer: an introduction. J Mol Cell Biol. 2011;3(1):1-3.

146. Hartlerode AJ, Scully R. Mechanisms of double-strand break repair in somatic mammalian cells. Biochem J. 2009;423(2):157-68.

147. Symington LS, Gautier J. Double-strand break end resection and repair pathway choice. Annu Rev Genet. 2011;45:247-71.

148. Karanam K, Kafri R, Loewer A, Lahav G. Quantitative live cell imaging reveals a gradual shift between DNA repair mechanisms and a maximal use of HR in mid S phase. Mol Cell. 2012;47(2):320-9.

149. Yang G, Liu C, Chen SH, Kassab MA, Hoff JD, Walter NG, et al. Super-resolution imaging identifies PARP1 and the Ku complex acting as DNA double-strand break sensors. Nucleic Acids Res. 2018;46(7):3446-57.

150. Huang Y, Shao Q, Luo X, Yang D, Zeng B, Xiang T, et al. Poly(ADP-ribose) polymerase-1 promotes recruitment of meiotic recombination-11 to chromatin and DNA double-strand break repair in Ku70-deficient breast cancer cells. Faseb j. 2018:fj201800092R.

151. Paull TT. Mechanisms of ATM Activation. Annu Rev Biochem. 2015;84:711-38.

152. Hustedt N, Durocher D. The control of DNA repair by the cell cycle. Nat Cell Biol. 2016;19(1):1-9.

153. Mirman Z, Lottersberger F, Takai H, Kibe T, Gong Y, Takai K, et al. 53BP1-RIF1-shieldin counteracts DSB resection through CST- and Polα-dependent fill-in. Nature. 2018;560(7716):112-6.

154. Setiaputra D, Durocher D. Shieldin - the protector of DNA ends. EMBO Rep. 2019;20(5).

155. Sfeir A, Symington LS. Microhomology-Mediated End Joining: A Back-up Survival Mechanism or Dedicated Pathway? Trends Biochem Sci. 2015;40(11):701-14.

156. Huertas P, Jackson SP. Human CtIP mediates cell cycle control of DNA end resection and double strand break repair. J Biol Chem. 2009;284(14):9558-65.

157. Nimonkar AV, Genschel J, Kinoshita E, Polaczek P, Campbell JL, Wyman C, et al. BLM-DNA2-RPA-MRN and EXO1-BLM-RPA-MRN constitute two DNA end resection machineries for human DNA break repair. Genes Dev. 2011;25(4):350-62.

158. Orthwein A, Noordermeer SM, Wilson MD, Landry S, Enchev RI, Sherker A, et al. A mechanism for the suppression of homologous recombination in G1 cells. Nature. 2015;528(7582):422-6.

159. Jensen RB, Carreira A, Kowalczykowski SC. Purified human BRCA2 stimulates RAD51-mediated recombination. Nature. 2010;467(7316):678-83.

160. Wyatt HD, Sarbajna S, Matos J, West SC. Coordinated actions of SLX1-SLX4 and MUS81-EME1 for Holliday junction resolution in human cells. Mol Cell. 2013;52(2):234-47.
161. Bizard AH, Hickson ID. The dissolution of double Holliday junctions. Cold Spring Harb Perspect Biol. 2014;6(7):a016477.
162. Wohlbold L, Merrick KA, De S, Amat R, Kim JH, Larochelle S, et al. Chemical genetics reveals a specific requirement for Cdk2 activity in the DNA damage response and identifies Nbs1 as a Cdk2 substrate in human cells. PLoS Genet. 2012;8(8):e1002935.
163. Tomimatsu N, Mukherjee B, Catherine Hardebeck M, Ilcheva M, Vanessa Camacho C, Louise Harris J, et al. Phosphorylation of EXO1 by CDKs 1 and 2 regulates DNA end resection and repair pathway choice. Nat Commun. 2014;5:3561.
164. Tkáč J, Xu G, Adhikary H, Young JTF, Gallo D, Escribano-Díaz C, et al. HELB Is a Feedback Inhibitor of DNA End Resection. Mol Cell. 2016;61(3):405-18.
165. Bakkenist CJ, Kastan MB. DNA damage activates ATM through intermolecular autophosphorylation and dimer dissociation. Nature. 2003;421(6922):499-506.
166. Matsuoka S, Ballif BA, Smogorzewska A, McDonald ER, 3rd, Hurov KE, Luo J, et al. ATM and ATR substrate analysis reveals extensive protein networks responsive to DNA damage. Science. 2007;316(5828):1160-6.
167. Guo X, Ward MD, Tiedebohl JB, Oden YM, Nyalwidhe JO, Semmes OJ. Interdependent phosphorylation within the kinase domain T-loop Regulates CHK2 activity. J Biol Chem. 2010;285(43):33348-57.
168. Matsuoka S, Huang M, Elledge SJ. Linkage of ATM to cell cycle regulation by the Chk2 protein kinase. Science. 1998;282(5395):1893-7.
169. Lopez-Girona A, Furnari B, Mondesert O, Russell P. Nuclear localization of Cdc25 is regulated by DNA damage and a 14-3-3 protein. Nature. 1999;397(6715):172-5.
170. Bunz F, Dutriaux A, Lengauer C, Waldman T, Zhou S, Brown JP, et al. Requirement for p53 and p21 to sustain G2 arrest after DNA damage. Science. 1998;282(5393):1497-501.
171. Cheng Q, Chen J. Mechanism of p53 stabilization by ATM after DNA damage. Cell Cycle. 2010;9(3):472-8.

172. Banin S, Moyal L, Shieh S, Taya Y, Anderson CW, Chessa L, et al. Enhanced phosphorylation of p53 by ATM in response to DNA damage. Science. 1998;281(5383):1674-7.

173. Shieh SY, Ahn J, Tamai K, Taya Y, Prives C. The human homologs of checkpoint kinases Chk1 and Cds1 (Chk2) phosphorylate p53 at multiple DNA damage-inducible sites. Genes Dev. 2000;14(3):289-300.

174. Stad R, Little NA, Xirodimas DP, Frenk R, van der Eb AJ, Lane DP, et al. Mdmx stabilizes p53 and Mdm2 via two distinct mechanisms. EMBO Rep. 2001;2(11):1029-34.

175. Kubbutat MH, Jones SN, Vousden KH. Regulation of p53 stability by Mdm2. Nature. 1997;387(6630):299-303.

176. Jones SN, Roe AE, Donehower LA, Bradley A. Rescue of embryonic lethality in Mdm2-deficient mice by absence of p53. Nature. 1995;378(6553):206-8.

177. el-Deiry WS, Tokino T, Velculescu VE, Levy DB, Parsons R, Trent JM, et al. WAF1, a potential mediator of p53 tumor suppression. Cell. 1993;75(4):817-25.

178. Harper JW, Adami GR, Wei N, Keyomarsi K, Elledge SJ. The p21 Cdk-interacting protein Cip1 is a potent inhibitor of G1 cyclin-dependent kinases. Cell. 1993;75(4):805-16.

179. Harper JW, Elledge SJ, Keyomarsi K, Dynlacht B, Tsai LH, Zhang P, et al. Inhibition of cyclin-dependent kinases by p21. Mol Biol Cell. 1995;6(4):387-400.

180. Lu X, Nannenga B, Donehower LA. PPM1D dephosphorylates Chk1 and p53 and abrogates cell cycle checkpoints. Genes Dev. 2005;19(10):1162-74.

181. Leng RP, Lin Y, Ma W, Wu H, Lemmers B, Chung S, et al. Pirh2, a p53-induced ubiquitin-protein ligase, promotes p53 degradation. Cell. 2003;112(6):779-91.

182. Dornan D, Wertz I, Shimizu H, Arnott D, Frantz GD, Dowd P, et al. The ubiquitin ligase COP1 is a critical negative regulator of p53. Nature. 2004;429(6987):86-92.

183. Jain AK, Allton K, Duncan AD, Barton MC. TRIM24 is a p53-induced E3-ubiquitin ligase that undergoes ATM-mediated phosphorylation and autodegradation during DNA damage. Mol Cell Biol. 2014;34(14):2695-709.

184. Liu J, Zhang C, Wang XL, Ly P, Belyi V, Xu-Monette ZY, et al. E3 ubiquitin ligase TRIM32 negatively regulates tumor suppressor p53 to promote tumorigenesis. Cell Death Differ. 2014;21(11):1792-804.

185. Hafner A, Reyes J, Stewart-Ornstein J, Tsabar M, Jambhekar A, Lahav G. Quantifying the Central Dogma in the p53 Pathway in Live Single Cells. Cell Syst. 2020;10(6):495-505.e4.
186. Tsabar M, Mock CS, Venkatachalam V, Reyes J, Karhohs KW, Oliver TG, et al. A Switch in p53 Dynamics Marks Cells That Escape from DSB-Induced Cell Cycle Arrest. Cell Rep. 2020;32(5):107995.
187. Porter JR, Fisher BE, Batchelor E. p53 Pulses Diversify Target Gene Expression Dynamics in an mRNA Half-Life-Dependent Manner and Delineate Co-regulated Target Gene Subnetworks. Cell Syst. 2016;2(4):272-82.
188. Lue NF. Evolving Linear Chromosomes and Telomeres: A C-Strand-Centric View. Trends Biochem Sci. 2018;43(5):314-26.
189. Nguyen THD, Tam J, Wu RA, Greber BJ, Toso D, Nogales E, et al. Cryo-EM structure of substrate-bound human telomerase holoenzyme. Nature. 2018;557(7704):190-5.
190. Doksani Y, Wu JY, de Lange T, Zhuang X. Super-resolution fluorescence imaging of telomeres reveals TRF2-dependent T-loop formation. Cell. 2013;155(2):345-56.
191. de Lange T. Shelterin-Mediated Telomere Protection. Annu Rev Genet. 2018;52:223-47.
192. Lim CJ, Zaug AJ, Kim HJ, Cech TR. Reconstitution of human shelterin complexes reveals unexpected stoichiometry and dual pathways to enhance telomerase processivity. Nat Commun. 2017;8(1):1075.
193. Vannier JB, Pavicic-Kaltenbrunner V, Petalcorin MI, Ding H, Boulton SJ. RTEL1 dismantles T loops and counteracts telomeric G4-DNA to maintain telomere integrity. Cell. 2012;149(4):795-806.
194. Sarek G, Kotsantis P, Ruis P, Van Ly D, Margalef P, Borel V, et al. CDK phosphorylation of TRF2 controls t-loop dynamics during the cell cycle. Nature. 2019;575(7783):523-7.
195. Arnoult N, Karlseder J. Complex interactions between the DNA-damage response and mammalian telomeres. Nat Struct Mol Biol. 2015;22(11):859-66.
196. Sfeir A, de Lange T. Removal of shelterin reveals the telomere end-protection problem. Science. 2012;336(6081):593-7.

197. Allsopp RC, Vaziri H, Patterson C, Goldstein S, Younglai EV, Futcher AB, et al. Telomere length predicts replicative capacity of human fibroblasts. Proc Natl Acad Sci U S A. 1992;89(21):10114-8.

198. Counter CM, Avilion AA, LeFeuvre CE, Stewart NG, Greider CW, Harley CB, et al. Telomere shortening associated with chromosome instability is arrested in immortal cells which express telomerase activity. EMBO J. 1992;11(5):1921-9.

199. Baird DM, Rowson J, Wynford-Thomas D, Kipling D. Extensive allelic variation and ultrashort telomeres in senescent human cells. Nat Genet. 2003;33(2):203-7.

200. Herbig U, Jobling WA, Chen BP, Chen DJ, Sedivy JM. Telomere shortening triggers senescence of human cells through a pathway involving ATM, p53, and p21(CIP1), but not p16(INK4a). Mol Cell. 2004;14(4):501-13.

201. Fumagalli M, Rossiello F, Clerici M, Barozzi S, Cittaro D, Kaplunov JM, et al. Telomeric DNA damage is irreparable and causes persistent DNA-damage-response activation. Nat Cell Biol. 2012;14(4):355-65.

202. d'Adda di Fagagna F, Reaper PM, Clay-Farrace L, Fiegler H, Carr P, Von Zglinicki T, et al. A DNA damage checkpoint response in telomere-initiated senescence. Nature. 2003;426(6963):194-8.

203. Rodier F, Campisi J. Four faces of cellular senescence. J Cell Biol. 2011;192(4):547-56.

204. Hayflick L. The Limited in Vitro Lifetime of Human Diploid Cell Strains. Exp Cell Res. 1965;37:614-36.

205. Choudhury AR, Ju Z, Djojosubroto MW, Schienke A, Lechel A, Schaetzlein S, et al. Cdkn1a deletion improves stem cell function and lifespan of mice with dysfunctional telomeres without accelerating cancer formation. Nat Genet. 2007;39(1):99-105.

206. Muñoz-Lorente MA, Cano-Martin AC, Blasco MA. Mice with hyper-long telomeres show less metabolic aging and longer lifespans. Nat Commun. 2019;10(1):4723.

207. Tomás-Loba A, Flores I, Fernández-Marcos PJ, Cayuela ML, Maraver A, Tejera A, et al. Telomerase reverse transcriptase delays aging in cancer-resistant mice. Cell. 2008;135(4):609-22.

208. Shay JW, Pereira-Smith OM, Wright WE. A role for both RB and p53 in the regulation of human cellular senescence. Exp Cell Res. 1991;196(1):33-9.
209. Nassour J, Radford R, Correia A, Fusté JM, Schoell B, Jauch A, et al. Autophagic cell death restricts chromosomal instability during replicative crisis. Nature. 2019;565(7741):659-63.
210. Hayashi MT, Cesare AJ, Rivera T, Karlseder J. Cell death during crisis is mediated by mitotic telomere deprotection. Nature. 2015;522(7557):492-6.
211. Roake CM, Artandi SE. Regulation of human telomerase in homeostasis and disease. Nat Rev Mol Cell Biol. 2020;21(7):384-97.
212. Schmidt JC, Cech TR. Human telomerase: biogenesis, trafficking, recruitment, and activation. Genes Dev. 2015;29(11):1095-105.
213. Patrick EM, Slivka JD, Payne B, Comstock MJ, Schmidt JC. Observation of processive telomerase catalysis using high-resolution optical tweezers. Nat Chem Biol. 2020;16(7):801-9.
214. Wang F, Podell ER, Zaug AJ, Yang Y, Baciu P, Cech TR, et al. The POT1-TPP1 telomere complex is a telomerase processivity factor. Nature. 2007;445(7127):506-10.
215. Xi L, Cech TR. Inventory of telomerase components in human cells reveals multiple subpopulations of hTR and hTERT. Nucleic Acids Res. 2014;42(13):8565-77.
216. Tong AS, Stern JL, Sfeir A, Kartawinata M, de Lange T, Zhu XD, et al. ATM and ATR Signaling Regulate the Recruitment of Human Telomerase to Telomeres. Cell Rep. 2015;13(8):1633-46.
217. Nandakumar J, Bell CF, Weidenfeld I, Zaug AJ, Leinwand LA, Cech TR. The TEL patch of telomere protein TPP1 mediates telomerase recruitment and processivity. Nature. 2012;492(7428):285-9.
218. Schmidt JC, Dalby AB, Cech TR. Identification of human TERT elements necessary for telomerase recruitment to telomeres. Elife. 2014;3.
219. Laprade H, Querido E, Smith MJ, Guérit D, Crimmins H, Conomos D, et al. Single-Molecule Imaging of Telomerase RNA Reveals a Recruitment-Retention Model for Telomere Elongation. Mol Cell. 2020;79(1):115-26.e6.

220. Zhao Y, Sfeir AJ, Zou Y, Buseman CM, Chow TT, Shay JW, et al. Telomere extension occurs at most chromosome ends and is uncoupled from fill-in in human cancer cells. Cell. 2009;138(3):463-75.

221. Kim NW, Piatyszek MA, Prowse KR, Harley CB, West MD, Ho PL, et al. Specific association of human telomerase activity with immortal cells and cancer. Science. 1994;266(5193):2011-5.

222. Lorbeer FK, Hockemeyer D. TERT promoter mutations and telomeres during tumorigenesis. Curr Opin Genet Dev. 2020;60:56-62.

223. Stern JL, Theodorescu D, Vogelstein B, Papadopoulos N, Cech TR. Mutation of the TERT promoter, switch to active chromatin, and monoallelic TERT expression in multiple cancers. Genes Dev. 2015;29(21):2219-24.

224. Sobinoff AP, Pickett HA. Alternative Lengthening of Telomeres: DNA Repair Pathways Converge. Trends Genet. 2017;33(12):921-32.

225. Lu R, O'Rourke JJ, Sobinoff AP, Allen JAM, Nelson CB, Tomlinson CG, et al. The FANCM-BLM-TOP3A-RMI complex suppresses alternative lengthening of telomeres (ALT). Nat Commun. 2019;10(1):2252.

226. Silva B, Pentz R, Figueira AM, Arora R, Lee YW, Hodson C, et al. FANCM limits ALT activity by restricting telomeric replication stress induced by deregulated BLM and R-loops. Nat Commun. 2019;10(1):2253.

227. Dilley RL, Verma P, Cho NW, Winters HD, Wondisford AR, Greenberg RA. Break-induced telomere synthesis underlies alternative telomere maintenance. Nature. 2016;539(7627):54-8.

228. Viceconte N, Dheur MS, Majerova E, Pierreux CE, Baurain JF, van Baren N, et al. Highly Aggressive Metastatic Melanoma Cells Unable to Maintain Telomere Length. Cell Rep. 2017;19(12):2529-43.

229. Dagg RA, Pickett HA, Neumann AA, Napier CE, Henson JD, Teber ET, et al. Extensive Proliferation of Human Cancer Cells with Ever-Shorter Telomeres. Cell Rep. 2017;19(12):2544-56.

230. Taboski MA, Sealey DC, Dorrens J, Tayade C, Betts DH, Harrington L. Long telomeres bypass the requirement for telomere maintenance in human tumorigenesis. Cell Rep. 2012;1(2):91-8.

231. Pascolo E, Wenz C, Lingner J, Hauel N, Priepke H, Kauffmann I, et al. Mechanism of human telomerase inhibition by BIBR1532, a synthetic, non-nucleosidic drug candidate. J Biol Chem. 2002;277(18):15566-72.

232. Damm K, Hemmann U, Garin-Chesa P, Hauel N, Kauffmann I, Priepke H, et al. A highly selective telomerase inhibitor limiting human cancer cell proliferation. EMBO J. 2001;20(24):6958-68.

233. Zanetti M. A second chance for telomerase reverse transcriptase in anticancer immunotherapy. Nat Rev Clin Oncol. 2017;14(2):115-28.

234. Hu J, Hwang SS, Liesa M, Gan B, Sahin E, Jaskelioff M, et al. Antitelomerase therapy provokes ALT and mitochondrial adaptive mechanisms in cancer. Cell. 2012;148(4):651-63.

235. Chin L, Artandi SE, Shen Q, Tam A, Lee SL, Gottlieb GJ, et al. p53 deficiency rescues the adverse effects of telomere loss and cooperates with telomere dysfunction to accelerate carcinogenesis. Cell. 1999;97(4):527-38.

236. Maciejowski J, Chatzipli A, Dananberg A, Chu K, Toufektchan E, Klimczak LJ, et al. APOBEC3-dependent kataegis and TREX1-driven chromothripsis during telomere crisis. Nat Genet. 2020.

237. Maciejowski J, Li Y, Bosco N, Campbell PJ, de Lange T. Chromothripsis and Kataegis Induced by Telomere Crisis. Cell. 2015;163(7):1641-54.

238. Umbreit NT, Zhang CZ, Lynch LD, Blaine LJ, Cheng AM, Tourdot R, et al. Mechanisms generating cancer genome complexity from a single cell division error. Science. 2020;368(6488).

239. Kuzmin E, VanderSluis B, Wang W, Tan G, Deshpande R, Chen Y, et al. Systematic analysis of complex genetic interactions. Science. 2018;360(6386).

240. Costanzo M, VanderSluis B, Koch EN, Baryshnikova A, Pons C, Tan G, et al. A global genetic interaction network maps a wiring diagram of cellular function. Science. 2016;353(6306).

241. Jiang F, Doudna JA. CRISPR-Cas9 Structures and Mechanisms. Annu Rev Biophys. 2017;46:505-29.

242. Brouns SJ, Jore MM, Lundgren M, Westra ER, Slijkhuis RJ, Snijders AP, et al. Small CRISPR RNAs guide antiviral defense in prokaryotes. Science. 2008;321(5891):960-4.

243. Garneau JE, Dupuis M, Villion M, Romero DA, Barrangou R, Boyaval P, et al. The CRISPR/Cas bacterial immune system cleaves bacteriophage and plasmid DNA. Nature. 2010;468(7320):67-71.

244. Jinek M, Chylinski K, Fonfara I, Hauer M, Doudna JA, Charpentier E. A programmable dual-RNA-guided DNA endonuclease in adaptive bacterial immunity. Science. 2012;337(6096):816-21.

245. Cong L, Ran FA, Cox D, Lin S, Barretto R, Habib N, et al. Multiplex genome engineering using CRISPR/Cas systems. Science. 2013;339(6121):819-23.

246. Mali P, Yang L, Esvelt KM, Aach J, Guell M, DiCarlo JE, et al. RNA-guided human genome engineering via Cas9. Science. 2013;339(6121):823-6.

247. Doench JG, Fusi N, Sullender M, Hegde M, Vaimberg EW, Donovan KF, et al. Optimized sgRNA design to maximize activity and minimize off-target effects of CRISPR-Cas9. Nat Biotechnol. 2016;34(2):184-91.

248. Liu M, Rehman S, Tang X, Gu K, Fan Q, Chen D, et al. Methodologies for Improving HDR Efficiency. Front Genet. 2018;9:691.

249. van Overbeek M, Capurso D, Carter MM, Thompson MS, Frias E, Russ C, et al. DNA Repair Profiling Reveals Nonrandom Outcomes at Cas9-Mediated Breaks. Mol Cell. 2016;63(4):633-46.

250. Allen F, Crepaldi L, Alsinet C, Strong AJ, Kleshchevnikov V, De Angeli P, et al. Predicting the mutations generated by repair of Cas9-induced double-strand breaks. Nat Biotechnol. 2018.

251. Brinkman EK, Chen T, de Haas M, Holland HA, Akhtar W, van Steensel B. Kinetics and Fidelity of the Repair of Cas9-Induced Double-Strand DNA Breaks. Mol Cell. 2018;70(5):801-13.e6.

252. Chakrabarti AM, Henser-Brownhill T, Monserrat J, Poetsch AR, Luscombe NM, Scaffidi P. Target-Specific Precision of CRISPR-Mediated Genome Editing. Mol Cell. 2019;73(4):699-713.e6.

253. Chen W, McKenna A, Schreiber J, Haeussler M, Yin Y, Agarwal V, et al. Massively parallel profiling and predictive modeling of the outcomes of CRISPR/Cas9-mediated double-strand break repair. Nucleic Acids Res. 2019;47(15):7989-8003.

254. Elbashir SM, Harborth J, Lendeckel W, Yalcin A, Weber K, Tuschl T. Duplexes of 21-nucleotide RNAs mediate RNA interference in cultured mammalian cells. Nature. 2001;411(6836):494-8.

255. Wilson RC, Doudna JA. Molecular mechanisms of RNA interference. Annu Rev Biophys. 2013;42:217-39.

256. Khan AA, Betel D, Miller ML, Sander C, Leslie CS, Marks DS. Transfection of small RNAs globally perturbs gene regulation by endogenous microRNAs. Nat Biotechnol. 2009;27(6):549-55.

257. Kuscu C, Arslan S, Singh R, Thorpe J, Adli M. Genome-wide analysis reveals characteristics of off-target sites bound by the Cas9 endonuclease. Nat Biotechnol. 2014;32(7):677-83.

258. Aguirre AJ, Meyers RM, Weir BA, Vazquez F, Zhang CZ, Ben-David U, et al. Genomic Copy Number Dictates a Gene-Independent Cell Response to CRISPR/Cas9 Targeting. Cancer Discov. 2016;6(8):914-29.

259. Smith I, Greenside PG, Natoli T, Lahr DL, Wadden D, Tirosh I, et al. Evaluation of RNAi and CRISPR technologies by large-scale gene expression profiling in the Connectivity Map. PLoS Biol. 2017;15(11):e2003213.

260. Jackson AL, Burchard J, Schelter J, Chau BN, Cleary M, Lim L, et al. Widespread siRNA "off-target" transcript silencing mediated by seed region sequence complementarity. Rna. 2006;12(7):1179-87.

261. de Groot R, Lüthi J, Lindsay H, Holtackers R, Pelkmans L. Large-scale image-based profiling of single-cell phenotypes in arrayed CRISPR-Cas9 gene perturbation screens. Mol Syst Biol. 2018;14(1):e8064.

262. Shalem O, Sanjana NE, Hartenian E, Shi X, Scott DA, Mikkelson T, et al. Genome-scale CRISPR-Cas9 knockout screening in human cells. Science. 2014;343(6166):84-7.

263. Wang T, Wei JJ, Sabatini DM, Lander ES. Genetic screens in human cells using the CRISPR-Cas9 system. Science. 2014;343(6166):80-4.

264. Bertomeu T, Coulombe-Huntington J, Chatr-Aryamontri A, Bourdages KG, Coyaud E, Raught B, et al. A High-Resolution Genome-Wide CRISPR/Cas9 Viability Screen Reveals Structural Features and Contextual Diversity of the Human Cell-Essential Proteome. Mol Cell Biol. 2017;38(1).

265. Wang T, Birsoy K, Hughes NW, Krupczak KM, Post Y, Wei JJ, et al. Identification and characterization of essential genes in the human genome. Science. 2015;350(6264):1096-101.

266. Hart T, Chandrashekhar M, Aregger M, Steinhart Z, Brown KR, MacLeod G, et al. High-Resolution CRISPR Screens Reveal Fitness Genes and Genotype-Specific Cancer Liabilities. Cell. 2015;163(6):1515-26.

267. Munoz DM, Cassiani PJ, Li L, Billy E, Korn JM, Jones MD, et al. CRISPR Screens Provide a Comprehensive Assessment of Cancer Vulnerabilities but Generate False-Positive Hits for Highly Amplified Genomic Regions. Cancer Discov. 2016;6(8):900-13.

268. Meyers RM, Bryan JG, McFarland JM, Weir BA, Sizemore AE, Xu H, et al. Computational correction of copy number effect improves specificity of CRISPR-Cas9 essentiality screens in cancer cells. Nat Genet. 2017;49(12):1779-84.

269. Ghandi M, Huang FW, Jané-Valbuena J, Kryukov GV, Lo CC, McDonald ER, 3rd, et al. Next-generation characterization of the Cancer Cell Line Encyclopedia. Nature. 2019;569(7757):503-8.

270. Larson MH, Gilbert LA, Wang X, Lim WA, Weissman JS, Qi LS. CRISPR interference (CRISPRi) for sequence-specific control of gene expression. Nat Protoc. 2013;8(11):2180-96.

271. Gilbert LA, Horlbeck MA, Adamson B, Villalta JE, Chen Y, Whitehead EH, et al. Genome-Scale CRISPR-Mediated Control of Gene Repression and Activation. Cell. 2014;159(3):647-61.

272. Chavez A, Scheiman J, Vora S, Pruitt BW, Tuttle M, E PRI, et al. Highly efficient Cas9-mediated transcriptional programming. Nat Methods. 2015;12(4):326-8.

273. Konermann S, Brigham MD, Trevino AE, Joung J, Abudayyeh OO, Barcena C, et al. Genome-scale transcriptional activation by an engineered CRISPR-Cas9 complex. Nature. 2015;517(7536):583-8.

274. Horlbeck MA, Gilbert LA, Villalta JE, Adamson B, Pak RA, Chen Y, et al. Compact and highly active next-generation libraries for CRISPR-mediated gene repression and activation. Elife. 2016;5.

275. Liu SJ, Horlbeck MA, Cho SW, Birk HS, Malatesta M, He D, et al. CRISPRi-based genome-scale identification of functional long noncoding RNA loci in human cells. Science. 2017;355(6320).

276. Sharma S, Petsalaki E. Application of CRISPR-Cas9 Based Genome-Wide Screening Approaches to Study Cellular Signalling Mechanisms. Int J Mol Sci. 2018;19(4).

277. Parnas O, Jovanovic M, Eisenhaure TM, Herbst RH, Dixit A, Ye CJ, et al. A Genome-wide CRISPR Screen in Primary Immune Cells to Dissect Regulatory Networks. Cell. 2015;162(3):675-86.

278. Costanzo M, Kuzmin E, van Leeuwen J, Mair B, Moffat J, Boone C, et al. Global Genetic Networks and the Genotype-to-Phenotype Relationship. Cell. 2019;177(1):85-100.

279. Gonatopoulos-Pournatzis T, Aregger M, Brown KR, Farhangmehr S, Braunschweig U, Ward HN, et al. Genetic interaction mapping and exon-resolution functional genomics with a hybrid Cas9-Cas12a platform. Nat Biotechnol. 2020;38(5):638-48.

280. Shen JP, Zhao D, Sasik R, Luebeck J, Birmingham A, Bojorquez-Gomez A, et al. Combinatorial CRISPR-Cas9 screens for de novo mapping of genetic interactions. Nat Methods. 2017;14(6):573-6.

281. Hegde M, Strand C, Hanna RE, Doench JG. Uncoupling of sgRNAs from their associated barcodes during PCR amplification of combinatorial CRISPR screens. PLoS One. 2018;13(5):e0197547.

282. Han K, Jeng EE, Hess GT, Morgens DW, Li A, Bassik MC. Synergistic drug combinations for cancer identified in a CRISPR screen for pairwise genetic interactions. Nat Biotechnol. 2017;35(5):463-74.

283. Najm FJ, Strand C, Donovan KF, Hegde M, Sanson KR, Vaimberg EW, et al. Orthologous CRISPR-Cas9 enzymes for combinatorial genetic screens. Nat Biotechnol. 2018;36(2):179-89.

284. DeWeirdt PC, Sangree AK, Hanna RE, Sanson KR, Hegde M, Strand C, et al. Genetic screens in isogenic mammalian cell lines without single cell cloning. Nat Commun. 2020;11(1):752.

285. Zetsche B, Heidenreich M, Mohanraju P, Fedorova I, Kneppers J, DeGennaro EM, et al. Multiplex gene editing by CRISPR-Cpf1 using a single crRNA array. Nat Biotechnol. 2017;35(1):31-4.

286. Gier RA, Budinich KA, Evitt NH, Cao Z, Freilich ES, Chen Q, et al. High-performance CRISPR-Cas12a genome editing for combinatorial genetic screening. Nat Commun. 2020;11(1):3455.

287. Horlbeck MA, Xu A, Wang M, Bennett NK, Park CY, Bogdanoff D, et al. Mapping the Genetic Landscape of Human Cells. Cell. 2018;174(4):953-67.e22.

288. Boettcher M, Tian R, Blau JA, Markegard E, Wagner RT, Wu D, et al. Dual gene activation and knockout screen reveals directional dependencies in genetic networks. Nat Biotechnol. 2018;36(2):170-8.

289. Hartwell LH, Szankasi P, Roberts CJ, Murray AW, Friend SH. Integrating genetic approaches into the discovery of anticancer drugs. Science. 1997;278(5340):1064-8.

290. Hillenmeyer ME, Fung E, Wildenhain J, Pierce SE, Hoon S, Lee W, et al. The chemical genomic portrait of yeast: uncovering a phenotype for all genes. Science. 2008;320(5874):362-5.

291. Guénolé A, Srivas R, Vreeken K, Wang ZZ, Wang S, Krogan NJ, et al. Dissection of DNA damage responses using multiconditional genetic interaction maps. Mol Cell. 2013;49(2):346-58.

292. Lee AY, St Onge RP, Proctor MJ, Wallace IM, Nile AH, Spagnuolo PA, et al. Mapping the cellular response to small molecules using chemogenomic fitness signatures. Science. 2014;344(6180):208-11.

293. Keiser MJ, Setola V, Irwin JJ, Laggner C, Abbas AI, Hufeisen SJ, et al. Predicting new molecular targets for known drugs. Nature. 2009;462(7270):175-81.

294. Mair B, Moffat J, Boone C, Andrews BJ. Genetic interaction networks in cancer cells. Curr Opin Genet Dev. 2019;54:64-72.

295. Steinhart Z, Pavlovic Z, Chandrashekhar M, Hart T, Wang X, Zhang X, et al. Genome-wide CRISPR screens reveal a Wnt-FZD5 signaling circuit as a druggable vulnerability of RNF43-mutant pancreatic tumors. Nat Med. 2017;23(1):60-8.

296. Huang A, Garraway LA, Ashworth A, Weber B. Synthetic lethality as an engine for cancer drug target discovery. Nat Rev Drug Discov. 2020;19(1):23-38.

297. Bryant HE, Schultz N, Thomas HD, Parker KM, Flower D, Lopez E, et al. Specific killing of BRCA2-deficient tumours with inhibitors of poly(ADP-ribose) polymerase. Nature. 2005;434(7035):913-7.

298. Lord CJ, Ashworth A. PARP inhibitors: Synthetic lethality in the clinic. Science. 2017;355(6330):1152-8.

299. Behan FM, Iorio F, Picco G, Gonçalves E, Beaver CM, Migliardi G, et al. Prioritization of cancer therapeutic targets using CRISPR-Cas9 screens. Nature. 2019;568(7753):511-6.

300. Jost M, Chen Y, Gilbert LA, Horlbeck MA, Krenning L, Menchon G, et al. Combined CRISPRi/a-Based Chemical Genetic Screens Reveal that Rigosertib Is a Microtubule-Destabilizing Agent. Mol Cell. 2017;68(1):210-23.e6.

301. Ho CH, Piotrowski J, Dixon SJ, Baryshnikova A, Costanzo M, Boone C. Combining functional genomics and chemical biology to identify targets of bioactive compounds. Curr Opin Chem Biol. 2011;15(1):66-78.

302. Bouwman P, Jonkers J. The effects of deregulated DNA damage signalling on cancer chemotherapy response and resistance. Nat Rev Cancer. 2012;12(9):587-98.

303. Zimmermann M, Murina O, Reijns MAM, Agathanggelou A, Challis R, Tarnauskaitė Ž, et al. CRISPR screens identify genomic ribonucleotides as a source of PARP-trapping lesions. Nature. 2018;559(7713):285-9.

304. Wang C, Wang G, Feng X, Shepherd P, Zhang J, Tang M, et al. Genome-wide CRISPR screens reveal synthetic lethality of RNASEH2 deficiency and ATR inhibition. Oncogene. 2019;38(14):2451-63.

305. MacLeod G, Bozek DA, Rajakulendran N, Monteiro V, Ahmadi M, Steinhart Z, et al. Genome-Wide CRISPR-Cas9 Screens Expose Genetic Vulnerabilities and Mechanisms of Temozolomide Sensitivity in Glioblastoma Stem Cells. Cell Rep. 2019;27(3):971-86.e9.

306. Olivieri M, Cho T, Álvarez-Quilón A, Li K, Schellenberg MJ, Zimmermann M, et al. A Genetic Map of the Response to DNA Damage in Human Cells. Cell. 2020;182(2):481-96.e21.

307. Álvarez-Quilón A, Wojtaszek JL, Mathieu MC, Patel T, Appel CD, Hustedt N, et al. Endogenous DNA 3' Blocks Are Vulnerabilities for BRCA1 and BRCA2 Deficiency and Are Reversed by the APE2 Nuclease. Mol Cell. 2020;78(6):1152-65.e8.

308. Hustedt N, Saito Y, Zimmermann M, Álvarez-Quilón A, Setiaputra D, Adam S, et al. Control of homologous recombination by the HROB-MCM8-MCM9 pathway. Genes Dev. 2019;33(19-20):1397-415.

309. Hustedt N, Alvarez-Quilon A, McEwan A, Yuan JY, Cho T, Koob L, et al. A consensus set of genetic vulnerabilities to ATR inhibition. Open Biol. 2019;9(9):190156.

310. Jang M, Cai L, Udeani GO, Slowing KV, Thomas CF, Beecher CW, et al. Cancer chemopreventive activity of resveratrol, a natural product derived from grapes. Science. 1997;275(5297):218-20.

311. Howitz KT, Bitterman KJ, Cohen HY, Lamming DW, Lavu S, Wood JG, et al. Small molecule activators of sirtuins extend Saccharomyces cerevisiae lifespan. Nature. 2003;425(6954):191-6.

312. Baur JA, Pearson KJ, Price NL, Jamieson HA, Lerin C, Kalra A, et al. Resveratrol improves health and survival of mice on a high-calorie diet. Nature. 2006;444(7117):337-42.

313. Pearson KJ, Baur JA, Lewis KN, Peshkin L, Price NL, Labinskyy N, et al. Resveratrol delays age-related deterioration and mimics transcriptional aspects of dietary restriction without extending life span. Cell Metab. 2008;8(2):157-68.

314. Singh AP, Singh R, Verma SS, Rai V, Kaschula CH, Maiti P, et al. Health benefits of resveratrol: Evidence from clinical studies. Med Res Rev. 2019;39(5):1851-91.

315. Kulkarni SS, Canto C. The molecular targets of resveratrol. Biochim Biophys Acta. 2015;1852(6):1114-23.

316. Houtkooper RH, Cantó C, Wanders RJ, Auwerx J. The secret life of NAD+: an old metabolite controlling new metabolic signaling pathways. Endocr Rev. 2010;31(2):194-223.

317. Hardie DG, Ross FA, Hawley SA. AMPK: a nutrient and energy sensor that maintains energy homeostasis. Nat Rev Mol Cell Biol. 2012;13(4):251-62.

318. Lagouge M, Argmann C, Gerhart-Hines Z, Meziane H, Lerin C, Daussin F, et al. Resveratrol improves mitochondrial function and protects against metabolic disease by activating SIRT1 and PGC-1alpha. Cell. 2006;127(6):1109-22.

319. Um JH, Park SJ, Kang H, Yang S, Foretz M, McBurney MW, et al. AMP-activated protein kinase-deficient mice are resistant to the metabolic effects of resveratrol. Diabetes. 2010;59(3):554-63.

320. Price NL, Gomes AP, Ling AJ, Duarte FV, Martin-Montalvo A, North BJ, et al. SIRT1 is required for AMPK activation and the beneficial effects of resveratrol on mitochondrial function. Cell Metab. 2012;15(5):675-90.

321. Hawley SA, Ross FA, Chevtzoff C, Green KA, Evans A, Fogarty S, et al. Use of cells expressing gamma subunit variants to identify diverse mechanisms of AMPK activation. Cell Metab. 2010;11(6):554-65.

322. Cantó C, Gerhart-Hines Z, Feige JN, Lagouge M, Noriega L, Milne JC, et al. AMPK regulates energy expenditure by modulating NAD+ metabolism and SIRT1 activity. Nature. 2009;458(7241):1056-60.

323. Cantó C, Jiang LQ, Deshmukh AS, Mataki C, Coste A, Lagouge M, et al. Interdependence of AMPK and SIRT1 for metabolic adaptation to fasting and exercise in skeletal muscle. Cell Metab. 2010;11(3):213-9.

324. Li YR, Li S, Lin CC. Effect of resveratrol and pterostilbene on aging and longevity. Biofactors. 2018;44(1):69-82.
325. Kim EC, Kim JR. Senotherapeutics: emerging strategy for healthy aging and age-related disease. BMB Rep. 2019;52(1):47-55.
326. Pezzuto JM. Resveratrol: Twenty Years of Growth, Development and Controversy. Biomol Ther (Seoul). 2019;27(1):1-14.
327. Wood JG, Rogina B, Lavu S, Howitz K, Helfand SL, Tatar M, et al. Sirtuin activators mimic caloric restriction and delay ageing in metazoans. Nature. 2004;430(7000):686-9.
328. Lee SH, Lee JH, Lee HY, Min KJ. Sirtuin signaling in cellular senescence and aging. BMB Rep. 2019;52(1):24-34.
329. Dang W. The controversial world of sirtuins. Drug Discov Today Technol. 2014;12:e9-e17.
330. Pacholec M, Bleasdale JE, Chrunyk B, Cunningham D, Flynn D, Garofalo RS, et al. SRT1720, SRT2183, SRT1460, and resveratrol are not direct activators of SIRT1. J Biol Chem. 2010;285(11):8340-51.
331. Hubbard BP, Gomes AP, Dai H, Li J, Case AW, Considine T, et al. Evidence for a common mechanism of SIRT1 regulation by allosteric activators. Science. 2013;339(6124):1216-9.
332. Dasgupta B, Milbrandt J. Resveratrol stimulates AMP kinase activity in neurons. Proc Natl Acad Sci U S A. 2007;104(17):7217-22.
333. Park SJ, Ahmad F, Philp A, Baar K, Williams T, Luo H, et al. Resveratrol ameliorates aging-related metabolic phenotypes by inhibiting cAMP phosphodiesterases. Cell. 2012;148(3):421-33.
334. Chao SC, Chen YJ, Huang KH, Kuo KL, Yang TH, Huang KY, et al. Induction of sirtuin-1 signaling by resveratrol induces human chondrosarcoma cell apoptosis and exhibits antitumor activity. Sci Rep. 2017;7(1):3180.
335. Ko JH, Sethi G, Um JY, Shanmugam MK, Arfuso F, Kumar AP, et al. The Role of Resveratrol in Cancer Therapy. Int J Mol Sci. 2017;18(12).
336. Ma Z, Zhang X, Xu L, Liu D, Di S, Li W, et al. Pterostilbene: Mechanisms of its action as oncostatic agent in cell models and in vivo studies. Pharmacol Res. 2019;145:104265.

337. Rimando AM, Cuendet M, Desmarchelier C, Mehta RG, Pezzuto JM, Duke SO. Cancer chemopreventive and antioxidant activities of pterostilbene, a naturally occurring analogue of resveratrol. J Agric Food Chem. 2002;50(12):3453-7.

338. Kampmann M. Elucidating drug targets and mechanisms of action by genetic screens in mammalian cells. Chem Commun (Camb). 2017;53(53):7162-7.

339. Baccelli I, Gareau Y, Lehnertz B, Gingras S, Spinella JF, Corneau S, et al. Mubritinib Targets the Electron Transport Chain Complex I and Reveals the Landscape of OXPHOS Dependency in Acute Myeloid Leukemia. Cancer Cell. 2019;36(1):84-99 e8.

340. Gandhi V, Plunkett W, Kantarjian H, Talpaz M, Robertson LE, O'Brien S. Cellular pharmacodynamics and plasma pharmacokinetics of parenterally infused hydroxyurea during a phase I clinical trial in chronic myelogenous leukemia. J Clin Oncol. 1998;16(7):2321-31.

341. Koc A, Wheeler LJ, Mathews CK, Merrill GF. Hydroxyurea arrests DNA replication by a mechanism that preserves basal dNTP pools. J Biol Chem. 2004;279(1):223-30.

342. Slater ML. Effect of reversible inhibition of deoxyribonucleic acid synthesis on the yeast cell cycle. J Bacteriol. 1973;113(1):263-70.

343. Hart T, Tong AHY, Chan K, Van Leeuwen J, Seetharaman A, Aregger M, et al. Evaluation and Design of Genome-Wide CRISPR/SpCas9 Knockout Screens. G3 (Bethesda). 2017;7(8):2719-27.

344. Guilliam TA, Doherty AJ. PrimPol-Prime Time to Reprime. Genes (Basel). 2017;8(1).

345. Wan L, Lou J, Xia Y, Su B, Liu T, Cui J, et al. hPrimpol1/CCDC111 is a human DNA primase-polymerase required for the maintenance of genome integrity. EMBO Rep. 2013;14(12):1104-12.

346. Beck H, Nahse-Kumpf V, Larsen MS, O'Hanlon KA, Patzke S, Holmberg C, et al. Cyclin-dependent kinase suppression by WEE1 kinase protects the genome through control of replication initiation and nucleotide consumption. Mol Cell Biol. 2012;32(20):4226-36.

347. Pai CC, Hsu KF, Durley SC, Keszthelyi A, Kearsey SE, Rallis C, et al. An essential role for dNTP homeostasis following CDK-induced replication stress. J Cell Sci. 2019;132(6).

348. Crona M, Codo P, Jonna VR, Hofer A, Fernandes AP, Tholander F. A ribonucleotide reductase inhibitor with deoxyribonucleoside-reversible cytotoxicity. Mol Oncol. 2016;10(9):1375-86.

349. Lagergren J, Reichard P. Purine deoxyribonucleosides counteract effects of hydroxyurea on deoxyribonucleoside triphosphate pools and DNA synthesis. Biochem Pharmacol. 1987;36(18):2985-91.

350. Young CW, Schochetman G, Karnofsky DA. Hydroxyurea-induced inhibition of deoxyribonucleotide synthesis: studies in intact cells. Cancer Res. 1967;27(3):526-34.

351. Marechal A, Zou L. RPA-coated single-stranded DNA as a platform for post-translational modifications in the DNA damage response. Cell Res. 2015;25(1):9-23.

352. Blundred R, Myers K, Helleday T, Goldman AS, Bryant HE. Human RECQL5 overcomes thymidine-induced replication stress. DNA Repair (Amst). 2010;9(9):964-75.

353. Chen E, Ahn JS, Sykes DB, Breyfogle LJ, Godfrey AL, Nangalia J, et al. RECQL5 Suppresses Oncogenic JAK2-Induced Replication Stress and Genomic Instability. Cell Rep. 2015;13(11):2345-52.

354. Di Marco S, Hasanova Z, Kanagaraj R, Chappidi N, Altmannova V, Menon S, et al. RECQ5 Helicase Cooperates with MUS81 Endonuclease in Processing Stalled Replication Forks at Common Fragile Sites during Mitosis. Mol Cell. 2017;66(5):658-71 e8.

355. Urban V, Dobrovolna J, Huhn D, Fryzelkova J, Bartek J, Janscak P. RECQ5 helicase promotes resolution of conflicts between replication and transcription in human cells. J Cell Biol. 2016;214(4):401-15.

356. Murai J, Tang SW, Leo E, Baechler SA, Redon CE, Zhang H, et al. SLFN11 Blocks Stressed Replication Forks Independently of ATR. Mol Cell. 2018;69(3):371-84 e6.

357. Murai J, Thomas A, Miettinen M, Pommier Y. Schlafen 11 (SLFN11), a restriction factor for replicative stress induced by DNA-targeting anti-cancer therapies. Pharmacol Ther. 2019;201:94-102.

358. Austin S, St-Pierre J. PGC1alpha and mitochondrial metabolism--emerging concepts and relevance in ageing and neurodegenerative disorders. J Cell Sci. 2012;125(Pt 21):4963-71.

359. Madeo F, Carmona-Gutierrez D, Hofer SJ, Kroemer G. Caloric Restriction Mimetics against Age-Associated Disease: Targets, Mechanisms, and Therapeutic Potential. Cell Metab. 2019;29(3):592-610.

360. Fontecave M, Lepoivre M, Elleingand E, Gerez C, Guittet O. Resveratrol, a remarkable inhibitor of ribonucleotide reductase. FEBS Lett. 1998;421(3):277-9.

361. Kuwajerwala N, Cifuentes E, Gautam S, Menon M, Barrack ER, Reddy GP. Resveratrol induces prostate cancer cell entry into s phase and inhibits DNA synthesis. Cancer Res. 2002;62(9):2488-92.

362. Li B, Hou D, Guo H, Zhou H, Zhang S, Xu X, et al. Resveratrol sequentially induces replication and oxidative stresses to drive p53-CXCR2 mediated cellular senescence in cancer cells. Sci Rep. 2017;7(1):208.

363. Pozo-Guisado E, Alvarez-Barrientos A, Mulero-Navarro S, Santiago-Josefat B, Fernandez-Salguero PM. The antiproliferative activity of resveratrol results in apoptosis in MCF-7 but not in MDA-MB-231 human breast cancer cells: cell-specific alteration of the cell cycle. Biochem Pharmacol. 2002;64(9):1375-86.

364. Ragione FD, Cucciolla V, Borriello A, Pietra VD, Racioppi L, Soldati G, et al. Resveratrol arrests the cell division cycle at S/G2 phase transition. Biochem Biophys Res Commun. 1998;250(1):53-8.

365. Chen CW, Li Y, Hu S, Zhou W, Meng Y, Li Z, et al. DHS (trans-4,4'-dihydroxystilbene) suppresses DNA replication and tumor growth by inhibiting RRM2 (ribonucleotide reductase regulatory subunit M2). Oncogene. 2019;38(13):2364-79.

366. Li Z, Chen QQ, Lam CWK, Guo JR, Zhang WJ, Wang CY, et al. Investigation into perturbed nucleoside metabolism and cell cycle for elucidating the cytotoxicity effect of resveratrol on human lung adenocarcinoma epithelial cells. Chin J Nat Med. 2019;17(8):608-15.

367. Guo S, Liao H, Liu J, Liu J, Tang F, He Z, et al. Resveratrol Activated Sonic Hedgehog Signaling to Enhance Viability of NIH3T3 Cells in Vitro via Regulation of Sirt1. Cell Physiol Biochem. 2018;50(4):1346-60.

368. Buhrmann C, Popper B, Aggarwal BB, Shakibaei M. Resveratrol downregulates inflammatory pathway activated by lymphotoxin alpha (TNF-beta) in articular chondrocytes: Comparison with TNF-alpha. PLoS One. 2017;12(11):e0186993.

369. Ling L, Gu S, Cheng Y. Resveratrol inhibits adventitial fibroblast proliferation and induces cell apoptosis through the SIRT1 pathway. Mol Med Rep. 2017;15(2):567-72.

370. Yang Q, Wang B, Zang W, Wang X, Liu Z, Li W, et al. Resveratrol inhibits the growth of gastric cancer by inducing G1 phase arrest and senescence in a Sirt1-dependent manner. PLoS One. 2013;8(11):e70627.

371. Zhu X, Liu Q, Wang M, Liang M, Yang X, Xu X, et al. Activation of Sirt1 by resveratrol inhibits TNF-alpha induced inflammation in fibroblasts. PLoS One. 2011;6(11):e27081.

372. Hills SA, Diffley JF. DNA replication and oncogene-induced replicative stress. Curr Biol. 2014;24(10):R435-44.

373. Ruzankina Y, Asare A, Brown EJ. Replicative stress, stem cells and aging. Mech Ageing Dev. 2008;129(7-8):460-6.

374. Pardo B, Crabbe L, Pasero P. Signaling pathways of replication stress in yeast. FEMS Yeast Res. 2017;17(2).

375. Weinberger M, Feng L, Paul A, Smith DL, Jr., Hontz RD, Smith JS, et al. DNA replication stress is a determinant of chronological lifespan in budding yeast. PLoS One. 2007;2(8):e748.

376. McCormick MA, Delaney JR, Tsuchiya M, Tsuchiyama S, Shemorry A, Sim S, et al. A Comprehensive Analysis of Replicative Lifespan in 4,698 Single-Gene Deletion Strains Uncovers Conserved Mechanisms of Aging. Cell Metab. 2015;22(5):895-906.

377. Ross EM, Maxwell PH. Low doses of DNA damaging agents extend Saccharomyces cerevisiae chronological lifespan by promoting entry into quiescence. Exp Gerontol. 2018;108:189-200.

378. Kaeberlein M, McVey M, Guarente L. The SIR2/3/4 complex and SIR2 alone promote longevity in Saccharomyces cerevisiae by two different mechanisms. Genes Dev. 1999;13(19):2570-80.

379. Kaeberlein M, Kirkland KT, Fields S, Kennedy BK. Sir2-independent life span extension by calorie restriction in yeast. PLoS Biol. 2004;2(9):E296.

380. Kwan EX, Foss EJ, Tsuchiyama S, Alvino GM, Kruglyak L, Kaeberlein M, et al. A natural polymorphism in rDNA replication origins links origin activation with calorie restriction and lifespan. PLoS Genet. 2013;9(3):e1003329.

381. Salvi JS, Chan JN, Pettigrew C, Liu TT, Wu JD, Mekhail K. Enforcement of a lifespan-sustaining distribution of Sir2 between telomeres, mating-type loci, and rDNA repeats by Rif1. Aging Cell. 2013;12(1):67-75.

382. Hoopes LL, Budd M, Choe W, Weitao T, Campbell JL. Mutations in DNA replication genes reduce yeast life span. Mol Cell Biol. 2002;22(12):4136-46.

383. Cornacchia D, Dileep V, Quivy JP, Foti R, Tili F, Santarella-Mellwig R, et al. Mouse Rif1 is a key regulator of the replication-timing programme in mammalian cells. EMBO J. 2012;31(18):3678-90.

384. Hafner L, Lezaja A, Zhang X, Lemmens L, Shyian M, Albert B, et al. Rif1 Binding and Control of Chromosome-Internal DNA Replication Origins Is Limited by Telomere Sequestration. Cell Rep. 2018;23(4):983-92.

385. Hiraga SI, Monerawela C, Katou Y, Shaw S, Clark KR, Shirahige K, et al. Budding yeast Rif1 binds to replication origins and protects DNA at blocked replication forks. EMBO Rep. 2018;19(9).

386. Mukherjee C, Tripathi V, Manolika EM, Heijink AM, Ricci G, Merzouk S, et al. RIF1 promotes replication fork protection and efficient restart to maintain genome stability. Nat Commun. 2019;10(1):3287.

387. Shyian M, Mattarocci S, Albert B, Hafner L, Lezaja A, Costanzo M, et al. Budding Yeast Rif1 Controls Genome Integrity by Inhibiting rDNA Replication. PLoS Genet. 2016;12(11):e1006414.

388. Matsuno Y, Atsumi Y, Alauddin M, Rana MM, Fujimori H, Hyodo M, et al. Resveratrol and its Related Polyphenols Contribute to the Maintenance of Genome Stability. Sci Rep. 2020;10(1):5388.

389. Agathokleous E, Calabrese EJ. Hormesis: The dose response for the 21st century: The future has arrived. Toxicology. 2019;425:152249.

390. Stebbing AR. Hormesis--the stimulation of growth by low levels of inhibitors. Sci Total Environ. 1982;22(3):213-34.

391. Walter DM, Venancio OS, Buza EL, Tobias JW, Deshpande C, Gudiel AA, et al. Systematic In Vivo Inactivation of Chromatin-Regulating Enzymes Identifies Setd2 as a Potent Tumor Suppressor in Lung Adenocarcinoma. Cancer Res. 2017;77(7):1719-29.

392. Sanjana NE, Shalem O, Zhang F. Improved vectors and genome-wide libraries for CRISPR screening. Nat Methods. 2014;11(8):783-4.

393. Langmead B, Salzberg SL. Fast gapped-read alignment with Bowtie 2. Nat Methods. 2012;9(4):357-9.

394. Raudvere U, Kolberg L, Kuzmin I, Arak T, Adler P, Peterson H, et al. g:Profiler: a web server for functional enrichment analysis and conversions of gene lists (2019 update). Nucleic Acids Res. 2019;47(W1):W191-W8.

395. Stewart SA, Dykxhoorn DM, Palliser D, Mizuno H, Yu EY, An DS, et al. Lentivirus-delivered stable gene silencing by RNAi in primary cells. RNA. 2003;9(4):493-501.

396. Brinkman EK, Chen T, Amendola M, van Steensel B. Easy quantitative assessment of genome editing by sequence trace decomposition. Nucleic Acids Res. 2014;42(22):e168.

397. Ray Chaudhuri A, Callen E, Ding X, Gogola E, Duarte AA, Lee JE, et al. Replication fork stability confers chemoresistance in BRCA-deficient cells. Nature. 2016;535(7612):382-7.

398. Forment JV, Jackson SP. A flow cytometry-based method to simplify the analysis and quantification of protein association to chromatin in mammalian cells. Nat Protoc. 2015;10(9):1297-307.

399. Bean DM, Heimbach J, Ficorella L, Micklem G, Oliver SG, Favrin G. esyN: network building, sharing and publishing. PLoS One. 2014;9(9):e106035.

400. Franz M, Rodriguez H, Lopes C, Zuberi K, Montojo J, Bader GD, et al. GeneMANIA update 2018. Nucleic Acids Res. 2018;46(W1):W60-W4.

401. Oughtred R, Stark C, Breitkreutz BJ, Rust J, Boucher L, Chang C, et al. The BioGRID interaction database: 2019 update. Nucleic Acids Res. 2019;47(D1):D529-D41.

402. Gibson DG, Young L, Chuang RY, Venter JC, Hutchison CA, 3rd, Smith HO. Enzymatic assembly of DNA molecules up to several hundred kilobases. Nat Methods. 2009;6(5):343-5.

403. Bliss CI. The toxicity of poisons applied jointly. Annals of Applied Biology. 1939;26(3):585-615.

404. Demidenko E, Miller TW. Statistical determination of synergy based on Bliss definition of drugs independence. PLoS One. 2019;14(11):e0224137.

405. Pfeiffer V, Lingner J. Replication of telomeres and the regulation of telomerase. Cold Spring Harb Perspect Biol. 2013;5(5):a010405.

406. Ding Z, Wu CJ, Jaskelioff M, Ivanova E, Kost-Alimova M, Protopopov A, et al. Telomerase reactivation following telomere dysfunction yields murine prostate tumors with bone metastases. Cell. 2012;148(5):896-907.

407. Acosta JC, Banito A, Wuestefeld T, Georgilis A, Janich P, Morton JP, et al. A complex secretory program orchestrated by the inflammasome controls paracrine senescence. Nat Cell Biol. 2013;15(8):978-90.

408. Gonzalez LC, Ghadaouia S, Martinez A, Rodier F. Premature aging/senescence in cancer cells facing therapy: good or bad? Biogerontology. 2016;17(1):71-87.

409. Malaquin N, Martinez A, Rodier F. Keeping the senescence secretome under control: Molecular reins on the senescence-associated secretory phenotype. Exp Gerontol. 2016;82:39-49.

410. Wright WE, Pereira-Smith OM, Shay JW. Reversible cellular senescence: implications for immortalization of normal human diploid fibroblasts. Mol Cell Biol. 1989;9(7):3088-92.

411. Counter CM, Botelho FM, Wang P, Harley CB, Bacchetti S. Stabilization of short telomeres and telomerase activity accompany immortalization of Epstein-Barr virus-transformed human B lymphocytes. J Virol. 1994;68(5):3410-4.

412. Harley CB, Kim NW, Prowse KR, Weinrich SL, Hirsch KS, West MD, et al. Telomerase, cell immortality, and cancer. Cold Spring Harb Symp Quant Biol. 1994;59:307-15.

413. Sharpless NE, DePinho RA. p53: good cop/bad cop. Cell. 2002;110(1):9-12.

414. Wu D, Prives C. Relevance of the p53-MDM2 axis to aging. Cell Death Differ. 2018;25(1):169-79.

415. Claude E, Decottignies A. Telomere maintenance mechanisms in cancer: telomerase, ALT or lack thereof. Curr Opin Genet Dev. 2020;60:1-8.

416. Harari Y, Kupiec M. Genome-wide studies of telomere biology in budding yeast. Microb Cell. 2014;1(3):70-80.

417. Narayanan S, Dubarry M, Lawless C, Banks AP, Wilkinson DJ, Whitehall SK, et al. Quantitative Fitness Analysis Identifies exo1 and Other Suppressors or Enhancers of Telomere Defects in Schizosaccharomyces pombe. PLoS One. 2015;10(7):e0132240.

418. Holstein EM, Ngo G, Lawless C, Banks P, Greetham M, Wilkinson D, et al. Systematic Analysis of the DNA Damage Response Network in Telomere Defective Budding Yeast. G3 (Bethesda). 2017;7(7):2375-89.

419. Mazzucco AE, Smogorzewska A, Kang C, Luo J, Schlabach MR, Xu Q, et al. Genetic interrogation of replicative senescence uncovers a dual role for USP28 in coordinating the p53 and GATA4 branches of the senescence program. Genes Dev. 2017;31(19):1933-8.

420. Wang Y, Xu Q, Sack L, Kang C, Elledge SJ. A gain-of-function senescence bypass screen identifies the homeobox transcription factor DLX2 as a regulator of ATM-p53 signaling. Genes Dev. 2016;30(3):293-306.

421. Zhang D, Zaugg K, Mak TW, Elledge SJ. A role for the deubiquitinating enzyme USP28 in control of the DNA-damage response. Cell. 2006;126(3):529-42.

422. Filippini G, Griffin S, Uhr M, Eppenberger H, Bonilla J, Cavalli F, et al. A novel flow cytometric method for the quantification of p53 gene expression. Cytometry. 1998;31(3):180-6.

423. Nakashima M, Nandakumar J, Sullivan KD, Espinosa JM, Cech TR. Inhibition of telomerase recruitment and cancer cell death. J Biol Chem. 2013;288(46):33171-80.

424. Bryan C, Rice C, Hoffman H, Harkisheimer M, Sweeney M, Skordalakes E. Structural Basis of Telomerase Inhibition by the Highly Specific BIBR1532. Structure. 2015;23(10):1934-42.

425. Bashash D, Zareii M, Safaroghli-Azar A, Omrani MD, Ghaffari SH. Inhibition of telomerase using BIBR1532 enhances doxorubicin-induced apoptosis in pre-B acute lymphoblastic leukemia cells. Hematology. 2017;22(6):330-40.

426. Liu C, Zhou H, Sheng XB, Liu XH, Chen FH. Design, synthesis and SARs of novel telomerase inhibitors based on BIBR1532. Bioorg Chem. 2020;102:104077.

427. Benslimane Y, Bertomeu T, Coulombe-Huntington J, McQuaid M, Sanchez-Osuna M, Papadopoli D, et al. Genome-Wide Screens Reveal that Resveratrol Induces Replicative Stress in Human Cells. Mol Cell. 2020;79(5):846-56.E8.

428. Evans DR, Guy HI. Mammalian pyrimidine biosynthesis: fresh insights into an ancient pathway. J Biol Chem. 2004;279(32):33035-8.

429. Ashby MN, Edwards PA. Elucidation of the deficiency in two yeast coenzyme Q mutants. Characterization of the structural gene encoding hexaprenyl pyrophosphate synthetase. J Biol Chem. 1990;265(22):13157-64.

430. Forsgren M, Attersand A, Lake S, Grunler J, Swiezewska E, Dallner G, et al. Isolation and functional expression of human COQ2, a gene encoding a polyprenyl transferase involved in the synthesis of CoQ. Biochem J. 2004;382(Pt 2):519-26.

431. Matmati S, Lambert S, Geli V, Coulon S. Telomerase Repairs Collapsed Replication Forks at Telomeres. Cell Rep. 2020;30(10):3312-22 e3.

432. Sfeir A, Kosiyatrakul ST, Hockemeyer D, MacRae SL, Karlseder J, Schildkraut CL, et al. Mammalian telomeres resemble fragile sites and require TRF1 for efficient replication. Cell. 2009;138(1):90-103.

433. Margalef P, Kotsantis P, Borel V, Bellelli R, Panier S, Boulton SJ. Stabilization of Reversed Replication Forks by Telomerase Drives Telomere Catastrophe. Cell. 2018;172(3):439-53 e14.

434. Perera ON, Sobinoff AP, Teber ET, Harman A, Maritz MF, Yang SF, et al. Telomerase promotes formation of a telomere protective complex in cancer cells. Sci Adv. 2019;5(10):eaav4409.

435. Yu EY, Steinberg-Neifach O, Dandjinou AT, Kang F, Morrison AJ, Shen X, et al. Regulation of telomere structure and functions by subunits of the INO80 chromatin remodeling complex. Mol Cell Biol. 2007;27(16):5639-49.

436. Morrison AJ, Shen X. Chromatin remodelling beyond transcription: the INO80 and SWR1 complexes. Nat Rev Mol Cell Biol. 2009;10(6):373-84.

437. Hu Y, Tang HB, Liu NN, Tong XJ, Dang W, Duan YM, et al. Telomerase-null survivor screening identifies novel telomere recombination regulators. PLoS Genet. 2013;9(1):e1003208.

438. Min JN, Tian Y, Xiao Y, Wu L, Li L, Chang S. The mINO80 chromatin remodeling complex is required for efficient telomere replication and maintenance of genome stability. Cell Res. 2013;23(12):1396-413.

439. Zhou W, Gao J, Ma J, Cao L, Zhang C, Zhu Y, et al. Distinct roles of the histone chaperones NAP1 and NRP and the chromatin-remodeling factor INO80 in somatic homologous recombination in Arabidopsis thaliana. Plant J. 2016;88(3):397-410.

440. Chen SF, Perrella FW, Behrens DL, Papp LM. Inhibition of dihydroorotate dehydrogenase activity by brequinar sodium. Cancer Res. 1992;52(13):3521-7.

441. D'Arcy P, Brnjic S, Olofsson MH, Fryknas M, Lindsten K, De Cesare M, et al. Inhibition of proteasome deubiquitinating activity as a new cancer therapy. Nat Med. 2011;17(12):1636-40.

442. Griffiths M, Beaumont N, Yao SY, Sundaram M, Boumah CE, Davies A, et al. Cloning of a human nucleoside transporter implicated in the cellular uptake of adenosine and chemotherapeutic drugs. Nat Med. 1997;3(1):89-93.

443. Kapuria V, Peterson LF, Fang D, Bornmann WG, Talpaz M, Donato NJ. Deubiquitinase inhibition by small-molecule WP1130 triggers aggresome formation and tumor cell apoptosis. Cancer Res. 2010;70(22):9265-76.

444. Knecht W, Henseling J, Loffler M. Kinetics of inhibition of human and rat dihydroorotate dehydrogenase by atovaquone, lawsone derivatives, brequinar sodium and polyporic acid. Chem Biol Interact. 2000;124(1):61-76.

445. McLean JE, Neidhardt EA, Grossman TH, Hedstrom L. Multiple inhibitor analysis of the brequinar and leflunomide binding sites on human dihydroorotate dehydrogenase. Biochemistry. 2001;40(7):2194-200.

446. Chen D, Kon N, Li M, Zhang W, Qin J, Gu W. ARF-BP1/Mule is a critical mediator of the ARF tumor suppressor. Cell. 2005;121(7):1071-83.

447. Cummins JM, Rago C, Kohli M, Kinzler KW, Lengauer C, Vogelstein B. Tumour suppression: disruption of HAUSP gene stabilizes p53. Nature. 2004;428(6982):1 p following 486.

448. Hu M, Gu L, Li M, Jeffrey PD, Gu W, Shi Y. Structural basis of competitive recognition of p53 and MDM2 by HAUSP/USP7: implications for the regulation of the p53-MDM2 pathway. PLoS Biol. 2006;4(2):e27.

449. Sheng Y, Saridakis V, Sarkari F, Duan S, Wu T, Arrowsmith CH, et al. Molecular recognition of p53 and MDM2 by USP7/HAUSP. Nat Struct Mol Biol. 2006;13(3):285-91.

450. Canman CE, Lim DS, Cimprich KA, Taya Y, Tamai K, Sakaguchi K, et al. Activation of the ATM kinase by ionizing radiation and phosphorylation of p53. Science. 1998;281(5383):1677-9.

451. Dulic V, Kaufmann WK, Wilson SJ, Tlsty TD, Lees E, Harper JW, et al. p53-dependent inhibition of cyclin-dependent kinase activities in human fibroblasts during radiation-induced G1 arrest. Cell. 1994;76(6):1013-23.

452. Hirao A, Kong YY, Matsuoka S, Wakeham A, Ruland J, Yoshida H, et al. DNA damage-induced activation of p53 by the checkpoint kinase Chk2. Science. 2000;287(5459):1824-7.

453. Branon TC, Bosch JA, Sanchez AD, Udeshi ND, Svinkina T, Carr SA, et al. Efficient proximity labeling in living cells and organisms with TurboID. Nat Biotechnol. 2018;36(9):880-7.

454. Giles AC, Grill B. Roles of the HUWE1 ubiquitin ligase in nervous system development, function and disease. Neural Dev. 2020;15(1):6.

455. Gong X, Du D, Deng Y, Zhou Y, Sun L, Yuan S. The structure and regulation of the E3 ubiquitin ligase HUWE1 and its biological functions in cancer. Invest New Drugs. 2020;38(2):515-24.

456. Kao SH, Wu HT, Wu KJ. Ubiquitination by HUWE1 in tumorigenesis and beyond. J Biomed Sci. 2018;25(1):67.

457. Kaushik S, Cuervo AM. Proteostasis and aging. Nat Med. 2015;21(12):1406-15.

458. Vilchez D, Simic MS, Dillin A. Proteostasis and aging of stem cells. Trends Cell Biol. 2014;24(3):161-70.

459. Lin DH, Hoelz A. The Structure of the Nuclear Pore Complex (An Update). Annu Rev Biochem. 2019;88:725-83.

460. Pritchard CE, Fornerod M, Kasper LH, van Deursen JM. RAE1 is a shuttling mRNA export factor that binds to a GLEBS-like NUP98 motif at the nuclear pore complex through multiple domains. J Cell Biol. 1999;145(2):237-54.

461. Umlauf D, Bonnet J, Waharte F, Fournier M, Stierle M, Fischer B, et al. The human TREX-2 complex is stably associated with the nuclear pore basket. J Cell Sci. 2013;126(Pt 12):2656-67.

462. Wickramasinghe VO, McMurtrie PI, Mills AD, Takei Y, Penrhyn-Lowe S, Amagase Y, et al. mRNA export from mammalian cell nuclei is dependent on GANP. Curr Biol. 2010;20(1):25-31.

463. Cenci S, Pengo N, Sitia R. Proteotoxic stress and cell lifespan control. Mol Cells. 2008;26(4):323-8.

464. Dai C. The heat-shock, or HSF1-mediated proteotoxic stress, response in cancer: from proteomic stability to oncogenesis. Philos Trans R Soc Lond B Biol Sci. 2018;373(1738).

465. Guang MHZ, Kavanagh EL, Dunne LP, Dowling P, Zhang L, Lindsay S, et al. Targeting Proteotoxic Stress in Cancer: A Review of the Role that Protein Quality Control Pathways Play in Oncogenesis. Cancers (Basel). 2019;11(1).

466. Korbelik M. Role of cell stress signaling networks in cancer cell death and antitumor immune response following proteotoxic injury inflicted by photodynamic therapy. Lasers Surg Med. 2018;50(5):491-8.

467. Shibata Y, Morimoto RI. How the nucleus copes with proteotoxic stress. Curr Biol. 2014;24(10):R463-74.

468. Van Maerken T, Rihani A, Van Goethem A, De Paepe A, Speleman F, Vandesompele J. Pharmacologic activation of wild-type p53 by nutlin therapy in childhood cancer. Cancer Lett. 2014;344(2):157-65.

469. Secchiero P, Bosco R, Celeghini C, Zauli G. Recent advances in the therapeutic perspectives of Nutlin-3. Curr Pharm Des. 2011;17(6):569-77.

470. Vassilev LT, Vu BT, Graves B, Carvajal D, Podlaski F, Filipovic Z, et al. In vivo activation of the p53 pathway by small-molecule antagonists of MDM2. Science. 2004;303(5659):844-8.

471. Tewey KM, Rowe TC, Yang L, Halligan BD, Liu LF. Adriamycin-induced DNA damage mediated by mammalian DNA topoisomerase II. Science. 1984;226(4673):466-8.

472. Hein MY, Hubner NC, Poser I, Cox J, Nagaraj N, Toyoda Y, et al. A human interactome in three quantitative dimensions organized by stoichiometries and abundances. Cell. 2015;163(3):712-23.

473. Thompson JW, Nagel J, Hoving S, Gerrits B, Bauer A, Thomas JR, et al. Quantitative Lys--Gly-Gly (diGly) proteomics coupled with inducible RNAi reveals ubiquitin-mediated proteolysis of DNA damage-inducible transcript 4 (DDIT4) by the E3 ligase HUWE1. J Biol Chem. 2014;289(42):28942-55.

474. Kurokawa M, Kim J, Geradts J, Matsuura K, Liu L, Ran X, et al. A network of substrates of the E3 ubiquitin ligases MDM2 and HUWE1 control apoptosis independently of p53. Sci Signal. 2013;6(274):ra32.

475. Qi CF, Kim YS, Xiang S, Abdullaev Z, Torrey TA, Janz S, et al. Characterization of ARF-BP1/HUWE1 interactions with CTCF, MYC, ARF and p53 in MYC-driven B cell neoplasms. Int J Mol Sci. 2012;13(5):6204-19.

476. Yang D, Cheng D, Tu Q, Yang H, Sun B, Yan L, et al. HUWE1 controls the development of non-small cell lung cancer through down-regulation of p53. Theranostics. 2018;8(13):3517-29.

477. Zhang Y, Zhang Y, Xu H. LIMCH1 suppress the growth of lung cancer by interacting with HUWE1 to sustain p53 stability. Gene. 2019;712:143963.

478. Sung MK, Porras-Yakushi TR, Reitsma JM, Huber FM, Sweredoski MJ, Hoelz A, et al. A conserved quality-control pathway that mediates degradation of unassembled ribosomal proteins. Elife. 2016;5.

479. Punta M, Coggill PC, Eberhardt RY, Mistry J, Tate J, Boursnell C, et al. The Pfam protein families database. Nucleic Acids Res. 2012;40(Database issue):D290-301.

480. Xu Y, Anderson DE, Ye Y. The HECT domain ubiquitin ligase HUWE1 targets unassembled soluble proteins for degradation. Cell Discov. 2016;2:16040.

481. Gomez-Herreros F, Margaritis T, Rodriguez-Galan O, Pelechano V, Begley V, Millan-Zambrano G, et al. The ribosome assembly gene network is controlled by the feedback regulation of transcription elongation. Nucleic Acids Res. 2017;45(16):9302-18.

482. Jorgensen P, Rupes I, Sharom JR, Schneper L, Broach JR, Tyers M. A dynamic transcriptional network communicates growth potential to ribosome synthesis and critical cell size. Genes Dev. 2004;18(20):2491-505.

483. Hipp MS, Kasturi P, Hartl FU. The proteostasis network and its decline in ageing. Nat Rev Mol Cell Biol. 2019;20(7):421-35.

484. Deisenroth C, Zhang Y. Ribosome biogenesis surveillance: probing the ribosomal protein-Mdm2-p53 pathway. Oncogene. 2010;29(30):4253-60.

485. Albert B, Knight B, Merwin J, Martin V, Ottoz D, Gloor Y, et al. A Molecular Titration System Coordinates Ribosomal Protein Gene Transcription with Ribosomal RNA Synthesis. Mol Cell. 2016;64(4):720-33.

486. Albert B, Kos-Braun IC, Henras AK, Dez C, Rueda MP, Zhang X, et al. A ribosome assembly stress response regulates transcription to maintain proteome homeostasis. Elife. 2019;8.

487. Rudra D, Mallick J, Zhao Y, Warner JR. Potential interface between ribosomal protein production and pre-rRNA processing. Mol Cell Biol. 2007;27(13):4815-24.

488. Tye BW, Commins N, Ryazanova LV, Wuhr M, Springer M, Pincus D, et al. Proteotoxicity from aberrant ribosome biogenesis compromises cell fitness. Elife. 2019;8.

489. Dai C, Sampson SB. HSF1: Guardian of Proteostasis in Cancer. Trends Cell Biol. 2016;26(1):17-28.

490. Vihervaara A, Sergelius C, Vasara J, Blom MA, Elsing AN, Roos-Mattjus P, et al. Transcriptional response to stress in the dynamic chromatin environment of cycling and mitotic cells. Proc Natl Acad Sci U S A. 2013;110(36):E3388-97.

491. Brennan CM, Vaites LP, Wells JN, Santaguida S, Paulo JA, Storchova Z, et al. Protein aggregation mediates stoichiometry of protein complexes in aneuploid cells. Genes Dev. 2019;33(15-16):1031-47.

492. Ohashi A, Ohori M, Iwai K, Nakayama Y, Nambu T, Morishita D, et al. Aneuploidy generates proteotoxic stress and DNA damage concurrently with p53-mediated post-mitotic apoptosis in SAC-impaired cells. Nat Commun. 2015;6:7668.

493. Oromendia AB, Dodgson SE, Amon A. Aneuploidy causes proteotoxic stress in yeast. Genes Dev. 2012;26(24):2696-708.

494. Torres EM, Williams BR, Amon A. Aneuploidy: cells losing their balance. Genetics. 2008;179(2):737-46.

495. Donehower LA, Harvey M, Slagle BL, McArthur MJ, Montgomery CA, Jr., Butel JS, et al. Mice deficient for p53 are developmentally normal but susceptible to spontaneous tumours. Nature. 1992;356(6366):215-21.

496. Hainaut P, Hollstein M. p53 and human cancer: the first ten thousand mutations. Adv Cancer Res. 2000;77:81-137.

497. Malkin D, Li FP, Strong LC, Fraumeni JF, Jr., Nelson CE, Kim DH, et al. Germ line p53 mutations in a familial syndrome of breast cancer, sarcomas, and other neoplasms. Science. 1990;250(4985):1233-8.

498. Srivastava S, Zou ZQ, Pirollo K, Blattner W, Chang EH. Germ-line transmission of a mutated p53 gene in a cancer-prone family with Li-Fraumeni syndrome. Nature. 1990;348(6303):747-9.

499. Gebel J, Tuppi M, Krauskopf K, Coutandin D, Pitzius S, Kehrloesser S, et al. Control mechanisms in germ cells mediated by p53 family proteins. J Cell Sci. 2017.

500. Herbert BS, Hochreiter AE, Wright WE, Shay JW. Nonradioactive detection of telomerase activity using the telomeric repeat amplification protocol. Nat Protoc. 2006;1(3):1583-90.

501. Yuste VJ, Bayascas JR, Llecha N, Sánchez-López I, Boix J, Comella JX. The absence of oligonucleosomal DNA fragmentation during apoptosis of IMR-5 neuroblastoma cells: disappearance of the caspase-activated DNase. J Biol Chem. 2001;276(25):22323-31.

502. Chu TW, D'Souza Y, Autexier C. The Insertion in Fingers Domain in Human Telomerase Can Mediate Enzyme Processivity and Telomerase Recruitment to Telomeres in a TPP1-Dependent Manner. Mol Cell Biol. 2016;36(1):210-22.
503. Vandesompele J, De Preter K, Pattyn F, Poppe B, Van Roy N, De Paepe A, et al. Accurate normalization of real-time quantitative RT-PCR data by geometric averaging of multiple internal control genes. Genome Biol. 2002;3(7):Research0034.
504. Méant A, Gao B, Lavoie G, Nourreddine S, Jung F, Aubert L, et al. Proteomic Analysis Reveals a Role for RSK in p120-catenin Phosphorylation and Melanoma Cell-Cell Adhesion. Mol Cell Proteomics. 2020;19(1):50-64.
505. Välikangas T, Suomi T, Elo LL. A systematic evaluation of normalization methods in quantitative label-free proteomics. Brief Bioinform. 2018;19(1):1-11.
506. Mellacheruvu D, Wright Z, Couzens AL, Lambert JP, St-Denis NA, Li T, et al. The CRAPome: a contaminant repository for affinity purification-mass spectrometry data. Nat Methods. 2013;10(8):730-6.
507. Love MI, Huber W, Anders S. Moderated estimation of fold change and dispersion for RNA-seq data with DESeq2. Genome Biol. 2014;15(12):550.
508. Varet H, Brillet-Guéguen L, Coppée JY, Dillies MA. SARTools: A DESeq2- and EdgeR-Based R Pipeline for Comprehensive Differential Analysis of RNA-Seq Data. PLoS One. 2016;11(6):e0157022.
509. Supek F, Bošnjak M, Škunca N, Šmuc T. REVIGO summarizes and visualizes long lists of gene ontology terms. PLoS One. 2011;6(7):e21800.
510. Fischer M. Census and evaluation of p53 target genes. Oncogene. 2017;36(28):3943-56.
511. Metsalu T, Vilo J. ClustVis: a web tool for visualizing clustering of multivariate data using Principal Component Analysis and heatmap. Nucleic Acids Res. 2015;43(W1):W566-70.
512. Jost M, Weissman JS. CRISPR Approaches to Small Molecule Target Identification. ACS Chem Biol. 2018;13(2):366-75.
513. Wang J, Lohman GJ, Stubbe J. Mechanism of inactivation of human ribonucleotide reductase with p53R2 by gemcitabine 5'-diphosphate. Biochemistry. 2009;48(49):11612-21.

514. Nyholm S, Thelander L, Gräslund A. Reduction and loss of the iron center in the reaction of the small subunit of mouse ribonucleotide reductase with hydroxyurea. Biochemistry. 1993;32(43):11569-74.

515. Davies BW, Kohanski MA, Simmons LA, Winkler JA, Collins JJ, Walker GC. Hydroxyurea induces hydroxyl radical-mediated cell death in Escherichia coli. Mol Cell. 2009;36(5):845-60.

516. Puig S, Ramos-Alonso L, Romero AM, Martínez-Pastor MT. The elemental role of iron in DNA synthesis and repair. Metallomics. 2017;9(11):1483-500.

517. Dubacq C, Chevalier A, Courbeyrette R, Petat C, Gidrol X, Mann C. Role of the iron mobilization and oxidative stress regulons in the genomic response of yeast to hydroxyurea. Mol Genet Genomics. 2006;275(2):114-24.

518. Tkach JM, Yimit A, Lee AY, Riffle M, Costanzo M, Jaschob D, et al. Dissecting DNA damage response pathways by analysing protein localization and abundance changes during DNA replication stress. Nat Cell Biol. 2012;14(9):966-76.

519. Travesa A, Kuo D, de Bruin RA, Kalashnikova TI, Guaderrama M, Thai K, et al. DNA replication stress differentially regulates G1/S genes via Rad53-dependent inactivation of Nrm1. Embo j. 2012;31(7):1811-22.

520. Huang ME, Facca C, Fatmi Z, Baïlle D, Bénakli S, Vernis L. DNA replication inhibitor hydroxyurea alters Fe-S centers by producing reactive oxygen species in vivo. Sci Rep. 2016;6:29361.

521. Singh A, Xu YJ. The Cell Killing Mechanisms of Hydroxyurea. Genes (Basel). 2016;7(11).

522. López-Otín C, Blasco MA, Partridge L, Serrano M, Kroemer G. The hallmarks of aging. Cell. 2013;153(6):1194-217.

523. Purvis JE, Karhohs KW, Mock C, Batchelor E, Loewer A, Lahav G. p53 dynamics control cell fate. Science. 2012;336(6087):1440-4.

524. Hafner A, Stewart-Ornstein J, Purvis JE, Forrester WC, Bulyk ML, Lahav G. p53 pulses lead to distinct patterns of gene expression albeit similar DNA-binding dynamics. Nat Struct Mol Biol. 2017;24(10):840-7.

525. Pelletier J, Riaño-Canalias F, Almacellas E, Mauvezin C, Samino S, Feu S, et al. Nucleotide depletion reveals the impaired ribosome biogenesis checkpoint as a barrier against DNA damage. Embo j. 2020;39(13):e103838.
526. Choe KN, Nicolae CM, Constantin D, Imamura Kawasawa Y, Delgado-Diaz MR, De S, et al. HUWE1 interacts with PCNA to alleviate replication stress. EMBO Rep. 2016;17(6):874-86.
527. Salim D, Bradford WD, Freeland A, Cady G, Wang J, Pruitt SC, et al. DNA replication stress restricts ribosomal DNA copy number. PLoS Genet. 2017;13(9):e1007006.
528. Holohan B, Wright WE, Shay JW. Cell biology of disease: Telomeropathies: an emerging spectrum disorder. J Cell Biol. 2014;205(3):289-99.
529. Wienert B, Wyman SK, Richardson CD, Yeh CD, Akcakaya P, Porritt MJ, et al. Unbiased detection of CRISPR off-targets in vivo using DISCOVER-Seq. Science. 2019;364(6437):286-9.
530. Schmid-Burgk JL, Gao L, Li D, Gardner Z, Strecker J, Lash B, et al. Highly Parallel Profiling of Cas9 Variant Specificity. Mol Cell. 2020;78(4):794-800.e8.
531. Smits AH, Ziebell F, Joberty G, Zinn N, Mueller WF, Clauder-Münster S, et al. Biological plasticity rescues target activity in CRISPR knock outs. Nat Methods. 2019;16(11):1087-93.
532. Colic M, Wang G, Zimmermann M, Mascall K, McLaughlin M, Bertolet L, et al. Identifying chemogenetic interactions from CRISPR screens with drugZ. Genome Med. 2019;11(1):52.
533. Jost M, Santos DA, Saunders RA, Horlbeck MA, Hawkins JS, Scaria SM, et al. Titrating gene expression using libraries of systematically attenuated CRISPR guide RNAs. Nat Biotechnol. 2020;38(3):355-64.
534. Chen J, Brunner AD, Cogan JZ, Nuñez JK, Fields AP, Adamson B, et al. Pervasive functional translation of noncanonical human open reading frames. Science. 2020;367(6482):1140-6.
535. Wang C, Lu T, Emanuel G, Babcock HP, Zhuang X. Imaging-based pooled CRISPR screening reveals regulators of lncRNA localization. Proc Natl Acad Sci U S A. 2019;116(22):10842-51.
536. Feldman D, Singh A, Schmid-Burgk JL, Carlson RJ, Mezger A, Garrity AJ, et al. Optical Pooled Screens in Human Cells. Cell. 2019;179(3):787-99.e17.

537. Mimitou EP, Cheng A, Montalbano A, Hao S, Stoeckius M, Legut M, et al. Multiplexed detection of proteins, transcriptomes, clonotypes and CRISPR perturbations in single cells. Nat Methods. 2019;16(5):409-12.

538. Wroblewska A, Dhainaut M, Ben-Zvi B, Rose SA, Park ES, Amir ED, et al. Protein Barcodes Enable High-Dimensional Single-Cell CRISPR Screens. Cell. 2018;175(4):1141-55.e16.

539. Rubin AJ, Parker KR, Satpathy AT, Qi Y, Wu B, Ong AJ, et al. Coupled Single-Cell CRISPR Screening and Epigenomic Profiling Reveals Causal Gene Regulatory Networks. Cell. 2019;176(1-2):361-76.e17.

540. Replogle JM, Norman TM, Xu A, Hussmann JA, Chen J, Cogan JZ, et al. Combinatorial single-cell CRISPR screens by direct guide RNA capture and targeted sequencing. Nat Biotechnol. 2020;38(8):954-61.

541. Adamson B, Norman TM, Jost M, Cho MY, Nuñez JK, Chen Y, et al. A Multiplexed Single-Cell CRISPR Screening Platform Enables Systematic Dissection of the Unfolded Protein Response. Cell. 2016;167(7):1867-82.e21.

542. Norman TM, Horlbeck MA, Replogle JM, Ge AY, Xu A, Jost M, et al. Exploring genetic interaction manifolds constructed from rich single-cell phenotypes. Science. 2019;365(6455):786-93.

543. Jaitin DA, Weiner A, Yofe I, Lara-Astiaso D, Keren-Shaul H, David E, et al. Dissecting Immune Circuits by Linking CRISPR-Pooled Screens with Single-Cell RNA-Seq. Cell. 2016;167(7):1883-96.e15.

544. Datlinger P, Rendeiro AF, Schmidl C, Krausgruber T, Traxler P, Klughammer J, et al. Pooled CRISPR screening with single-cell transcriptome readout. Nat Methods. 2017;14(3):297-301.

545. Dixit A, Parnas O, Li B, Chen J, Fulco CP, Jerby-Arnon L, et al. Perturb-Seq: Dissecting Molecular Circuits with Scalable Single-Cell RNA Profiling of Pooled Genetic Screens. Cell. 2016;167(7):1853-66.e17.

Appendix

Appendix I

Supplementary tables related to the manuscript presented in chapter 2.

Supplementary table 2.1 | sgRNA sequences and associated indel sequencing primers for indicated genes

Gene	sgRNA #	sgRNA sequence (5'-3')	Indel sequencing primers (5'-3')
RECQL5	1	GGACACCAGGGAGTTCAGGG	PCR_F: TCTGACTTCAGAGCCTGTGC PCR_R: ACAAGCCTGACAGACTGCAT Seq.: ACACTTTTGGTCCCAAGCATTTG
RECQL5	2	GAAGGCCTCTGAAAGAACGC	PCR_F: TCTGACTTCAGAGCCTGTGC PCR_R: ACAAGCCTGACAGACTGCAT Seq.: CTTCCTTCCCCTCTAGCCCT
SLFN11	1	TGAGTCCATGGAACGCACAG	PCR_F: CGAATGGCCAAGAAGGTTGAG PCR_R: TGGCCATTTATAGACATGTGAGTT Seq.: CGAATGGCCAAGAAGGTTGAG
SLFN11	2	CTGACAACCGAGAAATGGGT	PCR_F: CGAATGGCCAAGAAGGTTGAG PCR_R: TGGCCATTTATAGACATGTGAGTT Seq.: TGGCCATTTATAGACATGTGAGTT
Non-targeting (AAVS1)	1	GGGGCCACTAGGGACAGGAT	PCR_F: TGTGCCATCTCTCGTTTCTTA PCR_R: CACAAAGGGAGTTTTCCACA Seq.: GTCATGGCATCTTCCAGGGGTC
Non-targeting (AzGreen)	2	GGCCACAACTTCGTGATCGA	PCR_F: NA PCR_R: NA Seq.: NA
SIRT1	1	TCGTACAAGTTGTCGGCCAG	PCR_F: GCAGTTGGAAGATGGCGGAC PCR_R: GGACGGAGGAAAAGAGCGAAT Seq.: GGACGGAGGAAAAGAGCGAAT
SIRT1	2	GCGGCGGCGATTGGGTACCG	PCR_F: GCAGTTGGAAGATGGCGGAC PCR_R: GGACGGAGGAAAAGAGCGAAT Seq.: GGACGGAGGAAAAGAGCGAAT

Supplementary table 2.2 | Indel sequencing and decomposition

Figure panel	Sample	TIDE efficiency	Frameshift genotype	R-squared
Figure 2.4B-C, Supplementary figure 2.4A-D	NALM-6 RECQL5 KO #1, day 14	48.2	NA	0.97
	NALM-6 RECQL5 KO #2, day 14	66.5	NA	0.96
	NALM-6 SLFN11 KO #1, day 14	79.1	NA	0.97
	NALM-6 SLFN11 KO #2, day 14	77.6	NA	0.97
	NALM-6 Non-targeting #1, day 14	78.2	NA	0.98
	NALM-6 Non-targeting #2, day 14	NA	NA	NA
Supplementary figure 2.4E	Jurkat RECQL5 KO #1, day 14	53.7	NA	0.92
	Jurkat RECQL5 KO #2, day 14	68.9	NA	0.92
	Jurkat Non-targeting #1, day 14	88.3	NA	0.92
	Jurkat Non-targeting #2, day 14	NA	NA	NA
Supplementary figure 2.4F-G	NALM-6 Non-targeting clone #1	NA	(+1, -1)	0.95
	NALM-6 Non-targeting clone #2	NA	(+1, -14)	0.92
	NALM-6 Non-targeting clone #3	NA	(+4, +4)	0.96
	NALM-6 RECQL5 KO clone #1	NA	(+4, +7)	0.9
	NALM-6 RECQL5 KO clone #2	NA	(+2, -8)	0.93
	NALM-6 RECQL5 KO clone #3	NA	(+2, +1)	0.96
Figure 24D-C, Supplementary figure 2.4H-I	NALM-6 SIRT1 KO clone #1	NA	(+1, +4)	0.95
	NALM-6 SIRT1 KO clone #2	NA	(+2, +4)	0.94
	NALM-6 SIRT1 KO clone #3	NA	(+2, +5)	0.95
	NALM-6 SIRT1 KO clone #4	NA	(+2, +5)	0.94

Supplementary table 2.3 | Antibodies used for immunoblots, flow cytometry and DNA fiber analysis

Antibody	Manufacturer	Identifier
Mouse anti-phospho-Histone H2A.X (Ser139) [clone JBW301]	EMD Millipore	Cat# 05-636; RRID: AB_309864
Rabbit anti-RPA70 [clone EPR3472]	Abcam	Cat# ab79398; RRID: AB_1603759
Alexa Fluor 488 goat anti-mouse IgG (H+L)	Life Technologies	Cat# A11029; RRID: AB_2534088
Alexa Fluor 594 goat anti-rabbit IgG (H+L)	Life Technologies	Cat# A11012; RRID: AB_2534079
Rat anti-BrdU [clone BU1/75 (ICR1)]	Abcam	Cat# ab6326; RRID: AB_305426
Mouse anti-BrdU [clone B44]	BD Biosciences	Cat# 347580; RRID: AB_10015219
Alexa Fluor 594 goat anti-rat IgG (H+L)	Life Technologies	Cat# A11007; RRID: AB_10561522
Rabbit anti-phospho-Chk1 (S345) [clone 133D3]	Cell Signalling Technologies	Cat# 2348; RRID: AB_331212
Goat anti-Chk1	Bethyl Laboratories	Cat# A300-162A; RRID: AB_185532
Mouse anti-RECQL5 [clone 1A2]	Cell Signalling Technologies	Cat# 5847; RRID: AB_10834807
Rabbit anti-SLFN11 [clone D8W1B]	Cell Signalling Technologies	Cat# 34858; RRID: AB_2799063
Rabbit anti-SIRT1	EMD Millipore	Cat# 07-131; RRID: AB_2188349
Rabbit anti-GAPDH [clone 14C10]	Cell Signalling Technologies	Cat# 2118; RRID: AB_561053
Rabbit anti-Alpha-Tubulin [clone EPR13478(B)]	Abcam	Cat# ab176560; RRID: AB_2860019
Donkey anti-goat IgG-HRP	Santa Cruz	Cat# sc-2020; RRID: AB_631728
Goat anti-mouse IgG-HRP (H+L)	Promega	Cat# W4021; RRID: AB_430834
Goat anti-rabbit IgG-HRP (H+L)	Jackson immunoresearch	Cat# #111-035-003; RRID: AB_2313567

Appendix II

Supplementary tables related to the manuscript presented in chapter 3.

Supplementary table 3.1 | sgRNA sequences and associated indel sequencing primers for indicated genes

Gene	sgRNA #	sgRNA sequence (5'-3')	Indel sequencing primers (5'-3')
TERT	1	GCTGCGCAGCCACTACCGCG	PCR_F: CTTCACGTCCGGCATTCGT PCR_R: AGGAAGAGGGGGTTCTCGTC Seq.: CTCCTTCAGGCAGGACAC
TERT	2	ACGAAGCCGTACACCTGCCA	PCR_F: CTTCACGTCCGGCATTCGT PCR_R: AGGAAGAGGGGGTTCTCGTC Seq.: CGTGACGATGGAGACAGGAG
TERT	3	CCAAGAAGTTCATCTCCCTG	PCR_F: CTTCACGTCCGGCATTCGT PCR_R: AGGAAGAGGGGGTTCTCGTC Seq.: CGTGACGATGGAGACAGGAG
TAPR1	1	GCCGTGGCCCAGCTCTACAA	PCR_F: GGCAGCGGTTATCTGGTCC PCR_R: TAACATGCGCGCAGATGACT Seq.: GGCAGCGGTTATCTGGTCC
TAPR1	2	TTTGTAGAGATTGGTGACGG	PCR_F: GGCAGCGGTTATCTGGTCC PCR_R: TAACATGCGCGCAGATGACT Seq.: AAAGTTCGTCCCACTTCCGA
TP53	1	GAGAGAATCTCCGCAAGAAAG	PCR_F: NA PCR_R: NA Seq.: NA
Non-targeting (AAVS1)	1	GGGGCCACTAGGGACAGGAT	PCR_F: TGTGCCATCTCTCGTTTCTTA PCR_R: CACAAAGGGAGTTTTCCACA Seq.: GTCATGGCATCTTCCAGGGGTC
Non-targeting (AzGreen)	2	GGCCACAACTTCGTGATCGA	PCR_F: NA PCR_R: NA Seq.: NA

Supplementary table 3.2 | Clonal populations indel genotyping

Gene targeted and clone number	Frameshift genotype
TERT KO, clone #1	(+5, +7)
TERT KO, clone #2	(+1, +2)
TERT KO, clone #3	(+4, +2)
TERT KO, clone #4	(+7, -4)
TAPR1 KO, clone #1	(+1, +5)
TAPR1 KO, clone #2	(+2, -11)
TAPR1 KO, clone #3	(+5, +5)
TAPR1 KO, clone #4	(+2, +2)
TAPR1 KO, clone #5	(-1, +4)
TAPR1 KO, clone #6	(+2, +4)

Supplementary table 3.3 | Differentially expressed genes in TAPR1- and TERT-depleted NALM-6 cells. Genes upregulated in both TAPR1-deleted and TERT-deleted cells are highlighted in green.

Differential expression	Gene list
Upregulated in TAPR1-depleted NALM-6 cells	ABCF2, ACOT7, **AEN**, AHSA1, AIMP2, ATAD3A, ATAD3B, AVEN, **AVPR2**, B3GLCT, **BICDL1**, BOP1, BTBD6, BTBD9, C11orf98, C12orf43, C16orf72, CALR, **CCDC183-AS1**, CCDC86, **CCM2L**, CD3EAP, CDC20, CDK2AP2, **CDKN1A**, CHCHD4, CHORDC1, CLUH, COA7, CPSF2, CRELD2, **CROT**, CUEDC1, CYCS, DDC, DDN, DDX21, DHX37, DNAJA1, DNLZ, DPH2, DUSP2, EIF2B3, EIF3J, EIF4G1, **ELL3**, ETF1, FABP5, FABP5P3, FAIM, FAM136A, FAM166A, FAM222A, FAM86C1, **FAS**, FAT1, FCF1P2, FGFBP3, FKRP, GALNT10, GAR1, GPATCH4, **GPX1**, GRWD1, GTPBP4, HGH1, HIGD1A, HIVEP3, HNRNPAB, HSP90AA1, HSP90B1, HSP90B2P, HSPA1A, HSPA1B, HSPA5, HSPA8, HSPBP1, HSPE1, HSPE1-MOB4, HSPH1, HYOU1, **IER5**, IPO4, ISOC2, KLHL18, KLHL21, KPNA2, LANCL2, LARP4, LBHD1, LINC01963, LYAR, LYSMD2, MANF, MBNL1, METTL1, MFSD2A, MGC4859, **MICAL2**, **MPV17L2**, MRPL1, MRPL20, MRPS12, MRTO4, MYBBP1A, NCOA5, NDUFAF4, **NEB**, NGRN, NIFK, NME1, NOL6, NOP16, NOP56, **NR1D1**, PAK1IP1, PDSS1, PERP, PIGW, PLD6, **PLK3**, PNO1, POLR1A, POLR1B, POLR3B, POP1, PPARGC1B, PPIB, PPIF, PPIL1, PPRC1, **PRDM11**, PUS1, PYCR3, RABEPK, RCL1, RFK, RIOK1, RPF2, RPP40, **RPS27L**, RRP12, RRP15, RRP1B, RRP36, RRP7A, RRP9, RRS1, **SCAMP5**, SCO2, SDF2L1, SEC11C, SELENOS, **SERHL**, **SERHL2**, **SGPP2**, SHROOM3, SLC19A1, SLC25A19, SLC27A4, SLC35F2, SLC39A14, SLC5A6, SLIRP, SMIM4, SNHG12, SNHG16, SNHG3, SNHG4, SNORA100, SNORA105A, SNORA105B, SNX22, SORD2P, **SPNS2**, SPR, **SPTLC3**, SRM, **ST20-MTHFS**, **SULF2**, SURF2, TFB2M, TLR9, TOMM40, **TRIAP1**, TRMT61A, TSTA3, TWNK, UBXN8, URB1, UTP14A, UTP15, UTP20, VPS35L, VPS9D1-AS1, WDR3, WDR4, WDR43, WDR74, WDR77, **ZMAT3**, ZMPSTE24
Downregulated in TAPR1-depleted NALM-6 cells	ABCA2, ADGRE2, AGPAT2, AJUBA, AK1, ALDOC, ARHGAP29, BAHCC1, BEND5, BHLHE40, BIRC3, BLACE, BNIP3, BNIP3L, C2orf48, CBX7, CCDC26, CCDC74A, CCDC87, CCNG2, CCS, CD248, CD48, CD52, CDKN1C, CELSR3, CLEC11A, COL5A1, CORO6, DANT2, DDR1, DENND3, DNAAF4, DPEP1, EFNA1, EFNA3, EGFL7, EGR1, ELFN2, ENO2, ERVH48-1, FAM129B, FAM46C, FAM69B, FGD5, FMO5, FSTL4, FUT11, GBE1, GBP2, GDF9, GNA11, GOLGA8O, GYPC, HECTD2-AS1, HHIP-AS1, HSF4, HSPG2, IGFBP4, INSIG2, IRF8, ISG20, ITGB2, ITM2A, KCNN3, KCTD17, KDM4B, KDM7A, KIAA0895, KIAA1107, KIAA1147, KIAA1522, KLHL32, LGALS9, LINC00426, LINC00458, LINC00678, LINC01225, LINC01226, LINC01356, LINC01559, LINC02367, LOC101060391, LOC154761, LOC285766, LOC388436, LOC729291, LPIN3, MADCAM1, MDFI, MEGF6, MGC32805, MIR210HG, MMP25-AS1, MOB3A, MRC2, MST1, MYO15B, MYO1G, MYO7B, NDRG1, NEDD4L, NEDD9, NFATC1, NKD2, NRN1, ONECUT1, OPRL1, P2RX1, P3H2-AS1, P4HA2, PALM, PAM, PDE4B, PFKFB4, PICK1, PITPNM3, PLCH1, PPM1N, PRKCZ, PRKCZ-AS1, PTPRN2, PYGM, RAB17, RARA-AS1, RNASET2, RRAS, S100A10, SCNN1D, SERINC2, SFTPB, SH2D3C, SH3D21, SH3PXD2A, SLC12A7, SLC2A14, SLC2A3, SLC9A3-AS1, SPHK1, SPSB1, ST3GAL1, ST3GAL6, SYTL1, TBX2, TCL6, TCP11L2, TERT, TMCC2, TMEM107, TMEM119, TMEM44, TMEM8B, TNFRSF1B, TNS3, TOM1L2, TRAF1, TRIOBP, TSPAN9, TTC9, TUBA8, VEGFA, WT1, ZC3H6, ZDHHC24, ZNF436-AS1, ZNF516, ZNF844

Upregulated in TERT-depleted NALM-6 cells	A2M, AATBC, ABCA12, ABCA7, ACER2, ACSBG1, ACTA2, ADAM11, ADAM8, ADCY10P1, ADTRP, **AEN**, AJM1, AKR1B15, ALLC, ALPK3, AMY1A, AMY2B, AMZ2P1, ANK1, ANKAR, ANKRD20A12P, ANKRD20A19P, ANKRD20A9P, AOC2, AOC3, APCDD1, APOBEC3H, ARHGAP24, ARHGAP27P1-BPTFP1-KPNA2P3, ARHGEF40, ASCC3, ATE1-AS1, ATF3, ATP8B4, AVIL, AVPR1B, **AVPR2**, BASP1-AS1, BBC3, BCL3, BCO2, **BICDL1**, BIK, BIRC3, BLCAP, BMPER, C19orf18, C1S, C22orf46, C2orf16, C2orf66, C6orf163, CABLES1, CACFD1, CACNA1E, CALHM2, CALML6, CAMKK1, CAPN13, CAPN3, CARD14, CARD6, CASZ1, CBLN3, CCDC13, CCDC162P, **CCDC183-AS1**, CCDC9B, **CCM2L**, CCNA1, CCND2, CCR4, CCR7, CD1C, CD200R1, CD38, CD44, CD68, CD69, CD82, CD96, CDH4, CDHR2, CDIP1, CDKL2, **CDKN1A**, CEACAM1, CEACAM20, CEL, CELF6, CES4A, CFAP70, CHI3L2, CILP2, CLEC12B, CLEC14A, CLEC1B, CMAHP, CMPK2, CMTM3, CNR2, CNTD2, COL11A2, COL5A2, COL7A1, CPLX3, CPNE5, CPT1A, **CROT**, CSPG5, CUBN, CXCL8, CXCR2, CXorf21, CYB561A3, CYP2F1, CYP4F2, CYP4F3, DAPL1, DAPP1, DCAF4L1, DENND6B, DGCR9, DHRS2, DINOL, DNAH10, DNAH12, DNAH3, DNAJB13, DNAJB2, DNM3, DPEP2, DQX1, DRAM1, DRAXIN, DTX4, EDA2R, EFCAB5, EFEMP1, EFNB2, **ELL3**, ELOA2, ENDOD1, EPHA2, EPS8L2, ESYT3, ETV7, FAM13C, FAM3B, FAM49A, FAM71F2, **FAS**, FBXO32, FCGBP, FDXR, FGF7, FGF7P3, FGF7P6, FHDC1, FHL5, FLJ16779, FLJ32255, FLJ42969, FMO4, FN1, FOS, GABRB3, GALNT11, GALNT3, GAPT, GAS6-AS1, GBAT2, GBP2, GBP5, GDNF-AS1, GGT1, GHRLOS, GIMAP8, GJD3, GPR132, GPR35, GPR65, GPR68, **GPX1**, GRIN2C, GSDME, GTF2IRD2B, GVINP1, H3.Y, HAR1B, HCN2, HCST, HERC6, HGSNAT, HID1, HLA-DQA1, HLA-DQA2, HSF2BP, IDUA, **IER5**, IGF1, IL12RB1, IL12RB2, IL15, IL18RAP, IMPG2, IQCN, IRGM, ITGA10, ITIH4, JCHAIN, JUN, KALRN, KATNAL2, KCNJ12, KCNJ2-AS1, KCNK10, KCNMB1, KCNN2, KDM4E, KDR, KLHL14, KLHL31, KLK10, KLLN, KREMEN2, LAMB1, LAMB4, LCT, LGSN, LHFPL2, LIMD2, LIN7A, LINC00565, LINC00624, LINC00685, LINC00852, LINC00861, LINC00894, LINC00921, LINC00923, LINC00977, LINC01030, LINC01252, LINC01262, LINC01278, LINC01419, LINC01447, LINC01554, LINC01647, LINC01707, LINC01758, LINC02012, LINC02158, LINC02204, LINC02397, LINC02421, LINC02432, LINC02446, LINC02447, LINC02569, LOC100506258, LOC100506606, LOC100507053, LOC100507487, LOC100652768, LOC101927237, LOC101927402, LOC101927446, LOC101927623, LOC101928336, LOC101929748, LOC101930421, LOC102606465, LOC102723769, LOC105369486, LOC105371267, LOC105371855, LOC105372582, LOC105375218, LOC105379514, LOC150935, LOC155060, LOC339166, LOC401357, LOC643201, LOC653712, LOXL2, LRRC43, LRRN2, LTB, LTBP2, LY6G5C, MACROD2, MAFA, MALL, MAMDC4, MAPK11, MC1R, MDM2, METTL7A, MGAT3, **MICAL2**, MIR22HG, MIR3142HG, MMP11, MPEG1, **MPV17L2**, MS4A1, MTUS2, MUC16, MUC19, MUC20, MVP, MXD4, MXRA8, MYH15, MYO1A, MYO1C, MYO1E, MYOF, MYRFL, NEAT1, **NEB**, NECAB3, NECTIN4, NEK10, NFKBIA, NFKBID, NFKBIZ, NHLH1, NID2, NNAT, NODAL, NOTCH1, NOTCH3, NOXO1, NPEPL1, NPHP1, NPIPB6, NPIPB9, NPY, **NR1D1**, NR1H4, NTN1, NTNG2, OGFR-AS1, OGN, OR13A1, OR2B6, OR7E37P, P2RY14, PAPSS2, PATL2, PCNX2, PDCD4, PDCD4-AS1, PDE2A, PDE4B, PDE4D, PGAM2, PHLDA3, PIK3IP1, PIK3R5, PINCR, PLA2G4C, PLAC8L1, PLEK, PLEKHG1, PLEKHM1P1, PLGLB1, PLGLB2, **PLK3**, PLXNB3, POTEC, POU2F2, PRAMEF1, PRAMEF12, PRAMEF13, PRAMEF14, PRAMEF2, PRAMEF34P, PRAMEF36P, PRAMEF8, PRDM1, **PRDM11**, PRKCG, PRKY, PRODH, PROM1, PTGER4P2-CDK2AP2P2, PTPRH, PURPL, PVT1, PYY2, QRICH2, RELB, RGS1, RGS16, RGS8, RHCE, RHEX, RHOBTB1, RNA5-8SN1, RNA5-8SN5, RNF19B, **RPS27L**, RSPH10B, RUBCNL, RYR3, SAP30L-AS1, SAXO2, **SCAMP5**, SCHLAP1, **SERHL**, **SERHL2**, SERPINE1, SERPINF2, SERTAD1, SESN1, SESN3, SGIP1, SGK1, **SGPP2**, SH3BP5-AS1, SH3PXD2A, SHB, SHISA4, SIDT2, SKI, SLC25A18, SLC26A1, SLC2A6, SLC34A2, SLC36A3, SLC44A5, SLC46A1, SLFN5, SMAD7, SMIM14, SMOC1, SNORA16A, SNORA52, SNORD133,

	SNORD97, SNX20, SOX15, **SPNS2**, SPOCK2, SPTBN5, **SPTLC3**, SSH3, SSPO, **ST20-MTHFS**, STMN3, STRCP1, **SULF2**, SUOX, SUSD1, SYT11, SYTL2, TAGAP, TARSL2, TCP11L2, TCTE1, TENM1, TEX14, THSD4, TMEM150A, TMEM229B, TMEM56, TMEM71, TMEM9B-AS1, TMTC2, TNF, TNFRSF10B, TNFSF13, TNFSF13B, TNFSF4, TNFSF9, TNRC6C-AS1, TP53INP1, TP53TG1, TP63, TPH1, TREML2, **TRIAP1**, TRIM22, TRIM43, TRIM43B, TRIM55, TSGA10, TSPAN8, TXK, UBL7-AS1, UMODL1, UNC79, VAV2, VGF, VMAC, VNN1, VPREB3, VPS26B, VWCE, WDR78, WHRN, XKR4, XPC, ZBED9, ZDHHC11, ZMAT1, **ZMAT3**, ZNF117, ZNF132, ZNF300, ZNF423, ZNF425, ZNF521, ZNF561-AS1, ZNF610, ZNF80, ZSCAN4
Downregulated in TERT-depleted NALM-6 cells	ADGRE5, ADORA2B, AJUBA, AKAP12, AKAP2, ALDOA, ALDOC, ANG, ANO7, APLN, ARHGAP6, ASAP2, ASS1, ATF5, BCKDHA, BEND5, BHLHE40, BLACE, BNIP3, BNIP3L, C17orf53, C18orf54, C2orf48, C3orf58, C4orf47, CA11, CAP2, CARD19, CARHSP1, CCDC110, CCDC74A, CCDC87, CCS, CD9, CDC7, CDKN1C, CDT1, CEP112, CIT, CLEC11A, CLIC4, CMTM7, COL5A1, CORO6, CTD-2201I18.1, DDIT4, DDR1, DEPP1, DHCR7, DLG3, DNM1, E2F8, EFNA3, ELFN2, EMP2, ENO1, ENO2, ERG, ERVH48-1, ETV5, FADS1, FADS2, FAM129B, FAM162A, FAM46C, FAM69B, FANCE, FBXO36, FGD5, FSBP, FSTL4, FUT11, GBE1, GJC1, GNA15, GNG12, GNRH1, GPER1, GPR146, GPT2, GSE1, HACD1, HECTD2-AS1, HIP1, HIST1H2BJ, HIST1H3B, HIST1H3C, HIST1H3H, HIST1H4C, HIST1H4J, HIST1H4L, HK1, HK2, HLTF-AS1, HSPB7, IL21R, IL2RB, ING2, INHBC, INSIG1, INSIG2, IRX1, ITGB2, ITM2A, KCNN1, KCNN3, KCTD17, KIAA1522, LDHA, LFNG, LGR6, LINC00163, LINC00458, LINC01225, LINC01226, LINC01559, LITAF, LOC100507599, LOC101448202, LOC101928163, LOC105370526, LOC105378853, LOC150051, LOC154761, LOC728715, LONRF1, LRRC15, LSP1, MADCAM1, MAML2, MAP2K1, MGC12916, MGLL, MID1, MIER2, MIF, MIR210HG, MND1, MNS1, MOB3A, MSMO1, MT1F, MT1G, MT1H, MT1X, MTFP1, MXI1, MYBPH, MYO7A, NCKIPSD, NEDD4L, NEDD9, NKD2, NRN1, NXN, ONECUT1, OTUD1, P3H2-AS1, P4HA1, P4HA2, P4HA2-AS1, PALM2-AKAP2, PAM, PCDH18, PCK2, PDK1, PDK3, PFKFB3, PFKFB4, PFKL, PFKP, PGAM1P5, PGAM4, PGK1, PGM1, PHACTR3, PHF19, PHGDH, PICK1, PICSAR, PKM, PLAUR, PLCH1, POLG, PPP4R4, PRKCZ, PRKCZ-AS1, PRR7, PTPRN2, RAB17, RAB20, RAD51AP1, RAD54L, RASD1, RASSF4, RFX2, RGS3, RIBC2, RIMS3, RLF, RMI2, RNASET2, RPRML, RRAS, SAP30, SAPCD1-AS1, SARDH, SCD, SCN4A, SERINC2, SERPINE2, SESTD1, SH3D21, SLC12A7, SLC29A4, SLC2A1, SLC2A14, SLC2A3, SNX24, SPC24, SPHK1, SPTB, SSR4P1, ST3GAL1, ST3GAL6, STC2, STON1, TCL1B, TCL6, TERT, TIMP2, TMCC2, TMEM119, TMEM8B, TMPRSS6, TNFRSF1A, TNFRSF1B, TNS3, TPI1, TPI1P3, TRAF5, TRIB3, TRIM47, TSPAN7, TSPAN9, TUBB2A, USP28, VEGFA, VLDLR, VLDLR-AS1, WDR54, WT1, WWC3, ZBED8, ZC3HAV1L, ZNF318, ZNF395, ZNF436, ZNF436-AS1, ZNF442, ZNF511, ZNF833P